OCT 8 1968

ORNL
MASTER COPY

ORNL-4280
UC-34 – Physics

NEUTRON PHYSICS DIVISION
ANNUAL PROGRESS REPORT
FOR PERIOD ENDING MAY 31, 1968

OAK RIDGE NATIONAL LABORATORY
operated by
UNION CARBIDE CORPORATION
for the
U.S. ATOMIC ENERGY COMMISSION

Printed in the United States of America. Available from Clearinghouse for Federal Scientific and Technical Information, National Bureau of Standards, U.S. Department of Commerce, Springfield, Virginia 22151
Price: Printed Copy $3.00; Microfiche $0.65

LEGAL NOTICE

This report was prepared as an account of Government sponsored work. Neither the United States, nor the Commission, nor any person acting on behalf of the Commission:

A. Makes any warranty or representation, expressed or implied, with respect to the accuracy, completeness, or usefulness of the information contained in this report, or that the use of any information, apparatus, method, or process disclosed in this report may not infringe privately owned rights; or

B. Assumes any liabilities with respect to the use of, or for damages resulting from the use of any information, apparatus, method, or process disclosed in this report.

As used in the above, "person acting on behalf of the Commission" includes any employee or contractor of the Commission, or employee of such contractor, to the extent that such employee or contractor of the Commission, or employee of such contractor prepares, disseminates, or provides access to, any information pursuant to his employment or contract with the Commission, or his employment with such contractor.

ORNL-4280

Contract No. W-7405-eng-26

NEUTRON PHYSICS DIVISION
ANNUAL PROGRESS REPORT
For Period Ending May 31, 1968

F. C. Maienschein, Director
A. D. Callihan, Associate Director

Group Leaders

C. E. Clifford, Reactor and Weapons Radiation Shielding
R. G. Alsmiller, Theoretical Space and High-Energy Accelerator Shielding
R. W. Peelle, Experimental Space and High-Energy Accelerator Shielding

OCTOBER 1968

OAK RIDGE NATIONAL LABORATORY
Oak Ridge, Tennessee
operated by
UNION CARBIDE CORPORATION
for the
U. S. ATOMIC ENERGY COMMISSION

Reports previously issued in this series are as follows:

ORNL-2081	Period Ending September 10, 1956
ORNL-2389	Period Ending September 1, 1957
ORNL-2609	Period Ending September 1, 1958
ORNL-2842	Period Ending September 1, 1959
ORNL-3016	Period Ending September 1, 1960
ORNL-3193	Period Ending September 1, 1961
ORNL-3360	Period Ending September 1, 1962
ORNL-3499, Vols. I and II	Period Ending August 1, 1963
ORNL-3714, Vols. I and II	Period Ending August 1, 1964
ORNL-3858, Vols. I and II	Period Ending August 1, 1965
ORNL-3973, Vols. I and II	Period Ending May 31, 1966
ORNL-4134	Period Ending May 31, 1967

Contents

1. NUCLEAR AND REACTOR PHYSICS 1

1.0 Introduction 1

1.1 Multilevel Analysis of the ^{235}U Capture, Fission, and Total Cross Sections up to 100 eV – H. Derrien and G. de Saussure 1

1.2 Multilevel Analysis of the ^{233}U Capture and Fission Cross Sections up to 60 eV – G. de Saussure 8

1.3 Multilevel Analysis of the ^{239}Pu Total Cross Section – H. Derrien 11

1.4 Measurement of the Neutron Fission and Capture Cross Sections for ^{233}U in the Energy Region 0.02 to 4 eV – L. W. Weston, R. Gwin, G. de Saussure, R. W. Ingle, J. H. Todd, F. E. Gillespie, and R. W. Hockenbury 12

1.5 Measurement of the Neutron Fission and Capture Cross Sections for ^{233}U in the Energy Region 0.4 to 2000 eV – L. W. Weston, R. Gwin, G. de Saussure, R. R. Fullwood, and R. W. Hockenbury 12

1.6 Measurement of the Neutron Fission and Absorption Cross Sections of ^{239}Pu Over the Energy Region 0.01 eV to 30 keV – R. Gwin, L. W. Weston, G. de Saussure, R. W. Ingle, J. H. Todd, F. E. Gillespie, R. W. Hockenbury, and R. C. Block 13

1.7 Invariant Imbedding Approach to Nuclear Reaction Theory – R. B. Perez 16

1.8 An Algorithm for the Inversion of the Level Matrix – R. B. Perez 17

1.9 An Optical-Model Global Search Code: GENOA – F. G. Perey 19

1.10 Optical-Model Studies – F. G. Perey and C. M. Perey 19

1.11 On the Real Part of the Proton Optical-Model Potential – C. M. Perey and F. G. Perey 20

1.12 Neutron-Scattering Experiments – E. Hungerford, W. E. Kinney, and F. G. Perey 20

1.13 Neutron Elastic and Inelastic Scattering from ^{56}Fe from 4.60 to 7.55 MeV – W. E. Kinney 20

1.14 Calculated ^{56}Fe Neutron-Scattering and Gamma-Ray-Production Cross Sections from 1.0 to 7.6 MeV – W. E. Kinney and F. G. Perey 21

1.15 Elastic and Inelastic Scattering of 11.0-MeV Protons from ^{48}Ti, ^{51}V, ^{52}Cr, ^{54}Fe, ^{56}Fe, ^{59}Co, ^{60}Ni, ^{62}Ni, ^{64}Ni, ^{63}Cu, ^{65}Cu, ^{64}Zn, ^{66}Zn, and ^{68}Zn: Tabulated Differential Cross Sections – J. K. Dickens, F. G. Perey, and R. J. Silva 21

1.16 A New Measurement of the Lifetime of the ^{72}Ge 0+ State – E. Eichler, P. H. Stelson, and J. K. Dickens 22

1.17 Study of Gamma Rays for $(p,n\gamma)$ Reactions on Separated Isotopes of Zr and Mo – J. K. Dickens, E. Eichler, and R. Kuebbing 22

1.18 The $^{14}N(n,n'\gamma)$ Reaction for $5.8 \leqq E_n \leqq 8.6$ MeV – J. K. Dickens, E. Eichler, F. G. Perey, P. H. Stelson, J. Ashe, and D. O. Nellis 23

1.19 The $^{90,92,94}Zr(p,p')$ Reactions at 12.7 MeV – J. K. Dickens, E. Eichler, and G. R. Satchler 23

1.20 Elastic and Inelastic Scattering of Protons from ^{120}Sn for $E_p = 20.6$, 25.2, 30.6, and 36.2 MeV: Tabulated Differential Cross Sections – F. E. Bertrand, T. A. Love, N. Baron, F. G. Perey, and J. K. Dickens 24

1.21 Elastic and Inelastic Scattering of 62-MeV Protons from ^{12}C, ^{54}Fe, and ^{209}Bi – F. E. Bertrand, R. W. Peelle, J. K. Dickens 24

1.22 Differential Cross Sections for Levels Observed in the (p,d) Reaction on ^{12}C, ^{54}Fe, and ^{209}Bi and the (p,t) Reaction on ^{12}C at 62 MeV – F. E. Bertrand and R. W. Peelle 28

1.23 Neutrons from $^{9}Be(\alpha,n)$ Reaction for E_α Between 6 and 10 MeV – V. V. Verbinski, F. G. Perey, J. K. Dickens, and W. R. Burrus 33

1.24 Measurements of (d,n) Reactions on ^{58}Ni, ^{60}Ni, ^{62}Ni, and ^{64}Ni – A. L. Marusak, F. G. Perey, and P. H. Stelson 33

1.25 Oak Ridge Electron Linear Accelerator (ORELA) – A. L. Boch, J. A. Harvey, T. A. Lewis, F. C. Maienschein, J. A. Murray, and H. A. Todd 33

1.26 Neutron Flux and Neutron and Gamma-Ray Spectra Measurements at the HFIR – T. V. Blosser and G. E. Thomas, Jr. 34

1.27 Computer Program Development for the ENDF/B Effort – D. Irving and J. Stockton 34

2. CRITICAL EXPERIMENTS 36

2.0 Introduction 36

2.1 Preliminary Static Experiments with the ORNL Repetitively Pulsed Critical Assembly – J. T. Mihalczo 37

2.2 An Instrument for Measuring Mechanical Vibrations in Fast-Pulse Reactor Cores – James F. Ellis 37

2.3 Design and Mechanical Behavior of the Movable Reflector for the ORNL Repetitively Pulsed Critical Assembly – W. C. Tunnell and J. F. Ellis 38

2.4 Reactivity Coupling and Neutron-Transit-Time Distribution in Assemblies of Enriched Uranium Metal Cylinders – J. T. Mihalczo 40

2.5 Monte Carlo Calculations of Thick-Graphite-Reflected Uranium-Metal Critical Assemblies – J. T. Mihalczo 41

2.6 Critical Parameters of Enriched Uranium Metal Partly Reflected by Polyethylene – J. T. Mihalczo 43

2.7 Critical Experiments with Enriched Uranium Metal-Polyethylene, -Plexiglas, and -Teflon Mixtures – D. W. Magnuson 43

2.8 Critical Dimensions of Aqueous Solutions of Highly ^{235}U-Enriched Uranium Containing Borosilicate Glass; a Comparison of Monte Carlo Calculations and Experiments – J. Wallace Webster 44

2.9 Critical Parameters of Lattices of $U(62)O_2$-BeO Fuel Pins Moderated and Reflected by Water, Dilute Aqueous $U(93)O_2(NO_3)_2$ Solution, and Aqueous Boron Solution as a Guide to the Design of a Dissolver – E. B. Johnson 45

2.10 Effect of Steel-Water Reflectors on the Criticality of Low-Enriched Uranyl Fluoride Solution – E. B. Johnson and C. E. Newlon 47

2.11 Critical Lattices of U(4.89) Rods in Water and in Aqueous Boron Solution – E. B. Johnson 48

2.12 Critical Dimensions of Lattices of U(3.85) Cylindrical Annuli – E. B. Johnson 49

2.13 Homogeneous Critical Assemblies of $U(2)F_4$ in Paraffin at an H: ^{235}U Atomic Ratio of 972 – S. J. Raffety 50

2.14 Neutron Age and Infinite-Medium Neutron Multiplication Factor for UF_4-Paraffin Mixtures with Low ^{235}U Enrichment – S. J. Raffety and J. T. Mihalczo 51

2.15 O5R Monte Carlo Calculations of Low-Enriched Uranium, Thermal, Critical Assemblies and Evidence of Errors in ^{238}U Cross Sections – J. Wallace Webster 53

2.16 Critical Experiments with Aqueous Solutions of $^{233}UO_2(NO_3)_2$ – J. T. Thomas 53

2.17 Monte-Carlo-Calculated Criticality of Subcritical Components of ^{233}U, ^{235}U, and ^{239}Pu Arrayed in Cubic Geometry – J. T. Thomas 56

2.18 HFIR Fuel Elements: Reactivity Measurements on Single Elements and Arrays of Elements Moderated and Reflected by Water – E. B. Johnson 57

3. REACTOR AND WEAPONS RADIATION SHIELDING 60

3.0 Introduction 60

3.1 Development of One-Dimensional Shield Optimization Techniques – W. W. Engle, Jr. and F. R. Mynatt 61

3.2 Some Characteristics of Secondary Gamma-Ray Transport in Asymmetric SNAP Shields – F. R. Mynatt 62

3.3 General Study of Angular Biasing Techniques for Three-Dimensional Neutron-Transport Problem – C. E. Burgart and V. R. Cain 63

3.4 The Use of Discrete Ordinates Adjoint Calculations – V. R. Cain 63

3.5 Analytical Approach to the Angular-Dependent Importance Function – F. A. R. Schmidt 63

3.6 A Method for the Calculation of Neutron-Capture Gamma-Ray Spectra – K. J. Yost 66

3.7 Calculation of Neutron Capture Gamma-Ray Spectra – A Survey – K. J. Yost 66

3.8 Energy Dependence of Gamma-Ray Production Cross Sections and Their Utilization in S_N Codes – K. J. Yost 67

3.9 Sensitivity of Gamma-Ray Dose Calculations to the Energy Dependence of Gamma-Ray Production Cross Sections – K. J. Yost and E. Solomito 67

3.10 A Method for Approximating the Effect of the Energy Dependence of Neutron-Capture Gamma-Ray Spectra on Capture Gamma-Ray Dose Calculations – K. J. Yost 68

3.11 Preliminary Results of Calculations of Fast-Neutron Transmission Through LiH Slabs Below the TSF-SNAP Reactor – F. A. R. Schmidt and V. R. Cain 69

3.12 Measurement of the Absolute Power and Fission Distribution in the TSF-SNAP Reactor and Comparison with Monte Carlo and Discrete Ordinates Calculations – E. A. Straker, T. V. Blosser, L. B. Holland, F. J. Muckenthaler, V. R. Cain, F. R. Mynatt, J. J. Manning, and J. L. Hull 71

3.13 Measurement of the Energy Spectra of Neutrons Above 1 MeV Leaking from the TSF-SNAP Reactor – F. J. Muckenthaler, K. M. Henry, J. J. Manning, J. L. Hull, and R. M. Freestone, Jr. 71

3.14 Use of Space-Energy-Time Kernels for Studying Neutron Transport Problems – N. Cramer, P. N. Stevens, and E. A. Straker 75

3.15 Neutron Transport in the Atmosphere – E. A. Straker and R. J. Rodgers 75

3.16 Calculations of Neutron Transport in the Atmosphere and the Effect of Input Cross Sections – E. A. Straker, N. M. Greene, and R. J. Rodgers 77

3.17 Time-Dependent Neutron and Secondary Gamma-Ray Transport in an Air-Over-Ground Geometry – E. A. Straker, F. R. Mynatt, R. J. Rodgers, M. B. Emmett, and C. L. Thompson 78

3.18 Weapons Radiation Shielding Handbook: Status Report – L. S. Abbott, H. C. Claiborne, and C. E. Clifford, Editors 80

3.19 Thermal-Neutron Fluxes Within a Large Ducted Concrete Room – R. E. Maerker 80

3.20 Semiempirical Equations for Neutron-Induced Doses Within Rectangular Concrete Ducts – R. E. Maerker 83

3.21 Neutron Fluxes in Concrete Ducts Arising from Incident Thermal Neutrons: Calculation and Experiment – R. E. Maerker and F. J. Muckenthaler 88

3.22 Neutron Fluxes in Concrete Ducts Arising from Incident Epicadmium Neutrons: Calculations and Experiments – R. E. Maerker and F. J. Muckenthaler 89

3.23 Angle-Dependent Neutron Spectra Emergent from Slab Shields: Comparison of Two-Dimensional Discrete Ordinates Calculations with Experiment – F. R. Mynatt, F. J. Muckenthaler, and P. N. Stevens 89

3.24 Discrete Ordinates Calculations of Angle-Dependent Neutron Spectra in One-Dimensional Polyethylene and Graphite Spheres – F. R. Mynatt, L. R. Williams, and D. H. Wallace 91

3.25 Differential Neutron and Gamma Current Albedos for Concrete – R. J. Rodgers and F. R. Mynatt 93

3.26 Development and Application of the Discrete Ordinates Method – Miscellaneous Projects – F. R. Mynatt, R. J. Rodgers, L. R. Williams and D. H. Wallace 95

3.27 The Discrete Ordinates Method – Problems Involving Deep Penetrations – F. R. Mynatt 97

3.28 Comparison of Two Methods of Inner-Iteration Convergence Acceleration in Discrete Ordinates Codes – W. W. Engle, Jr., and F. R. Mynatt 97

3.29 CSP-I: A Neutron Cross-Section Averaging Package for Use with the O5R Data Tape – K. J. Yost and N. M. Greene 99

3.30 Shield Analysis and Design Service – H. C. Claiborne and E. Solomito 99

3.31 Modifications of the Point-Kernel Code QAD-P5A: Conversion to the IBM-360 Computer and Incorporation of Additional Geometry Routines – E. Solomito and J. Stockton 99

3.32 Calculations of Neutron Fluence-to-Kerma Factors for the Human Body – J. J. Ritts, E. Solomito, and P. N. Stevens 100

3.33 Current-to-Dose Conversion Factors for Neutrons Incident on Phantoms with Energies of 0.5 to 13.5 MeV – J. J. Ritts, E. Solomito, and P. N. Stevens 100

3.34 Shipping Cask Shielding Requirements – E. Solomito and H. C. Claiborne 101

3.35 Comparison of the Building Protection Factor Codes CAPS-2 and PF-COMP – M. L. Gritzner, P. N. Stevens, and H. C. Claiborne 103

3.36 Spectrum of Gamma Rays Emitted by a Stainless-Steel-Clad Pool-Type Reactor (BSR-II) – G. T. Chapman and W. R. Burrus 103

3.37 The Spectrum of Prompt Gamma Rays Above 1.5 MeV from Fission of ^{235}U – R. W. Peelle, W. Zobel, and F. C. Maienschein 104

4. RADIATION SHIELDING INFORMATION CENTER 106

4.1 Recent Developments in RSIC Operations – D. K. Trubey and Betty F. Maskewitz 106

4.2 Use of ICRU Units in Shielding – D. K. Trubey 108

4.3 A Survey of Recent Soviet Radiation Shielding Work – J. Lewin and J. Gurney 108

4.4 Comparisons of Results Obtained with Several Proton Penetration Codes – Part II – W. Wayne Scott and R. G. Alsmiller, Jr. 108

4.5 Energy and Dose Buildup Factors for Various Concretes – F. H. Clark and D. K. Trubey 109

4.6 Comments on Benchmarks, Milestones, and Testing in the Area of Radiation Transport – E. A. Straker and D. K. Trubey 109

5. RADIATION DETECTION AND DATA-HANDLING TECHNIQUES 110

5.0 Introduction 110

5.1 Response Functions for a 5- × 5-in. NaI(Tl) Detector Inside a Simple Collimator – R. E. Maerker 110

5.2 Determination of Response Functions of a 5-in. NaI Crystal to Gamma Rays with Energies Above 1 MeV – F. J. Muckenthaler, J. L. Hull, J. J. Manning, and K. M. Henry 114

5.3 Calibration of an Organic Scintillator for Neutron Spectrometry – V. V. Verbinski, W. R. Burrus, T. A. Love, W. Zobel, N. W. Hill, and R. Textor 118

5.4 Fast-Neutron Spectroscopy with Thick Organic Scintillators – W. R. Burrus and V. V. Verbinski 118

5.5 A Pulse-Shape Discrimination System for Use with NE-213 Organic Scintillator in Neutron Flight-Time Spectroscopy – W. A. Gibson and R. T. Santoro 119

5.6 Monte Carlo Calculation of the Gamma-Ray Response of an NE-213 Liquid Scintillator Counter – V. R. Cain, C. Y. Fu, E. A. Straker, P. N. Stevens, and F. J. Muckenthaler 121

5.7 A Digital Filter for Unfolding Pulse-Height Distributions – Myron H. Young and W. R. Burrus 125

5.8 SEGO, A Computer Code for Unfolding Experimental Pulse-Height Distributions – W. R. Burrus 125

5.9 Counting Techniques for Small Computers – B. W. Rust and W. R. Burrus 126

5.10 A Proton Microstructure Monitor for Neutron Measurements at ORIC – R. T. Santoro, J. W. Wachter, T. A. Love, J. K. Millard, and C. O. McNew 126

5.11 DORO 2: An Organic Scintillator Pulse-Height Analysis Code – R. M. Freestone, Jr. 129

5.12 Rejection of Pileup Pulses in Pulse-Height Spectrometry by Use of Associated Fast Timing Signals – R. W. Peelle, T. A. Love, and F. E. Bertrand 129

5.13 FLOTSAM – A Two-Parameter On-Line Data Acquisition Program for the PDP-7 – A. L. Marusak 132

5.14 A PDP-8 Interface for a Charged-Particle Nuclear Physics Experiment – W. R. Burrus, E. Madden, C. O. McNew, and R. W. Peelle 132

5.15 PDP-8 Program Development for Interactive Analysis of Data from Charged-Particle Experiments – R. W. Peelle, D. I. Putzulu, and F. E. Bertrand 133

5.16 Magnetic-Field Compensation with Pairs of Rectangular Coils – E. G. Silver 135

5.17 Status of Design and Construction of ORELAST (ORELA Scintillator Tank) – E. G. Silver, J. Lewin, and J. Todd 135

5.18 ORELA Data-Handling System – J. W. Reynolds, N. A. Betz, and D. R. Winkler 138

5.19 Significance Arithmetic Based on a Random Computer – C. M. Schneeberger and W. R. Burrus 139

6. THEORETICAL STUDIES FOR MEDIUM- AND HIGH-ENERGY RADIATION SHIELDING 140

6.0 Introduction 140

6.1 Calculation of the Capture of Negative Pions in Light Elements and Comparison with Experiment – M. P. Guthrie, H. W. Bertini, and R. G. Alsmiller, Jr. 140

6.2 Nucleon Emission Spectra from High-Energy Photon-Nucleus Collisions – T. A. Gabriel and R. G. Alsmiller, Jr. 142

6.3 Variation of the Neutron Spectrum in the Forward Direction with Changes in the Nuclear Density Distribution Used in the Intranuclear Cascade Calculation – H. W. Bertini 144

6.4 Spectra from Intranuclear-Cascade Calculations Using Three Isolated Regions of the Nucleus for 200-MeV Protons on Copper – H. W. Bertini 146

6.5 Secondary Particle Spectra from the Interaction of 450-MeV Protons on Complex Nuclei – H. W. Bertini and J. W. Wachter 148

6.6 Proton Spectra from 2.7-GeV Protons on Ag, Br Nuclei – D. T. King 150

6.7 Pion-Nucleon Differential Cross Sections in the 0 to 700-MeV Energy Region in Terms of the Coulomb Scattering Amplitude, Coulomb Phase Shifts, and Nuclear Phase Shifts up to $l = 4$ – H. W. Bertini 154

6.8 EVAP-2, A Modified Version of the Evaporation Code EVAP – M. Guthrie 154

6.9 NCDATA – Nuclear Collision Data for Nucleon-Nucleus Collisions in the Energy Range 25 to 400 MeV – R. G. Alsmiller, Jr., and J. Barish 155

6.10 Calculation of the Dose in Spherical Phantoms and Comparison with Experiment – D. C. Irving, R. G. Alsmiller, Jr., and H. S. Moran 155

6.11 Solar Neutron Transport in the Earth's Atmosphere – R. G. Alsmiller, Jr., and R. T. Boughner 157

6.12 Thermal-Neutron Flux Generation by High-Energy Protons – W. A. Coleman 157

6.13 Mathematical Verification of a Certain Monte Carlo Sampling Technique and Applications of the Technique to Radiation Transport Problems – W. A. Coleman 158

6.14 Monte Carlo Calculations of the Nucleon-Meson Cascade in Iron Initiated by 1- and 3-GeV Protons and Comparison with Experiment – T. W. Armstrong and R. G. Alsmiller, Jr. 158

6.15 Residual Radiation Levels in the Tunnel of a 200-GeV Proton Accelerator as a Function of Time After Shutdown – T. W. Armstrong and R. G. Alsmiller, Jr. 158

6.16 High-Energy Muon Transport and the Muon Backstop for a 200-GeV Accelerator – R. G. Alsmiller, Jr., M. Leimdorfer, and J. Barish 160

6.17 Shielding Calculations for a 400-MeV Linear Electron Accelerator – R. G. Alsmiller, Jr., J. Barish, R. T. Boughner, and W. W. Engle 162

6.18 Dose Rate from High-Energy Electrons and Photons – R. G. Alsmiller, Jr., and H. S. Moran 162

6.19 The Electron-Photon Cascade Induced in Lead by Photons in the Energy Range 15 to 100 MeV – R. G. Alsmiller, Jr., and H. S. Moran 162

6.20 An Estimate of the Prompt Photon Spectrum Arising from Cosmic-Ray Bombardment of the Moon – T. W. Armstrong and R. G. Alsmiller, Jr. 162

7. EXPERIMENTAL STUDIES FOR MEDIUM-ENERGY RADIATION SHIELDING 164

7.0 Introduction 164

7.1 Differential Cross Sections for the Charged Particles Produced by 60-MeV Protons on Carbon, Iron, and Bismuth – F. E. Bertrand, R. W. Peelle, T. A. Love, N. W. Hill, and W. R. Burrus 164

7.2 Differential Cross Sections for the Proton Continuum Produced by 60-MeV Proton Bombardment of ^{12}C, ^{54}Fe, and ^{209}Bi and Comparison with Intranuclear Cascade Calculations – F. E. Bertrand and R. W. Peelle 165

7.3 Cross Sections for the Production of Proton, Deuteron, Triton, ^{3}He, and Alpha Particles by 60-MeV Proton Bombardment of Carbon, Iron, and Bismuth – F. E. Bertrand and R. W. Peelle 170

7.4 A Four-Parameter E vs dE/dx and Time-of-Flight Computerized Charged-Particle Experiment – F. E. Bertrand, W. R. Burrus, N. W. Hill, T. A. Love, R. W. Peelle, and B. W. Rust 175

7.5 Direct and Compound-Nucleus Neutrons from 14- to 18-MeV Protons on ^{9}Be, ^{14}N, ^{27}Al, ^{56}Fe, ^{115}In, ^{181}Ta, and ^{208}Pb and from 33-MeV Bremsstrahlung on ^{27}Al, ^{206}Pb, ^{208}Pb, and ^{209}Bi – V. V. Verbinski and W. R. Burrus 175

7.6 A Flight-Time Spectroscopy System for Neutrons from 25- to 60-MeV Protons on Nuclei – J. W. Wachter, R. T. Santoro, T. A. Love, and J. K. Millard 176

7.7 Neutron and Proton Spectra from Targets Bombarded by 450-MeV Protons – J. W. Wachter, W. A. Gibson, and W. R. Burrus 178

7.8 A Spectrometer System for Studying 2- to 40-MeV Neutrons in the Upper Atmosphere – W. Zobel, T. A. Love, and J. T. DeLorenzo 178

PUBLICATIONS AND PAPERS PRESENTED AT SCIENTIFIC MEETINGS 183

1. Nuclear and Reactor Physics

1.0 INTRODUCTION

Rarely a question concerning cross-section values occupies a central position in determining the feasibility or economic desirability of a reactor system. Recently such a question has apparently been raised by measurements in Britain and Europe which indicated that the value of the capture-to-fission ration $\alpha(E)$ for ^{239}Pu in the energy range 1 to 10 keV was much higher than had previously been assumed. Fortunately, the ORNL-RPI cooperative program to measure $\alpha(E)$ at the Rensselaer Polytechnic Institute linear accelerator facility enabled pertinent and perhaps definitive data to be obtained for the cross section in question. The *preliminary* results described in Section 1.6 indicate clearly that the recently reported British values of $\alpha(E)$ are too high and that the penalties in fast-reactor breeding and economics are not so great as have recently been feared. The results do support an appreciable increase in $\alpha(E)$ in the energy range under consideration from the assumptions of a year ago, however.

Other measurements of capture, fission, and total cross sections for the fissile isotopes have been carried out, together with multilevel analyses of the results. A program to provide theoretical support for measurements in the resonance energy region (resolved and unresolved) has been initiated on a limited basis. Progress has been made in obtaining a pulsed-neutron source at ORNL, and operation of this facility is planned within the next year.

A continuing program of neutron-scattering studies includes the direct measurement of neutron elastic and inelastic scattering for materials of interest to the US Atomic Energy Commission reactor program. A unique feature of these measurements is their extension in neutron energy to 11 MeV. In addition, equipment has been added for determining the spectra of gamma rays produced by neutron interactions. Cross sections for gamma-ray production are needed more than any others for the design of shields against nuclear weapons radiations.

Although these measurements are obtained with an efficient computer-centered data-handling system, they can never encompass the degree of detail required for reactor calculations. Thus considerable emphasis is given to the development of nuclear models that can be used to predict cross sections of interest, and a concomitant program of charged-particle measurements is carried out to provide precise data in support of this model development.

1.1 MULTILEVEL ANALYSIS OF THE ^{235}U CAPTURE, FISSION, AND TOTAL CROSS SECTIONS UP TO 100 eV

H. Derrien[1] G. de Saussure

In our 1967 Annual Progress Report a multilevel analysis of the ^{235}U capture and fission cross sections in the neutron energy range 0.4 to 30 eV was presented.[2] The analysis was based on a simultaneous least-squares fit of the capture and fission cross sections to the multilevel expression developed by Adler and Adler.[3] This analysis has now been extended to the energy region 0.035 to 100 eV. Below 0.4 eV the analysis is based on the data of Brooks and Jolly,[4] whereas above 0.4 eV it is based on results of an ORNL–Rensselaer Polytechnic Institute measurement.[5] The computed and experimental cross sections are compared in Fig. 1.1.1 for the energy range 30 to 60 eV and in Fig. 1.1.2 for the range 60 to 100 eV.

The parameters[6] which were used to compute the total cross section are given in Table 1.1.1. The

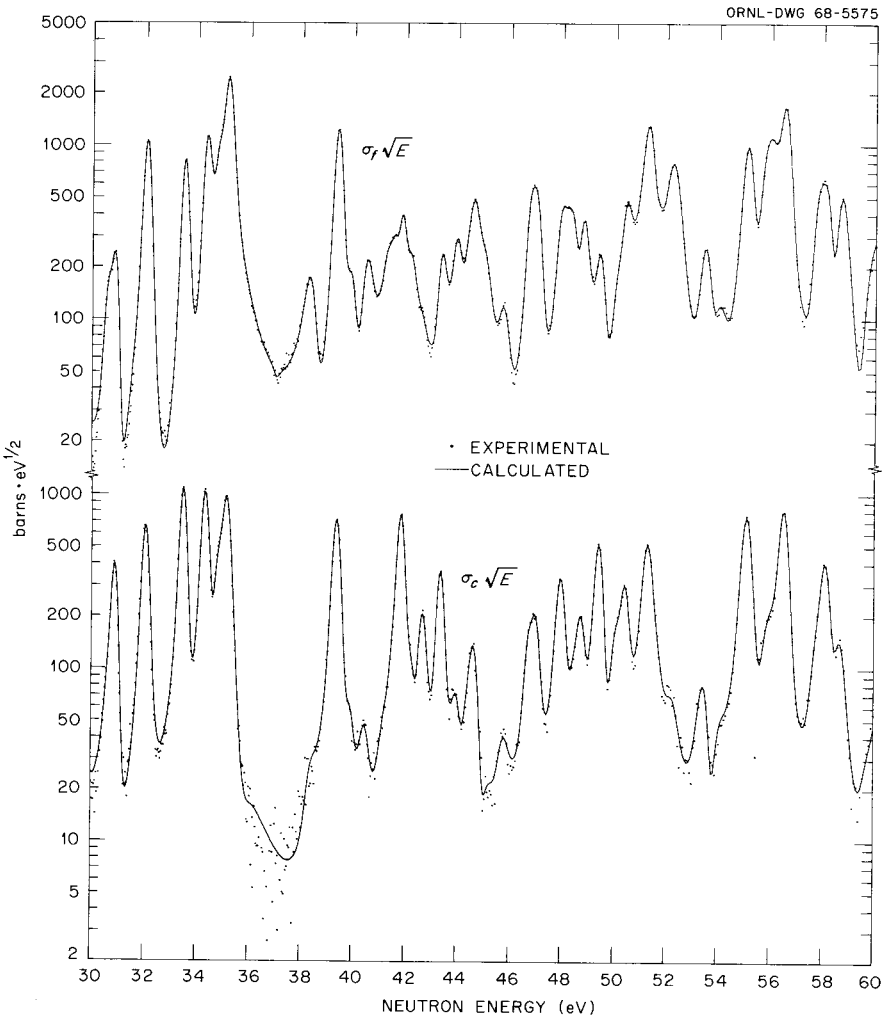

Fig. 1.1.1. Least-Squares Fit to the ^{235}U Capture and Fission Cross Sections.

result of this computation was compared with the total cross-section data from a transmission measurement done at Saclay,[7] with the sample kept at liquid nitrogen temperature (77°K). Systematic discrepancies were observed[8] between the computed and measured total cross sections, probably resulting from an underevaluation of the resolution function in the ORNL-RPI measurement[5] and from the basic uncertainties to be expected in unfolding the Doppler broadening.

A multilevel analysis of the total cross section measured at Saclay was also performed. Figure 1.1.3 shows a comparison of the computed cross section with the experimental data, as well as a comparison of the absorption cross section, computed with the same parameters, with the data from the ORNL-RPI measurement.

The Saclay transmission measurement will yield better values for the energy and total width of the resonances than can be obtained from the ORNL-RPI measurements because the measurement at Saclay had a better energy resolution. The Saclay transmission measurement was done on a flight path of 50 m with the sample at a temperature of 77°K, whereas the ORNL-RPI measurement was done on a flight path of 25 m with a sample temperature of 300°K. A consistent best set of resonance parameters is being developed for which the position and width of the levels are determined primarily from the Saclay transmission data, whereas the fission and capture amplitudes are derived from the ORNL-RPI data.

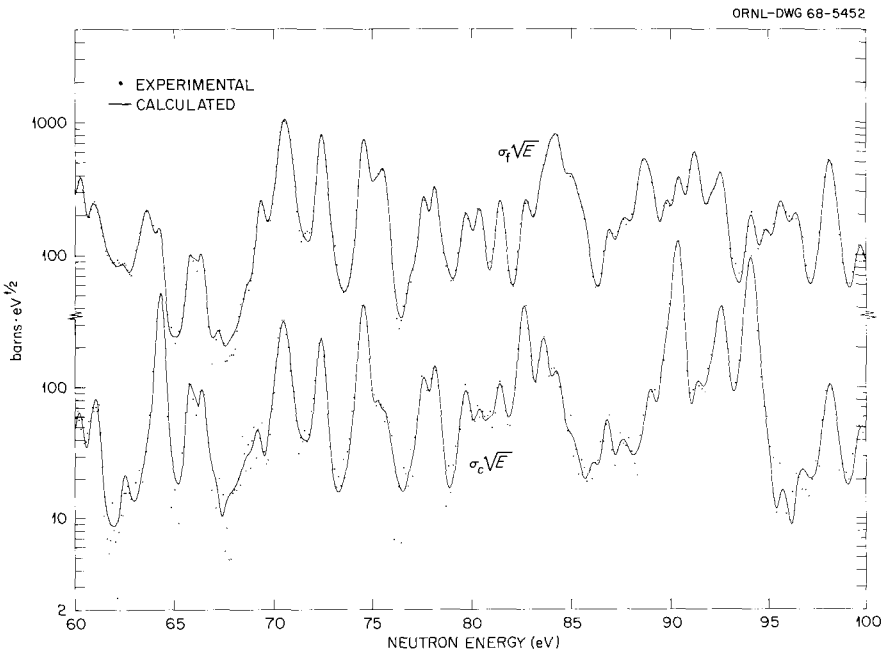

Fig. 1.1.2. Least-Squares Fit to the ^{235}U Capture and Fission Cross Sections.

Table 1.1.1. Resonance Parameters for ^{235}U

μ (eV)	ν (eV)	G_c (beV$^{3/2}$)	H_c (beV$^{3/2}$)	G_f (beV$^{3/2}$)	H_f (beV$^{3/2}$)
−1.05	0.10	355.17	19.22	1170.15	19.31
0.29	0.06	1.12	−0.10	2.35	−1.19
1.14	0.08	2.32	−0.28	6.69	2.79
2.03	0.03	2.80	0.12	0.83	0.15
2.73	0.07	0.23	0.06	−0.76	−0.59
3.16	0.08	2.03	0.31	5.90	2.45
3.61	0.05	6.53	0.19	9.95	3.21
4.84	0.02	16.14	0.19	1.73	0.11
5.42	0.16	0.57	−0.22	3.01	−1.99
6.23	0.10	1.85	−0.93	10.07	5.68
6.38	0.03	55.42	1.68	16.61	0.64
7.08	0.04	16.80	0.25	14.11	1.09
7.77	0.17	−0.12	−0.34	−1.44	0.95
8.44	0.18	−0.26	−0.97	−0.20	−3.19
8.77	0.07	61.63	0.51	177.22	−14.87
9.29	0.05	8.62	2.31	15.93	1.59
9.92	0.31	−0.19	3.75	−0.68	22.94
10.16	0.07	5.00	−0.10	9.60	−2.95
10.76	0.44	−1.94	1.92	11.56	5.53
11.66	0.03	97.29	3.58	13.89	3.91
12.40	0.04	133.06	5.85	103.06	14.61
12.86	0.10	3.59	−0.24	10.57	2.40
13.30	0.12	2.46	0.56	9.19	2.87
13.65	0.14	3.24	−1.60	9.18	−6.90
14.00	0.26	3.42	−0.42	79.98	2.54
14.55	0.04	12.47	0.18	6.09	4.39
15.42	0.06	17.41	0.64	22.70	5.30
16.09	0.04	38.70	1.66	23.95	3.43
16.66	0.09	10.72	0.70	35.34	−5.40
18.04	0.09	11.11	1.40	41.49	−4.07
18.98	0.08	8.68	−2.18	6.68	0.45
19.30	0.07	166.92	7.26	291.05	9.72
20.21	0.13	3.63	−0.57	7.23	7.86
20.61	0.07	9.49	−3.64	15.35	1.92
21.07	0.05	114.73	8.92	91.02	6.25
22.94	0.06	25.52	1.68	35.91	1.80
23.43	0.05	88.22	10.87	25.93	3.31
23.63	0.12	15.51	−5.08	85.95	−9.17
24.23	0.08	27.79	−1.69	22.44	−16.81
25.65	0.35	6.43	−0.66	138.42	83.69
26.44	0.16	11.22	0.41	69.42	−30.40
27.21	0.04	2.51	0.90	3.52	3.63
27.81	0.10	23.73	−0.35	69.31	−2.60
28.35	0.11	4.26	−0.08	16.91	−4.40
28.77	0.04	0.76	0.53	1.05	0.63
29.68	0.05	10.92	1.42	7.56	1.63
30.59	0.09	1.41	−0.99	12.53	−3.72
30.91	0.07	44.76	10.44	21.95	11.46

Table 1.1.1. (Continued)

μ (eV)	ν (eV)	G_c (beV$^{3/2}$)	H_c (beV$^{3/2}$)	G_f (beV$^{3/2}$)	H_f (beV$^{3/2}$)
32.10	0.08	83.36	5.24	135.24	12.63
33.55	0.07	123.20	14.48	95.21	4.06
34.39	0.09	142.82	20.02	139.89	−8.19
34.85	0.14	51.16	−30.97	113.40	−18.75
35.21	0.11	133.79	10.35	344.31	−2.53
35.75	0.49	−13.41	−14.72	22.87	−2.86
37.06	0.06	0	0	−0.69	0.13
38.42	0.19	2.37	−1.73	29.38	19.08
39.44	0.09	100.65	8.57	173.72	8.47
39.92	0.10	5.13	−2.73	19.61	−4.82
40.51	0.15	6.93	0.17	30.59	−15.07
41.39	0.14	4.04	6.14	28.45	15.81
41.64	0.06	8.12	5.79	22.59	9.43
41.91	0.08	116.62	8.35	55.77	3.87
42.16	0.13	6.34	−24.56	25.90	−27.25
42.70	0.06	19.46	−8.75	1.98	0.91
43.41	0.04	37.32	−2.68	16.39	−3.96
44.04	0.04	3.71	2.05	16.03	9.45
44.75	0.15	28.04	18.97	44.47	77.33
44.97	0.28	0.48	−18.58	115.80	−25.84
45.79	0.17	4.62	−2.13	19.94	0.81
46.92	0.06	23.63	46.08	76.90	122.36
46.98	0.05	18.05	−45.31	44.67	−112.13
48.06	0.12	63.65	15.86	57.16	27.75
48.35	0.20	0.34	−31.20	111.16	−31.57
48.82	0.03	12.20	2.97	24.51	−17.36
49.51	0.06	62.25	16.21	20.95	8.17
50.24	0.19	50.92	10.29	45.88	−11.55
50.45	0.02	17.73	−14.09	17.13	−18.65
51.37	0.13	95.45	11.14	219.55	95.05
51.68	0.11	7.72	−5.29	38.42	−18.29
52.27	0.25	13.54	−0.52	234.92	12.25
53.56	0.14	14.61	9.56	50.23	20.72
53.98	0.23	6.83	−9.89	31.35	−16.34
55.16	0.12	140.49	20.04	178.46	60.80
55.87	0.33	45.26	−47.31	369.01	−178.43
56.58	0.07	110.91	13.74	195.16	36.97
57.83	0.10	13.87	3.20	70.75	−9.76
58.15	0.08	60.82	0.75	69.04	9.23
58.68	0.12	22.27	−5.35	88.98	−34.96
59.75	0.28	4.39	−4.99	35.72	−67.35
60.25	0.10	7.56	−0.43	35.51	−8.03
60.76	0.05	0.96	−1.35	6.99	−10.52
61.10	0.12	12.44	2.61	13.09	−0.97
62.03	1.03	−4.42	−2.60	−8.48	23.61
62.49	0.10	2.13	−0.79	2.53	2.04
63.64	0.32	4.81	−2.67	65.30	10.05
64.31	0.08	81.38	2.17	15.31	5.56

Table 1.1.1. (Continued)

μ (eV)	ν (eV)	G_c (beV$^{3/2}$)	H_c (beV$^{3/2}$)	G_f (beV$^{3/2}$)	H_f (beV$^{3/2}$)
65.81	0.09	16.50	−0.82	12.70	−0.64
66.39	0.10	14.02	−2.27	13.74	3.02
67.29	0.03	−0.62	0.77	0.74	0.74
68.66	0.10	1.11	0.25	3.08	0.10
69.37	0.11	2.24	5.28	34.43	−0.41
70.54	0.26	97.61	7.57	276.76	9.37
70.80	0.16	1.00	−0	59.35	0.72
71.61	0.25	2.97	−0	8.33	−0
72.45	0.12	45.39	3.70	157.02	−0.91
72.91	0.16	0	−0	7.81	−0
74.62	0.14	95.32	11.38	153.92	−2.18
75.24	0.16	15.90	−9.64	58.38	0.78
75.62	0.09	3.69	−5.33	59.40	−0.24
76.94	0.15	1.71	−1.24	8.86	−1.93
77.62	0.17	26.06	−3.08	63.33	−3.83
78.18	0.03	13.25	−3.45	37.05	−2.14
78.51	0.16	3.35	5.18	11.20	−9.70
79.75	0.18	20.99	0.34	42.27	−1.66
80.45	0.12	9.03	0.44	36.86	0.17
80.95	0.16	7.30	0	0	0
81.49	0.12	16.84	0.41	46.71	0.32
82.06	0.16	2.61	−0	0	−0
82.73	0.14	90.59	4.23	42.63	−10.52
83.68	0.14	47.34	−0.91	54.65	16.13
84.06	0.09	0	−0	72.13	12.36
84.39	0.16	24.65	1.94	153.16	−2.97
85.08	0.33	9.59	−1.06	123.68	−12.55
85.75	0.16	−0.79	0.92	17.65	7.88
86.14	0.16	3.01	−0	0	−0
86.95	0.06	6.27	2.58	15.80	−0.34
87.72	0.35	11.52	3.55	56.54	3.12
88.72	0.22	−1.75	4.71	130.24	10.74
89.10	0.16	20.53	6.88	55.09	−4.85
89.90	0.16	37.91	6.33	55.82	−3.85
90.44	0.10	263.08	−2.56	56.92	−26.97
91.32	0.16	10.85	−19.53	128.32	−7.41
92.25	0.16	20.66	1.32	40.27	13.21
92.68	0.11	76.76	−0.11	74.11	4.36
93.30	0.16	0	−0	6.04	−0
94.16	0.14	222.21	7.08	40.04	−0.13
94.89	0.16	3.73	−0	27.21	−2.84
95.66	0.20	2.09	−4.90	57.80	−5.30
96.50	0.20	1.24	−5.78	44.65	8.82
98.16	0.21	29.27	−1.57	150.43	0.51
99.69	0.16	8.54	−2.01	23.96	−1.42
100.48	0.16	18.89	−0	28.24	0.98
101.07	0.16	37.23	−0	27.96	−5.73

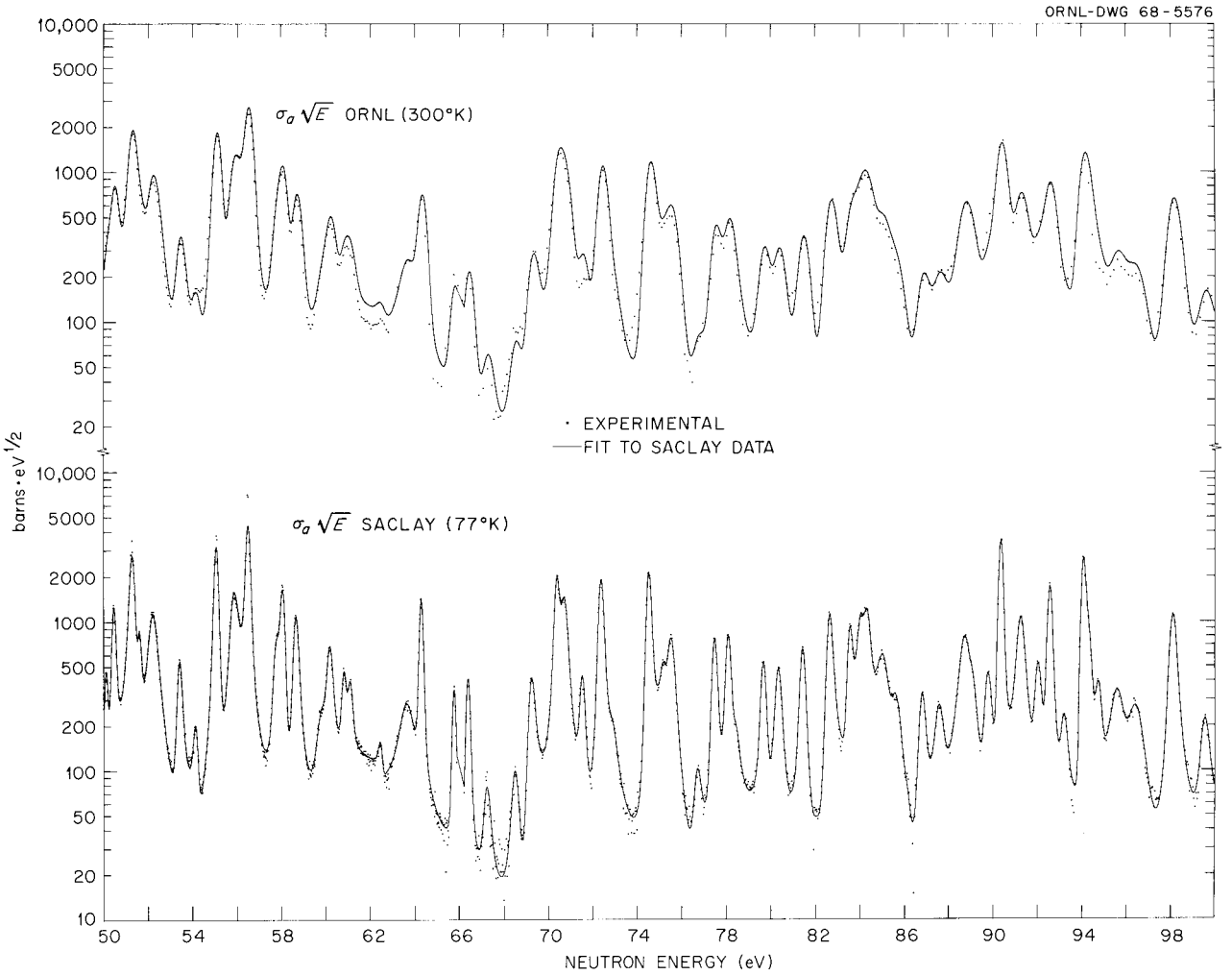

Fig. 1.1.3. Least-Squares Fit to the ^{235}U Absorption Cross Section at 77°K – Comparison with Data at 300°K.

References

[1]On loan from Centre d'Études Nucléaires de Saclay, France.

[2]G. de Saussure, *Neutron Phys. Div. Ann. Progr. Rept. May 31, 1967,* ORNL-4134, p. 1.

[3]D. B. Adler and F. T. Adler, p. 695 in *Proceedings of the Conference on Breeding, Economics and Safety in Large Fast Power Reactors, October 7–10, 1963,* ANL-6792. See also D. B. Adler and F. T. Adler, *Multilevel Analysis of the U^{235} Total and Fission Cross Sections in the Energy Region Below 37 eV,* BNL-50045 (T-455) (March 1967).

[4]F. D. Brooks *et al., Eta and Neutron Cross Sections of U-235 from 0.04 to 200 eV,* AERE-M-1670 (1966).

[5]G. de Saussure *et al.,* p. 233 in *Proceedings of the IAEA Symposium on Nuclear Data – Microscopic Cross Sections and Other Data Basic for Reactors, Paris, October 17–21, 1966,* Vol. II, IAEA, Vienna, 1967. A tabulation of these data is given in ORNL-TM-1804 (1967).

[6]For a definition of the resonance parameters see Eq. 1 of Ref. 2.

[7]A. Michaudon *et al., Nucl. Phys.* **69**, 545–572 (1965).

[8]This comparison was discussed at the American Nuclear Society Winter Meeting, November 5–9, 1967, in Chicago.

1.2 MULTILEVEL ANALYSIS OF THE ^{233}U CAPTURE AND FISSION CROSS SECTIONS UP TO 60 eV

G. de Saussure

The need for resonance parameters which accurately describe the low-energy cross sections of fissile nuclides has recently been re-emphasized by Harris,[1] Perry,[2] and others.[3]

In our 1967 Annual Progress Report a multilevel analysis of the ^{233}U capture and fission cross sections in the neutron energy range 0.4 to 30 eV was presented.[4] This analysis has now been extended to the range 0.01 to 60 eV.

Above 0.4 eV the analysis was based on experimental data obtained in 1966 by Weston *et al.*[5] Below 0.4 eV it was based on evaluated data provided by Craven.[6] The computed and experimental cross sections in the range 30 to 60 eV are shown in Fig. 1.2.1. This figure suggests that the resonance parameters provide an accurate representation of the fission cross section. The uncertainties in the measured capture cross section are illustrated by the scatter in the experimental data. Because of these uncertainties the analysis of the capture cross section is meaningful only in the vicinity of the peak of some of the most important resonances.

The large uncertainties in the measured capture cross section are partly due to the low value of this cross section compared with the fission cross section.[5] Hence the capture is only a small contribution to the absorption in ^{233}U, and the absorption and total cross sections can be computed fairly accurately in spite of the poor knowledge of the capture parameters. This is illustrated in Fig. 1.2.2, where the total cross section computed with the resonance parameters obtained by fitting the fission and capture measurements is compared with experimental data from the transmission measurement of Pattenden and Harvey.[7] For the calculation of the total cross section of Fig. 1.2.2, a constant scattering cross section of 12.5 barns was assumed.[8]

More precise data from a measurement performed in 1967 have recently become available,[9] and the resonance parameters are being updated by a least-squares fit to the new data. Table 1.2.1 lists preliminary values of these parameters.[10]

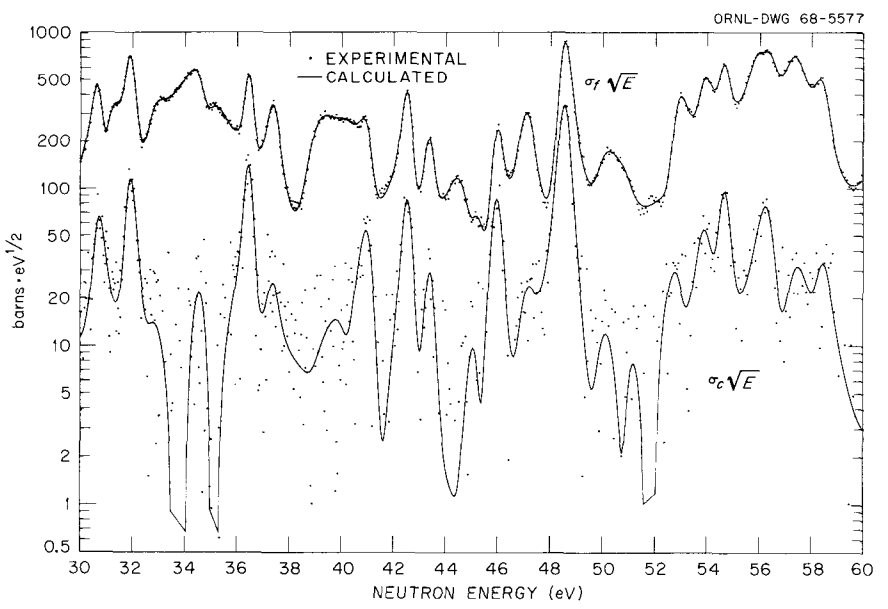

Fig. 1.2.1. Least-Squares Fit to the ^{233}U Capture and Fission Cross Sections.

Table 1.2.1. Preliminary Resonance Parameters of ^{233}U

μ (eV)	ν (eV)	G_c (beV$^{3/2}$)	H_c (beV$^{3/2}$)	G_f (beV$^{3/2}$)	H_f (beV$^{3/2}$)
−2.79	0.37	120.75	−3.51	−1511.99	−513.24
0.18	0.07	0.27	−0.04	−0.19	−0.83
1.43	0.35	2.70	−7.24	66.91	−31.81
1.78	0.12	26.06	5.47	111.08	−1.78
2.29	0.05	37.05	1.89	42.47	17.64
3.29	0.51	1.26	1.12	36.93	−42.08
3.63	0.08	9.29	0.93	20.91	7.23
4.53	0.39	3.89	−2.24	44.29	−51.91
5.74	0.18	3.41	−1.79	11.04	−24.25
6.80	0.09	57.38	3.05	168.68	35.89
7.50	0.11	1.97	1.33	5.93	2.23
8.67	0.26	2.50	−0.76	15.01	4.05
9.15	0.15	3.77	−0.44	17.63	−15.41
10.35	0.16	55.23	3.35	276.95	7.65
11.20	0.27	2.68	−3.19	41.21	−4.76
12.76	0.16	32.11	2.06	226.13	44.65
13.51	0.14	7.76	1.11	−12.21	4.42
13.63	0.24	5.49	−2.16	101.85	3.03
15.28	0.12	46.08	−2.03	118.40	−33.36
16.15	0.22	6.91	−1.14	106.78	7.14
16.51	0.13	20.72	2.55	97.21	17.74
17.92	0.10	8.63	1.66	37.37	4.27
18.46	0.25	10.00	2.14	78.36	20.69
18.86	0.15	36.00	0.17	213.21	−61.33
20.53	0.21	20.01	1.15	116.58	6.91
21.85	0.13	34.39	13.11	131.87	95.43
22.23	0.24	66.98	−8.29	545.37	−90.62
22.94	0.38	−6.43	−7.82	96.53	−6.68
23.54	0.33	5.05	1.07	61.03	−95.86
25.13	0.19	15.88	0.18	85.00	−44.81
26.57	0.28	13.75	1.21	58.70	19.73
28.42	0.28	17.47	6.33	29.85	86.46
28.91	0.31	13.81	−15.88	233.67	−62.48
29.68	0.11	2.97	−0.04	−0.16	16.34
30.15	0.10	−0.96	−1.11	2.27	−0.71
30.76	0.15	11.69	0.88	52.79	51.39
31.20	0.47	12.41	−4.82	149.57	−72.18
31.97	0.15	23.63	−8.15	113.99	6.79
32.74	0.43	−1.78	−10.47	42.61	−96.58
34.03	0.66	−22.26	−21.40	112.79	26.70
34.53	0.42	6.33	13.71	168.73	21.71
35.19	0.12	−2.92	1.08	27.07	−8.85
35.49	0.16	0.98	5.12	10.72	−24.48
36.52	0.09	20.52	4.03	59.13	11.50
37.46	0.19	4.64	1.81	64.70	14.44
39.48	0.22	1.39	−2.51	67.55	76.24
39.71	0.11	−2.94	0.50	34.07	−27.73
40.15	0.45	4.87	7.67	97.39	−80.00

Table 1.2.1. (Continued)

μ (eV)	ν (eV)	G_c (beV$^{3/2}$)	H_c (beV$^{3/2}$)	G_f (beV$^{3/2}$)	H_f (beV$^{3/2}$)
41.08	0.10	10.80	4.27	19.88	13.37
42.62	0.11	17.35	3.72	62.23	15.86
43.47	0.13	6.76	0.67	32.49	6.16
44.70	0.56	7.79	12.83	93.00	36.62
45.21	0.25	2.46	−3.23	1.91	−23.98
45.99	0.12	17.43	−6.39	33.33	−26.17
47.17	0.23	3.55	−4.39	75.74	−9.08
48.64	0.13	80.38	2.44	167.38	−21.20
49.12	0.09	−2.74	−4.94	9.68	−6.64
50.21	0.45	−3.19	−4.48	55.75	−31.14
50.99	0.38	−2.27	−6.83	16.84	−4.13
51.95	0.62	−17.85	3.79	12.00	−41.84
52.93	0.22	8.85	4.14	53.45	−62.43
53.97	0.14	11.77	2.99	61.95	−25.09
54.77	0.09	20.52	3.05	61.08	6.13
56.09	0.27	3.83	2.11	69.62	128.22
56.35	0.30	25.61	6.04	211.98	−60.39
57.48	0.49	17.92	3.53	282.72	20.92
58.51	0.23	11.03	−2.43	91.51	26.41
61.30	0.40	8.35	−1.18	185.51	47.48
62.50	0.20	56.08	−2.62	107.86	−14.96
64.30	0.40	35.51	−16.18	228.02	−22.05

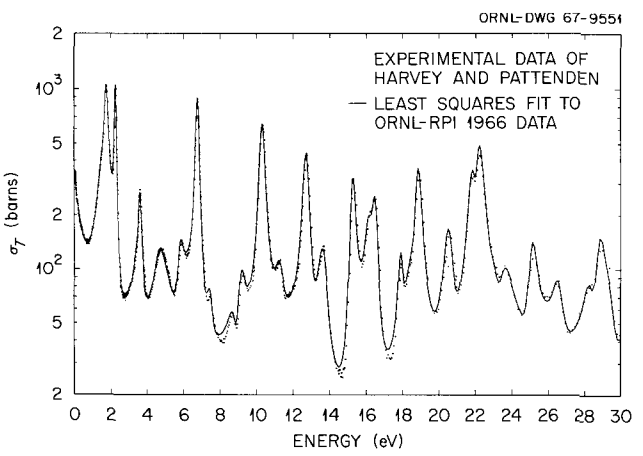

Fig. 1.2.2. ^{233}U Total Cross Section.

References

[1]D. R. Harris, p. 823 in *Conference on Neutron Cross Section Technology, March 22–24, 1966, Washington*, TID-4500, Conf-660303, Book 2.

[2]A. M. Perry, *Physics Program for Molten-Salt Breeder Reactors*, ORNL-TM-1857 (1967), p. 32.

[3]For instance, R. G. Fluharty *et al.*, TID-4500, Conf-660303, *op. cit.*, p. 985; see also requests 256 and 285 in *Compilation of Requests for Nuclear Cross Section Measurements*, WASH-1078 (1967).

[4]G. de Saussure, *Neutron Phys. Div. Ann. Progr. Rept. May 31, 1967*, ORNL-4134, p. 1.

[5]L. W. Weston *et al.*, *Measurement of the Neutron Fission and Capture Cross Sections for ^{233}U in the Energy Region from 0.4 to 1000 eV*, ORNL-TM 1751 (1967).

[6]C. W. Craven, private communication (1967). These data are based on a previous evaluation by M. Drake of Gulf General Atomic (GA-7076, 1966), on an ORNL measurement by L. W. Weston *et al.* reported in Section 1.4, and on recently re-analyzed data by M. Moore *et al.* (MTR, Idaho Falls).

[7]N. J. Pattenden and J. A. Harvey, *Nucl. Sci. Eng.* **17**, 404 (1963), and *Tabulation of the Neutron Total Cross Section of U^{233} from 0.07 to 10,000 eV Measured with the ORNL Fast Chopper*, ORNL-TM-556 (1963).

[8]The scattering cross section of ^{233}U has been measured by M. S. Moore and F. B. Simpson, *Nucl. Sci. Eng.* **13**, 18 (1962), and by G. D. Sauter and C. D. Bowman, *Second Conference on Neutron Cross Sections and Technology, Washington, Mar. 4–7, 1968.* From these data it appears that resonance scattering contributes less than 2% of the total cross section in the region covered by Fig. 1.2.2; hence this contribution to the total cross section was neglected.

[9]L. W. Weston *et al.*, *Measurement of the Neutron Fission and Capture Cross Sections for ^{233}U in the Energy Region 0.4 to 2000 eV,* ORNL-TM-2140 (in press); also reported in Section 1.5.

[10]For a definition of the parameters, see Eq. (1), p. 1, of the *Neutron Phys. Div. Ann. Progr. Rept. May 31, 1967,* ORNL-4134.

1.3 MULTILEVEL ANALYSIS OF THE ^{239}Pu TOTAL CROSS SECTION

H. Derrien[1]

A multilevel analysis of the ^{239}Pu total cross section has been initiated using the data from a transmission measurement performed recently at Saclay[2] and the formalism developed by Adler and Adler.[3] The cross section is analyzed in the energy region 5 to 200 eV. Figure 1.3.1 shows a comparison of the cross section, computed from a set of preliminary parameters, with the experimental data. The final set of parameters will be used to compute α, the ratio of the capture to the fission cross section, and the result of the computation will be compared with direct measurements of this parameter recently performed at Harwell[4] and at Rensselaer Polytechnic Institute by an ORNL-RPI group (Sect. 1.6).

References

[1]On loan from Centre d'Études Nucléaires de Saclay, France.

[2]H. Derrien *et al.*, p. 195 in *Proceedings of the IAEA Symposium on Nuclear Data – Microscopic Cross Sections and Other Data Basic for Reactors, Paris, October 17–21, 1966,* Vol. II, IAEA, Vienna, 1967.

[3]D. B. Adler and F. T. Adler, p. 695 in *Proceedings of the Conference on Breeding, Economics and Safety in Large Fast Power Reactors, October 7–10, 1963,* ANL-6792. See also D. B. Adler and F. T. Adler, *Multilevel Analysis of the Pu-239 Cross Sections Below 40 eV,* COO-1546-7 (1967).

[4]M. G. Schomberg *et al.*, paper SM-101/41 in *IAEA Symposium on Fast Reactor Physics and Related Safety Problems, October 30–November 3, 1967, Karlsruhe, Germany* (to be published).

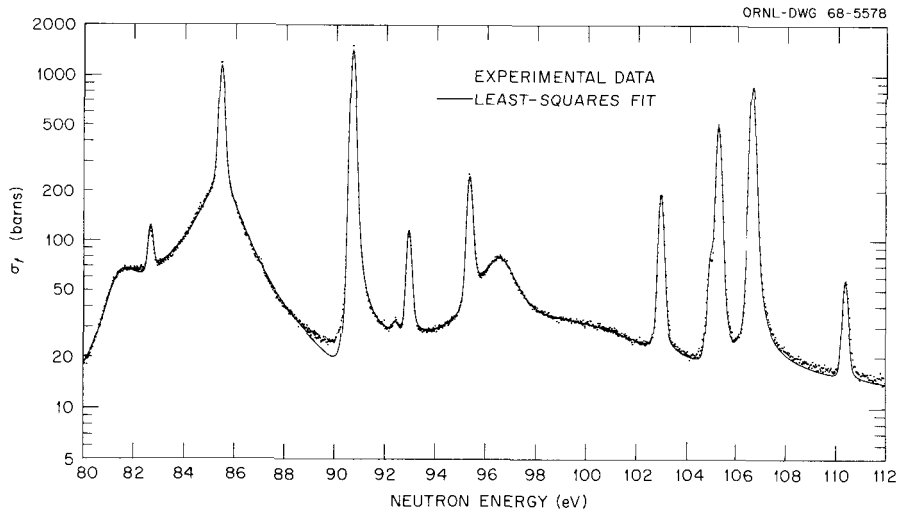

Fig. 1.3.1. Total Cross Section of ^{239}Pu.

1.4 MEASUREMENT OF THE NEUTRON FISSION AND CAPTURE CROSS SECTIONS FOR ^{233}U IN THE ENERGY REGION 0.02 TO 4 eV

L. W. Weston
R. Gwin
G. de Saussure
R. W. Ingle[1]
J. H. Todd[1]
F. E. Gillespie[1]
R. W. Hockenbury[2]

The capture and fission cross sections for ^{233}U in the predominant neutron energy range of a thermal breeder reactor were measured simultaneously at the Rensselaer Polytechnic Institute linac. The method used, as well as data at higher neutron energies, has been reported.[3]

Only very preliminary results of the new data below 4 eV are available at the present time. Figure 1.4.1 shows a comparison of the present results on the fission cross section with some previous results.[4–6] The neutron energy dependence of the fission cross section is consistent with the other data. The normalization of the data is via the total cross section of Pattenden and Harvey[7] from 1.0 to 2.75 eV, as has been described.[3] There are no other direct measurements of differential capture cross sections in this energy range with which to compare; however, comparisons of η can be made. Figure 1.4.2 is a comparison of previously reported values[3,4,8,9] with those calculated from the present data using an assumed constant value of $\bar{\nu}$.

Since the accuracy of the present measurements, by an appreciably different method, is comparable with that of previous measurements, the present measurements should give improved confidence in calculations concerning ^{233}U breeder reactors.

References

[1]Instrumentation and Controls Division.

[2]Rensselaer Polytechnic Institute, Troy, New York.

[3]L. W. Weston *et al.*, *Measurement of the Neutron Fission and Capture Cross Sections for ^{233}U in the Energy Region 0.4 to 2000 eV*, ORNL-TM-2140 (in press).

[4]M. S. Moore, L. G. Miller, and O. D. Simpson, *Phys. Rev.* **118**, 714 (1960).

[5]J. E. Sanders, B. T. Price, and R. Richmond, *J. Nucl. Energy* **6**, 114 (1957).

[6]Y. B. Adamchuk *et al.*, *Proc. Intern. Conf. Peaceful Uses At. Energy, Geneva, 1955* **4**, 216 (1956).

[7]N. J. Pattenden and J. A. Harvey, *Nucl. Sci. Eng.* **17**, 404 (1963).

[8]H. Palevsky *et al.*, *J. Nucl. Energy* **3**, 177 (1956).

[9]J. R. Smith and E. Fast, p. 919 in *Conference on Neutron Cross Section Technology*, Book 2, TID-4500, Conf.-660303 (1966).

1.5 MEASUREMENT OF THE NEUTRON FISSION AND CAPTURE CROSS SECTIONS FOR ^{233}U IN THE ENERGY REGION 0.4 TO 2000 eV[1]

L. W. Weston
R. Gwin
G. de Saussure
R. R. Fullwood[2]
R. W. Hockenbury[3]

The neutron capture cross section and fission cross section for ^{233}U have been measured

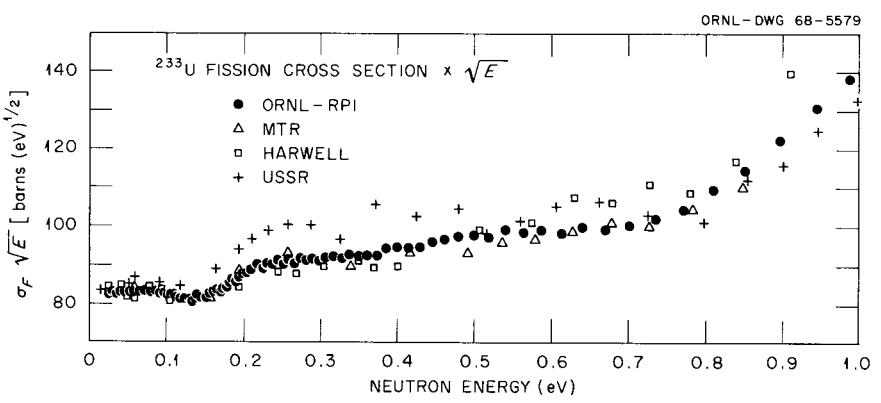

Fig. 1.4.1. The Fission Cross Section of ^{233}U Between 0.02 and 1.0 eV. (MTR – see Ref. 4: Harwell – see Ref. 5: USSR – see Ref. 6.)

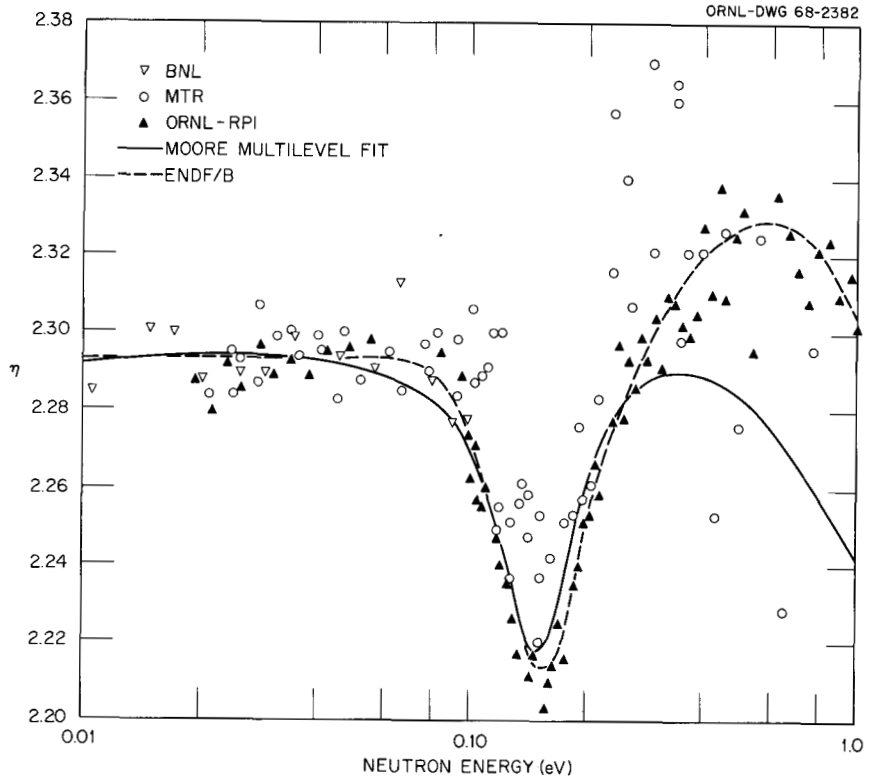

Fig. 1.4.2. Energy Dependence of Eta of ^{233}U, 0–1 eV. (BNL – Ref. 8: MTR – Ref. 9: ORNL-RPI – Ref. 3: Moore – Ref. 4.)

simultaneously in the neutron energy range 0.4 to 2000 eV. A pulsed and collimated neutron beam was passed through a ^{233}U fission chamber placed at the center of a large liquid scintillator. Capture and fission events in the ^{233}U chamber were detected in the scintillator by means of their prompt gamma rays. Coincident signals from the fission chamber and liquid scintillator distinguished fission from capture events. Comparisons with previously published data, using similar and different methods, are given.

References

[1]Abstract of ORNL-TM-2140 (in press); also to be published in *Nuclear Science and Engineering*.

[2]Present address: Los Alamos Scientific Laboratory.

[3]Rensselaer Polytechnic Institute, Troy, New York.

1.6 MEASUREMENT OF THE NEUTRON FISSION AND ABSORPTION CROSS SECTIONS OF ^{239}Pu OVER THE ENERGY REGION 0.01 eV TO 30 keV

R. Gwin
L. W. Weston
G. de Saussure
R. W. Ingle[1]
J. H. Todd[1]
F. E. Gillespie[1]
R. W. Hockenbury[2]
R. C. Block[2]

The neutron fission and absorption cross sections of ^{239}Pu have been measured over the neutron energy range from about 0.01 eV to 30 keV, with the Rensselaer Polytechnic Institute electron linear accelerator used as the neutron source. These measurements were similar in design and instrumentation to those used by Weston *et al.*[3] for ^{233}U measurements in the energy range 0.4 to 2000 eV. In each case, measurements were made with an ionization chamber (containing 1.4 g of ^{239}Pu in our case), but in our work we also performed some experiments with metal foils ranging in mass from 5 to 20 g of ^{239}Pu. The latter measurements were made in order to obtain values

of alpha, the ratio of the capture cross section to the fission cross section, in the higher energy range. Design limitations of the ionization chamber and the electronics for handling the high specific activity of the alpha particles associated with ^{239}Pu preclude, at present, the use of sufficient ^{239}Pu in an ionization chamber to obtain good signal-to-background ratios for the capture cross section at neutron energies greater than 1 keV. Figure 1.6.1 compares the absorption rate in ^{239}Pu to the background for the 20-g sample, which represents the best signal-to-background ratio, and the 1.4-g sample in the ionization chamber. The valleys in the absorption rate at 35 and 2.8 keV result from the use of aluminum and sodium as neutron filters in order to obtain the detector background. The depths of the valleys are a measure of the signal-to-background ratio.

The experiments with the ^{239}Pu foils were performed using a technique which permits derivation of the cross sections independently of the data obtained with the ionization chamber. This technique, which has been reported previously,[4]

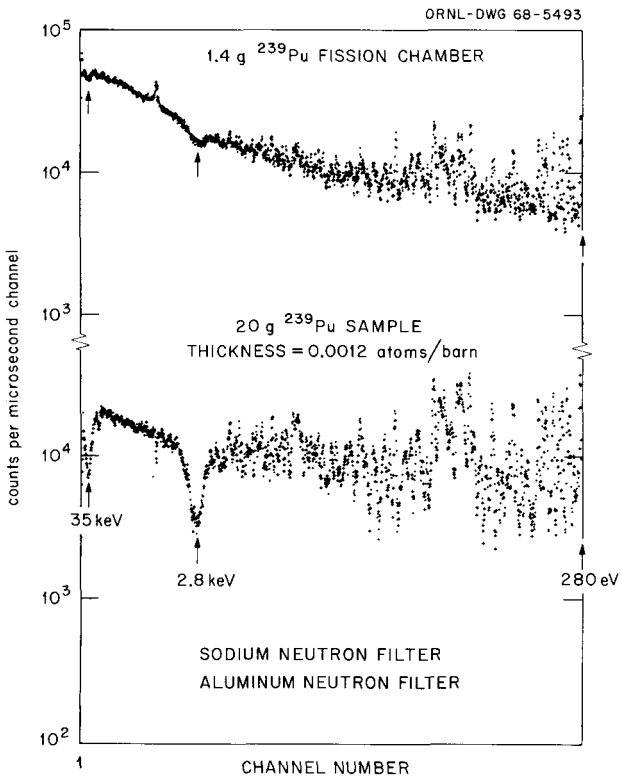

Fig. 1.6.1. Comparison of the Neutron Absorption to Background Signals for Experiments Involving the Ionization Chamber and the 20-g ^{239}Pu Sample.

utilizes the difference in the pulse-height response of a large liquid scintillator to prompt gamma rays resulting from capture and to those resulting from fission. About 15% of the fissions result in a pulse height which is larger than the pulse height produced by ~99% of the capture gamma-ray cascades. Experimentally, a discriminator is set to define gamma-ray events resulting in a pulse height greater than a fixed value, called the "high bias," with another electronic bias set at a lower pulse height to provide discrimination against backgrounds. The data recorded are the counts below and above the high bias. These count rates are related to the neutron fission and capture cross sections in the following manner:

$$\mathrm{lo} = S_c\phi\Sigma_c(1-\delta) + S_f\phi\Sigma_f(1-\epsilon)\,, \tag{1}$$

$$\mathrm{hi} = S_c\phi\Sigma_c\delta + S_f\phi\Sigma_f\epsilon\,, \tag{2}$$

where

lo = count rate below the high bias,
hi = count rate above the high bias,
S_c = fraction of capture events detected,
S_f = fraction of fission events detected,
δ = fraction of capture events above the high bias,
ϵ = fraction of fission events above the high bias,
ϕ = neutron flux,
Σ_c = macroscopic neutron capture cross section,
Σ_f = macroscopic neutron fission cross section.

Although our work has not yet progressed to the point that we can report cross-section values, we have made a preliminary evaluation of α to meet the urgent need for information in the energy range of interest, 1 to 30 keV.

The evaluation has been made using the correspondence between α and the count rates above and below the high bias. Equations (1) and (2) combine to yield the relation

$$\frac{\mathrm{lo}}{\mathrm{hi}} = R = \frac{(S_c/S_f)(1-\delta)\alpha + (1-\epsilon)}{(S_c/S_f)\alpha\delta + \epsilon}\,. \tag{3}$$

By using known values of α for the resolved resonances and the ratio R measured for that resonance with a ^{239}Pu foil, a calibration of α vs R can be obtained. This is the procedure used by Schomberg *et al.*[5] to obtain α values for ^{239}Pu

over the neutron energy region considered here. A calibration curve for the present data is shown in Fig. 1.6.2 for a measurement with a 10-g ^{239}Pu sample. The values of α for the resolved resonances used in the calibration are shown in Table 1.6.1. The ionization-chamber values shown in the table and on Fig. 1.6.2 were obtained from the data taken in this program by normalizing to the value of α of 0.65 for the 0.3-eV resonance in ^{239}Pu. Derrien[6] also normalized his values to the 0.3-eV resonance. The uncertainty in the α values derived from the ionization-chamber data is about 0.06 to 0.1, which results from counting statistics and from an uncertainty in the efficiency of the chamber. This efficiency was about 55%. The calibration curve shown in Fig. 1.6.2 is used to obtain values of α in the 1- to 30-keV range. An uncertainty in α of 0.1 due to uncertainties in calibration is assumed. Figure 1.6.3 shows a plot of $(\sigma_c)/(\sigma_f) = \overline{\alpha}$

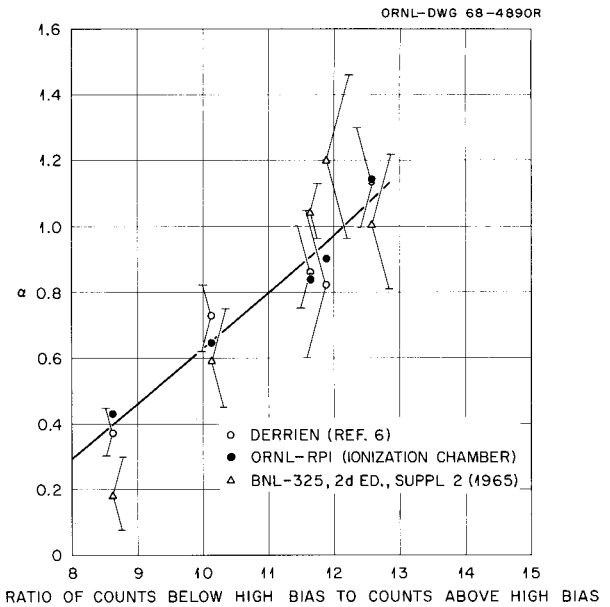

Fig. 1.6.2. Values of α for ^{239}Pu in Well-Resolved Resonances vs the Ratio of Counts Below the High Bias to Counts Above the High Bias for 10-g ^{239}Pu Sample.

Table 1.6.1. Comparison of Measured Values of α for ^{239}Pu in Low-Energy Resonances

Resonance Energy (eV)	Derrien[a]	ORNL-RPI[b]	Stehn *et al.*[c]
7.85	0.84 ± 0.09	0.85	1.04 ± 0.08
10.93	0.38 ± 0.08	0.27	0.32 ± 0.07
17.7	1.15 ± 0.07	1.14	1.0 ± 0.2
22.3	0.71 ± 0.07	0.64	0.59 ± 0.14
26.2	0.86 ± 0.17	0.90	1.22 ± 0.26
32.3	0.39 ± 0.10	0.43	0.18 ± 0.11
35.5	8.4	9.5	$9.0^{+10.0}_{-4.0}$
44.5	9.28 ± 0.4	9.5	$8.0^{+3.0}_{-1.5}$
47.6	0.32 ± 0.1	0.32	$0.16^{+0.14}_{-0.08}$

[a]H. Derrien *et al.*, p. 195 in *Proceedings of the IAEA Symposium on Nuclear Data – Microscopic Cross Sections and Other Data Basic for Reactors, Paris, October 17–21, 1966*, Vol. II, IAEA, Vienna, 1967.

[b]Ionization-chamber measurements (preliminary results).

[c]J. R. Stehn *et al.*, *Neutron Cross Sections*, BNL-325, Vol. 3, 2nd ed., Supplement No. 2 (February 1965).

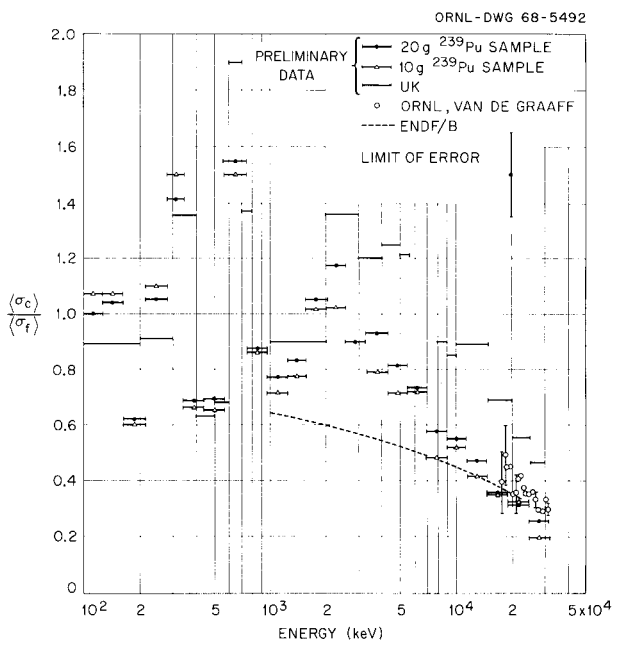

Fig. 1.6.3. Ratios of Capture Rates to Fission Rates vs Energy for ^{239}Pu.

vs neutron energy obtained using a 10- and 20-g ^{239}Pu sample. The term $(\sigma_c)/(\sigma_f)$ indicates an average over energy of quantities proportional to σ_c and to σ_f before the ratio $\bar{\alpha}$ is taken. The averages were over a neutron flux which had an energy dependence of $\sim E^{-0.95}$. Also shown in Fig. 1.6.3 are preliminary values for $\bar{\alpha}$ derived by Schomberg *et al.* and values of α given in ENDF/B. It is apparent that the experimental values of α are significantly higher than those given in ENDF/B. The combined uncertainties (the calibration uncertainty, an uncertainty in the background, and a small statistical uncertainty) are assigned a value of ±0.15 for all ORNL-RPI values of α shown in Fig. 1.6.3. The reasonable agreement between the values of $\bar{\alpha}$ obtained using the two different sample thicknesses indicates that the backgrounds are handled properly in this energy region since the signal-to-background ratios are different for the two samples.

References

[1]Instrumentation and Controls Division.

[2]Rensselaer Polytechnic Institute, Troy, N.Y.

[3]L. W. Weston *et al.*, "Measurement of the Neutron Fission and Capture Cross Sections for ^{233}U to the Energy Region 0.6 to 2000 eV," submitted to *Nuclear Science and Engineering;* also, see sect. 1.5, this report.

[4]R. Gwin *et al.*, *Neutron Phys. Div. Ann. Progr. Rept. Aug. 1, 1963,* ORNL-3499, vol. 1, p. 15.

[5]M. G. Schomberg, M. G. Sowerby, and F. W. Evans, *Progress Report on the Direct Measurement of $\alpha(E)$ for ^{239}Pu,* EANDC(UK)100 AL.

[6]H. Derrien *et al.*, p. 195 in *Proceedings of the IAEA Symposium on Nuclear Data – Microscopic Cross Sections and Other Data Basic for Reactors, Paris, October 17–21, 1966,* vol. II, IAEA, Vienna, 1967.

1.7 INVARIANT IMBEDDING APPROACH TO NUCLEAR REACTION THEORY

R. B. Perez

Invariant imbedding techniques have been widely used in particle-transport problems.[1] Only recently Devooght[2] has shown the applicability of this method to the quantum mechanical scattering problem. Based on the work of DeDonder,[3] Devooght has derived a general formalism to obtain the variation of the Green's function characterizing a given physical field. This method, which has many points of contact with Noether's theorem,[4] lends itself to various applications of the theory of nuclear reactions. An application to Wigner and Eisenbud's[5] R-matrix theory will be illustrated in that which follows.

Calling $G(\vec{r}_i|\vec{r}_{0i},\tau)$ the Green's function for the many-body quantum-mechanical problem, where $\vec{r}_i$ designates the coordinates of the ith nucleon and τ is a parameter (energy, momentum, spin, etc.), Devooght's formalism gives the following expression for the variation of the Green's function with respect to τ for the case in which the coordinates $\vec{r}_{i0}$ are independent of τ:

$$\frac{\partial}{\partial\tau}G(\vec{r}_{1i}|\vec{r}_{i0},\tau) = -\int_N dv\, G(\vec{r}_i|\vec{r}_{1i},\tau)\frac{\partial}{\partial\tau}[V(\vec{r}_i,\tau) - E(\tau)]\, G(\vec{r}_i|\vec{r}_{0i},\tau) + \sum_i \int_{N-1} d\Sigma_i\, D^{(i)}\mathfrak{L}\,, \quad (1)$$

where the first N-tuple integral goes over all nuclear coordinates and the second integral is evaluated over the surface bounding the system, $V(\vec{r}_i,\tau)$ is the many-body potential, and $\mathfrak{L}$ is the pertinent many-body Lagrangian density. The components $D^{(i)}$ of the vector operator $\vec{D}$ are given in terms of functional derivatives of the Lagrangian. To translate the above formalism into R-matrix language, one displaces the coordinates $\vec{r}_{1i}$, $\vec{r}_{0i}$ to the surface limiting the phase space volume. Then Eq. (1) relates the surface Green's function with the interior properties of the system, which is one of the central features of R-matrix theory. The "interior" dependence of the Green's functions in the volume integral is subsequently expanded in terms of the complete orthogonal set of interior eigenfunctions $X_\lambda(r_i)$,[6] whereas its surface dependence is first expressed in channel coordinates and later expanded in terms of the surface eigenfunctions, ϕ_c (Ref. 6):

$$G(\vec{r}_{1i}|\vec{r}_{0i},\tau) = \sum_{\lambda,c',c''}\left(\frac{2M_{c'}a_{c'}}{\hbar^2}\right)^{1/2}\left(\frac{2M_{c''}a_{c''}}{\hbar^2}\right)^{1/2} \times g_\lambda(\tau)\,\gamma_{\lambda c'}\gamma_{\lambda c''}\phi_{c'}\phi_{c''}\,, \quad (2)$$

where we have used the notation of Ref 6. The above expansions, together with the introduction of the boundary conditions

$$a_c G(\vec{\xi}_c|\xi_c', \tau) - B_c \vec{n}\, \overrightarrow{\text{grad}}_{\vec{\xi}_c}\, G(\vec{\xi}_c|\xi_c', \tau) = 0 , \quad (3)$$

and the restriction that the channel radius remain independent of τ yield the following expression:

$$\frac{\partial}{\partial\tau} R_{cc'}(\tau) = -\sum_{\lambda_1\lambda'} g_{\lambda'}(\tau)\, g_\lambda(\tau)\, \gamma_{\lambda c}\gamma_{\lambda' c'} M_{\lambda\lambda'} + \sum_{c''} R_{cc''}(\tau)\, R_{c''c'}(\tau) \frac{\partial B_{c''}}{\partial\tau} , \quad (4)$$

where $R_{cc'}$ is the (c,c') element of the R matrix

$$R_{cc'} = \sum_\lambda g_\lambda(\tau)\, \gamma_{\lambda c}\gamma_{\lambda c'} \quad (5)$$

and

$$M_{\lambda\lambda'} = \int_N dV\, X_\lambda \frac{\partial}{\partial\tau}[V(\vec{r}_i, \tau) - E(\tau)]\, X_{\lambda'} . \quad (6)$$

A class of relations satisfied by the R matrix is obtained by identifying τ with various physical magnitudes. For example, identification with the energy E yields, in view of the energy independence of the numbers $B_{c''}$ and of the potential, the relation

$$\frac{\partial}{\partial E} g_\lambda(E) = g_\lambda^2(E) , \quad (7)$$

from which one obtains the usual expression for the R matrix

$$R_{cc'}(E) = \sum_\lambda \frac{\gamma_{\lambda c}\gamma_{\lambda c'}}{E_\lambda - E} . \quad (8)$$

The identification of τ with the number $B_{c''}$ yields

$$\frac{\partial}{\partial B_{c''}} R_{cc'} = R_{cc''} R_{c''c'} , \quad (9)$$

which is a readily obtained generalization of the Ricatti equation satisfied by the R matrix in the one-channel approximation.[6]

The restriction that the coordinates be independent of τ was made only to simplify the presentation. The power of the invariant imbedding method lies precisely in the fact that it embodies the case of variable boundaries, which suggests applications to deformed nuclei.

References

[1] R. Bellman, R. Kalaba, and M. Wing, *J. Math. Phys.* **1**, 280 (1960).

[2] J. Devooght, *J. Math. Phys.* **7**, 1764 (1966).

[3] T. DeDonder, *Theorie Invariantive du Calcul des Variations*, Gauthier-Villars, Paris, 1935.

[4] E. Noether, *Nachr. Akad. Wiss. Gottingen Math.-Physik. Kl. II*, p. 235 (1918).

[5] E. P. Wigner and L. Eisenbud, *Phys. Rev.* **72**, 29 (1947).

[6] A. M. Lane and R. G. Thomas, *Rev. Mod. Phys.* **30**, 257 (1958).

1.8 AN ALGORITHM FOR THE INVERSION OF THE LEVEL MATRIX

R. B. Perez

Considerable success has been obtained recently in the use of multilevel formalisms for the fitting and interpolation of slow neutron cross sections of fissile nuclei.[1,2] The method is based on diagonalization of the reciprocal Wigner level matrix, which was accomplished via a complex orthogonal transformation involving a perturbative technique.[1] The resulting generalized Kapur-Peierls formalism[3] contains parameters exhibiting energy dependence arising from the energy-dependent neutron widths. There has been some criticism[4] of the Kapur-Peierls theory that the functional relation of the pertinent parameters with the energy is not given in explicit form. The purpose of this work is to show that this inconvenient feature of the Kapur-Peierls formalism can be removed by using the formal connection between this method and the R-matrix theory of Wigner and Eisenbud[5] and by the inversion of the level matrix based on a generalization of a method due to Souriau.[6] The inverse level matrix for s-wave neutrons $\mathbf{A}^{-1}$ can be written as

$$\mathbf{A}^{-1} = -\frac{\hbar^2}{2M}\mathbf{C}^{-1} , \quad (1)$$

with

$$\mathbf{C}^{-1} = (k^2\mathbf{I} + k\mathbf{M} + \mathbf{P}) , \tag{2}$$

where k is the modulus of the neutron propagation vector, $\mathbf{I}$ is the unit matrix, and the following matrices $\mathbf{M}$ and $\mathbf{P}$ have been introduced:

$$M_{\lambda\mu} = \frac{i}{2}\sum_n \left(\frac{2M}{\hbar^2}\Gamma^0_{\lambda n}\Gamma^0_{\mu n}\right)^{1/2} \tag{3}$$

$$P_{\lambda\mu} = \frac{i}{2}\left(\frac{2M}{\hbar^2}\right)\left[\sum_f (\Gamma_{\lambda f}\Gamma_{\mu f})^{1/2} + \sum_\gamma (\Gamma_{\lambda\gamma}\Gamma_{\mu\gamma})^{1/2}\right] - k_\lambda^2\delta_{\lambda\mu} , \tag{4}$$

where we used the customary notation for the neutron and reaction widths and k_λ^2 is the energy of the λth level. The inversion of the level matrix is first formally performed by writing

$$\mathbf{A} = \frac{\hbar^2}{2M}\frac{\mathbf{B}(k)}{d(k)} , \tag{5}$$

where $\mathbf{B}(k)$ is a matrix whose $B_{\lambda\mu}$ element is the cofactor of the (μ, λ) element in the matrix $\mathbf{C}^{-1}$, and

$$d(k) \equiv \det(\mathbf{C}^{-1}) . \tag{6}$$

Souriau's method is based on the proposition that if all the elements of the matrix $\mathbf{C}^{-1}$ are rational functions of the independent variable the matrix $\mathbf{B}(k)$ and the determinant $d(k)$ are polynomial functions; i.e.,

$$\mathbf{B}(k) = \sum_{s=0}^{2N-2} \mathbf{B}_s k^{[2N-(s+2)]} \tag{7}$$

and

$$d(k) = \sum_{s=0}^{2N} d_s k^{(2N-s)} . \tag{8}$$

Hence the level matrix is given as the ratio of two polynomials in the momentum variable, where the matrix coefficients $\mathbf{B}_s$ and the polynomial coefficients d_s are independent of the neutron energy. It can be shown that these coefficients are related to the matrices $\mathbf{M}$ and $\mathbf{P}$, containing the R-matrix parameters, via the relations

$$\mathbf{B}_s + \mathbf{M}\mathbf{B}_{s-1} + \mathbf{P}\mathbf{B}_{s-2} = d_s\mathbf{I} \tag{9}$$

$$\text{trace}\,(2\mathbf{B}_s + \mathbf{M}'\mathbf{B}_{s-1}) = (2N - s)\, d_s \tag{10}$$

$$M'_{\lambda\mu} = (-1)^{\lambda+\mu} M_{\lambda\mu} . \tag{11}$$

Equations (9) and (10) form two coupled sets of recursion formulas which are very suitable for machine calculations and lead to nonperturbative methods for the determination of the level matrix. Expansion of Eq. (5) in partial fractions transforms the level matrix and in turn the collision matrix into the usual Kapur-Peierls form with all the parameters rigorously independent of the energy. The present formalism also offers the advantage that the influence of the neutron widths on the magnitude of the Kapur-Peierls parameters is readily visualized. On the basis of the neutron widths being about an order of magnitude smaller than the fission and gamma widths, one can obtain, explicitly, the coefficients $\mathbf{B}_s$ and d_s from Eqs. (9) and (10). The result that is valid up to second order in the ratio of the neutron widths to the total width is

$$\mathbf{B}_s = \sum_{p=0}^{s/2;(s-1)/2} (-1)^p d_{s-2p}\mathbf{P}^p + \sum_{p=0}^{(s-1)/2;(s-2)/2} \times (-1)^{p+1} d_{s-(2p+1)}\{\mathbf{M}\mathbf{P}^p\} , \tag{12}$$

$$d_s = \sum_{p=0}^{(s-2)/2;(s-1)/2} (-1)^p d_{s-(2p+1)}\mathbf{P}^{(p+1)} + \sum_{p=0}^{(s-2)/2;(s-1)/2} (-1)^p d_{s-(2p+1)}\{\mathbf{M}'\mathbf{P}^p\} \tag{13}$$

where, for each value of the subindex s, the p subindex runs from zero up to either of the two upper limits, depending on the parity of s, and the braces have the following meaning

$$\{\mathbf{M}\mathbf{P}\} \equiv \mathbf{M}\mathbf{P} + \mathbf{P}\mathbf{M} \tag{14}$$

$$\{\mathbf{M}\mathbf{P}^p\} = \mathbf{M}\mathbf{P}^p + \mathbf{P}\{\mathbf{M}\mathbf{P}^{(p-1)}\} . \tag{15}$$

Hence the present algorithm allows the construction of a multilevel formalism in the form of a Kapur-Peierls theory free of any energy dependence of the parameters. The case in which higher angular moments are involved can, in principle, be handled in an analogous way, although the complexity of

the results increases rapidly with angular momentum. In general the relative smallness of the neutron widths makes the energy dependence of the Kapur-Peierls parameters a rather academic problem in the electron volt range of neutron energies. The usefulness of the method shown here is mostly at moderately high excitation energies, where one begins to enter into the unresolved region.

References

[1]F. T. Adler and D. B. Adler, p. 695 in *Proceedings of the Conference on Breeding, Economics and Safety in Large Fast Power Reactors, October 7–10, 1963,* ANL-6792.

[2]G. De Saussure, *Neutron Phys. Div. Ann. Progr. Rept. May 31, 1967,* ORNL-4134, p. 1.

[3]P. I. Kapur and R. E. Peierls, *Proc. Roy Soc. (London)* **A166**, 277 (1937).

[4]A. M. Lane and R. G. Thomas, *Rev. Mod. Phys.* **30**, 257 (1958).

[5]E. P. Wigner and L. Eisenbud, *Phys. Rev.* **72**, 29 (1947).

[6]J. M. Souriau, *Compt. Rend.* **227**, 1010 (1948).

1.9 AN OPTICAL-MODEL GLOBAL SEARCH CODE: GENOA

F. G. Perey

An optical-model analysis consists in adjusting the parameters of the optical-model potentials to obtain good fits to elastic-scattering data. Automatic parameter search codes, which will adjust the potentials to obtain good fits to one angular distribution, have been in use for some years and have proved to be very useful. Since in many analyses the aim is to find an average potential which will reproduce data over a range of energy and target nuclei, such programs, however, do not yield directly the answer and many external constraints on the parameters have to be applied in order to achieve the desired result. A computer program called GENOA has been developed for the IBM 360/75 which will facilitate this search. The code can easily be adapted to follow some constraints and to adjust parameters so that a best chi-square fit can be made to many angular distributions from different nuclei at different energies.

The idea behind the code is that one decides *a priori* how the parameters of the potentials will vary as a function of any number of nuclear variables and those formulas, which define the average potential, may contain parameters which can be varied by the code to obtain a best fit to the sets of data inputed. Up to 25 parameters may be adjusted simultaneously by the code to fit up to 30 data sets.

The code GENOA does not enable one to find the trends in optical-model parameters but speeds up considerably the investigation of the many physically acceptable ones. The code will be extremely useful for interpolating and extrapolating in a manner most consistent with the presently available data the elastic-scattering cross sections in energy regions and mass regions for which no data are available.

1.10 OPTICAL-MODEL STUDIES

F. G. Perey C. M. Perey[1]

The systematics in the variation of optical-model parameters obtained from the analysis of elastic scattering of nucleons and complex particles from nuclei make possible the calculation of cross sections at energies and for nuclei on which no data are available. Furthermore from the optical model we can obtain wave functions and penetrability which are required for the calculation of many other nuclear reactions, such as inelastic scattering. For this reason the optical-model potential occupies a central place in many low-energy nuclear reaction studies. Most of our effort in optical-model studies is geared to an understanding of the optical-model systematics below 20 MeV.

During the past year we have completed and will soon publish the results of an extensive analysis of 11-MeV proton elastic and inelastic scattering. This study raises some questions concerning the variation of the geometrical shape of the optical potential as a function of energy and raises some doubt as to our understanding of the isotopic spin dependence of the potential. These results have stimulated some studies, which have been initiated, on the analysis of 14.5-MeV scattering of protons and neutrons and on the effect of potential shape on the analysis of proton scattering from ^{40}Ca and ^{120}Sn as a function of energy.

Reference

[1]Consultant.

1.11 ON THE REAL PART OF THE PROTON OPTICAL-MODEL POTENTIAL[1]

C. M. Perey[2] F. G. Perey

The analysis of the differential elastic scattering and polarization of 11-MeV protons from over 20 isotopes in the mass region between ^{48}Ti and ^{76}Ge reveals an average set of parameters substantially different from those found at higher energies. The variation of the real-well depth as a function of mass number is very smooth but does not follow the expected isotopic spin dependence of the potential.

References

[1] Abstract of *Phys. Letters* **26B**, 123 (1968).
[2] Consultant.

1.12 NEUTRON-SCATTERING EXPERIMENTS

E. Hungerford[1] W. E. Kinney
F. G. Perey

During the past year neutron-scattering experiments were performed using the three ORNL Van de Graaff accelerators in the neutron energy range 4.5 to 11 MeV. A three-detector system coupled to our on-line PDP-7 was put in operation. Some of the data previously obtained have been completely corrected, and cross sections were released to the Brookhaven Sigma Center and sent to the users who requested them on the Nuclear Cross Section Advisory Group compilation.

Some of the measurements performed this year are the following:

1. With the 3-MeV Van de Graaff, final data were obtained at neutron energies of 4.50, 4.75, 5.00, 5.25, and 5.50 MeV on C, Na, Mg, Al, Si, S, V, Fe, Co, and Y targets. These data will complement our earlier measurements in this energy range on some of the nuclei.
2. With the 5.5-MeV accelerator, the angular distribution of neutron spectra from the bombardment of C, Al, Si, V, Fe, Co, and Y with 8.5-MeV neutrons was obtained with a 5-m flight path.
3. With the 12-MeV Tandem accelerator we used the pulsed deuteron beam to investigate the suitability of the (d,d) reaction for neutron inelastic studies. The deuterium gas cell was found to be suitable to extend the energy range of our measurements to at least 11-MeV incident neutron energy. Experiments are in progress on the Tandem accelerator, which measures the neutron spectra obtained with incident neutrons in the range 8.5 to 11 MeV.

Reference

[1] Electronuclear Division.

1.13 NEUTRON ELASTIC AND INELASTIC SCATTERING FROM ^{56}Fe FROM 4.60 TO 7.55 MeV[1]

W. E. Kinney

Neutron elastic- and inelastic-scattering cross sections for ^{56}Fe were measured in the energy range 4.60 to 7.55 MeV by the time-of-flight method in order to study the competition between direct interactions and compound nucleus decay in the excitation of the 2^+ collective level that has an excitation energy of 0.846 MeV, to test the validity of the statistical model in predicting the cross sections for inelastic scattering to the higher levels, and to obtain optical-model parameters from fits to the elastic-scattering data.

Neutrons were produced by the ^{2}D$(d,n)^3$He reaction in a deuterium gas cell and had an energy uncertainty of 40 keV. The neutrons were scattered by solid right cylindrical samples of natural iron and were detected in a shielded liquid scintillator optically coupled to a phototube whose output, together with a time reference signal, measured the flight time with a typical time resolution for the elastic neutrons of 3 nsec. Gamma rays were discriminated against to decrease the background, and the neutron production of the target was monitored by a simplified time-of-flight detection system. Measurements were made at angles ranging from 25 to 140° with 3.7- to 5.3-m flight paths.

Electronic walk was corrected by dividing the range of pulseheights of the detected neutrons into groups, taking a time-of-flight spectrum for each group, and aligning and adding the group spectra. Peak areas were extracted by isolating each peak visually on an oscilloscope screen by means of a light pen operating with a PDP-7 computer program which then computed the area of the isolated peak. The peak areas were combined with detector efficiency measurements, scattering-sample data, and geometric data to produce cross sections which were corrected for finite sample

effects by applying factors obtained from a Monte Carlo computer calculation.

Optical-model minimum χ^2 fits were made to the elastic-scattering data, with the real- and imaginary-well depths varied to achieve the best fits and the other parameters held constant at standard values. Optical-model calculations with average values of 46.6 and 11.8 MeV for the real- and imaginary-well depths, respectively, were in reasonable agreement with experiment from 4.0- to 7.6-MeV incident neutron energy (E_n).

Inelastic-scattering cross sections to levels and groups of levels to an excitation energy of 4.728 MeV were measured, and statistical model calculations were in good agreement below an E_n of 5.6 MeV with the measured values. The 2.085- and 2.654-MeV levels were predicted to within 20% up to an E_n of 7.6 MeV, but the calculated cross sections for the higher levels were greater by as much as a factor of 2.5 than those measured. On the basis of the agreement below 5.6 MeV, support was given to a previous suggestion of a triplet comprising the group of levels at 3.60-MeV excitation energy, with the spin of the third level having to be greater than zero for a good fit to the data to be achieved.

The addition of distorted-wave-Born-approximation and statistical model results have cross sections that were in good agreement with experiment for inelastic scattering to the 0.846-MeV level. The calculated contribution of direct interactions to the excitation of this level was equal to 21% at 4.0-MeV incident neutron energy, rose linearly with energy to a value of 57% at 6.6 MeV, and reached a value of 66% at 7.6 MeV.

Reference

[1] Abstract of ORNL-TM-2052 (January 1968).

1.14 CALCULATED ^{56}Fe NEUTRON-SCATTERING AND GAMMA-RAY-PRODUCTION CROSS SECTIONS FROM 1.0 TO 7.6 MeV[1]

W. E. Kinney F. G. Perey

Measurements of neutron elastic and inelastic scattering from ^{56}Fe which we have recently extended to incident neutron energies of 7.6 MeV have been analyzed theoretically, and this report compares the results of the analysis with both our experimental data and the data of others. The shape elastic cross sections, calculated with an optical-model potential using fixed values of the parameters, added to the compound elastic contribution, obtained from a Hauser-Feshbach calculation including width fluctuation corrections, agree reasonably well with the data from 4.0 to 7.6 MeV. Inelastic-scattering cross sections from a Hauser-Feshbach calculation agree well with the data from 1 to 7.6 MeV. The following quantities are tabulated in this report:

1. differential elastic-scattering cross sections at 4.00, 4.60, 5.00, 5.56, 6.12, 6.53, 7.00, and 7.55 MeV,
2. differential cross sections for inelastic scattering to the 0.846-MeV level at 4.60, 5.00, 5.56, 6.12, 6.53, and 7.55 MeV,
3. angle-integrated compound elastic- and inelastic-scattering cross sections at 1.0, 1.5, 2.0, 2.5, 3.0, 3.25, 3.5, 5.73, 4.0, 4.5, 5.0, 5.5, 6.2, 6.6, and 7.6 MeV,
4. total, elastic, and reaction cross sections at 4.00, 4.60, 5.00, 5.56, 6.12, 6.53, and 7.55 MeV,
5. gamma-ray production cross sections for neutron energies from 1 to 7.6 MeV.

Reference

[1] Abstract of report ORNL-4249 (to be published); work partly funded by Defense Atomic Support Agency under DASA Task No. RRP-3068.

1.15 ELASTIC AND INELASTIC SCATTERING OF 11.0-MeV PROTONS FROM ^{48}Ti, ^{51}V, ^{52}Cr, ^{54}Fe, ^{56}Fe, ^{59}Co, ^{60}Ni, ^{62}Ni, ^{64}Ni, ^{63}Cu, ^{65}Cu, ^{64}Zn, ^{66}Zn, AND ^{68}Zn: TABULATED DIFFERENTIAL CROSS SECTIONS[1]

J. K. Dickens F. G. Perey
R. J. Silva[2]

Numerical values of differential cross sections for elastic and inelastic scattering of 11.0-MeV protons from ^{48}Ti, ^{51}V, ^{52}Cr, ^{54}Fe, ^{56}Fe, ^{59}Co, ^{60}Ni, ^{62}Ni, ^{64}Ni, ^{63}Cu, ^{65}Cu, ^{64}Zn, ^{66}Zn, and ^{68}Zn are reported in tabular form. Cross sections were determined at 5° intervals between laboratory angles of 20 and 165°.

Inelastic-scattering data are reported for the following:

Nuclide	Number of Excited States	Nuclide	Number of Excited States
^{48}Ti	8	^{62}Ni	10
^{51}V	7	^{64}Ni	9
^{52}Cr	21	^{63}Cu	10
^{54}Fe	9	^{65}Cu	5
^{56}Fe	9	^{64}Zn	5
^{59}Co	9	^{66}Zn	6
^{60}Ni	13	^{68}Zn	6

References

[1] Abstract of ORNL-4182 (November 1967).
[2] Present address: University of California at Berkeley.

1.16 A NEW MEASUREMENT OF THE LIFETIME OF THE ^{72}Ge 0+ STATE[1]

E. Eichler[2] P. H. Stelson[3]
J. K. Dickens

By using a Ge(Li) detector as the target, the lifetime of the 0+ first excited state of ^{72}Ge has been remeasured. A value of 422 ± 13 nsec has been obtained.

References

[1] Abstract of paper submitted to *Nuclear Physics*.
[2] Chemistry Division.
[3] Physics Division.

1.17 STUDY OF GAMMA RAYS FOR $(p,n\gamma)$ REACTIONS ON SEPARATED ISOTOPES OF Zr AND Mo

J. K. Dickens E. Eichler[1]
R. Kuebbing[2]

We have continued our program of measuring gamma-ray energies and yields following (p,n) reactions, first reported last year.[3] Experiments have continued on the ^{94,96}Mo$(p,n\gamma)^{94,96}$Tc reactions, and the reactions ^{92,94}Zr$(p,n\gamma)^{92,94}$Nb and ^{95}Mo$(p,n\gamma)^{95}$Tc have been studied. A large-volume Ge(Li) detector was used in these experiments.

The object of these studies is to deduce the energy level structures of the residual nuclei and to compare these level structures with theoretical predictions obtained from the nuclear shell model. Measurement of gamma-ray energies is the most precise method for determining energies of nuclear levels, provided that the gamma rays are placed correctly in the level structure. In this experiment this placement is obtained by measuring the bombarding energy threshold for each gamma transition. In addition, to obtain information on the spins and parities of the levels, we have measured excitation functions of most of the gamma transitions.

A few of the excited states in the residual nuclei have lifetimes ≥ 10 nsec, and we have measured several of these lifetimes using pulsed proton beams. Several transitions, notably the strong 9-keV transition in ^{92}Nb and the strong 99-keV transition in ^{94}Nb, have half-lives ≥ 30 nsec. These results are interpreted as indicating that these two gamma transitions are "*L*-hindered"; that is, the parent states are negative parity states described by a wave function consisting principally of the

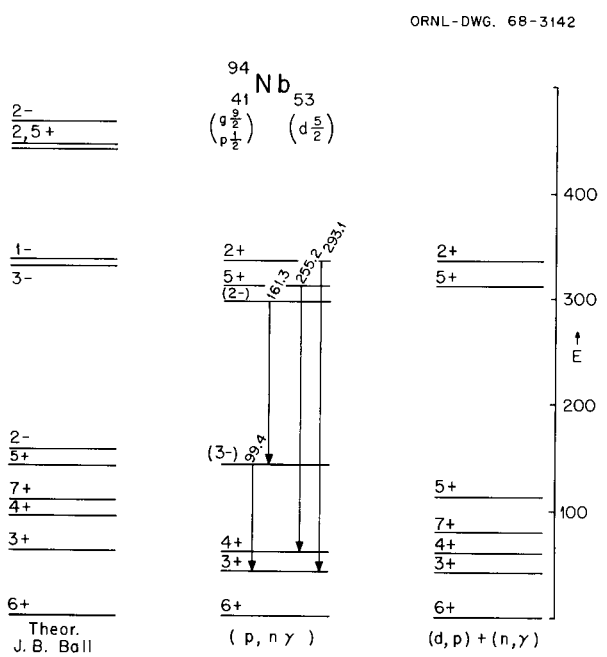

Fig. 1.17.1. Level Structure of ^{94}Nb Deduced from ^{94}Zr$(p,n\gamma)^{94}$Nb Reaction Compared with Theoretical Predictions and Experimental Data Obtained from the ^{93}Nb$(d,p)^{94}$Nb and ^{93}Nb$(n,\gamma)^{94}$Nb Reactions.

odd neutron in a $d_{5/2}$ orbit and the odd proton in a $p_{1/2}$ orbit, and the daughter states are of positive parity described by a wave function in which the odd proton occupies a $g_{9/2}$ orbit, with the odd neutron remaining in the $d_{5/2}$ orbit.

The level structure for ^{94}Nb deduced from gamma rays seen from the ^{94}Zr$(p,n\gamma)^{94}$Nb reaction, which is of considerable current interest, is shown in Fig. 1.17.1. Our level structure is compared with theoretical predictions[4] and with experimental results from the ^{93}Nb$(d,p)^{94}$Nb reaction[4] and the neutron-capture ^{93}Nb$(n,\gamma)^{94}$Nb experiment.[5]

We intend to extend these measurements to the remaining molybdenum isotopes. In addition, we plan gamma-gamma coincidence with an NaI crystal used as the second gamma-ray detector.

References

[1] Chemistry Division.
[2] Graduate student, Physics Department, Case Western Reserve University, Cleveland, Ohio.
[3] J. K. Dickens *et al.*, *Neutron Phys. Div. Ann. Progr. Rept. May 31, 1967*, ORNL-4134, p. 22.
[4] R. K. Sheline *et al.*, *Nucl. Phys.* **61**, 342 (1965); J. B. Ball (private communication).
[5] U. Gruber *et al.*, *Nucl. Phys.* **67**, 433 (1965).

1.18 THE ^{14}N$(n,n'\gamma)$ REACTION FOR $5.8 \leq E_n \leq 8.6$ MeV[1]

J. K. Dickens — P. H. Stelson [3]
E. Eichler [2] — J. Ashe [4]
F. G. Perey — D. O. Nellis[4]

We have obtained gamma-ray spectra for the reactions ^{14}N$(n,n'\gamma)^{14}$N, ^{14}N$(n,n\gamma)^{14}$C, and ^{14}N$(n,\alpha\gamma)^{11}$B for incident mean neutron energies E_n = 5.8, 6.4, 6.9, 7.4, 8.0, and 8.6 MeV. The gamma rays were detected using a coaxial Ge(Li) detector of 30-cc active volume. The detector was placed at 55 and 90° with respect to the direction of the incident neutron, and was 77 cm from the sample; time-of-flight was used with the gamma-ray detector to discriminate against pulses due to neutrons and background gamma radiation. The sample was 100 g of Be_3N_2 in the form of a right circular cylinder. Data were also obtained using a 75-g beryllium sample to provide an estimate of the background. The incident neutron beam was produced by bombarding a deuterium-filled gas cell with the pulsed deuteron beam of appropriate energy from the ORNL 6-MV Van de Graaff. The resulting neutron beam was monitored with a scintillation counter; a time-of-flight spectrum from this detector was recorded simultaneously with the gamma-ray data. These data have been studied to obtain absolute cross sections for production of gamma rays from ^{14}N for the incident neutron energies quoted above.

References

[1] Abstract of paper presented at Second Conference on Neutron Cross Sections and Technology, Washington, D.C., March 1968; work funded by Defense Atomic Support Agency under DASA Task No. RRP-3068.
[2] Chemistry Division.
[3] Physics Division.
[4] Texas Nuclear Corporation, Austin.

1.19 THE ^{90,92,94}Zr(p,p') REACTIONS AT 12.7 MeV[1]

J. K. Dickens — E. Eichler[2]
G. R. Satchler[3]

The elastic and inelastic scattering of 12.7-MeV protons from ^{90,92,94}Zr has been studied. Angular distributions were measured for the elastic group and for 40 inelastic groups. An optical-model analysis of the elastic scattering was performed. The inelastic scattering was interpreted using the usual "collective" model interaction and the distorted-wave approximation. Multipolarities L were assigned where possible, and strength parameters β_L deduced. The inelastic scattering to some states was also compared with the predictions of the shell model using a simple two-body interaction of the Yukawa type and including the effects of core polarization. Reasonable agreement was obtained, although the angular distributions for the 0^+ and 3^- excitations imply that a more sophisticated effective interaction is required.

References

[1] Abstract of *Phys. Rev.* **168**, 1355 (1968).
[2] Chemistry Division.
[3] Physics Division.

1.20 ELASTIC AND INELASTIC SCATTERING OF PROTONS FROM ^{120}Sn FOR E_p = 20.6, 25.2, 30.6, AND 36.2 MeV: TABULATED DIFFERENTIAL CROSS SECTIONS[1]

F. E. Bertrand N. Baron[2]
T. A. Love F. G. Perey
J. K. Dickens

Numerical values of differential cross sections for elastic and inelastic scattering of protons from ^{120}Sn for bombarding proton energies of 20.6, 25.2, 30.6, and 36.2 MeV are reported in tabular form. Inelastic-scattering data are reported for the 1.17-MeV (2^+) state at all incident energies and for the 2.35-MeV (3^-) state at 20.6-, 25.2-, and 36.2-MeV incident energies. Cross sections were obtained at ~5° intervals between laboratory angles of 15 and 110°.

References

[1] Abstract of ORNL-4252 (in press); work funded by the National Aeronautics and Space Administration under NASA Orders R-104(1) and L-12, 186.

[2] National Aeronautics and Space Administration, Lewis Research Center, Cleveland, Ohio.

1.21 ELASTIC AND INELASTIC SCATTERING OF 62-MeV PROTONS FROM ^{12}C, ^{54}Fe, AND ^{209}Bi[1]

F. E. Bertrand R. W. Peelle
J. K. Dickens

Elastic and inelastic differential cross sections have been obtained from ^{12}C, ^{54}Fe, and ^{209}Bi at 15 to 20 angles between 12 and 135° with incident 62-MeV protons. The data were taken with a three-counter, all-solid-state telescope, utilizing lithium-drifted germanium as a total-absorption detector. An overall energy resolution of ~150 keV (FWHM) was obtained. The angular resolution was ~ ±1.2° and the nonstatistical error was ~ ±3% for ^{12}C and ^{54}Fe and ~ ±4% for ^{209}Bi. The complete detection and analysis system is described elsewhere,[2] along with a tabulation of the cross sections for the levels discussed here as well as others less accurately known.

The differential cross sections for the elastic scattering from ^{12}C, ^{54}Fe, and ^{209}Bi are shown in Fig. 1.21.1 and are compared with optical-model

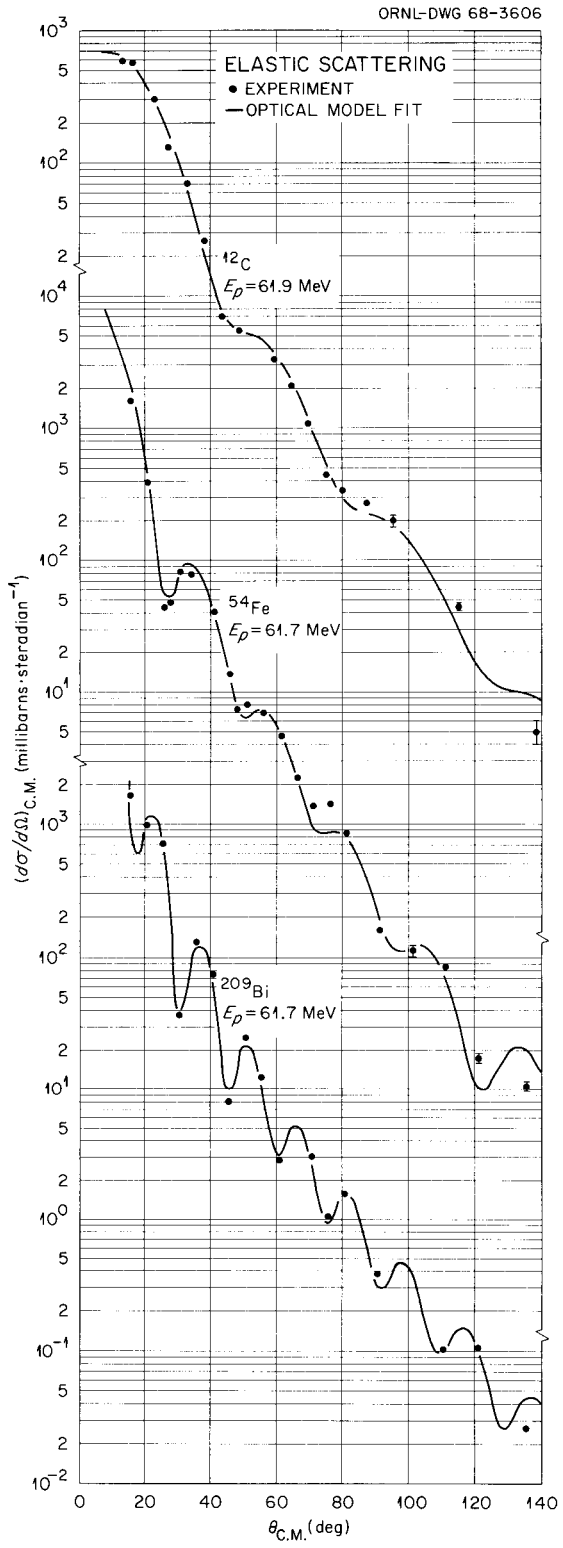

Fig. 1.21.1. Elastic Scattering of 62-MeV Protons from ^{12}C, ^{54}Fe, and ^{209}Bi Compared with Optical-Model Calculations.

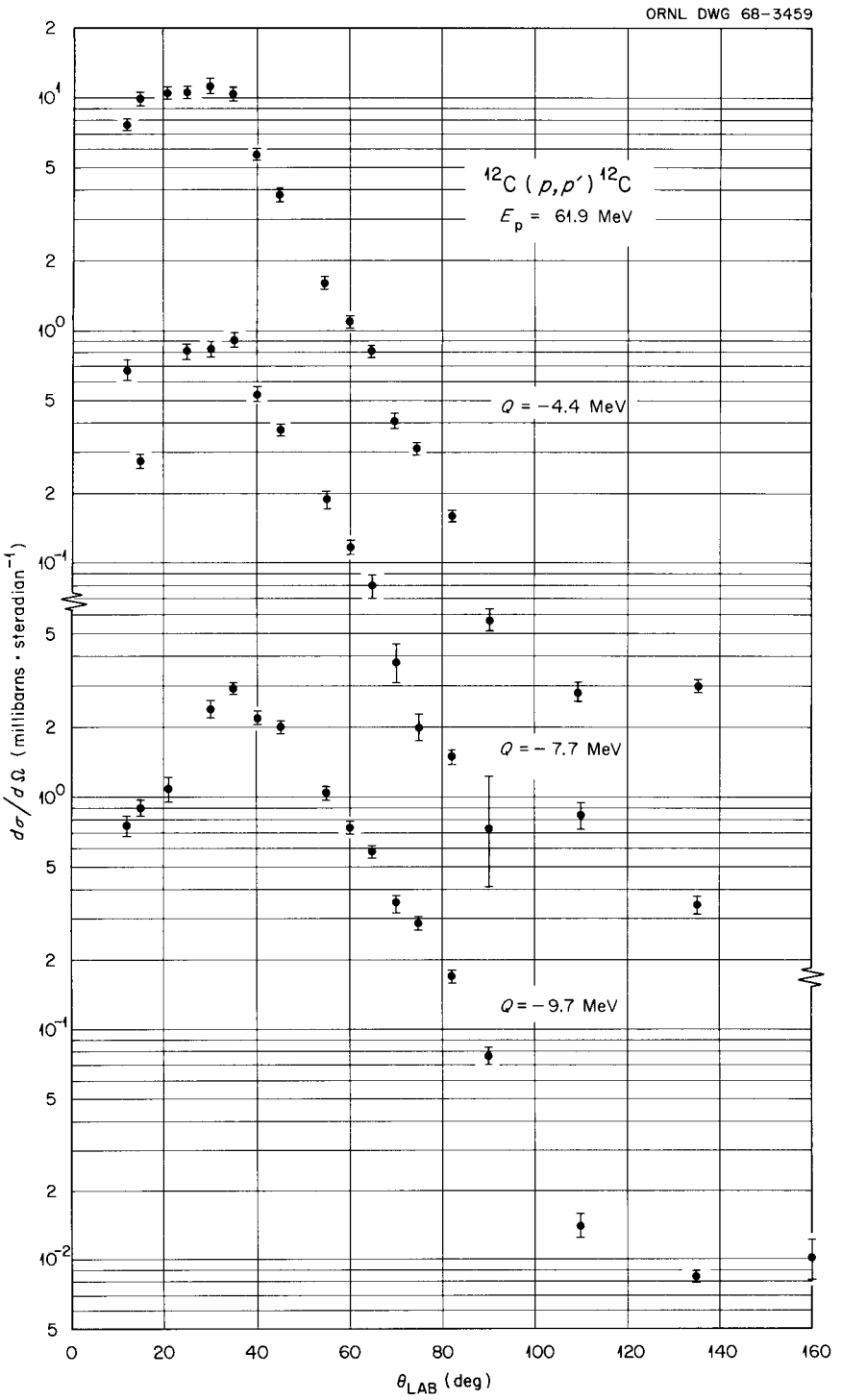

Fig. 1.21.2. Differential Cross Sections for the 4.4-, 7.7-, and 9.7-MeV Levels in ^{12}C.

fits. The optical-model fits to the data were calculated with the computer program JIB-3[3] using an optical-model potential of the form

$$V(r) = V_C(r) - V\frac{1}{e^x+1} - i\left(W_V - 4aW_D\frac{d}{dx}\right)\frac{1}{e^x+1} + \left(\frac{\hbar}{m_\pi c}\right)^2 V_S\frac{d}{dr}\frac{1}{e^x+1}\vec{\sigma}\cdot\vec{l}\ .$$

In this expression $V_C(r)$ is the Coulomb potential for a uniformly charged sphere, V is the real potential, W_V and W_D are the volume and surface parts, respectively, of the imaginary potential, and V_S is the real part of the spin-orbit potential. The remaining factors contain the Woods-Saxon radius and diffuseness parameters (a) for each of the parameters in the form $x = (r - R/a)$, where $R = r_0A^{1/3}$. Initial potential parameters were obtained from earlier 60-MeV work,[4] and were varied until a best fit was obtained to the present data. The parameters which were varied are indicated in Table 1.21.1, which also lists the best-fit parameters obtained. The analysis of ^{12}C is confused by the ability to fit the experimental data equally well with any of several sets of potential parameters, a problem encountered at lower proton energies as well.[5]

The inelastic proton spectra from ^{12}C show, in addition to the strongly excited 4.43-, 7.66-, and 9.76-MeV levels, prominent peaks with Q values of −10.3, −11.85, −12.8, −15.25, and −16.25 MeV. In addition, several peaks were consistently observed in the inelastic spectra in the dipole resonance region; the strongest of these peaks have Q values of −18.7, −19.8, −21.0, and −22.2 MeV. The differential cross sections for excitation of the 4.43-, 7.66-, and 9.76-MeV levels are shown in Fig. 1.21.2.

Figure 1.21.3 shows a spectrum of the inelastic proton peaks observed from ^{54}Fe at 30°. Because of the narrow energy resolution, proton peaks corresponding to many levels were well-separated, and differential cross sections were obtained for the elastic −1.42-, 2.5-, −2.9-, −3.8-, −4.8-, and −6.4-MeV levels. The differential cross sections for the inelastic scattering from the above levels are shown in Fig. 1.21.4.

The proton spectrum from ^{209}Bi shows the presence of inelastic levels with Q values of

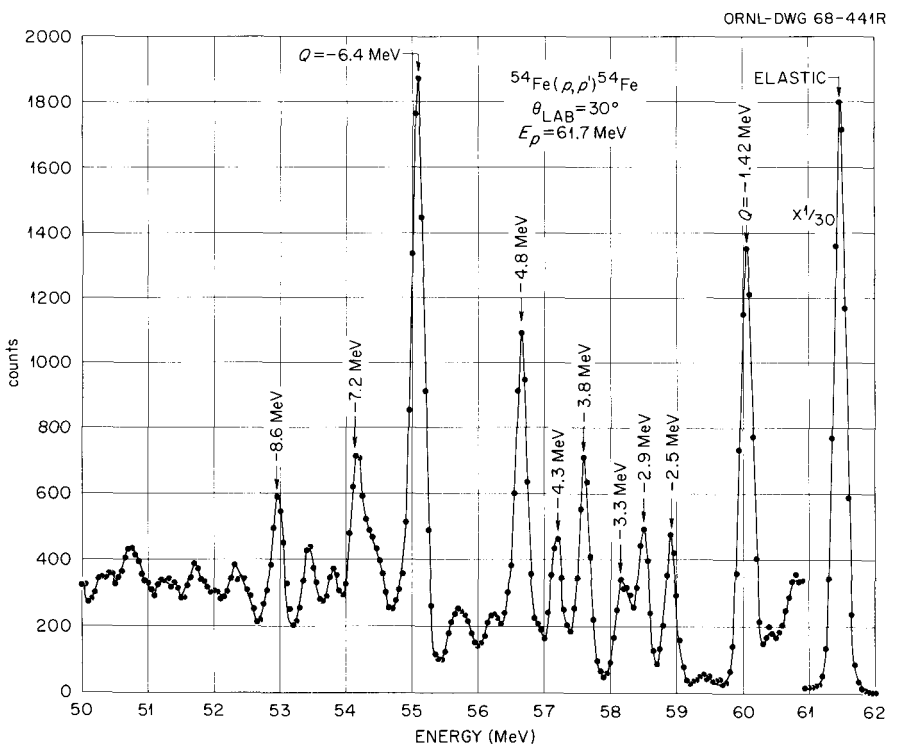

Fig. 1.21.3. Spectrum of Inelastic Proton Peaks from ^{54}Fe at 30°.

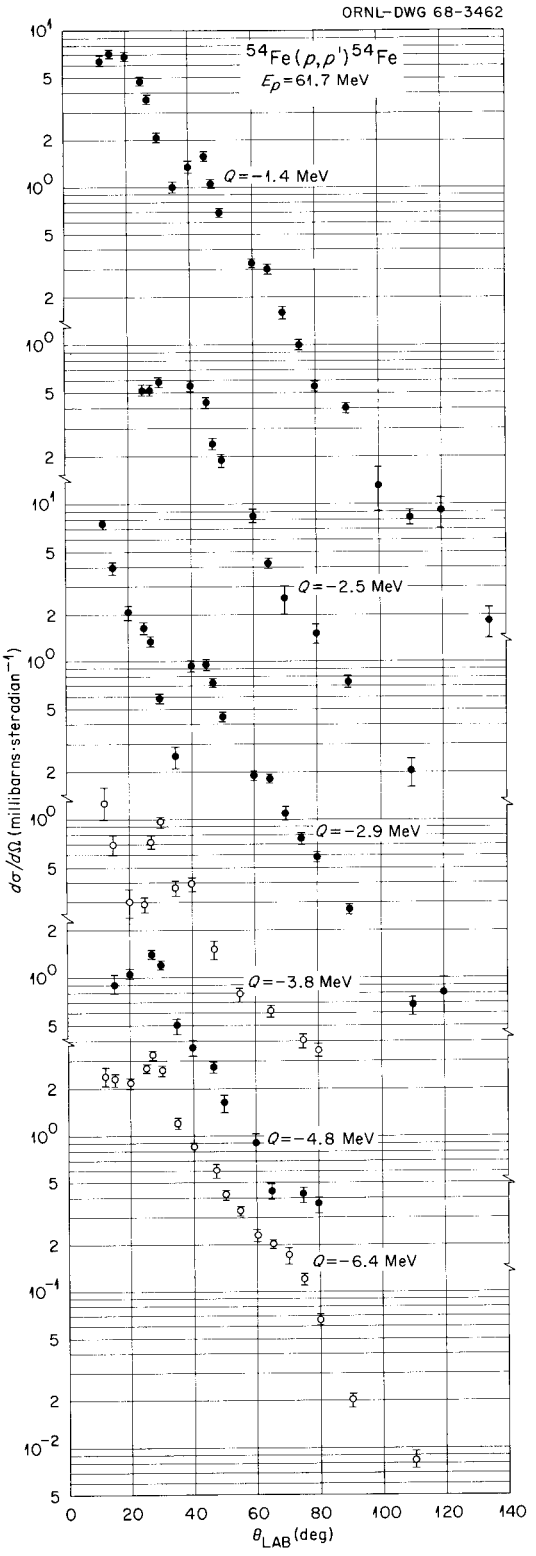

Fig. 1.21.4. Differential Cross Sections for Inelastic Proton Levels from ^{54}Fe.

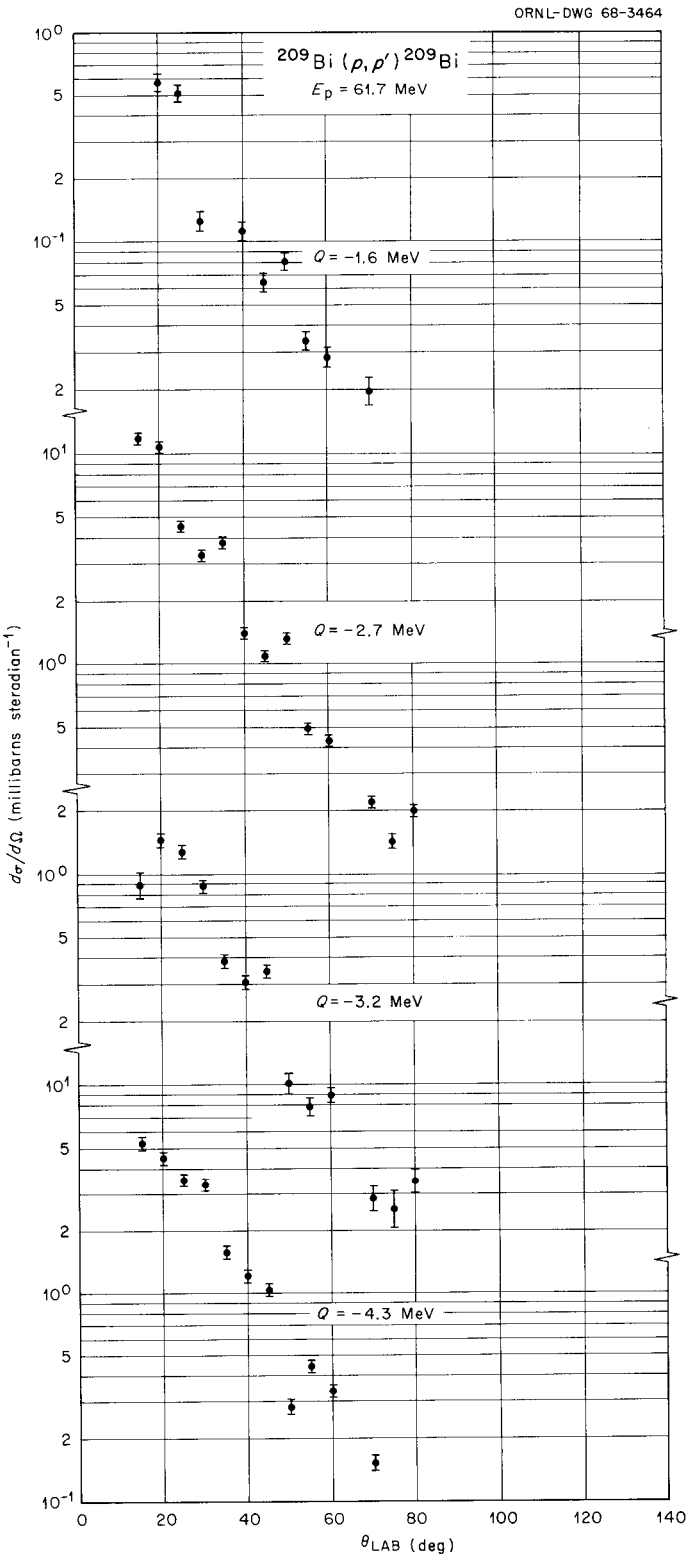

Fig. 1.21.5. Differential Cross Sections for Inelastic Proton Levels from ^{209}Bi.

Table 1.21.1. Optical-Model Parameters

Element	Real Potential			Imaginary Potential				Spin-Orbit Potential			χ_T^2
	V (MeV)	r (F)	a (F)	W_V (MeV)	W_D (MeV)	r (F)	a (F)	V_{SO} (MeV)	r_{SO} (F)	a_{SO} (F)	
^{12}C	26.09	1.160[a]	0.7477	6.618	0.7000	1.400	0.6300	12.0	1.060	0.7000	166
^{54}Fe	38.40	1.160	0.7177	6.751	1.879	1.330	0.5000	6.0	1.060	0.7380	416
^{209}Bi	38.60	1.220	0.7422	4.238	3.964	1.320	0.6700	6.0	1.060	0.7380	135

[a]Underscored parameters not varied.

-1.62, -2.69, -3.17, and -4.38 MeV; however, the peak at 4.38 MeV is too broad to be produced by excitation from a single state. The first excited state in ^{209}Bi ($Q \simeq -0.95$ MeV) was so weakly excited that it was distinguished from the tail of the elastic peak at only a few angles. A prominent and broad peak was observed in the proton spectra with an approximate Q value of -6 MeV. This peak seems to be composed of several completely unresolved components. The differential cross sections for the inelastic levels observed in ^{209}Bi are plotted in Fig. 1.21.5.

References

[1]Work funded by the National Aeronautics and Space Administration under NASA Orders R-104(1), L-12,186, and H-38280A.

[2]F. E. Bertrand *et al.*, *Differential Cross Sections for the Charged Particles Produced by 60-MeV Protons on Carbon, Iron, and Bismuth*, ORNL-4274 (1968).

[3]F. G. Perey, unpublished.

[4]C. B. Fulmer *et al.*, *Phys. Rev. Letters* **24B**, 505 (1967).

[5]G. R. Satchler, *Nucl. Phys.* **A100**, 497 (1967).

1.22 DIFFERENTIAL CROSS SECTIONS FOR LEVELS OBSERVED IN THE (p,d) REACTION ON ^{12}C, ^{54}Fe, AND ^{209}Bi AND THE (p,t) REACTION ON ^{12}C AT 62 MeV[1]

F. E. Bertrand R. W. Peelle

Differential cross sections have been obtained for several levels in the deuteron spectra from ^{12}C, ^{54}Fe, and ^{209}Bi bombarded by 62-MeV protons. Differential cross sections have also been obtained for two levels from the reaction $^{12}C(p,t)^{10}C$ and for the ground-state transitions of the reactions $^{12}C(p,{}^3He)^{10}B$, $^{12}C(p,\alpha)^9B$. The particles were detected and identified in a three-counter, all-solid-state, total-absorption detector telescope, and the overall energy resolution was ~ 150 keV (FWHM). The nonstatistical error in the cross sections was $\sim \pm 3\%$ and the angular resolution was $\sim \pm 1.2°$. The detection and analysis systems are described in detail elsewhere,[2] where extracted numerical cross sections for the levels listed below are given.

Figure 1.22.1 shows the upper few MeV of excitation of the deuteron, triton, ^3He, and alpha spectra from ^{12}C at a laboratory angle of 35°. Six prominent peaks are observed in the deuteron spectra which correspond to ^{11}C states with approximate excitations of 0.0, 2.0, 4.4, 4.9, 6.6, and 7.0 MeV, and, although the statistics are poor, two other levels with excitations of 8.2 and 8.5 MeV are observed. Figure 1.22.2 shows the differential cross sections for the first four levels.

Three prominent peaks, which correspond to known levels in ^{10}C of 0.0-, 3.4-, and 5.3-MeV excitations, are observed in the triton spectrum from ^{12}C. The 5.3-MeV level is consistently observed to have a low-energy shoulder, which indicates that the peak has unresolved components. The differential cross sections for the ground state and the 3.4-MeV level are plotted in Fig. 1.22.3.

Four levels with excitations of 0.0, 0.7, 1.8, and 2.2 MeV are clearly observed in the ^3He spectrum shown in Fig. 1.22.1, and two levels are consistently observed in the alpha spectra from ^{12}C, which correspond to the ground state and 2.2-MeV level in ^9B. For each particle type only the ground-state differential cross sections were extracted.

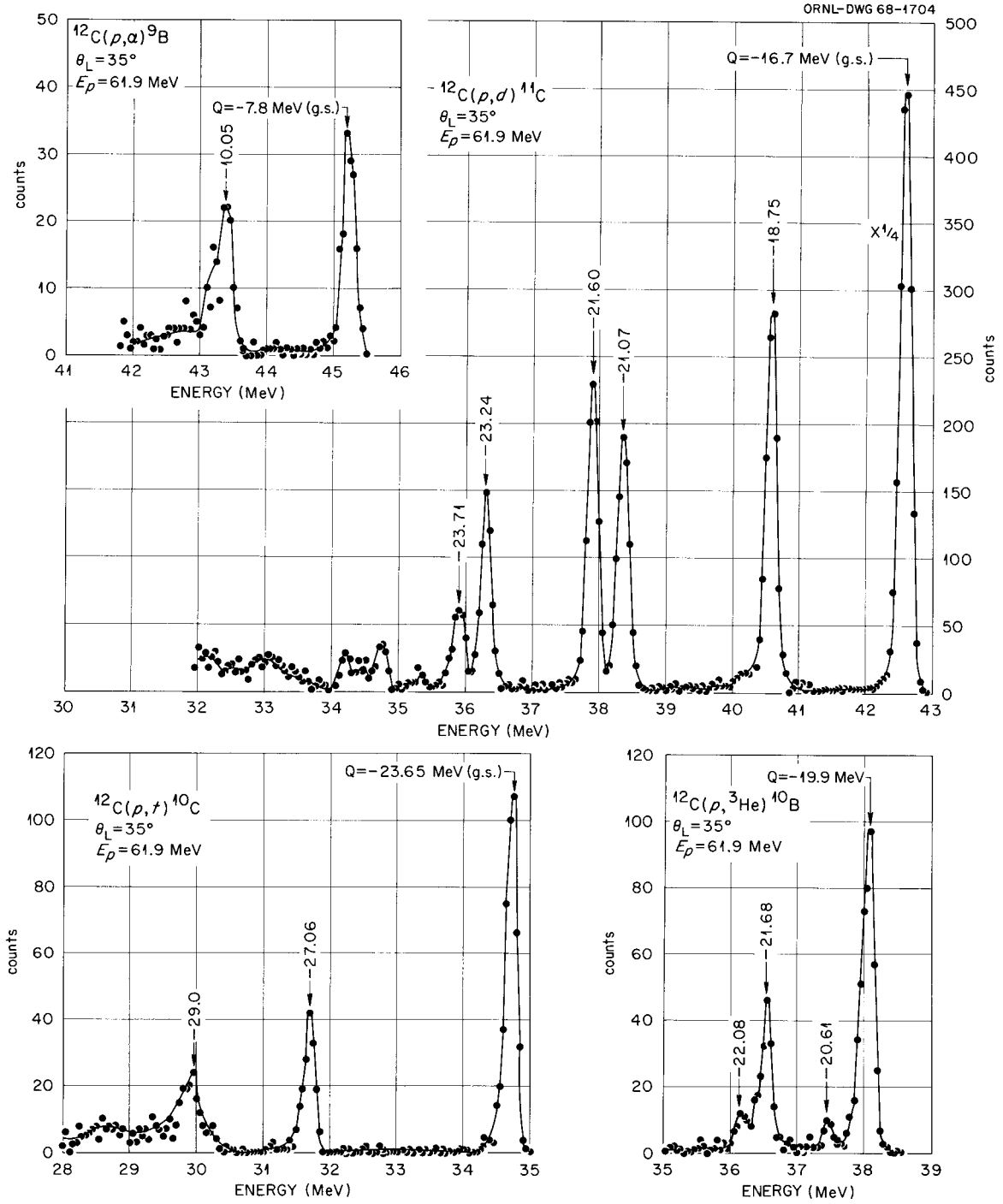

Fig. 1.22.1. High-Energy Deuteron, Triton, ^{3}He, and Alpha Spectra from ^{12}C at 35°.

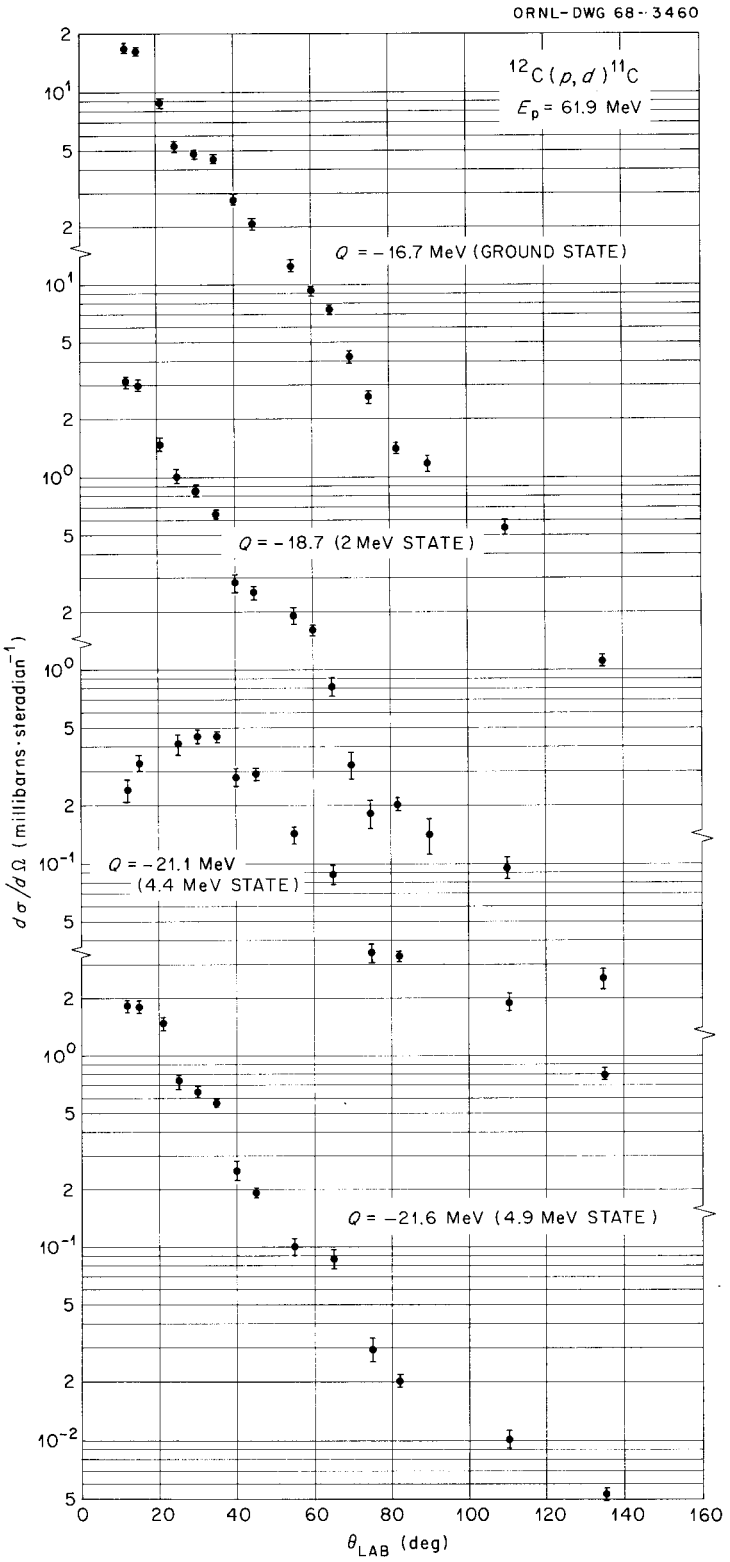

Fig. 1.22.2. Differential Cross Sections for the Levels Observed in the $^{12}C(p,d)^{11}C$ Reaction.

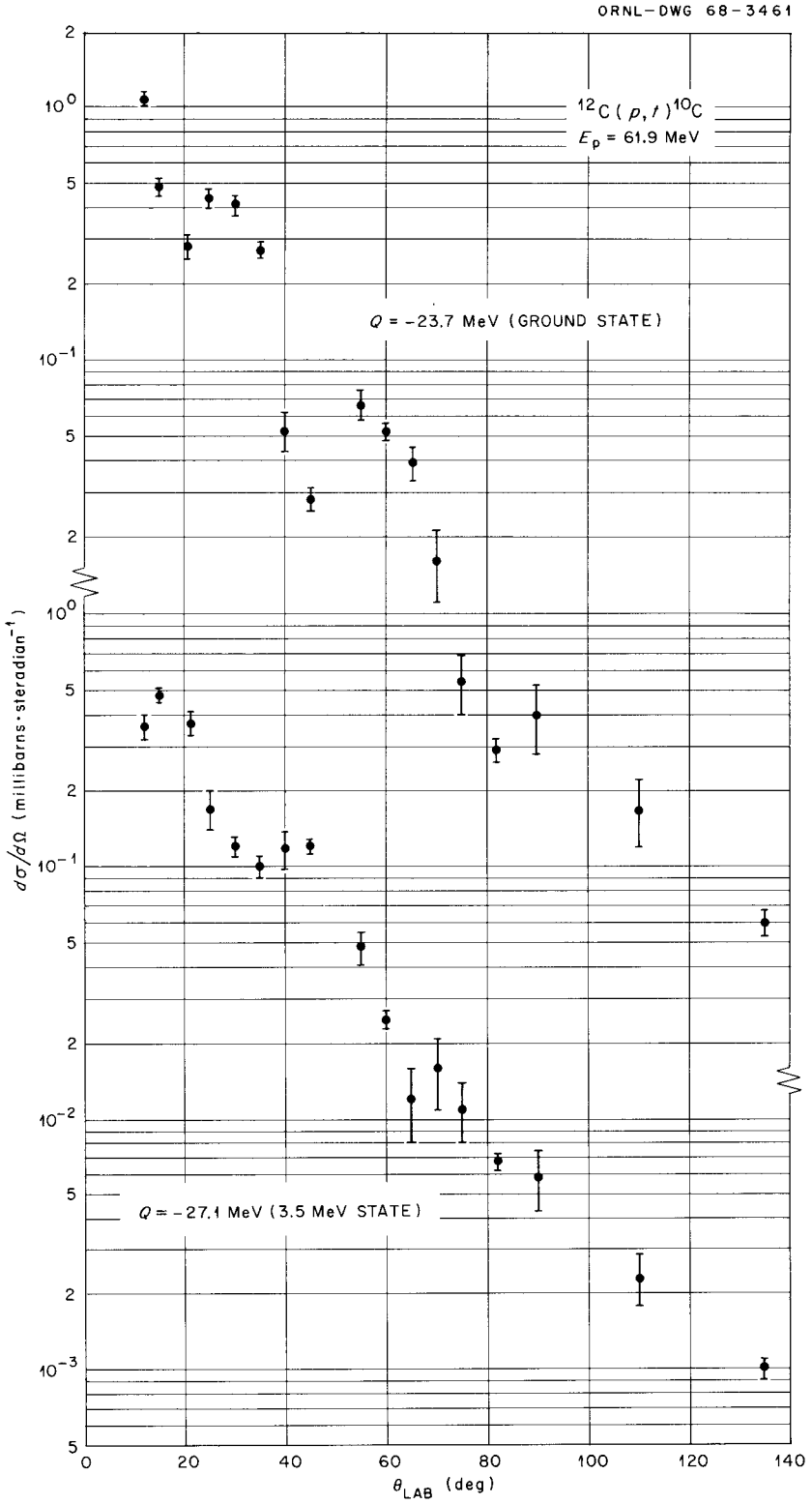

Fig. 1.22.3. Differential Cross Sections for the Levels Observed in the $^{12}C(p,t)^{10}C$ Reaction.

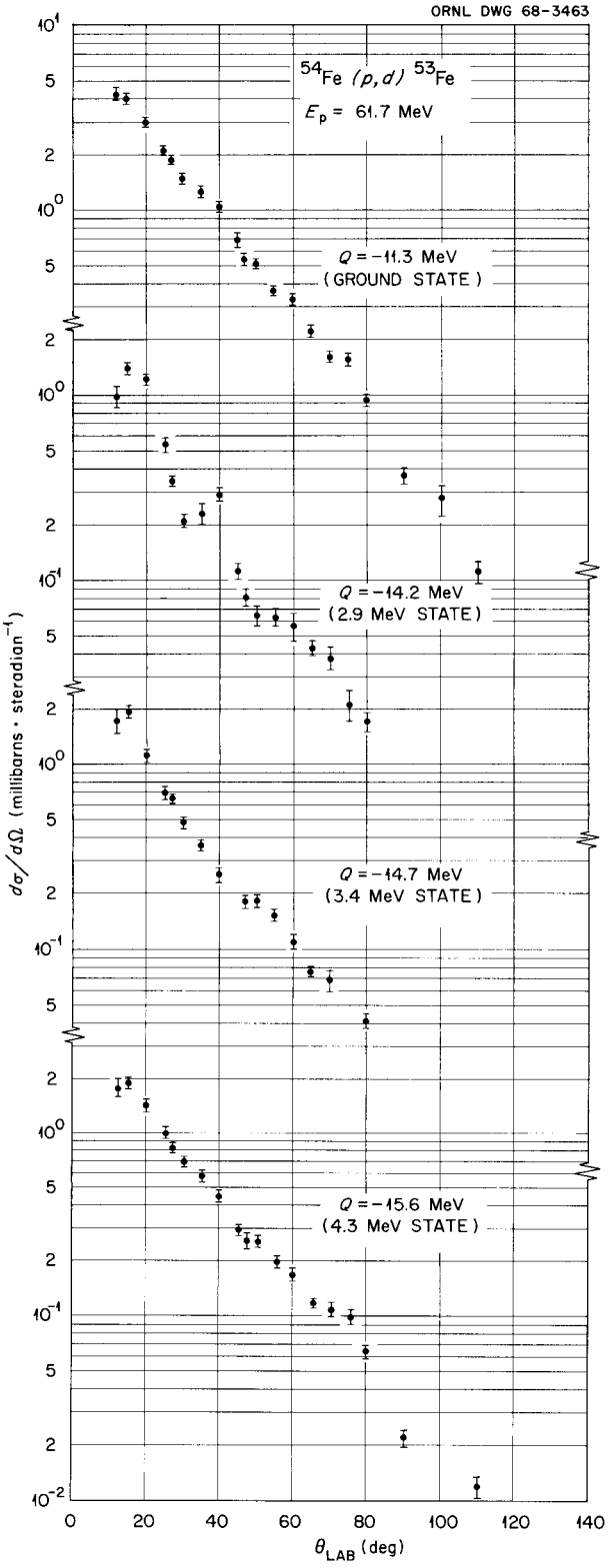

Fig. 1.22.4. Differential Cross Sections for Levels Observed in the $^{54}Fe(p,d)^{53}Fe$ Reaction.

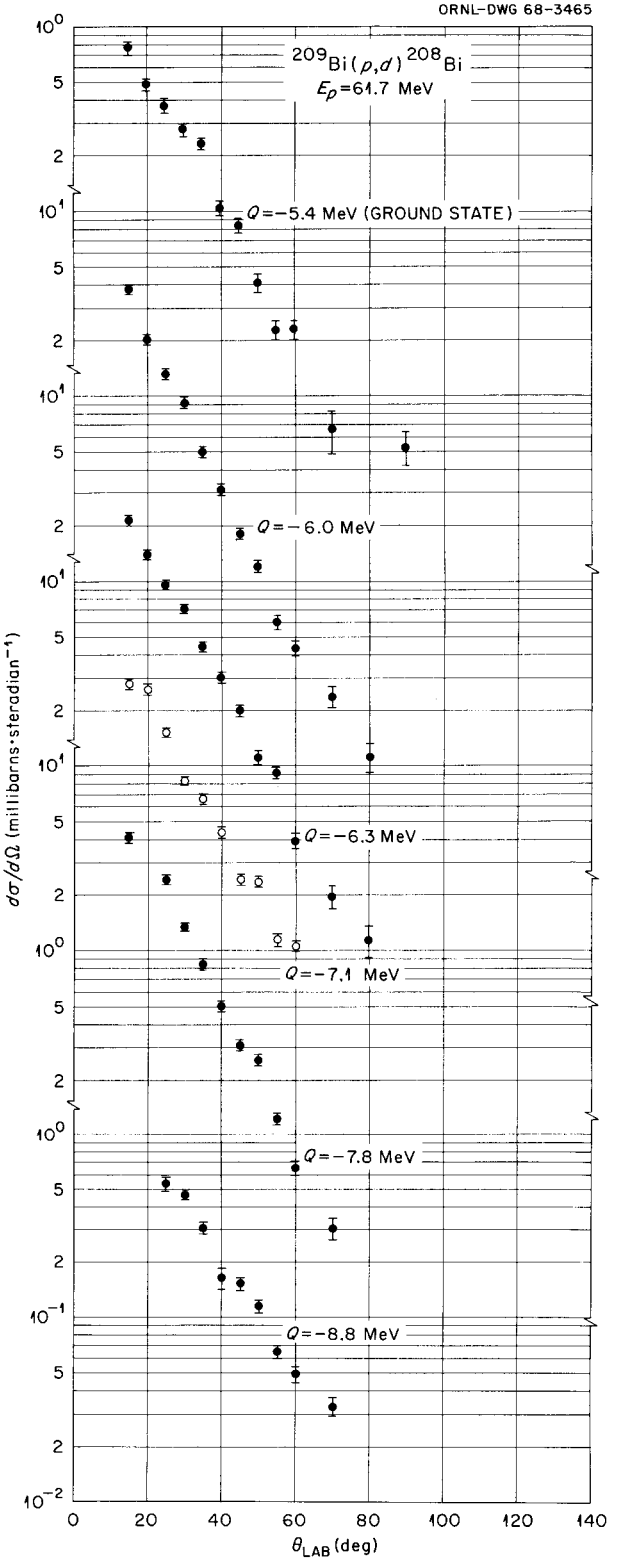

Fig. 1.22.5. Differential Cross Sections for Levels Observed in the $^{209}Bi(p,d)^{208}Bi$ Reaction.

The deuteron spectra from ^{54}Fe show the presence of four strongly excited peaks, which correspond to the ground state and 2.9-, 3.5-, and 4.3-MeV levels in the ^{53}Fe nucleus. The differential cross sections for these levels are shown in Fig. 1.22.4.

Six prominent peaks are observed from the reaction $^{209}Bi(p,d)^{208}Bi$. The levels have excitations of 0.0, 0.60, 0.95, 1.7, 2.85, and 3.45 MeV. The differential cross sections for these states are plotted in Fig. 1.22.5.

References

[1]Work funded by the National Aeronautics and Space Administration under NASA Orders R-104(1), L-12,186, and H-38280A.

[2]F. E. Bertrand *et al.*, *Differential Cross Sections for Charged Particles Produced by 60-MeV Protons on Carbon, Iron, and Bismuth*, ORNL-4274 (May 1968).

1.23 NEUTRONS FROM $^{9}Be(\alpha,n)$ REACTION FOR E_{α} BETWEEN 6 AND 10 MeV[1]

V. V. Verbinski[2] J. K. Dickens
F. G. Perey W. R. Burrus[3]

Absolute differential cross sections have been measured for the reaction $^{9}Be(\alpha,n)^{12}C$ leaving ^{12}C in its ground, first-excited, and second-excited states as a function of angle and alpha bombarding energy. The angular distribution for the ground-state (0+ state) transition changed from a fore-aft peaking at $E_{\alpha} = 9.9$ MeV. Similar behavior was observed for the second-excited-state transition (0+). The angular distribution for the first-excited-state transition (2+) displayed fore-aft peaking and was not sensitive to bombarding energy. A strong, low-energy neutron component, present at forward angles at all bombarding energies, can be accounted for by three- and four-body breakup reactions. We determined that neutrons with energy ≤ 0.5 MeV account for $\sim 30\%$ of the total neutron production cross section from this reaction.

References

[1]Abstract of paper to be published in *Physical Review;* also published as ORNL-TM-1891 (Aug. 24, 1967); work funded by National Aeronautics and Space Administration under NASA Orders R-104(1) and L-12,186.

[2]Present address: Gulf General Atomic, San Diego, California.

[3]Present address: Tennecomp, Inc., P.O. Box J, Oak Ridge, Tennessee.

1.24 MEASUREMENTS OF (d,n) REACTIONS ON ^{58}Ni, ^{60}Ni, ^{62}Ni, AND ^{64}Ni[1]

A. L. Marusak[2] F. G. Perey
P. H. Stelson[3]

Differential cross sections for $^{58}Ni(d,n)^{59}Cu$, $^{60}Ni(d,n)^{61}Cu$, $^{62}Ni(d,n)^{63}Cu$, and $^{64}Ni(d,n)^{65}Cu$ at 5 MeV and for $^{58}Ni(d,n)^{59}Cu$ at 10 MeV have been measured by time-of-flight techniques. Angular distributions were taken from 15 to 140°, with flight paths from 7 to 25 m. From the ^{58}Ni and ^{60}Ni data, about 25 energy levels were accurately obtained. From the ^{62}Ni and ^{64}Ni data only the first four levels were examined. The angular distributions calculated with the JULIE computer code, using the distorted-wave Born approximation, were compared with the experimental data for a stripping reaction for the ground state ($\frac{3}{2}^-$) and the first two excited states ($\frac{1}{2}^-$, $\frac{5}{2}^-$) of ^{59}Cu, ^{61}Cu, ^{63}Cu, and ^{65}Cu at 5 MeV and for these three states in ^{59}Cu at 10 MeV. The prominent 3.9-MeV analog state in ^{59}Cu was also studied.

References

[1]Abstract of paper presented at American Physical Society Meeting, Washington, D.C., April 1968.

[2]Oak Ridge Graduate Fellow from the University of Tennessee, Knoxville, under appointment from the Oak Ridge Associated Universities, Inc.

[3]Physics Division.

1.25 OAK RIDGE ELECTRON LINEAR ACCELERATOR (ORELA)

A. L. Boch[1] F. C. Maienschein
J. A. Harvey[2] J. A. Murray[4]
T. A. Lewis[3] H. A. Todd[3]

The Oak Ridge Electron Linear Accelerator (ORELA) has been designed to provide an intense

pulsed-neutron source for performing neutron cross-section measurements by the time-of-flight technique. The cross-section measurements assigned the highest priority will be those for materials of importance in the US Atomic Energy Commission breeder reactor program.

Construction of the underground facility housing the linear accelerator and flight stations and of the associated laboratory and office building was completed on schedule in March 1968.

The four-section linear accelerator was designed by Varian Associates to be powered by four 30-MW peak power, 65 kW average power, *L*-band klystrons. The design performance includes 140-MeV electron energy with beam powers up to 50 kW, repetition rates to 1000 pulses/sec, and currents to 15 amp for pulses as narrow as 2.3 nsec. The accelerator has been constructed by Varian Associates in accordance with this design, and assembly at Oak Ridge is complete (May 1, 1968) except for the injection system and energy analyzer. The four klystrons, which have been operated at average powers of up to about 25 kW by the manufacturer, Litton Industries, have been installed, and the x-ray shielding installation by ORNL has been completed. As of May 1, 1968, processing of the wave guides by baking at an elevated temperature ($\sim$200°C) and by the injection of rf power from the klystrons is being started by Varian.

The pacing item for the completion of the accelerator is clearly the electron gun and injection system. Bench tests of the gun by Varian at Palo Alto have shown that it is capable of producing peak currents in excess of 30 amp with switching times of $\sim$2 nsec, obtained by using ferrite-loaded delay lines for pulse shaping. The above current is the total output of the gun, and no tests have been completed of the fraction of this current transmitted through the remainder of the injection system. Such tests have been delayed by mechanical problems with vacuum valves and the pressurized freon-filled gun tank.

The present schedule indicates that beam tests should begin in the summer, with acceptance of the accelerator planned for late in 1968. The design of all the necessary equipment for the beam tests is completed (with the exception of a calorimeter for beam power determination), and fabrication of this equipment has been initiated by ORNL. The neutron-producing target and positioning mechanism has been designed and constructed by ORNL. Collimators, beam plugs, and filter changers have been designed and are under construction for two of the eleven neutron flight paths in the facility. These designs with minor modifications will be adapted for most of the other flight paths.

The data-acquisition system that has been obtained for use at ORELA is described in detail in Section 5.20, which also discusses the system planned for rapid data analysis. A very large scintillation tank for detecting gamma rays from neutron-induced capture or fission in fissile isotopes is under construction as described in Section 5.19.

References

[1] Director's Division.
[2] Physics Division.
[3] Instrumentation and Controls Division.
[4] General Engineering and Construction Division.

1.26 NEUTRON FLUX AND NEUTRON AND GAMMA-RAY SPECTRA MEASUREMENTS AT THE HFIR[1]

T. V. Blosser G. E. Thomas, Jr.[2]

Preliminary neutron flux and neutron and gamma-ray spectra measurements were made at the exit of the High Flux Intensity Reactor (HFIR) beam tubes HB-2 (radial beam tube) and HB-3 (tangential beam tube) to determine the effect of the location of the beam tube on the emerging radiation. A comparison of the neutron flux at various energies showed a variation between HB-2 and HB-3 of from about 11% at thermal energies to a factor of 10.2 at 6.3 MeV.

There is a marked difference between the gamma-ray spectrum that each beam tube exhibits.

References

[1] Abstract of ORNL-TM-2221 (in press).
[2] Argonne National Laboratory.

1.27 COMPUTER PROGRAM DEVELOPMENT FOR THE ENDF/B EFFORT

D. Irving J. Stockton[1]

As a part of Oak Ridge's contribution to the cooperative ENDF/B effort to develop and implement

a universal format and library for evaluated neutron cross sections, several computer programs have been written. These programs have been transmitted to the National Neutron Cross Section Center, who has distributed them to the other cooperating installations. EDIT is a program designed to provide easily readable printouts for ENDF/B data but it also contains some tape-copying capabilities. It was originally programmed for the CDC 1604 but had to be somewhat redesigned to be usable on other computers. In addition, changes were made to compress the printed output. A subroutine package, LEGCK, was written to check Legendre coefficients to determine whether the angular distributions generated by the coefficients are everywhere positive. LEGCK was initially used to check the data on the preliminary ENDF/B tapes but has now been incorporated into the checking program, CHECKER, written at Brookhaven, in order that data originators may check Legendre coefficients before the data are placed on the ENDF/B tapes. The SAD program was written to provide a means for converting ENDF/B angular distribution data from one allowed form to another. It will make conversions from the laboratory system to the center-of-mass system, from Legendre coefficients to tabular distributions, and vice versa. It will also carry out miscellaneous operations such as the calculation of the laboratory to center-of-mass transformation matrix or the calculation of the average cosine in the laboratory system.

Reference

[1]Mathematics Division.

2. Critical Experiments

2.0. INTRODUCTION

The fundamental budgetary motivations of critical experiments at the Oak Ridge National Laboratory continue to be the support of nuclear reactor concepts and the establishment of bases for safe and economic processes with fissile material. As the programs are developed and the experiments are designed, however, their results are perhaps even more valuable in providing insight into the physics and the analyses of nuclear chain-reacting arrangements of fissile and other materials. This is true because usually the experiments are performed in simple arrangements with a minimum of material extraneous to the study itself, conditions which characterize the results reported over many years. In most instances the measurements are paralleled by calculations.

For some time the Laboratory has been engaged in a cooperative effort with EURATOM directed toward the design of a reactor for the production of pulses of fission radiation during short periods of superprompt criticality. Investigation of many design parameters has been reported in the past. Sections 2.1, 2.2, and 2.3 this year describe preparations, including a description of the new mechanical and electrical components, for operating a critical assembly whereby it will be repetitively superprompt critical by the periodic addition of reactivity by motion of a reflector. The remainder of this section is directed more to safety matters than to reactors.

Sections 2.4–2.7 report work with assemblies of highly ^{235}U-enriched uranium metal. Section 2.4 concerns the exchange of neutrons between the cylindrical units of a two-component array, and is followed by reports on the reactivity effects of various neutron reflecting and moderating substances.

Experiments performed at Oak Ridge as early as ten years ago have resulted in significant economy in chemical operations, without degrading safety, by the introduction of borosilicate glass into vessels of large capacity for aqueous solutions. Recent Monte Carlo analyses of these experiments are recorded in Section 2.8. Once established, the calculational scheme can be used to extrapolate the experimental results to evaluate margins of safety in specifications which are to become a proposed USA Standard. This work is under the Criticality Data Center.

The ^{235}U quality of the fuel for the current round of nuclear power reactors has brought out a need for values of critical parameters of various uranium materials in environments typical of chemical processes. The work is summarized in Sections 2.9 through 2.15, which cover uranium of relatively low ^{235}U enrichment in a variety of forms – elemental, as aqueous solutions, and as homogeneous mixtures of a salt with an hydrogenous plastic. The measurements have included the critical dimensions of lattices of elemental rods in neutron moderators and reflectors comprised of water, of aqueous solutions of boron and of uranium salts, and of mixtures of the two solutions, the last simulating the materials present in reactor fuel dissolvers where, in some installations, boron is added for increased safety and capacity. Section 2.9 concerns uranium enriched to 66% in ^{235}U in a special study for the Idaho Nuclear Corporation and Section 2.15 analyzes possible reasons for the disagreement of results from theory and from experiment with slightly ^{235}U-enriched uranium.

Section 2.16 reports an extended series of experiments with aqueous solutions of ^{233}U directed to filling gaps in existing knowledge of the critical parameters of this isotope. Section 2.17 covers calculations, sponsored by the Criticality Data Center, of permissive spacings of quantities of ^{235}U, ^{233}U, or ^{239}Pu, in both elemental and oxide form, which will meet regulations estab-

lished by the Department of Transportation and the AEC for transportation of fissile materials.

The Critical Experiments Group continues to measure the subcritical reactivity of each commercially manufactured fuel element for the High Flux Isotope Reactor and now records, in Section 2.18, the variation among the first 41 elements examined.

Finally, an activity of the Criticality Data Center that is not reported elsewhere consists of very significant contributions by several members of the Group to the development of industry-produced Standards by technical societies and the USA Standards Institute. This effort is commensurate with the continuing expression by the Commission of the urgent need for standardization in the nuclear industry.

2.1 PRELIMINARY STATIC EXPERIMENTS WITH THE ORNL REPETITIVELY PULSED CRITICAL ASSEMBLY

J. T. Mihalczo

In preparation for a series of measurements in which pulses of neutrons will be produced by periodically varying the reactivity of a critical assembly to above prompt criticality, the SORA mockup[1] has been modified by incorporation of a mechanism for rotating a beryllium reflector across the unreflected face of the assembly (Sect. 2.3, this report). This modification has changed some of the nuclear characteristics of the assembly, particularly those associated with the beryllium reflector. The assembly now differs from the SORA mockup in that the plane of rotation of the reflector is tangent to the core surface rather than perpendicular to it. The beryllium itself is 20.3 cm high, 12.7 cm wide, and 3.16 cm thick rather than 24, 11, and 7 cm, respectively, as in the SORA reference assembly.[1] The beryllium is mounted in a titanium alloy rotor which passes the core surface 60 times per second at a speed of about 2.7×10^4 cm/sec. The thickness of the fixed iron reflector has been reduced from 29 cm to 17 cm.

Preliminary measurements required for a safety analysis and those necessary to obtain some estimates of the expected pulse shape have been completed for a 24-cm-high core.

The critical mass, the prompt neutron time behavior, the total reactivity of the new movable reflector and its variation as a function of displacement both in the plane of rotation and perpendicular to it, power density distributions, void coefficients, and reactivity effects of the various parts of the core and the fixed reflector of the assembly have been measured. The results indicate that the 24-cm-high core and the modified reflector will produce neutron pulses slightly wider than those of the SORA reference assembly.

Reference

[1]G. Kistner and J. T. Mihalczo, *Critical Experiments for the Repetitively Pulsed Reactor SORA*, ORNL-4263 (in press).

2.2 AN INSTRUMENT FOR MEASURING MECHANICAL VIBRATIONS IN FAST-PULSE REACTOR CORES[1]

James F. Ellis

Proximity gages are advantageous for measuring mechanical displacements and vibrations in pulse reactor cores because they require no physical attachment to the core material. However, the intense ionizing radiation produced during pulses presents a serious problem for the more common proximity devices, especially those employing a variable capacitance. Inductive probes using high-frequency magnetic fields to generate eddy currents on the surface of a highly conductive material are useful. As the probe approaches the surface, the induced eddy currents reduce its inductance and this alteration is measured in terms of circuit unbalance resulting in an output potential. These instruments also suffer some adverse effects of intense radiation and heating.

During initial tests of the Army Pulse Radiation Facility Reactor conducted at the Oak Ridge Critical Experiments Facility, a newly developed proximity gage was tested. It comprised a 30 MHz oscillator driving a differential probe whose input and dual outputs matched the connecting coaxial lines. The unit was operated within 0.10 in. of the reactor core surface. The close proximity of the probe to the core distorted the rf flux in the probe's tip and produced an unbalanced signal in

the otherwise identical probe outputs. This unbalance was displayed on a Textronix Model 543 oscilloscope after being rectified and filtered. Cable lengths between probe and readout station were 125 ft and could have been extended without complication. The differential nature of the instrument virtually cancelled the effects of radiation and heating.

Sensitivity of the instrument depends on its distance from the object detected and may be expressed in millivolts per mil of gap variation at a given gap width. The static sensitivity of the instrument, measured with the aid of a micrometer, ranged from 1.9 mV/mil at a gap width of 0.200 in. to 56 mV/mil at contact.

Frequency response was measured using a variable-speed rotating wheel having shaped notches on its periphery. By placing the probe near the wheel, equivalent vibrations of up to 80 kHz could be generated. Other frequency response measurements were made by placing the probe within the field of a specially designed tank circuit whose Q could be modulated by a variable frequency oscillator. Signals from the oscillator and the proximity detector were simultaneously monitored on the oscilloscope. The amplitude of the modulating signal was held constant while variations in the output signal were measured. Frequency response showed a smooth roll-off amounting to a 27% decrease at 200 kHz equivalent mechanical vibration.

Figure 2.2.1 is an oscilloscope trace of a single radiation pulse and of the resultant radial vibration of one of the center core sections. The yield was 2.30×10^{17} fissions and the radial displacement was approximately 0.042 in. The unit has been used with peak core surface temperatures of up to 300°C.

Reference

[1]Summary of paper to be presented at the Fourteenth Annual Meeting of the American Nuclear Society, Toronto, Ontario, Canada, June 9–13, 1968, and published in *Trans. Am. Nucl. Soc.*, Vol. 11, No. 1 (1968).

2.3 DESIGN AND MECHANICAL BEHAVIOR OF THE MOVABLE REFLECTOR FOR THE ORNL REPETITIVELY PULSED CRITICAL ASSEMBLY

W. C. Tunnell J. F. Ellis

A proposal to extend the static measurements of the SORA critical experiments, as previously re-

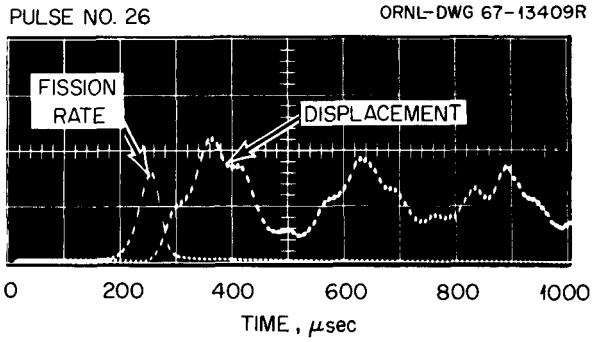

PULSE NUMBER	FISSION YIELD ($\times 10^{17}$)	REACTOR PERIOD μsec	DISPLACEMENT (10^{-3} in.)[a] THERMAL	VIBRATIONAL[b]
26	2.30	14.8	~30	~42

a. DISPLACEMENT OF OUTER SURFACE OF CENTRAL FUEL ANNULUS.
b. FIRST MAXIMUM TO MINIMUM.

Fig. 2.2.1. Radial Displacement of Reactor Core Surface and Fission Rate During a Pulse of 2.30×10^{17} Fissions. In the range of displacement the detector sensitivity was approximately 0.020 in./large division.

ported,[1] to the production of pulses of radiation has required the development of a method to dynamically pulse the existing assembly. A feasibility study resulted in a design which incorporates a counterbalanced rotor that includes a beryllium-reflector insert and is mounted directly to the shaft of an electric motor (see Fig. 2.3.1). Such a device was fabricated in which the plane of rotation of the rotor and insert is parallel with the open face of the critical assembly and is enclosed in a metal housing or shroud. Rate of motion is such that the beryllium insert passes the core face 60 times per second at a speed of ~1000 fps. Titanium alloyed with 6% aluminum and 4% vanadium was selected as the rotor material and ^{238}U rods were used as the counterbalance material.

The rotating assembly was statically balanced using gas-supported bearings and was then dynamically balanced on the precision microbalance equipment at the Oak Ridge Gaseous Diffusion Plant. A calculated unbalance at a speed of 3600 rpm of ~5 oz-in. due to strain was subseqeuntly verified and corrected by experimentally removing material from the hub until vibration characteristics were acceptable.

Since operation with air in the shroud resulted in excessive friction and exorbitant heating (~1°C/sec), helium was substituted for air, and water cooling was applied to the shroud exterior. Stable operating characteristics under these conditions exceeded expectations. The overall deviation of the rotor from its plane of motion was measured by a proximity gage developed by Ellis (see Sect. 2.2, this report) to be 0.0003 in. (see Fig. 2.3.2). The equilibrium gas temperature was ~37°C, and the pressure developed in the shroud was ~11 in. of H_2O. Vibration, measured simul-

ORNL-DWG 68-5414

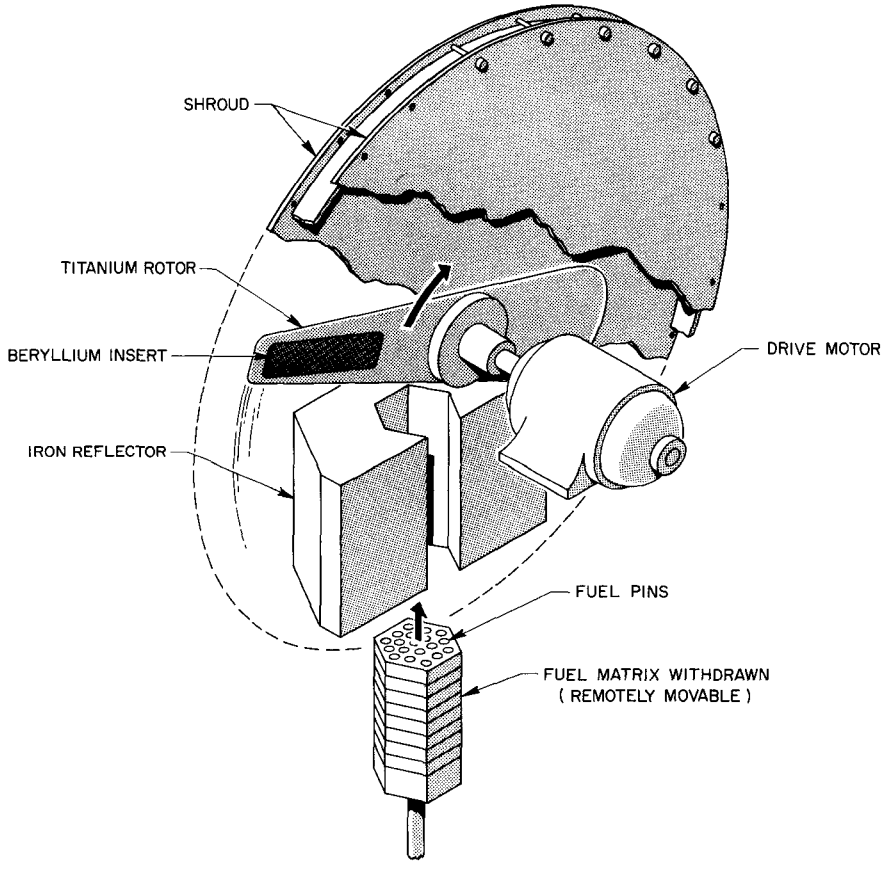

Fig. 2.3.1. Diagramatic of the Rotor Constructed for the Repetitively Pulsed Critical Assembly.

ORNL-DWG 68-5415

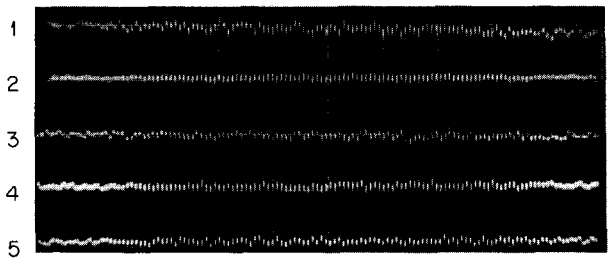

Fig. 2.3.2. Typical Oscillogram of the Signals from the Proximity Gage Showing Multiple Exposures in Which Individual Short Vertical Lines Represent Rotor Positions. Variations in the location of the short vertical lines relative to the horizontal grid represent displacements, in the axial direction, of the rotor, from a plane of rotation. Trace Nos. 1, 3, 4, and 5 show displacements of the rotor as it passes the fuel matrix; trace No. 2 is from a less sensitive gage 90° away. One small vertical scale division $\cong$ 0.0002 in.

taneously at four locations by vibration meters,[2] was quite satisfactory with peak-to-peak movements of 0.0002 in. of the assembly fuel-matrix, 0.0005 to 0.0035 in. of the reflector components, 0.0002 in. of the drive motor, and 0.020 in. of the top of the shroud. The latter was the maximum observed in the entire assembly. The device has experienced 60 startups and has run for more than 23 hr at operating conditions with no evidence of malfunction. Some periods of continuous operation have been as long as 6 hr.

References

[1]G. Kistner and J. T. Mihalczo, *Neutron Phys. Div. Ann. Progr. Rept. May 31, 1966,* ORNL-3973, Vol. 1, pp. 20–22.

[2]General Radio Co. Type 1553A using a vibration pickup, Type 1560-P52, consisting of an inertia-operated lead-zirconate-titanate ceramic pickup which delivers a voltage proportionate to the acceleration of the vibratory motion. The signals were recorded by Honeywell Viscorder oscilloscope Model 906B.

2.4 REACTIVITY COUPLING AND NEUTRON-TRANSIT-TIME DISTRIBUTION IN ASSEMBLIES OF ENRICHED URANIUM METAL CYLINDERS

J. T. Mihalczo

Previous calculations[1] of the neutron behavior in assemblies comprised of two coaxial 93.2%-enriched uranium metal cylinders based on space-independent neutron kinetics assuming a uniform neutron transit time between the components, or cores, have not satisfactorily predicted the results of pulsed neutron measurements. The time distribution of neutrons was measured in each cylinder after a pulse of neutrons was injected into one of the cylinders. The discrepancy, at early times, between the calculated distribution in the cylinder which is not pulsed and the experimental value may be due to the assumption of a single

ORNL-DWG 68-5566

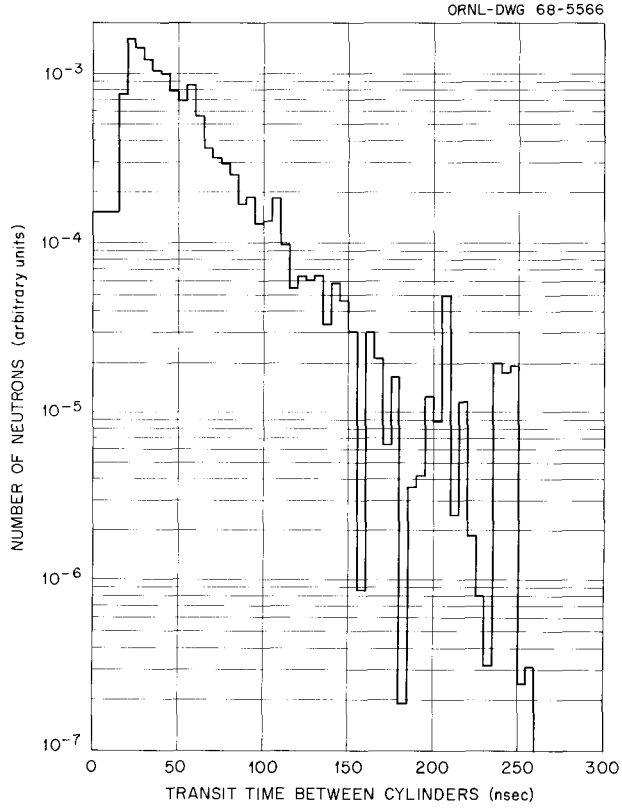

Fig. 2.4.1. Distribution of Neutron Transit Times Between Two 27.94-cm-diam, 8.426-cm-high Coaxial Uranium Cylinders Spaced 52.5 cm.

Table 2.4.1. Coupling Reactivity of Two Sets of Coupled Uranium Metal Cylinders

Cylinder Dimensions		Component Spacing (cm)	Coupling Reactivity (dollars)	
Diameter (cm)	Thickness (cm)		Calculated	Measured
27.94	8.255	37.0	3.58	3.7
27.94	8.426	52.5	1.91	2.0

transit time rather than a distribution of times within the neutron population. This distribution has now been calculated by the 05R Monte Carlo neutron transport theory code.[2] Typical results are given in Fig. 2.4.1. Recalculation of the time distribution of neutrons based on this variable transit time has not yet been completed.

The applicability of the Monte Carlo method to calculations of the neutron behavior in two-component assemblies has been tested by comparison of calculated and experimental values of the coupling reactivity between the components. In these two-core assemblies the coupling reactivity is just that by which an individual core is subcritical when the other one is removed and was, in these cases, determined from the prompt neutron decay constant in isolated cylinders. The comparison reported in Table 2.4.1 is good.

References

[1]J. T. Mihalczo, p. 484 in *Proceedings of the National Topical Meeting on Coupled Reactor Kinetics, Texas A & M College, January 23–24, 1967,* Texas A & M Press.

[2]D. C. Irving *et al., 05R, A General Purpose Monte Carlo Neutron Transport Code,* ORNL-3622 (1965).

2.5 MONTE CARLO CALCULATIONS OF THICK-GRAPHITE-REFLECTED URANIUM-METAL CRITICAL ASSEMBLIES[1]

J. T. Mihalczo

The neutron multiplication factor for a variety of uranium-metal annuli and cylinders surrounded with thick carbon reflectors has been measured and calculated by a Monte Carlo method. The material within the annuli was carbon or air. The thicknesses of the side, top, and bottom reflectors were equal in any one assembly. The density of the individual pieces of Type HLM graphite varied between 1.688 and 1.783 g/cm^3. The uranium metal was enriched to 93.2% in ^{235}U and has previously been described.[2]

The multiplication factors were calculated using the 16-group cross sections of Hansen and Roach[3] for uranium and carbon and the KENO code,[4] which is a multigroup Monte Carlo method with isotropic scattering and with neutron slowing down treated by a transfer matrix. Twenty-one thousand neutron histories (105 batches of 200 source neutrons each) were calculated, requiring ~20 min on the IBM 360-75 for each problem. The source neutrons were put in the uranium uniformly, and the first five batches were discarded.

The neutron weight below which neutrons were killed by Russian roulette was a function of the distance in the reflector from the core. This function was inversely proportional to the adjoint flux, obtained from S_n transport theory calculations of a uranium-metal sphere surrounded by an 18-in. carbon reflector. This function was used for all assemblies. The standard deviations on the multiplication factors are between 0.9 and 1.3%.

These assemblies all have one small uranium dimension and would require a high-order S_n calculation for a good transport theory solution. The running time for S_6 transport theory calculations using the DOT code[5] for these assemblies is ~90 min.

The results of the experiments and calculations are given in Table 2.5.1. Since the calculated multiplication factors are, on the average, about 0.6% higher than the experimental ones, a slight

Table 2.5.1. Carbon-Reflected Uranium Metal Annuli and Cylinders

Uranium		Reflector Thickness (in.)	Material Within the Annulus	Height of Fuel for Radial Increments of[a] (in.)					Average Density (g/cm^3)		Multiplication Factor	
OD (in.)	ID (in.)			0-3.5	3.5-4.5	4.5-5.5	5.5-6.5	6.5-7.5	Uranium	Carbon	Measured[b]	Calculated
15	0	15		0.749	0.687	0.691	0.689	0.685	18.734	1.756	1.000	1.018 ± 0.012
15	11	15	Carbon				1.695	1.696	18.722	1.760	1.000	0.999 ± 0.011
15	9	15	Carbon			1.170	1.191	1.172	18.717	1.762	1.001	1.011 ± 0.011
13	9	16	Carbon			1.756	1.755		18.727	1.757	1.002	1.005 ± 0.011
11	9	17	Air			4.019			18.706	1.757	1.002	0.987 ± 0.009
9	0	18		1.256	1.288				18.678	1.757	1.000	1.018 ± 0.009
9	7	18	Air		4.386				18.727	1.757	1.000	1.012 ± 0.013
9	7	18	Carbon		4.069				18.745	1.757	1.001	1.009 ± 0.011

[a]These dimensions show the unevenness of the upper surface of the assembly.

[b]Corrected for the effect of support structure. This correction was less than 3 cents in reactivity.

adjustment of the cross sections may be required for exact agreement with experiment.

References

[1]Summary of paper to be presented at the Fourteenth Annual Meeting of the American Nuclear Society, Toronto, Ontario, Canada, June 9–13, 1968, and to be published in *Trans. Am. Nucl. Soc.*, Vol. 11, No. 1 (1968).

[2]John T. Mihalczo, *Nucl. Sci. Eng.* **20**, 60 (1964).

[3]Lucie D. Connolly, *Los Alamos Group-Averaged Cross Sections*, LAMS-2941 (1963).

[4]G. E. Whitesides, G. W. Morrison, and E. C. Crume, *Trans. Am. Nucl. Soc.* **9**, 133 (1966).

[5]F. R. Mynatt, *A User's Manual for DOT, A Two-Dimensional Discrete Ordinates Transport Code with Anisotropic Scattering*, K-1694 (to be published).

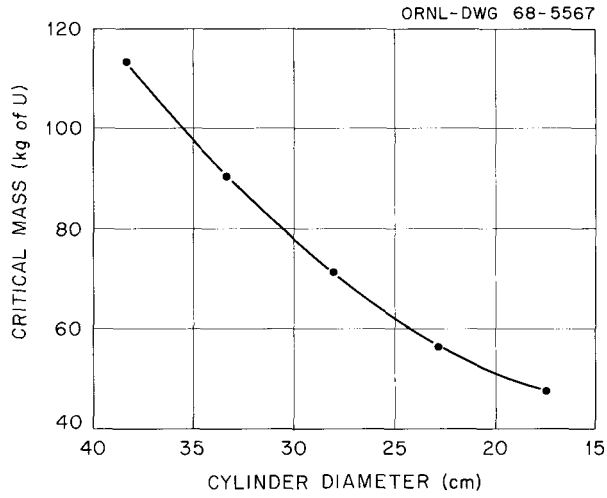

Fig. 2.6.1. Critical Mass of Partly Reflected U(93.15) Metal Cylinders as a Function of Cylinder Diameter. An effectively infinite polyethylene reflector was adjacent to one flat surface.

2.6 CRITICAL PARAMETERS OF ENRICHED URANIUM METAL PARTLY REFLECTED BY POLYETHYLENE

J. T. Mihalczo

Uranium metal cylinders with diameters ranging from 17.71 to 38.09 cm have been assembled to delayed criticality with a polyethylene reflector on one flat surface. The uranium was enriched to 93.15 wt % in ^{235}U and had an average density in these assemblies of 18.70 g/cm^3. The dimensions of the reflector were 112 × 112 × 15.2 cm and the density was 0.916 g/cm^3. It was of effective infinite thickness and, as shown below, also effectively infinite in area. A plot of the critical mass as a function of diameter is given in Fig. 2.6.1.

In a measurement with the cylinder of largest diameter the area of the polyethylene reflector was reduced from 112 cm square to 82 cm square with a decrease in reactivity of less than 1 cent, showing that these areas are effectively infinite. The critical mass of this partly reflected cylinder, 113 kg, is 3.3 kg less than that reported from an earlier experiment by Hansen *et al.*,[1] in which, however, the diameter of the reflector was equal to that of the uranium, 38.09 cm.

Reference

[1]G. E. Hansen, D. P. Wood, and B. Peña, *Reflector Savings of Moderating Materials on Large Diameter U(93.2%) Slabs*, LAMS-2744 (1962).

2.7 CRITICAL EXPERIMENTS WITH ENRICHED URANIUM METAL-POLYETHYLENE, -PLEXIGLAS, AND -TEFLON MIXTURES[1]

D. W. Magnuson

Reflected and unreflected critical experiments were performed at H:^{235}U atomic ratios of from 0 to 5 in rectangular geometry with layers of enriched uranium and polyethylene. Base dimensions of the assemblies were 5 × 10 and 10 × 10 in. In some unreflected experiments the metal was interleaved with Plexiglas and with Teflon at only the latter base dimensions. Heterogeneity effects were found to be small from experiments assembled from the same or approximately the same materials but with different layer thicknesses. Values of k_{eff}, calculated with the KENO Monte Carlo code, are in excellent agreement with the experimental values. By equating geometrical bucklings for

rectangular and spherical geometry, these data were converted to critical masses for spheres. Comparisons of the experimental values were made to the critical masses calculated by the ANISN transport code for homogeneous spheres.

Reference

[1]Abstract of ORNL-TM-2082 (February 1968).

2.8 CRITICAL DIMENSIONS OF AQUEOUS SOLUTIONS OF HIGHLY ^{235}U-ENRICHED URANIUM CONTAINING BOROSILICATE GLASS; A COMPARISON OF MONTE CARLO CALCULATIONS AND EXPERIMENTS

J. Wallace Webster

The computations reported below have as their motivation the establishment of further technical foundation for a proposed standard titled "Use of Borosilicate Glass Raschig Rings as a Fixed Neutron Absorber in Solutions of Fissile Material."

The first experiments relating to this subject were reported by Fox and Gilley.[1] In 1962 and 1963 further relevant experiments were conducted and reported by Thomas *et al.*;[2] in Section 2.16 of this report Thomas describes similar experiments conducted with ^{233}U uranyl nitrate solutions, the previous work having dealt with ^{235}U uranyl nitrate solutions only.

Reference 1 was concerned with regular arrays in triangular pattern of borosilicate glass pipes containing 4 wt % natural boron. It was decided to start the computational program with 05R Monte Carlo calculations with selected cases from Ref. 1 because the pipe assemblies are, of course, much simpler geometrically than the random configurations of rings, the diameter of each ring being about the same as its length.[2] The Monte Carlo method was selected partly because of a general interest in an application of the Monte Carlo method to strongly heterogeneous systems. Table 2.8.1 presents these results.

It is worthwhile pointing out that the standard deviation and the spread of values of k_{eff} for the 400-neutron batches that were used in the Monte Carlo calculations are not any greater for strongly heterogeneous systems like Experiments 2 and 3 of the table than for homogeneous systems, e.g., Experiment 1. This observation is in accordance with Monte Carlo theory.[3]

Examination of the energy spectrum of leakage, absorption, and fission-producing neutrons in Experiment No. 3 of Table 2.8.1 shows that for this case about 21% of the neutrons starting out from fission end up being absorbed in the glass.

Table 2.8.1. Calculated Multiplication Factor[a] for Critical Mixtures of Borosilicate Glass Pipes and Aqueous $UO_2(NO_3)_2$ Solution with No Reflector

^{235}U enrichment: 87.4 wt %
Uranium concentration: 320 g/liter
H/^{235}U ratio: 81.4
Boron content of glass: 4%

Experiment No.	Pipe Diameter (in.)		Center-to-Center Pipe Spacing (in.)	Glass Content (vol %)	Diameter of Vessel (in.)	Solution Height (in.)	Calculated k_{eff}
	Outside	Inside					
1	None	None		0.0	20.0	5.97	1.00 ± 0.01
2	2.38	2.00	3.00	7.8	20.0	16.7	0.99 ± 0.01
3	1.88	1.50	2.75	9.78	20.0	26.6	0.99 ± 0.01

[a]In all calculations the one-group option for thermal neutrons was used, with the boron cross section assigned its 0.025-eV value.

The final phase of the program, which is still in a preliminary stage, will be to develop a procedure for computing or estimating the values of k_{eff} of random configurations of glass raschig rings in solutions of fissile material.

Because the geometrical description of a completely random array of rings is beyond the storage limitations of the available computing machines, a program was written which prepares input cards to the GEOM portion of 05R for a configuration that has the axes of all adjacent rings mutually perpendicular. Such a configuration has some of the neutronic aspects of the random arrays.

For the purpose of investigating the utility of such an orderly pattern to Monte Carlo calculations, values of k_{eff} and k_∞ were obtained for several such arrays and for several arrays of parallel glass pipes having the same inner and outer diameters as the rings, a range of glass fraction in the mixture with fissile solution, and the same chemical composition of the glass. The properties of the solution are the same as those in Table 2.8.1. Table 2.8.2 presents the results.

The preliminary conclusion from this table is that the glass content of the mixture is a somewhat more important factor in determining the difference between values of k_∞ of solutions with rings and with pipes than is the diameter of the glass pieces themselves, all other parameters remaining unchanged.

The idealization to pipes appears to be a consistently conservative approach to the development of the standard mentioned in the first paragraph, the degree of conservativeness being about 6% in k_∞.

Table 2.8.2. Change in k_∞ Due to Substitution of Mutually Perpendicular Raschig Rings for Parallel Pipes, with Inner Diameter and Volume Percent Glass as Constants

Inside Diameter (in.)	Outside Diameter (in.)	Volume Percent Glass	Percent Decrease in k_∞
Inner Diameter Constant			
3	3.437	18.72	4.7 ± 1.2
3	3.563	22.84	5.3 ± 1.2
3	3.816	30.00	6.0 ± 1.2
Volume Percent Glass Constant			
3	3.563	22.84	5 ± 1
2	2.375	22.84	6 ± 1
1.5	1.781	22.84	6 ± 1
3	3.816	30.00	6 ± 1
1.5	1.908	30.00	6 ± 1

References

[1] J. K. Fox and L. W. Gilley, *Neutron Phys. Div. Ann. Progr. Rept. Sept. 1, 1959*, ORNL-2842, p. 82.

[2] J. T. Thomas *et al.*, *Critical Mass Studies, Part XIII*, ORNL-TM-499 (1963).

[3] R. R. Coveyou, private communication, 1968.

2.9 CRITICAL PARAMETERS OF LATTICES OF $U(62)O_2$-BeO FUEL PINS MODERATED AND REFLECTED BY WATER, DILUTE AQUEOUS $U(93)O_2(NO_3)_2$ SOLUTION, AND AQUEOUS BORON SOLUTION AS A GUIDE TO THE DESIGN OF A DISSOLVER[1]

E. B. Johnson

The uranium remaining in spent fuel elements from reactors is generally recovered by chemical processes in which the material is first put into solution in a dissolver. For reasons of economics the charge into the dissolver should be as large as possible consistent with nuclear criticality safety. In order to increase the permissible size of a charge, some chemical plants[2] are using boron as a soluble neutron absorber in the dissolver solution. Experiments have been reported[3] (see also Sect. 2.11, this report) in which boron was added to the moderator-reflector water of lattices of fuel elements to determine the increase in critical mass. The present investigation is an extension of these measurements to fuel containing 62.4%-^{235}U-enriched uranium.

The fuel consisted of pellets of homogeneously mixed $U(62.4)O_2$-BeO, 50.2 wt % uranium and 43 wt % BeO at 94% of theoretical density. The pellets were encased in 0.051-cm-thick, 0.932-cm-od

Hastelloy to a fuel length of 193 cm. The Be:^{235}U atomic ratio was 13. The fuel pins were first latticed in water in order to determine the spacing at which the critical mass of the lattice was minimal. As shown in Fig. 2.9.1, this spacing was about 2.5 cm between centers. A subcritical close-packed lattice of 59.4 kg of ^{235}U (380) pins is also noted in the figure.

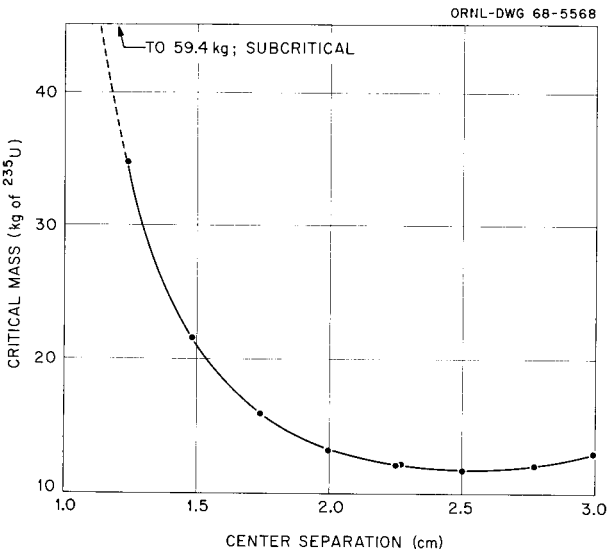

Fig. 2.9.1. Effect of Separation Between $U(62.4)O_2$-BeO Fuel Pins Arranged in Square Lattices on the Critical Mass of the Lattice.

The effect of the dissolver solution on the criticality of this fuel was investigated at the lattice spacing which gave minimum critical mass in the water-moderated and -reflected lattices. Slab-shaped lattices as large as 45.6 × 15.8 cm in cross section in a square pattern at a pitch of 2.48 cm were made critical in a 50.8-cm-diam cylinder to which the aqueous solutions of neutron absorber and/or fissile material could be added; the cylinder was surrounded on its lateral surface by an effectively infinite water reflector. The concentration of boron was adjusted to that necessary to the criticality of a specific lattice; the concentration of the uranyl nitrate was the maximum to be expected in a chemical dissolver. The results of these experiments are summarized in Table 2.9.1.

References

[1]Work supported by the Idaho Nuclear Corporation.

[2]W. G. Morrison, *Criticality Aspects of the Revised Zirconium Dissolution System at the Idaho Chemical Processing Plant,* IN-1173 (1968).

[3]E. B. Johnson and R. K. Reedy, Jr., *Critical Experiments with SPERT-D Fuel Elements,* ORNL-TM-1207 (1965).

Table 2.9.1. Slab Lattices[a] of $U(62)O_2$-BeO Fuel Pins in Aqueous Solutions

Composition of Moderator and Reflector[b]		Critical Number of Fuel Pins	Mass of ^{235}U in Fuel Pins (kg)
H_3BO_3 (g of boron/liter)	$U(93)O_2(NO_3)_2$ (g of ^{235}U/liter)		
0	0	99	15.47
0.039	0	113	17.66
0.190	0	133	20.78
0	3.68	83	12.97
0.315	3.68	133	20.78

[a]The lattices were constructed in a square pattern at a pitch of 2.48 cm. The ratio of the length to the width of the horizontal cross section of each lattice was approximately 3:1.

[b]The lattices were constructed in a 50.8-cm-diam cylinder to which the moderator and reflector could be added; this cylinder was surrounded by an infinitely thick water reflector.

2.10 EFFECT OF STEEL-WATER REFLECTORS ON THE CRITICALITY OF LOW-ENRICHED URANYL FLUORIDE SOLUTION[1]

E. B. Johnson C. E. Newlon[2]

The effect of composite reflectors of steel and water on the reactivity of single cylinders of aqueous solution of low-enriched uranium has been studied. The results are applicable in the evaluation of the nuclear criticality safety of shipping containers and provide bases for the verification of calculational models.

The solution was contained in each of two stainless steel cylinders having 0.079-cm-thick walls; the solution diameters were 33.02 and 39.09 cm. Lateral steel reflectors adjacent to the solution ranged in thickness up to 5.08 cm and were surrounded by an infinitely thick water reflector. There was no top or bottom reflector. Similar experiments using $U(93.3)O_2(NO_3)_2$ have been reported.[3] Table 2.10.1 summarizes the data.

It was found that the presence of 1.27-cm-thick steel outside either container resulted in the maximum decrease in reactivity from that with

Table 2.10.1. Experimental Critical Heights and Computed k_{eff} of Cylinders of $U(4.98)O_2F_2$ Solution with Lateral Composite Steel-Water Reflectors[a]

	Reflector Steel Thickness (cm)						
	0	0.64	1.27	1.90	2.54	3.81	5.08
33.02-cm-diam Cylinder							
Composite steel-water reflector[b,c]							
Critical height, cm	84.60	158.85	201.60	172.80	143.00	109.10	91.95
k_{eff}[d]	1.009	0.999	0.995	0.998	0.998	1.001	1.003
39.09-cm-diam Cylinder							
Steel reflector (no water)[e]							
Critical height, cm	98.80	74.65	64.75	59.30	55.70	50.90	48.20
k_{eff}[d]	1.000	1.003	1.007	1.009	1.011	1.013	1.016
Composite steel-water reflector[b,e]							
Critical height, cm	44.70	48.70	49.40	48.95	48.20	46.50	45.10
k_{eff}[d]	1.012	1.004	1.003	1.004	1.005	1.006	1.006
Composite 0.081-cm-thick cadmium-steel-water reflector[e,f]							
Critical height, cm	64.90				54.45		50.80
k_{eff}[d]	1.002				1.011		1.008

[a]The solution concentration was 909.1 g of U/liter (H:^{235}U = 488). The cylindrical container was 0.079-cm-thick type 304 stainless steel with no top or bottom reflector.

[b]Values computed by ANISN Code.

[c]The steel was adjacent to the solution cylinder; the thickness of the water was effectively infinite.

[d]The steel reflector and the water had a common height of 243.9 cm measured from the same reference as the solution height.

[e]The steel reflector and the water when present had a height of 106.2 cm measured from the same reference as the solution height.

[f]The cadmium was between the solution container and the steel.

water alone; this reactivity change was approximately 2.8 and 1.8 dollars for the 33.02- and 39.09-cm-diam cylinders, respectively. Further increase in steel thickness up to 5.08 cm increased the reactivity, but not to that existing with water alone. Interposition of 0.081-cm-thick cadmium between the 39.09-cm-diam solution cylinder and the steel decreased the reactivity of the cylindrical volume from that without the cadmium; however, the presence of cadmium between the 5.08-cm-thick steel reflector and the water resulted in no reactivity change. These latter measurements emphasize the importance of relative locations of neutron-absorbing materials in the evaluation of the nuclear criticality safety of water-reflected containers.

A one-dimensional transport theory code, ANISN,[4] together with the Hansen-Roach cross-section set[5] and a buckling approximation of the form $DB^2\phi$ for the finite longitudinal cylinder dimension, was used for the analysis of the experimental data. The largest difference between computed and experimental values of k_{eff} was 0.016, as shown in Table 2.10.1. The code also permitted calculation of the neutron current densities at the fuel-reflector interface and therefore provides an indication of the number and energy of the neutrons that are returned to the fuel region. The computations thus indicate that the changes in reactivity of the solution cylinders induced by the steel reflector are primarily the result of the competition between the effective decrease in the reflection of the thermal component and the effective increase in the reflection of the epithermal component of the neutron flux at the fuel-reflector interface with increasing thicknesses of steel.

References

[1]Summary of paper to be presented at the Fourteenth Annual Meeting of the American Nuclear Society, Toronto, Ontario, Canada, June 9–13, 1968, and to be published in *Trans. Am. Nucl. Soc.*, Vol. 11, No. 1 (1968).

[2]Oak Ridge Gaseous Diffusion Plant.

[3]Dixon Callihan *et al.*, *Critical Mass Studies, Part V*, K-643 (1950).

[4]Ward W. Engle, Jr., *A Users Manual for ANISN*, K-1693 (1967).

[5]Gordon E. Hansen and William H. Roach, *Six and Sixteen Group Cross Sections for Fast and Intermediate Critical Assemblies*, LAMS-2543 (1961).

2.11 CRITICAL LATTICES OF U(4.89) RODS IN WATER AND IN AQUEOUS BORON SOLUTION

E. B. Johnson

Measurements of critical water-moderated and -reflected lattices of 4.89% ^{235}U-enriched uranium [U(4.89)] rods 1.31, 2.07, and 2.49 cm in diameter have been reported.[1,2] The data were the first available to provide reference for calculation of the criticality of heterogeneous assemblies of uranium of this intermediate enrichment.

The measurements have been extended to rods 0.762 cm in diameter and 30 cm long, each containing, on the average, 13.06 g of ^{235}U. The influence of the lattice pitch on the critical dimensions was determined by constructing several lattices in both square and triangular patterns. The data were then transformed, by equating bucklings using an extrapolation distance of 6 cm, to equivalent spheres for comparison with Clark's[3] calculations. The results are shown in Fig. 2.11.1, where critical masses are plotted as a function of the ^{235}U concentration, which is, of course, a measure of the pitch. Shown for comparison are the earlier

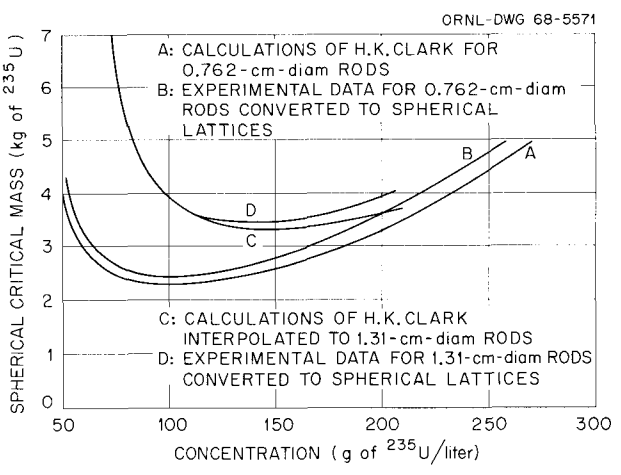

Fig. 2.11.1. Comparison of Calculated and Experimental Critical Spherical Lattices of U(4.89) Rods in Water.

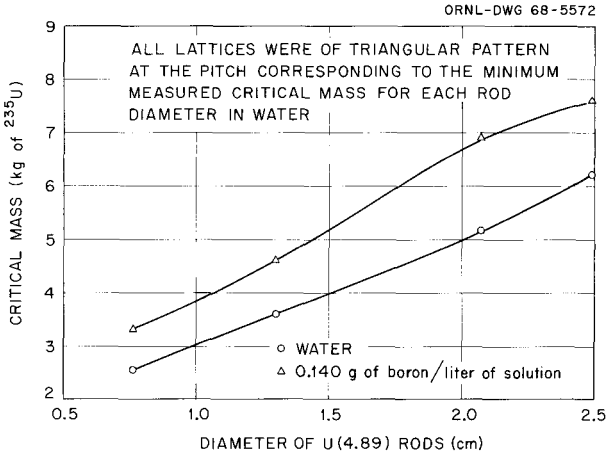

Fig. 2.11.2. Experimental Critical Mass of Lattices of Uranium Metal Rods Moderated and Reflected by Water and by Aqueous Boron Solution.

data for the 1.31-cm-diam rods. It is noted that the calculated masses of the 0.762-cm-diam rods are less than the experimental values at all concentrations.

In order to provide further guidance for the dissolution of rods of this ^{235}U enrichment in chemical processes, a limited number of experiments have been performed with an aqueous solution containing 0.140 g of boron per liter as the moderator and reflector. A lattice of rods of each of the above diameters was constructed in the boron solution at the pitch which had resulted in the minimum measured critical mass in the water-moderated and -reflected experiments. The results are shown in Fig. 2.11.2, where the experimentally determined critical mass is plotted as a function of rod diameter for both the water-moderated and the solution-moderated assemblies.

References

[1]E. B. Johnson, *Neutron Phys. Div. Ann. Progr. Rept. May 31, 1967,* ORNL-4134, p. 31.

[2]E. B. Johnson, *Trans. Am. Nucl. Soc.* **10**, 190 (1967).

[3]H. K. Clark, *Critical and Safe Masses and Dimensions of Lattices of U and UO_2 Rods in Water,* DP-1014 (1966).

2.12 CRITICAL DIMENSIONS OF LATTICES OF U(3.85) CYLINDRICAL ANNULI

E. B. Johnson

Earlier measurements have been reported[1,2] of the criticality of arrays of large cylindrical annuli of U(1.95) moderated and reflected by water. The results have served to establish safe handling and transport conditions for that material which is produced and shipped in approximately the physical dimensions of the experiment units as an early step in the fabrication of fuel elements for a Hanford reactor. The present study is an extension of this work to a uranium enrichment of 3.85% in ^{235}U.

Each unit was a 326-kg cylindrical annulus 76.2 cm (30 in.) long with outside and inside diameters of 18.3 cm (7.2 in.) and 6.6 cm (2.6 in.), respectively; the ^{235}U content was 12.55 kg. As many as 25 of these units were latticed in water in both square and triangular patterns; the number of units required for criticality was determined as a function of surface separation, or array moderation. Each array was surrounded by an effectively infinite water reflector on the bottom and lateral surfaces to the height required for criticality. The results are shown in Fig. 2.12.1, where the number of units required for criticality (on the left ordinate) and the ^{235}U mass (on the right ordinate) are plotted against the water-to-uranium volume ratio. Because of the rather significant reactivity associated with each unit, only a few of the arrays with an effectively infinite top reflector were sufficiently close to criticality for their reactivity to be determined; in most cases the addition of one unit to a subcritical lattice prohibited the presence of water above the metal. Therefore the data reported as describing truly submerged critical lattices were obtained by interpolation.

In a single experiment a 2.5-cm-diam cylinder of Styrofoam was inserted into the central region of each annulus of a five-unit critical array; the reactivity was decreased about 1 dollar by the exclusion of water by the Styrofoam.

It will be recalled that, in lattices of the U(1.95) annuli, the critical number of units at optimum moderation between the square and triangular patterns differed by a factor of 2. There was a difference of only 33% between lattices in the two patterns of the U(3.85) annuli, thus indicating that

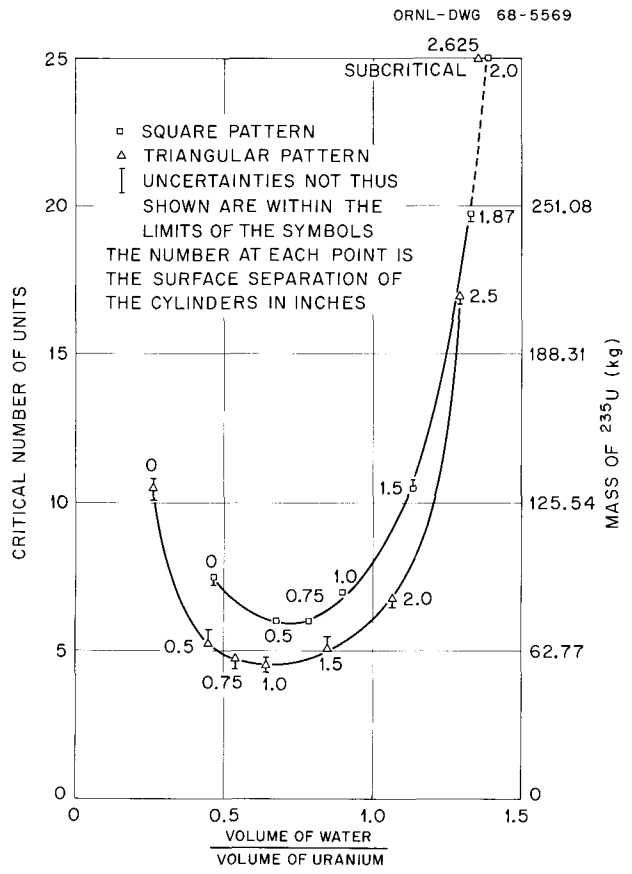

Fig. 2.12.1. Critical Lattices of U(3.85) Annular Cylinders Moderated and Reflected by Water.

the difference in patterns may depend on the uranium enrichment rather than solely on the physical dimensions of the units.

These data will be used to verify the applicability of KENO, a Monte Carlo neutron transport code,[3] for calculating the criticality of uranium of low enrichment.

References

[1]E. B. Johnson, *Neutron Phys. Div. Ann. Progr. Rept. May 31, 1966,* ORNL-3973, Vol. I, p. 15.

[2]E. B. Johnson, *Trans. Am. Nucl. Soc.* **9**, 185 (1966).

[3]G. E. Whitesides, personal communication, 1968.

2.13 HOMOGENEOUS CRITICAL ASSEMBLIES OF $U(2)F_4$ IN PARAFFIN AT AN $H:^{235}U$ ATOMIC RATIO OF 972

S. J. Raffety

A continuing program[1] of critical experiments with homogeneous hydrogen-moderated assemblies of low-enrichment UF_4 in paraffin has been extended to include a mixture containing 70.2 wt % $U(2)F_4$ with a resulting $H:^{235}U$ atomic ratio of 972. The density of this mixture within a single unit was 2.302 g/cm^3, but the average density in the experimental assemblies was 2.286 g/cm^3 due to irregularities in assembly.

The dimensions of several critical rectangular parallelepipeds of this material (corrected for neutron reflection from support structures) were determined by the usual procedures. The buckling, B^2, for each assembly was calculated from these measured dimensions and the extrapolation distance, 2.59 ± 0.11 cm, obtained from flux measurements in a critical assembly. The average material buckling thus obtained was $(3.616 \pm 0.030) \times 10^{-3}$ cm^{-2}. Minimum critical masses in unreflected rectangular, cylindrical, and spherical geometries were calculated from these data by standard buckling conversion techniques, and the results are shown, along with the results of previous experiments, in Fig. 2.13.1. A value of 3.45 ± 0.08 cm was found for the reflector savings in assemblies completely reflected by an effectively infinite thickness of polyethylene on the sides and top and of a methacrylate plastic on the bottom. This reflector savings was used to calculate the minimum critical masses for reflected geometries shown in Fig. 2.13.1.

A value of the $^{238}U:^{235}U$ fission ratio in a critical assembly was found to be $(5.00 \pm 0.27) \times 10^{-4}$ from measurements with miniature fission chambers ($\frac{1}{4}$ in. od × 1 in. long). This value was used to obtain 1.016 ± 0.002 for the fast fission factor ϵ.

The prompt-neutron decay constant α, measured by the pulsed neutron technique, was 105 ± 2 and 107 ± 2 sec^{-1} respectively in unreflected and reflected delayed critical assemblies.

Measurement of the infinite medium multiplication factor k_∞ for this fuel mixture is reported in Section 2.14.

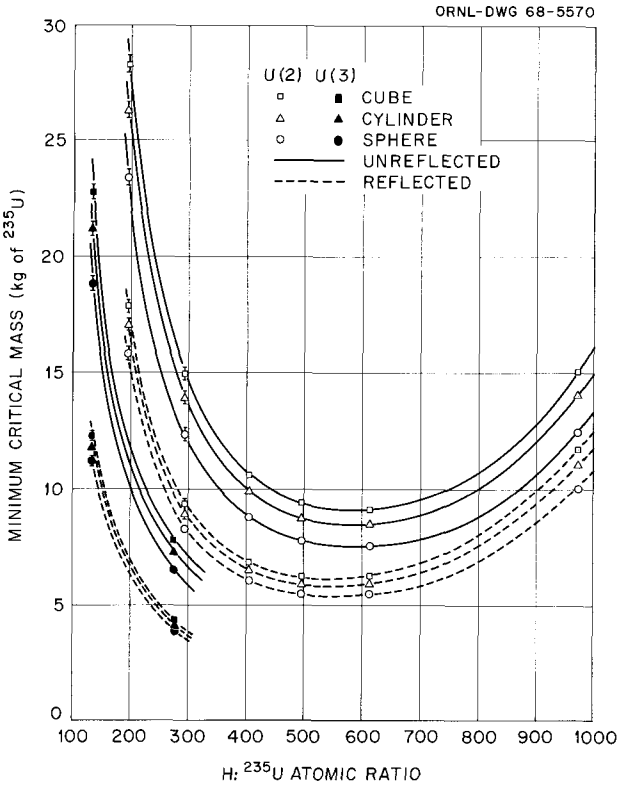

Fig. 2.13.1. Critical Mass of 2 and 3% ^{235}U-Enriched UF_4 and Paraffin Mixtures as a Function of the H:^{235}U Atomic Ratio. The values were derived from experimental data by buckling conversions.

Reference

[1]S. J. Raffety, *Neutron Phys. Div. Ann. Progr. Rept. May 31, 1967*, ORNL-4234, p. 28.

2.14 NEUTRON AGE AND INFINITE-MEDIUM NEUTRON MULTIPLICATION FACTOR FOR UF_4-PARAFFIN MIXTURES WITH LOW ^{235}U ENRICHMENT

S. J. Raffety J. T. Mihalczo

The infinite-medium neutron multiplication factor, k_∞, and the neutron age to thermal energy for UF_4-paraffin mixtures have been inferred from critical experiments with 2 and 3% ^{235}U-enriched uranium. The volume fraction of paraffin was varied so that the H:^{235}U atomic ratio was between 195 and 972 for the 2% enrichment and was 133 and 277 for the 3% enrichment.

The infinite medium multiplication factor is given as

$$k_\infty = \frac{1}{(1-\bar{\beta})\,K_p(B) + (\bar{\beta}/\epsilon)\,K_d(B)}, \qquad (1)$$

where $K_p(B)$ and $K_d(B)$, the nonleakage probabilities for prompt and delayed neutrons, respectively, are given by

$$K_{d[p]}(B) = \frac{1}{(1+\tau_{d[p]}B^2)\,(1+L^2B^2)}. \qquad (2)$$

The change in reactivity with a change in buckling is

$$\frac{\Delta\rho}{\Delta B^2} \simeq \frac{\epsilon(1-\bar{\beta})\,(1+\tau_d B^2)\,(L^2+\tau_p+2L^2\tau_p B^2)}{(1+\tau_p B^2)^2\,(1+L^2B^2)} + \frac{\bar{\beta}(L^2+\tau_d+2L^2\tau_d B^2)}{(1+\tau_d B^2)\,(1+L^2B^2)}. \qquad (3)$$

The fast fission factor ϵ, the material buckling B^2, and the quantity $\Delta\rho/\Delta B^2$ were measured in critical assemblies of each fuel mixture. The

Table 2.14.1. Transport Theory Calculations of the Age of Prompt Fission Neutrons in Water

Sphere Radius (cm)	Convergence Criterion $\times 10^3$	Order of S_n	Neutron Age[a] (cm^2)
49	1.0	4	21.4
99	1.0	4	21.8
199	1.0	4	21.8
199	1.0	8	24.6
199	0.5	8	24.6
199	0.5	16	26.0
199	0.5	32	27.2
199	0.1	32	27.2
Experimental value[b]			27.2

[a]One-sixth of the second moment of the neutron flux distribution of the 13th group (1 to 3 eV).

[b]Average of four experimental values of the age of ^{235}U fission neutrons to indium resonance given in *Reactor Physics Constants*, 2d ed., p. 138, ANL-5800 (1963).

Table 2.14.2. Neutron Age and Infinite-Medium Neutron Multiplication Factor for UF_4-Paraffin Mixtures with 2 and 3% ^{235}U Enrichment

	2% ^{235}U						3% ^{235}U	
N, ^{235}U atomic density (10^{20} atoms/cm^3)	1.581	1.330	1.119	0.992	0.867	0.623	2.349	1.671
H: ^{235}U atomic ratio	195 ± 3	294 ± 5	406 ± 7	496 ± 8	614 ± 10	972 ± 17	133 ± 2	277 ± 5
$\bar{\beta}$, delayed fraction of fission neutrons, measured (10^{-3})	7.06 ± 0.31	6.96 ± 0.29	6.89 ± 0.28	6.85 ± 0.27	6.81 ± 0.26	6.72 ± 0.24	7.10 ± 0.31	6.88 ± 0.28
ϵ, fast fission factor, measured	1.042 ± 0.007	1.034 ± 0.006	1.029 ± 0.005	1.026 ± 0.004	1.022 ± 0.004	1.016 ± 0.002	1.045 ± 0.008	1.028 ± 0.005
L^2, thermal neutron diffusion area, calculated (cm^2)	1.69 ± 0.08	1.67 ± 0.08	1.72 ± 0.09	1.79 ± 0.09	1.86 ± 0.09	2.11 ± 0.11	1.15 ± 0.06	1.22 ± 0.06
B^2, average critical buckling, measured (10^{-3} cm^{-2})	4.393 ±0.059	5.892 ± 0.118	6.568 ± 0.122	6.651 ± 0.116	6.205 ± 0.073	3.616 ± 0.030	6.561 ± 0.051	10.209 ± 0.122
$\Delta\rho/\Delta B^2$, change in reactivity per unit change in buckling, measured (cm^2)	−36.80 ± 0.52	*a*	−26.69 ± 0.37	−24.85 ± 0.35	−23.65 ± 0.33	−24.05 ± 0.34	−32.89 ± 0.46	−23.07 ± 0.32
Multiplier[b] for Hansen-Roach ^{238}U absorption cross sections for groups 8 through 12	0.74	0.78	0.83	0.87	0.93	1.00	0.74	0.83
τ_d, average age of delayed neutrons to thermal energy, calculated[c] (cm^2)	27.0	21.5	18.6	17.3	16.0	14.5	25.7	17.5
τ_p, age of prompt fission neutrons to thermal energy (cm^2)								
Measured	42.6 ± 3.2	*a*	31.8 ± 2.5	28.8 ± 2.0	26.4 ± 1.8	24.4 ± 1.6	42.8 ± 4.0	32.0 ± 3.1
Calculated[c]	45.5	37.9	33.9	32.0	30.1	27.5	44.1	32.6
k_∞, infinite-medium neutron multiplication factor								
Measured	1.196 ± 0.014	*a*	1.222 ± 0.018	1.205 ± 0.014	1.177 ± 0.011	1.096 ± 0.006	1.290 ± 0.027	1.343 ± 0.032
Calculated[d]	1.204	1.229	1.217	1.202	1.170	1.086	1.302	1.341

[a]These quantities were not measured for the second mixture.
[b]This modification of the Hansen-Roach cross sections was used in all transport theory calculations.
[c]One-sixth of the second moment of the flux distribution of the 16th (thermal) group of an S_{32} transport theory calculation.
[d]Calculated by transport theory.

thermal neutron diffusion area L^2 was calculated from thermal neutron cross sections.[1] The delayed neutron fraction $\overline{\beta}$ was determined from the delayed neutron fractions for ^{235}U and ^{238}U measured by Keepin[2] and from the ^{238}U-to-^{235}U fission ratio measured in the critical assemblies.

The age to thermal energy of delayed neutrons, τ_d, was obtained from the second monent of the flux distribution in 199-cm-radius spheres calculated by S_{32} transport theory using the ANISN[3] code, the energy distribution of delayed neutrons as the source spectrum, and a modification by Knight[4] of the Hansen-Roach[5] 16-group cross sections. With this modification, which was a reduction of the ^{238}U absorption in the resonance region, Knight's calculations of k_∞ agreed with experimental results from the Physical Constants Testing Reactor for the mixture with H:^{235}U atomic ratio of 195 and other low-enrichment materials. The effect of sphere size, the order of S_n, and the convergence criteria used in the calculation were investigated in calculations of the age of prompt fission neutrons in water, and the results are given in Table 2.14.1.

With all the other parameters obtained as described above, Eq. (3) can then be solved for the age of prompt fission neutrons to thermal energy, τ_p. The nonleakage probabilities $K_p(B)$ and $K_d(B)$ are then calculated by Eq. (2), and these quantities are used in Eq. (1) to obtain k_∞. The results are given in Table 2.14.2.

The age of prompt neutrons to thermal energy, calculated by the same method as that for the delayed neutrons, and values of k_∞ obtained from transport theory are also shown in Table 2.14.2. The values of k_∞ agree very well with experiment.

References

[1] *Neutron Cross Sections*, BNL-325, 2d ed., Vol. I, Supplement No. 2 (1964) and Vol. III (1965).

[2] G. R. Keepin, *Physics of Nuclear Kinetics*, Addison Wesley, Reading, Mass. (1965).

[3] Ward W. Engle, Jr., *A User's Manual for ANISN, A One Dimensional Discrete Ordinates Transport Code with Anisotropic Scattering*, K-1693 (1967).

[4] J. R. Knight in Appendix I of Report K-1663, *Hydrogen Moderation – A Primary Nuclear Safety Control for Handling and Transporting Low-Enrichment UF_6*, by C. E. Newlon and A. J. Mallett (1966).

[5] Gordon E. Hansen and William H. Roach, *Six- and Sixteen-Group Cross Sections for Fast and Intermediate Critical Assemblies*, LAMS-2543 (1961).

2.15 O5R MONTE CARLO CALCULATIONS OF LOW-ENRICHED URANIUM, THERMAL, CRITICAL ASSEMBLIES AND EVIDENCE OF ERRORS IN ^{238}U CROSS SECTIONS[1]

J. Wallace Webster

As criticality calculation methods have become more exact and capable of utilizing cross sections in all their detail, instead of in the form of integral values such as age and resonance escape probability, evidence has been growing that the computed multiplication factors k_{eff} of low-enriched uranium thermal systems are low compared with experimental values.

The work reported here was initiated to see whether this discrepancy occurs when the Monte Carlo method is used together with point-set representations of the cross sections. Considerable analysis was devoted to the representation of the ^{238}U cross sections with point sets of data, and the results are presented by Calcomp plots of cross section vs neutron energy and tables of the resonance integrals.

The critical experiments chosen for comparisons with computations were all unreflected, homogeneous, and representative of a broad range of resonance capture in ^{238}U. A definite pattern emerged from these comparisons: the greater the neutron capture in ^{238}U, the lower the computed k_{eff}. The evidence of errors in the cross sections of ^{238}U or their representation, previously noted by others, is thus strengthened by this report.

Reference

[1] Abstract of ORNL-TM-2187 (in press).

2.16 CRITICAL EXPERIMENTS WITH AQUEOUS SOLUTIONS OF $^{233}UO_2(NO_3)_2$

J. T. Thomas

The criticality of ^{233}U under conditions of interest to nuclear criticality safety as well as in

basic geometries suitable for theoretical analysis has been studied in a series of experiments conducted over the past 18 months. In one series aqueous uranyl nitrate solutions of ^{233}U were examined in a large capacity vessel containing borosilicate glass in order to define systems having k_∞ of unity or less. In a second series as many as 27 nearly identical subcritical cylindrical volumes of the solution were assembled in air-spaced arrays both unreflected and reflected by polyethylene to establish parameters useful in storage and transport specifications. A final series of experiments determined the criticality of water-reflected and unreflected spherical and cylindrical volumes.

The ^{233}U isotopic content of the uranium of the uranyl nitrate solution was 97.59%. There were no impurities present in significant quantities.

Borosilicate Glass Experiments

Exponential experiments with uranyl nitrate solution having uranium concentrations of 333 and 204 g/liter were performed in an unreflected aluminum cylinder 50.8 cm in diameter and 18.3 cm high having a lateral wall thickness of 1.5 mm and a 1.27-cm-thick bottom. Flux traverses were made with a 6.4-mm-diam BF_3 counter along the axis of the cylinder through a mixture of solution and randomly oriented glass raschig rings. A neutron source was provided by adding sufficient solution above the glass rings to produce a critical slab.

A description of the raschig rings is given in Table 2.16.1. The conditions described in this table define mixtures having a negative material buckling and hence values of k_∞ less than unity. Thus, ^{233}U as an aqueous uranyl nitrate solution at a uranium concentration of 333 g/liter may be stored in any quantity, either mass or volume, provided that the borosilicate glass uniformly occupies 38% of the volume of the container.

Spaced Subcritical Components

Cylindrical containers, of 4.63 liters capacity and fabricated of 0.25-mm-thick stainless steel, had an outside diameter and a height of 18.28 and 17.67 cm, respectively. They were identically filled to within ±0.5 g of solution. Critical assemblies of reflected and unreflected arrays at uranium concentrations of 333 and 204 g/liter were constructed. The reflector material was 15.2-cm-thick polyethylene (ρ = 0.93 g/cm^3) located from the peripheral cylinders of the array by a distance equal to one-half the surface separation between cylinders. The critical conditions for the arrays of cylinders at the two uranium concentrations are summarized in Table 2.16.2.

Table 2.16.1. Conditions for Mixtures of Uranyl Nitrate Solutions of ^{233}U and Glass Raschig Rings Whereby $k_\infty < 1$

Uranium concentration (g/liter)	333	204
Natural-boron content of glass (wt %)	3.9	3.9
Glass content of mixture (vol %)	38	33
Dimensions (cm) of borosilicate glass raschig rings		
Length	4.45	1.59
Outside diameter	3.81	1.59
Wall thickness	0.56	0.43
Isotopic content of uranium (%)		
^{232}U (ppm)	6.47	
^{233}U	97.54	
^{234}U	1.05	
^{235}U	0.03	
^{236}U	<0.01	
^{238}U	1.39	
Isotopic content of boron (%)		
^{10}B	19.74	
^{11}B	80.26	

Simple Geometries

Presented in Table 2.16.3 are the critical conditions for water-reflected and unreflected spherical and cylindrical volumes of the solution which had a value of k_{eff} of 1.0000 ± 0.0005. A concentration at which a sphere was critical was first established, and then several critical cylindrical volumes were measured. The results for unreflected cylinders have been corrected for the 1.27-cm-thick aluminum base of the container, so the results describe cylindrical volumes having aluminum on the lateral surface only.

Table 2.16.2. Critical Parameters for Unreflected and Reflected Arrays of Units of Uranyl Nitrate Solution of Uranium Containing 97.5% ^{233}U

No. of Units in Array[a]	Polyethylene Reflector Thickness[b] (cm)	Center-to-Center Separation of Units (cm)		Average Uranium[c] Density (g/cm^3)
		Horizontal	Vertical	
333 g of U per liter; H:^{233}U = 73; specific gravity, 1.468; 1.432 kg of U per container				
8 (2 × 2 × 2)	0	20.44	19.13	0.179
27 (3 × 3 × 3)	0	25.72	24.57	0.088
8 (2 × 2 × 2)	15.2	31.95	30.36	0.046
27 (3 × 3 × 3)	15.2	41.03	38.57	0.022
204 g of U per liter; H:^{233}U = 119; specific gravity, 1.280; 0.885 kg of U per container				
8 (2 × 2 × 2)	0	20.16	18.81	0.116
27 (3 × 3 × 3)	0	25.01	23.89	0.059
8 (2 × 2 × 2)	15.2	30.23	25.51	0.034
27 (3 × 3 × 3)	15.2	38.05	36.74	0.017

[a]The solution was contained in cylinders of 0.25-mm-thick stainless steel with an outside diameter of 18.28 cm and height of 17.67 cm. The number of units along the edges of the array is given in parentheses.

[b]The polyethylene reflector was located at the cell boundaries.

[c]See Table 2.16.1 for isotopic content.

Table 2.16.3. Critical Conditions of $^{233}UO_2(NO_3)_2$ Aqueous Solution in Water-Reflected and Unreflected Simple Geometries

$UO_2(NO_3)_2$ Solution[a]			Critical Dimensions									
			Spheres		Cylinders[b]							
					50.8-cm diam		38.1-cm diam		25.3-cm diam		20.3-cm diam	
Uranium Concentration (g/liter)	Specific Gravity	H:^{233}U	Radius (cm)	Mass (kg of U)	Height (cm)	Mass (kg of U)	Height (cm)	Mass (kg of U)	Height (cm)	Mass (kg of U)	Height (cm)	Mass (kg of U)
Unreflected Assemblies												
333	1.468	73			13.36	9.02						
204	1.280	122			13.51	5.59	15.14	3.52	24.69	2.53		
131	1.183	195	14.579	1.70	14.07	3.74	16.35	2.44	28.52	1.88		
102	1.144	253	15.078	1.46			17.60	2.05	33.40	1.71		
74.6	1.106	349	15.821	1.24			19.35	1.65	43.69	1.64		
44.6	1.050	581	18.378	1.16			26.37	1.34				
Water-Reflected Assemblies[c]												
132	1.186	194	11.170	0.769			13.42	1.77	17.22	1.14	22.86	0.976
95.0	1.135	273	11.847	0.662			*d*	*d*	19.67	0.939	20.02	0.824
47.9	1.068	548	14.579	0.621			19.6	1.07	31.53	0.757	*d*	*d*

[a]See Table 2.16.1 for isotopic content of the uranium.

[b]Aluminum cylinders had a 1.5-mm-thick wall and 1.27-cm-thick bottom. Spheres were of aluminum with 1.22-mm-thick wall.

[c]There was no reflector on the top of any cylinder. The surface of the reflector water was 24.3 cm above the solution, a distance equal to the bottom reflector thickness.

[d]There was insufficient solution inventory to achieve criticality; the maximum solution height was 12.5 cm in the 38.1-cm-diam cylinder and 68.2 cm in the 20.3-cm-diam cylinder.

2.17 MONTE-CARLO-CALCULATED CRITICALITY OF SUBCRITICAL COMPONENTS OF ^{233}U, ^{235}U, AND ^{239}Pu ARRAYED IN CUBIC GEOMETRY

J. T. Thomas

The criticality of spaced, individually subcritical quantities of fissile materials as an oxide and as metal is currently being investigated by a calculational program supported by the Criticality Data Center. The information is necessary for safety specifications for handling large but realistic quantities of the materials and will be incorporated in the revision of the *Nuclear Safety Guide.*[1]

Since experience with the above materials in simple spaced configurations is limited[2] to ^{235}U metal and since there is no work reported for the pure oxides, reliance must be based upon validated calculational techniques. The demonstrated[3] ability of Monte Carlo codes to properly handle the geometry of air-spaced components makes them particularly suited to this problem. The large safety factors imposed by regulations in specifying operating limits for these materials makes acceptable the knowledge of the number of components required for criticality to within 5 or 10%. This condition corresponds to an uncertainty in the neutron multiplication factor of an assembly of 3% at a 95% confidence interval. The KENO Monte Carlo code[4] and the Hansen-Roach 16-group cross-section set[5] have been shown[3] to provide this accuracy in calculating known critical configurations of fissile metals.[6] The uncertainty in the computed values of the oxides is believed to be no greater than the criteria defined above.

The arrays considered were three dimensional and of cubic geometry with the same number of equally spaced components along each edge. The components were spherical in all cases. The

Table 2.17.1. Calculated Critical Unreflected Arrays of ^{233}U-Metal Spheres

Number of Spheres[a] in Array N	Sphere Radius (cm)	Sphere Mass (kg of U)	Center-to-Center Separation (cm)	Array Uranium Density[b] (g/cm^3)	k_{eff} from KENO Code[c]
64	4.672	7.88	18.080	1.333	0.995
216	4.672	7.88	22.661	0.677	1.002
8000	4.672	7.88	42.315	0.104	1.008
64	4.404	6.60	15.620	1.732	0.995
216	4.404	6.60	19.518	0.888	0.994
349	4.404	6.60	21.185	0.694	1.000
64	3.998	4.94	12.514	2.514	0.996
216	3.998	4.94	15.626	1.294	1.001
512	3.998	4.94	18.182	0.822	1.011
64	3.573	3.53	9.952	3.576	1.002
216	3.573	3.53	12.511	1.800	1.006
1000	3.573	3.53	16.417	0.797	1.005
216	3.386	3.0	11.290	2.085	1.000
64	3.186	2.5	7.967	4.944	1.003
64	2.958	2.0	6.985	5.868	1.007

[a] $N^{1/3}$ spheres arranged along each edge of array.

[b] Uranium density in unit cell of the lattice.

[c] Neutron multiplication factors have a standard deviation of ±0.005.

calculations were based on the following material properties:

Isotopic Composition	Density (g/cm^3)	
	Metal	Oxide
93.2 wt % ^{235}U, 6.8 wt % ^{238}U	18.76	10.5
98 wt % ^{233}U, 2 wt % ^{238}U	18.45	10.5
94.8 wt % ^{239}Pu, 5.2 wt % ^{240}Pu	19.74	11.4

Presented in Table 2.17.1 are the calculated critical conditions of unreflected arrays of ^{233}U metal spheres; they are typical of those for the other materials. The multiplication factors were obtained with 30×10^3 neutron histories and have a standard deviation of ± 0.005.

References

[1]Subcommittee 8 of the American Standards Association Sectional Committee N6 and Project 8 of the American Nuclear Society Standards Committee, *Nuclear Safety Guide*, TID-7016, Rev. 1 (1961).

[2]A program of experiments is being initiated at the Lawrence Radiation Laboratory, Livermore, to measure the critical dimensions of arrays of plutonium metal clad in aluminum. Preliminary data have appeared in: J. R. Morton III *et al.*, *Summary Report of Critical Experiments Plutonium Array Studies, Phase I*, UCRL-50175 (1966).

[3]J. T. Thomas, *A Method for Estimating Critical Conditions of Large Arrays of Uranium*, SC-DC-67-1305, p. 189 (1967).

[4]G. E. Whitesides and Nancy Cross, Oak Ridge Computing Technology Center, private communication (1968); see also G. E. Whitesides *et al.*, *Trans. Am. Nucl. Soc.* **9**, 133 (1966).

[5]Gordon E. Hansen and William H. Roach, *Six and Sixteen Group Cross Sections for Fast and Intermediate Critical Assemblies*, LAMS-2543 (1961).

[6]W. R. Stratton, *Criticality Data and Factors Affecting Criticality of Single Homogeneous Units*, LA-3612 (1967).

2.18 HFIR FUEL ELEMENTS: REACTIVITY MEASUREMENTS ON SINGLE ELEMENTS AND ARRAYS OF ELEMENTS MODERATED AND REFLECTED BY WATER

E. B. Johnson

The reactivity of each fuel element for the High Flux Isotope Reactor, moderated and reflected by water, is determined prior to its use in the reactor. These determinations provide a measure of conformity in the manufacture to design specifications. Each element nominally contains 9.4 kg of ^{235}U as U_3O_8 enriched to 93.2% in ^{235}U. The fuel plates of the inner annulus also contain 2.8 g of ^{10}B, according to the manufacturer's certification.

Each element was mounted in a tank which could be remotely filled with water to provide moderator and an effectively infinite reflector. Since each element was subcritical when submerged, sufficient reactivity was added to the element by plates containing enriched uranium placed in the target region to make the system critical when submerged; most of any resulting net positive reactivity was compensated by neutron-absorbing strips placed between fuel plates in the outer annulus, and any remaining reactivity was measured directly from the resulting positive reactor period. The reactivity associated with the uranium-bearing plates and with the neutron-absorbing strips had been determined previously.[1] Figure 2.18.1 shows the reactivity of each element that has been measured.

Another experiment was performed to investigate possible modifications of methods of storing elements in the pool to increase the storage capacity. The original storage pattern located the elements in racks on 76-cm-center separation. Each rack consists of an annulus of cadmium clad in stainless steel located in the target region of the element and of an outer cylinder, also of stainless-steel-clad cadmium, which surrounds the outer annulus. For the experiment, cadmium was positioned so that its height and its vertical and radial locations relative to the fuel region were the same as those of the storage racks. No attempt was made to duplicate the stainless steel of the racks. Nine complete elements were as-

sembled in the simulated storage racks in a square pattern, as shown in Fig. 2.18.2. The elements were spaced with 0-, 1.27-, and 2.54-cm separation between the outer surfaces of the cadmium, corresponding to center separations of 45.0, 46.2, and 47.5 cm, respectively. In no case was any apparent source neutron multiplication observed.

Reference

[1] J. T. Thomas and S. J. Raffety, *Neutron Phys. Div. Ann. Progr. Rept. Aug. 1, 1965*, ORNL-3858, Vol. 1, p. 18.

ORNL-DWG 67-12984

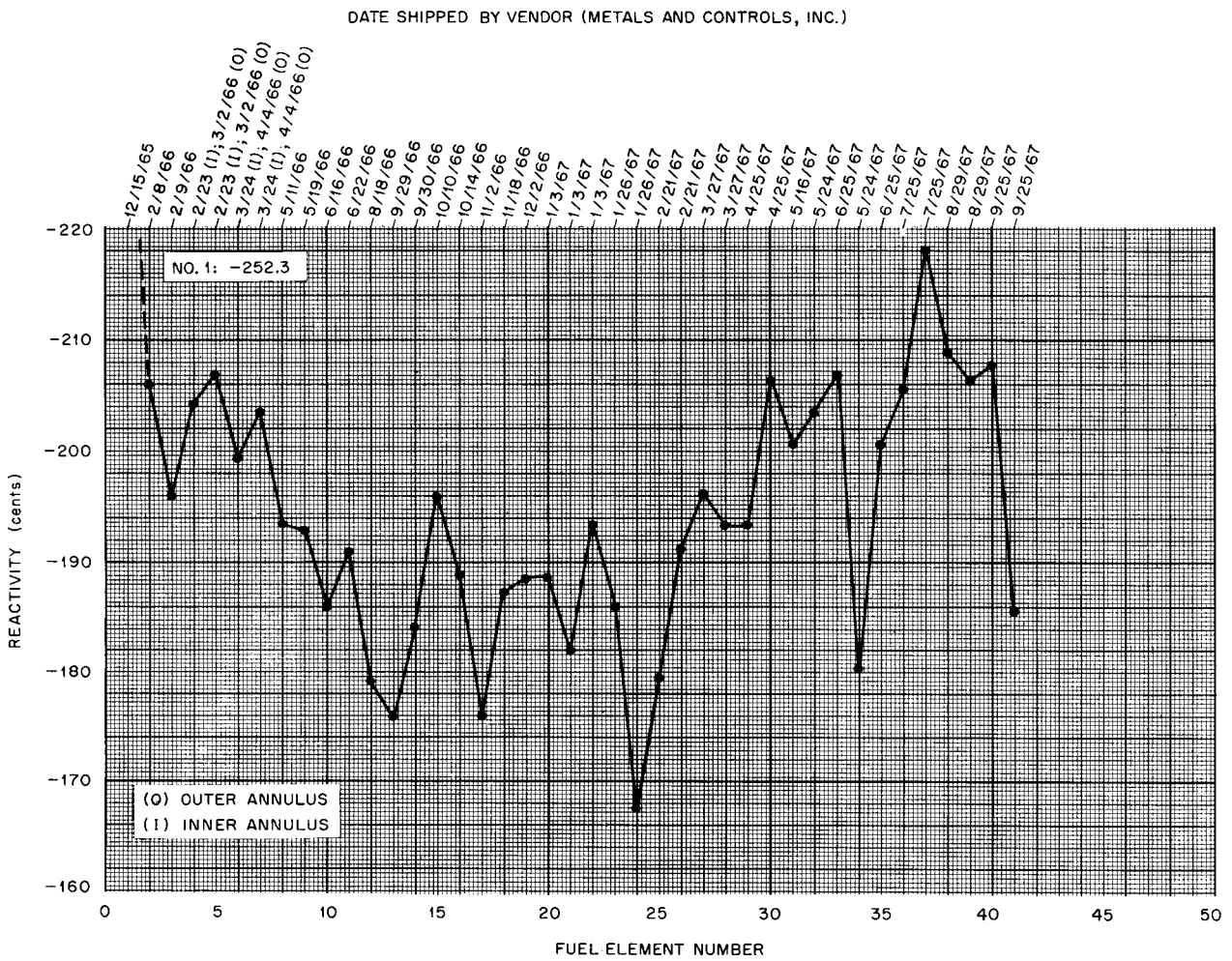

Fig. 2.18.1. Reactivity of HFIR Fuel Elements Moderated and Reflected by Water.

Fig. 2.18.2. High Flux Isotope Reactor Fuel Elements in Simulated Pool Storage Conditions.

3. Reactor and Weapons Radiation Shielding

3.0 INTRODUCTION

The objectives of the ORNL shielding program, which is largely supported by the Space Nuclear Auxiliary Power (SNAP) project and the Defense Atomic Support Agency (DASA), are the development of basic methods for solving radiation transport problems in complex geometries, the testing of these methods by comparison with experimental results, and the development of data and techniques that engineers can use with a high degree of competence in designing shields to meet their requirements. Further, the intent is to provide design techniques that are general in nature so that shields can be optimized not only with respect to weight, as required for the SNAP program, but also with respect to cost, radiation heating, radiation damage, or any other requirement or constraint that may be imposed by the design engineers.

During the past year the emphasis in the theoretical shielding work was the application of available discrete ordinates and Monte Carlo methods to problems of particular interest. The one- and two-dimensional discrete ordinates codes ANISN and DOT were greatly improved in efficiency and were used in the SNAP program to optimize, with respect to minimum weight, shields of lithium hydride and heavy metal for an idealized SNAP-8 reactor configuration. In the DASA program, which is concerned with protection against radiation from nuclear weapons bursts, very detailed DOT calculations were completed of steady-state weapons radiation transport from a source near an air-ground interface. The DOT code was also used to obtain neutron albedo data for laminated iron and concrete slabs for use as input to an albedo Monte Carlo duct code.

A number of Monte Carlo calculations were required for the preanalysis of the SNAP experiment to be performed at the Tower Shielding Facility this year. These include calculations of the power distribution within the SNAP reactor core and of the neutron spectra leaking from the bottom face of the core as a function of position and angle. Calculations of the excess reactivity of the core were also made for comparison with experimental results. Other Monte Carlo calculations were performed to carry out a comprehensive study of time-dependent neutron and secondary gamma-ray transport through the atmosphere for the case of a source near an air-ground interface. None of these Monte Carlo calculations could have been done within reasonable machine times without the considerable progress that has been made in developing *a priori* biasing techniques.

One of the most critical problems in a majority of shield designs is calculation of the secondary gamma rays produced by neutron interactions in shield materials. Except for thermal-neutron capture gamma rays for a few elements, the energies and angular distributions of the secondary gamma rays emitted in a neutron interaction are not known as a function of neutron energy. Significant progress has been made in the development of a method which will calculate these gamma-ray spectra.

The major experimental effort at the Tower Shielding Facility in both the SNAP and the DASA programs during the past several months has been concerned with development and improvement of techniques for measuring gamma-ray spectra. This effort is considered vital to these programs, and it will provide important gamma-ray milestone experiments. Experimental data will be provided to adequately test the methods for treating secondary gamma-ray production in complex shields of materials such as uranium and tungsten, where the neutron absorption in the resonance region controls the transport. For the DASA program the experiments will aid in the evaluation of available data on the production and number spectra of gamma

rays in shields of concrete, as well as in most of the lighter elements used in military applications. Gamma-ray spectra have been measured in a clean-geometry configuration with various neutron spectra incident on shield slabs. From these data a study can be made of the gamma rays produced by thermal neutrons, by neutrons from 0.4 eV to approximately 1 keV, and by neutrons with a fission-like spectrum.

3.1 DEVELOPMENT OF ONE-DIMENSIONAL SHIELD OPTIMIZATION TECHNIQUES

W. W. Engle, Jr.[1] F. R. Mynatt[1]

A one-dimensional shield optimization code, ASOP, using the paired boundary method,[2] has been developed to an operational state. A study of one- and two-cycle tungsten–lithium hydride spherical shields gave encouraging results with weight savings of up to 25%. When calculations were attempted for a three-cycle shield, the increased number of boundaries introduced inefficient and sometimes unstable calculations, possibly because in one optimization step a first-order approximation to the derivative of the total dose with respect to boundary position is obtained for each boundary (using ANISN calculations); however, since only two of the boundaries are subsequently moved, the remaining information is discarded.

A new method was developed in which two one-dimensional calculations are performed at each boundary with the boundary displaced a different amount for each calculation. A linear relation between dD/dW and the boundary position is thus established. When these relations are coupled with an equation describing the logarithm of the total dose as a linear function of each boundary position, a closed-form solution which yields a new set of boundary positions may be obtained. This method, which gives as a result a shield with a design dose and minimum weight, has been implemented in a modified ASOP program and is operational. Values for the boundary displacements used in the first set of calculations are required as input. Thereafter, the displacements are computed by ASOP using a first approximation to dD/dr such that the predicted change in dose is 10%. Furthermore, each time new boundary positions are computed, the mesh intervals used in the ANISN calculations are reallocated in order to maintain a constant interval density in each zone. Appropriate precautions are taken to prevent negative zone widths, and undesirable zones may be removed by the program although new zones are never created.

The new program has resolved the inefficiencies and stability problems which became apparent in the paired boundary method by successfully designing three- and four-cycle tungsten–lithium hydride spherical shields. Figure 3.1.1 shows a

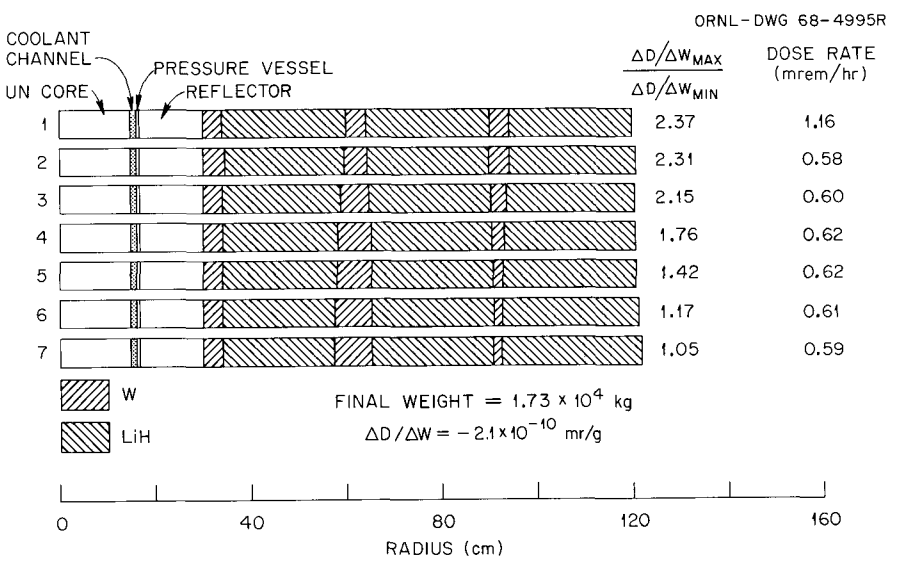

Fig. 3.1.1. Optimization of Tungsten–Lithium Hydride Shield, Spherical Geometry.

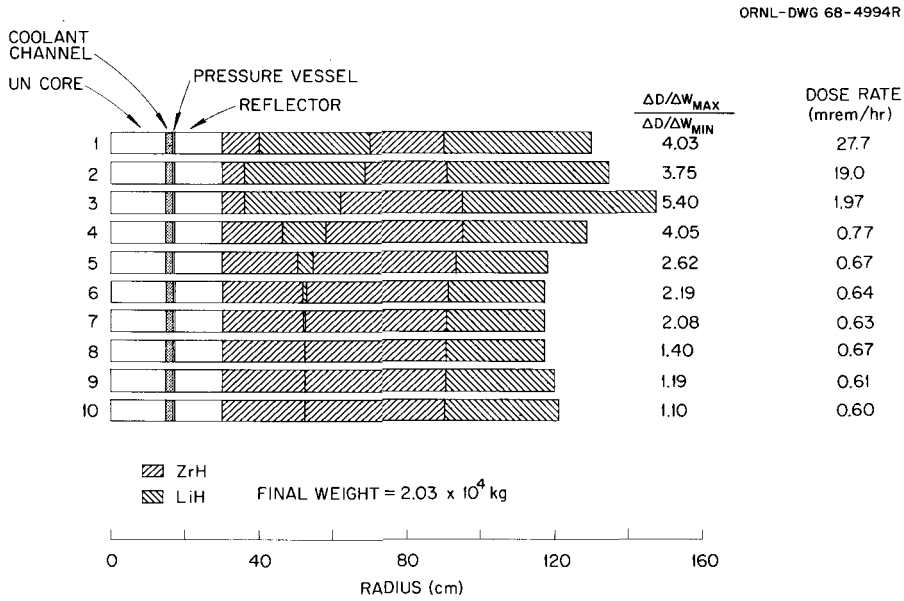

Fig. 3.1.2. Optimization of Zirconium Hydride–Lithium Hydride Shield, Spherical Geometry.

schematic representation of the steps in the optimization of a three-cycle spherical shield for a spherical SNAP core with UN fuel. For this case, the desired total (neutron + gamma) dose rate of 0.6 mrem/hr/MW for a detector at 50-m radius is obtained in three steps of the optimization procedure. The $(\Delta D/\Delta\omega)_{max}/(\Delta D/\Delta\omega)_{min}$ ratio indicates the relative efficiency of the shield design. At the final ratio of 1.05, the shield is not optimized in a literal mathematical sense, but further steps result in little total weight savings. The weight of this shield (1.73×10^4 kg) may be compared with that for an optimized one-cycle W-LiH shield (4.8×10^4 kg). Figure 3.1.2 shows a similar schematic for a two-cycle ZrH-LiH shield. For this system the code reduced the two-cycle design to a one-cycle shield which had the same dimensions as were obtained in a similar calculation for a one-cycle ZrH-LiH initial design.

Limited experience with the new method has shown that the equations used do not apparently force a rapid variation of the position of certain zones. A preliminary investigation has indicated that allowing a simultaneous displacement of two or more selected boundaries and applying the solution of the coupled equations in a consistent manner will alleviate this problem. Work is continuing in this area.

References

[1]Computing Technology Center, Union Carbide Corporation, Oak Ridge, Tennessee.

[2]F. R. Mynatt *et al.*, *Neutron Phys. Div. Ann. Progr. Rept. May 31, 1967*, ORNL-4134, p. 55.

3.2 SOME CHARACTERISTICS OF SECONDARY GAMMA-RAY TRANSPORT IN ASYMMETRIC SNAP SHIELDS[1]

F. R. Mynatt[2]

The predominant radiation emergent from high-efficiency (man-rated) SNAP shields is due to secondary gamma rays produced in the shield. This somewhat incongruous situation, in that the radiation shield produces most of the penetrating radiation, is due primarily to good neutron attenuating materials weighing less than good gamma attenuating materials. Thus a shield that is efficient with respect to weight will be characterized by a low ratio of neutron to gamma-ray dose.

The radiation characteristics of an asymmetric SNAP shield consisting of a two-cycle cylindrical lamination of tungsten and lithium hydride were

computed using the two-dimensional discrete ordinates transport code DOT, which allows a generalized treatment of anisotropic scattering by the use of a Legendre series expansion. The most important characteristics revealed by these calculations are that the dominant radiation is due to secondary gamma rays produced in the shield; that 80 to 90% of the secondaries is due to resonance (nonthermal) capture in the tungsten; and that due to the asymmetry, essentially all the gamma radiation reaching the low-dose axis is from scattering in the radial shield.

Also discussed in the paper are the following:

1. the computational technique that was employed in the calculations,
2. selection of secondary-gamma-production data, including the dependence of gamma yield on neutron-capture energy,
3. data-handling techniques, including the execution of coupled neutron-gamma problems,
4. selection of the order of anisotropic-scattering approximation and its effect on the penetration of gamma rays in tungsten,
5. techniques that are being developed for future use.

References

[1]Summary of paper presented at the Winter Meeting of the American Nuclear Society, Chicago, Illinois, November 5–9, 1967, and published in *Trans. Am. Nucl. Soc.* **10**, 542 (1967).

[2]Computing Technology Center, Union Carbide Corporation, Oak Ridge, Tennessee.

3.3 GENERAL STUDY OF ANGULAR BIASING TECHNIQUES FOR THREE-DIMENSIONAL NEUTRON-TRANSPORT PROBLEM

C. E. Burgart[1] V. R. Cain

Solution of deep-penetration neutron transport problems by the Monte Carlo method requires the use of biasing techniques. A systematic approach of utilizing the spatial, energy, and angular-dependent adjoint flux as the importance function in biasing three-dimensional Monte Carlo calculations is being investigated.

The adjoint flux is calculated for a simplified geometry using one-dimensional S_n (discrete ordinate) methods. In order to utilize an angular-dependent importance function, a discrete angle approach is taken. A 30-direction model, in which neutrons must travel in one of the discrete directions, is being used.

Cross-section preparation and code modification for discrete angle scattering is being undertaken. Angular biasing will then be added to the code and its applicability to deep penetration problems investigated.

Reference

[1]University of Tennessee, Knoxville.

3.4 THE USE OF DISCRETE ORDINATES ADJOINT CALCULATIONS[1]

V. R. Cain

Most discrete ordinates computer codes have an option available for performing adjoint calculations. The formalism on which this option is based and some of the more important uses of calculational results are reviewed, especially as applied to adjoint biasing in Monte Carlo calculations. Some results of the latter calculations are given.

Reference

[1]Abstract of p. 85 in *A Review of the Discrete Ordinates S_n Method for Radiation Transport Calculations*, ORNL-RSIC-19 (March 1968).

3.5 ANALYTICAL APPROACH TO THE ANGULAR-DEPENDENT IMPORTANCE FUNCTION

F. A. R. Schmidt[1]

Coveyou, Cain, and Yost[2] have shown that the solution of the inhomogeneous adjoint equation with the Monte Carlo estimator as the source term, the so-called "value function," should lead to very good biasing parameters. Unfortunately, obtaining the value function exactly is as difficult

as solving the "forward" problem. Therefore, to generate biasing functions efficiently some approximation to the adjoint solution has to be made. In principle, this can be done by one of two ways: either use a simpler geometry than that used in the forward transport calculation or use a simpler physical model.

Simpler geometry, for example, would involve one-dimensional adjoint S_n calculations, from which relatively accurate but cumbersome biasing information could be obtained for making the three-dimensional Monte Carlo calculation. The simple physical model may involve less detail but yield relatively inaccurate results. In such cases, one should try to combine the advantages of both approaches by proper mixtures of the solutions. To get the value function from a simple physical model one normally starts with the value transport equation

$$V(x_i) = P(x_i) + \int K(x_i,x_j)\, V(x_j)\, dx_j \,, \qquad (1)$$

where

$V(x_i)$ = value function for an event at x_i in the phase space,

$P(x_i)$ = payoff function or immediate contribution to the value function at x_i,

$K(x_i,x_j)$ = probability distribution function of events around x_j provided that an event occurs at x_i.

Equation (1) may be solved by iteration, which leads to a Neumann series

$$\begin{aligned} V(x_i) &= P(x_i) + \int K(x_i,x_j)\, P(x_j)\, dx_j \\ &\quad + \int K(x_i,x_j)\, K(x_j,x_k)\, P(x_k)\, dx_k\, dx_j \qquad (2) \\ &= V^0\,(x_i) + V^1\,(x_i) + V^2\,(x_i) + \ldots \,, \end{aligned}$$

where $P(x_i)$, $K(x_i,x_j)$, and the number of terms of the series have to be determined by the model used. This may be illustrated by the following example. We are interested in the spectrum of neutrons that travel from a source at $z = 0$ through a shield with thickness L. The detector may be a plane somewhere behind the shield. So we can use slab geometry, express (x_i) by (E_i, z_i, μ_i), and write

$$P(x_i) = F(E_i)\, e^{-\Sigma_{T_i}[(L-z_i)/\mu_i]} \,, \quad \text{for } \mu_i \geqq 0 \,,$$

$$P(x_i) = 0 \,, \quad \text{for } \mu_i < 0 \,, \qquad (3)$$

$$K(x_i,x_j) = e^{-r_{i\to j}} \frac{\Sigma_{i\to j}}{\Sigma_{T_i}} \,,$$

where

$F(E_i)$ = detector response function,

μ_i = cosine of the angle between the z direction and the neutron direction at x_i,

Σ_{T_i} = total macroscopic cross section at x_i,

$\Sigma_{i\to j}$ = macroscopic cross section for transition from energy E_i to energy E_j,

$r_{i\to j}$ = number of mean free paths for a neutron going from x_i to x_j.

Of course, the simplest case will be the V^0 approximation. As Armstrong[3] showed, we can then replace the exponential in (3) with

$$e^{-\beta_i \Sigma_{T_i}(L-z_i)(2-\mu_i)} \,, \qquad (4)$$

where by the factor β_i one may try to take into account higher orders of scattering. Therefore the range of β_i should be $0 \leqq \beta_i \leqq 1$. There are two ways to determine β_i:

1. One is to determine $K(x_i,x_j)$ and then estimate the higher order contributions of the Neumann series. This seems to be a good technique especially if there is one dominant reaction. A frequently occurring example for this case is very peaked scattering which results in little energy transfer:

$$\Sigma_{i\to j} = \Sigma_{s_i}\, \delta(\mu_i - \mu_j) \,.$$

If at the same time $F(E)$ decreases very strongly with the group inverse, as it would if one takes the inverse of the fission spectrum for $F(E)$ (by which one gets equal statistics for a reactor leak-

age spectrum), the result will be

$$V(x_i) \approx F(E_i)\, e^{-\Sigma_{T_i}(L-z_i)(2-\mu_i)} + \int_0^{\Sigma_{T_i}(L-z_i)(2-\mu_i)} e^{-r_{i\to j}}\, e^{-\Sigma_{T_i}(L-z_j)(2-\mu_i)} \times \frac{\Sigma_{s_i}\,\delta(\mu_i-\mu_j)}{\Sigma_{T_i}} F(E_i)\, d\mu_i\, d_{r_{i\to j}} \,. \quad (5)$$

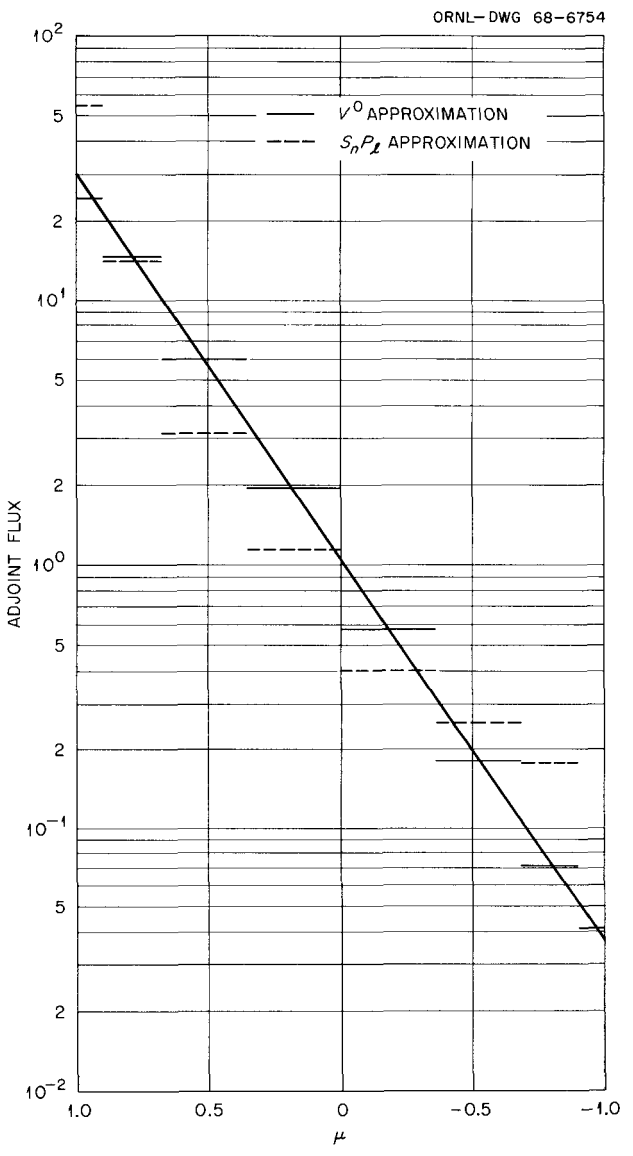

Fig. 3.5.1. Angular Dependence of Adjoint Flux for Air in the Energy Range 12 to 15 MeV for $\beta(L-z) \cong 3.36$.

Because now

$$r_{i\to j} = \Sigma_T \frac{z_j - z_i}{\mu_i},$$

one obtains

$$V(x_i) = F(E_i)\, e^{-\Sigma_T(L-z_i)(2-\mu_i)} \times [1 + \Sigma_{s_i}(L-z_i)(2-\mu_i)] \,. \quad (6)$$

The expression in brackets represents the first two terms of the series expansion of an exponential series. In fact, if one includes more terms of the V series more terms of the expansion will result. Therefore, the final answer will be

$$V(x_i) = F(E_i)\, e^{-(\Sigma_{T_i}-\Sigma_{s_i})(L-z_i)(2-\mu_i)} \,. \quad (6)$$

In Fig. 3.5.1 we compare predictions of Eq. (7) with $S_{16}P_3$ adjoint calculations done for air in the energy interval 12 to 15 MeV.

2. The other way to calculate β_i, which may be used if the above simple model does not lead to sufficient results, is to combine it with the approximation of simple geometry. In practice this means integration of the V^0 function – or if necessary a higher approximation for V – over μ_i and determination of β_i from the slope of S_nP_l

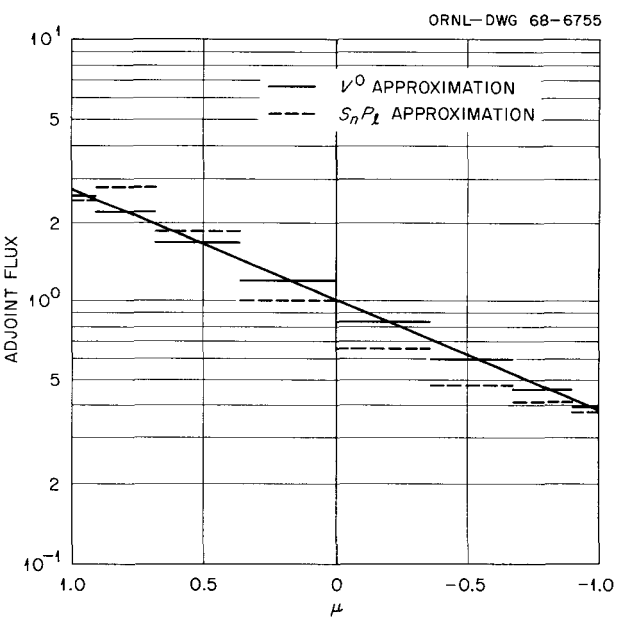

Fig. 3.5.2. Angular Dependence of Adjoint Flux for Air in the Energy Range 12 to 15 MeV for $\beta(L-z) \cong 1$.

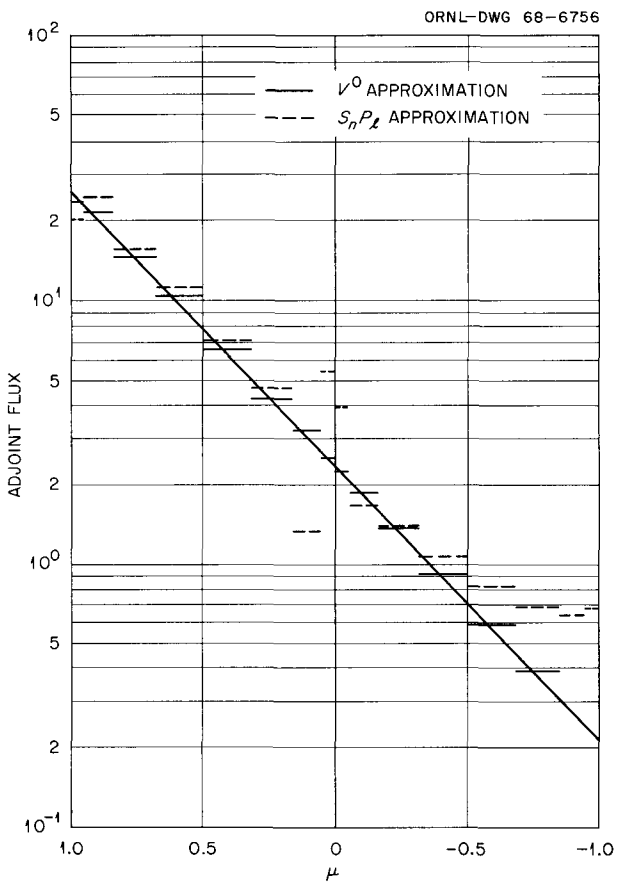

Fig. 3.5.3. Angular Dependence of Adjoint Flux for LiH in the Energy Range 1.35 to 1.65 MeV for $\beta(L - z) \cong 2.4$.

adjoint calculations. Figures 3.5.2 and 3.5.3 show comparisons of angular distributions obtained by this method with those obtained by $S_{16}P_3$ calculations for air and LiH. An expression like (4) should lead to sufficiently good results, because the main contributions to the importance function are from neutrons of the group under consideration, while the contributions of neutrons which scatter from this group to another group are small.

References

[1]On loan from Institut für Kernenergetik, Universität Stuttgart, Germany; work funded by Bundesuninisterium für wissenschaffliche Forschung, Germany.

[2]R. R. Coveyou, V. R. Cain, and K. J. Yost, *Nucl. Sci. Eng.* **27**, 219 (1967).

[3]T. Armstrong, *A* V^0 *Importance Function for the Monte Carlo Calculation of the Deep Penetration of Gamma Rays*, Ph.D. Thesis, University of Tennessee, 1967 (also submitted for publication to *Journal of Nuclear Energy*).

3.6 A METHOD FOR THE CALCULATION OF NEUTRON-CAPTURE GAMMA-RAY SPECTRA[1]

K. J. Yost

A model has been developed that is suitable for predicting gamma-ray spectra subsequent to the capture of neutrons in nuclear states of identifiable spin and parity. The dependence of radiative transition probabilities on the nuclear selection rules is explicitly accounted for. Means are provided for allowing dipole and quadrupole transitions in conjunction with variations in the magnitudes of corresponding transition "matrix elements." Comparisons are given between experimental capture spectra and corresponding spectra calculated with varying assumptions with respect to pertinent nuclear parameters for two capture states of ^{28}Al and one of ^{25}Mg. The comparison between calculations based on fitted and crudely approximated cascade parameters for the ^{28}Al capture state indicated few, if any, differences that would significantly change resultant neutron-capture gamma-ray-production cross sections.

Reference

[1]Abstract of *Nucl. Sci. Eng.* **32**, 62–75 (1968).

3.7 CALCULATION OF NEUTRON CAPTURE GAMMA-RAY SPECTRA – A SURVEY[1]

K. J. Yost

A review of techniques for the calculation of neutron-capture gamma-ray spectra is given. The purely statistical gamma-ray cascade models are contrasted to a model which accounts specifically for variations in spin-branching ratios and multipole transition probabilities. Means of determining empirically and/or calculating relative magnitudes of

transition matrix elements are discussed briefly. The utilization of capture gamma-ray spectra in the preparation of capture gamma-ray production cross sections is also covered.

Reference

[1]Abstract of invited paper presented at the 1967 Winter Meeting of the American Nuclear Society, Chicago, Illinois, November 5–9, 1967.

3.8 ENERGY DEPENDENCE OF GAMMA-RAY PRODUCTION CROSS SECTIONS AND THEIR UTILIZATION IN S_N CODES

K. J. Yost

It would be desirable to have a neutron-capture gamma-ray spectrum for every neutron resonance possessing an appreciable radiative partial width. This is evidently not feasible for materials with large numbers of capture resonances. Fortunately, such detail is unnecessary in that capture spectra *tend* to fall into categories defined by the spins and parities of the capture states. For example, with J_T^π denoting the ground-state spin and parity of a target nucleus, if target spin J_T is integral and nonzero, *s*-wave (zero angular momentum in the incident neutron-target nucleus two-body system) neutron capture can result in the excitation of two parity-π states. The latter holds for *all* half odd integral target spins. The relative probability of *p*-wave neutron capture (one unit of angular momentum) generally increases with energy and, where the increase is appreciable, results in the excitation of parity $(-\pi)$ states with spins ranging (excluding, of course, negative spins) from $J_T - 2$ to $J_T + 2$. Ignoring, then, the capture of neutrons of higher angular momenta, one would hope to describe all feasible capture spectra with no more than seven representative spectra (two *s* wave and five *p* wave) as defined by capture state spin and parity. Each spectrum to be included in a particular calculation should be expressed in terms of a common histogram format.

The intensity associated with the *i*th histogram bin for the *j*th spectrum can be denoted by H_{ij}, in which case the index *j* does not specify a particular resonance but rather a spectrum which may be associated with a number of resonances corresponding to compound capture states of like spin and parity. Letting the index *k* denote the *k*th neutron group bounded by energies (E_k, E_{k+1}) and dividing each neutron group into N_k segments within which particular gamma-ray spectra are valid, the group-averaged *i*th capture gamma-ray histogram bin for the *k*th neutron group would have the form

$$\bar{H}_i(k) = \sum_{n=1}^{N_k} \frac{\int_{E_{n+1}(k)}^{E_n(k)} \phi(E')\, dE'\, H_{ij}(n)}{\int_{E_{k+1}}^{E_k} \phi(E')\, dE'} .$$

3.9 SENSITIVITY OF GAMMA-RAY DOSE CALCULATIONS TO THE ENERGY DEPENDENCE OF GAMMA-RAY PRODUCTION CROSS SECTIONS[1]

K. J. Yost E. Solomito

The dependence of neutron-capture gamma-ray spectra on capture neutron energy is of particular importance in the design of optimized reactor shields. The heretofore common practice of assuming that neutron-capture gamma-ray spectra are invariant to neutron energy is expected to be an unacceptable approximation for a shield material exhibiting strong resonance characteristics. The importance of adequately predicting gamma-ray yields from the capture of nonthermal neutrons for a particular shield is clearly a function of (1) the relative magnitudes of thermal and nonthermal neutron capture rates in regions of the shield contributing substantially to the surface capture gamma-ray dose rate, (2) the magnitude of the capture gamma-ray dose rate compared with other sources of gamma radiation, and (3) the extent to which the capture gamma-ray dose rate is sensitive to changes in the shape of the capture gamma-ray spectrum. Each of these questions has been investigated in detail for three SNAP 10A core laminated tungsten–lithium hydride shield configurations. Results indicate that, depending upon the shield in question, nonthermal neutron capture accounts for 90 to ~100% of the capture gamma-ray dose rate from tungsten, that capture gammas in tungsten constitute a far larger component of the surface gamma-ray dose rate than

do either primary or tungsten inelastic-scattering gammas, and that the sensitivity of the capture gamma-ray dose to the shape of the capture spectrum is strongly dependent upon shield configuration.

Reference

[1]Abstract of ORNL-TM-2209 (to be published); also to appear in *Proceedings of Conference on Neutron Cross Sections and Technology, Washington, D.C., March 1968* (in press).

3.10 A METHOD FOR APPROXIMATING THE EFFECT OF THE ENERGY DEPENDENCE OF NEUTRON-CAPTURE GAMMA-RAY SPECTRA ON CAPTURE GAMMA-RAY DOSE CALCULATIONS[1]

K. J. Yost

A shield surface neutron-capture gamma-ray dose, $I(\mathbf{r},\Omega,E)$, corresponding to the birth of a photon of energy E, with velocity vector Ω at a point $\mathbf{r}$ in the shield satisfies the equation

$$I(\mathbf{r},\Omega,E) = P(\mathbf{r},\Omega,E)\, C(E) + \int dE' \int d\mathbf{r}' \int d\Omega'\, K(\mathbf{r} \to \mathbf{r}';\ \Omega \to \Omega';\ E \to E') \times I(\mathbf{r}',\Omega',E')\ , \quad (1)$$

where $P(\mathbf{r},\Omega,E)$ is the probability that the photon will escape from the shield without interaction, $C(E)$ is the flux-to-dose conversion ratio, and $K(\mathbf{r} \to \mathbf{r}';\ \Omega \to \Omega';\ E \to E')$ is the obvious kernel. Equation (1) has the form of an importance function with a flux-to-dose conversion-ratio-weighted payoff.[2] The resultant dose is given by

$$D(E) \equiv \int_{\text{shield}} d\mathbf{r} \int d\Omega \int dE'\, I(\mathbf{r},E,\Omega)\, A(\mathbf{r},E')\ , \quad (2)$$

where $A(\mathbf{r},E)$ denotes the neutron capture rate. The total capture gamma dose D_T then is given by

$$D_T = \int Y(E')\, D(E')\, dE'\ , \quad (3)$$

where

$$Y(E) \equiv \frac{\int_{\text{shield}} d\mathbf{r} \int dE'\, A(\mathbf{r},E')\, Y(E',E)}{\int_{\text{shield}} d\mathbf{r} \int dE'\, A(\mathbf{r},E')}$$

and $Y(E',E)$ is the yield of gamma rays of energy E following the capture of a neutron of energy E'.

Partial gamma widths for heavy nuclei are assumed to be statistically distributed about some mean value.[3] We indicate such a distribution function as $f(\Gamma_\gamma^j;\ \langle \Gamma_{\gamma j}^i \rangle)$, where i,j index the initial and final transition states, respectively, and $\langle \Gamma_{\gamma j}^i \rangle$ denotes a mean partial width sensitive to certain characteristics of the two states. (In the following discussion we assume no correlations among the radiative partial widths.) A mean surface capture gamma-ray dose is given by

$$\langle d(i) \rangle = \int d\Gamma_\gamma^1 \ldots \int d\Gamma_\gamma^{i-1} \prod_{j=1}^{i-1} f(\Gamma_\gamma^j;\ \langle \Gamma_{\gamma j}^i \rangle) \times \frac{\sum_{j=1}^{i-1} \Gamma_\gamma^j (E_i - E_k)^3\, D(E_i - E_j)}{\sum_{j=1}^{i-1} \Gamma_\gamma^j (E_i - E_j)^3}\ . \quad (4)$$

One can extend this analysis by defining $\langle d_n(E) \rangle$ as corresponding to a mean shield surface capture-gamma dose associated with the deexcitation of one of a class of states at an energy E, with the class or type of state indexed by m or n. The indices denote those state characteristics to which mean partial gamma widths are assumed to be sensitive.[4] Restricting the following to dipole transitions, we define

$$\langle d_n(E) \rangle = \int d\Gamma_\gamma' \ldots \int d\Gamma_\gamma^{N_T} \prod_{m'} \prod_{j=1}^{N_{m'}} f(\Gamma_\gamma^{m'j};\ \langle \Gamma_{\gamma n}^{m'} \rangle) \times \frac{\sum_{m'} \sum_{j=1}^{N_{m'}} \Gamma_\gamma^{m'j} (E - E_j^{m'})^3\, D(E - E_j^{m'})}{\sum_{m'} \sum_{j=1}^{N_{m'}} \Gamma_\gamma^{m'j} (E - E_j^{m'})^3}\ , \quad (5)$$

where m' denotes a class of states, and $E_j^{m'}$ is a solution of

$$\int_{E_{j-1}^{m'}}^{E_j^{m'}} \rho(E')\, dE' = \frac{1}{R^{m'}}\ , \quad j = 1, 2, \ldots, N_{m'}\ ,$$

with $\rho(E')$ denoting the nuclear level density and $R^{m'}$ the relative abundance of class m' states, assumed to be independent of energy. The $R^{m'}$

satisfy the condition that

$$\sum_{m'} R^{m'} = 1 .$$

Partial width distribution functions are generally represented as chi-squared distributions with ν degrees of freedom. If we set $\nu = 2$ in Eq. (4) and make the assumption that

$$\frac{1}{\sum_{j=1}^{i-1} \Gamma_\gamma^j (E_i - E_j)^3}$$

is approximately constant relative to the collective statistical variations of the Γ_γ^j, then the standard deviation of the shield surface capture gamma-ray dose corresponding to the deexcitation of the ith state is given by

$$\sigma\big(d(i)\big) \sim \frac{\left[\sum_{j=1}^{i-1} \left\langle \Gamma_{\gamma j}^i \right\rangle^2 (E_i - E_j)^6 \, D^2(E_i - E_j)\right]^{1/2}}{A} , \qquad (6)$$

where

$$A \equiv \left[\sum_{j=1}^{i-1} \left\langle \Gamma_{\gamma j}^i \right\rangle (E_i - E_j)^3\right] .$$

The total dose variance for a particular shield configuration can be approximated by weighting $d(i)$ or $d(E)$ by transition energy and either level population $W(i)$ or level density $W(E)$ computed from a gamma cascade based upon mean partial widths.[4] A measure of the total dose variance for a dipole cascade involving resolved levels exclusively is given by

$$\Delta D_T = \left\{ \sum_i W(i) \, \sigma^2\big(d(i)\big) \right\}^{1/2} . \qquad (7)$$

The method has been applied to the calculation of tungsten-capture gamma-ray dose for a laminated tungsten–lithium hydride shield configuration.[5] The quantity ΔD_T was found to represent 44% of the mean dose rate.

References

[1]Summary of paper to be presented at the Fourteenth Annual Meeting of the American Nuclear Society, Toronto, Ontario, Canada, June 9–13, 1968, and to be published in *Trans. Am. Nucl. Soc.*, Vol. 11, No. 1 (1968).

[2]R. R. Coveyou, V. R. Cain, and K. J. Yost, *Nucl. Sci. Eng.* **27**, 219 (1967).

[3]C. E. Porter and R. G. Thomas, *Phys. Rev.* **104**, 483 (1956).

[4]K. J. Yost, *Nuclear Science and Engineering* (in press).

[5]K. J. Yost and M. Solomito, "The Sensitivity of Gamma-Ray Dose Calculations to the Energy Dependence of Gamma-Ray Production Cross Sections," in *Proceedings of the Second Conference on Neutron Cross Sections and Technology, 1968* (in press); see also Section 3.9.

3.11 PRELIMINARY RESULTS OF CALCULATIONS OF FAST-NEUTRON TRANSMISSION THROUGH LiH SLABS BELOW THE TSF-SNAP REACTOR

F. A. R. Schmidt[1] V. R. Cain

As a preanalysis of experiments to be conducted at the Tower Shielding Facility, calculations have been made of neutron transport through various thicknesses of LiH placed below the TSF-SNAP reactor. The source for the calculation was neutrons selected from a tally of reactor leakage neutrons obtained in a previous calculation.[2] In that calculation importance sampling was used to provide a source tape for a 63.5-cm-thick LiH shield. Thus the adequacy of this source tape for calculations of thinner slabs must be evaluated. Also 05R-ACTIFK Monte Carlo codes had to be modified to include use of correlated sampling to obtain in one calculation the emergent neutron spectra for several thicknesses of slabs.

Importance-sampling parameters were taken from S_N adjoint calculations and were used as described in Sect. 3.5. In particular, angular, energy, and spatial dependent weight standards were used for splitting and Russian roulette. In addition to spectra, the dose in an uncollimated detector at a distance of 522 cm below the reactor is desired.

To determine the effectiveness of the correlated sampling and to determine the adequacy of the source tape, preliminary calculations were compared with measurements by Wogulis and Rooney.[3] The source for the measurements of Wogulis and

Rooney was a fission plate, and the dose transmitted by various layers of LiH encapsulated in aluminum was measured with a Hurst detector 72 in. from the source. Comparisons were also made with a 16-fast-neutron group P_7 spherical harmonics calculation performed by Hehn[4] in which Hubner's[2] calculated SNAP leakage spectrum was the source (Fig. 3.11.1). The asymptotic slopes of the dose curves in the range 30 to 50 cm in LiH exhibit relaxation lengths of 6.02, 6.5, and 6.18 cm, respectively for the spherical harmonics calculation, the Monte Carlo calculation, and the experiment.

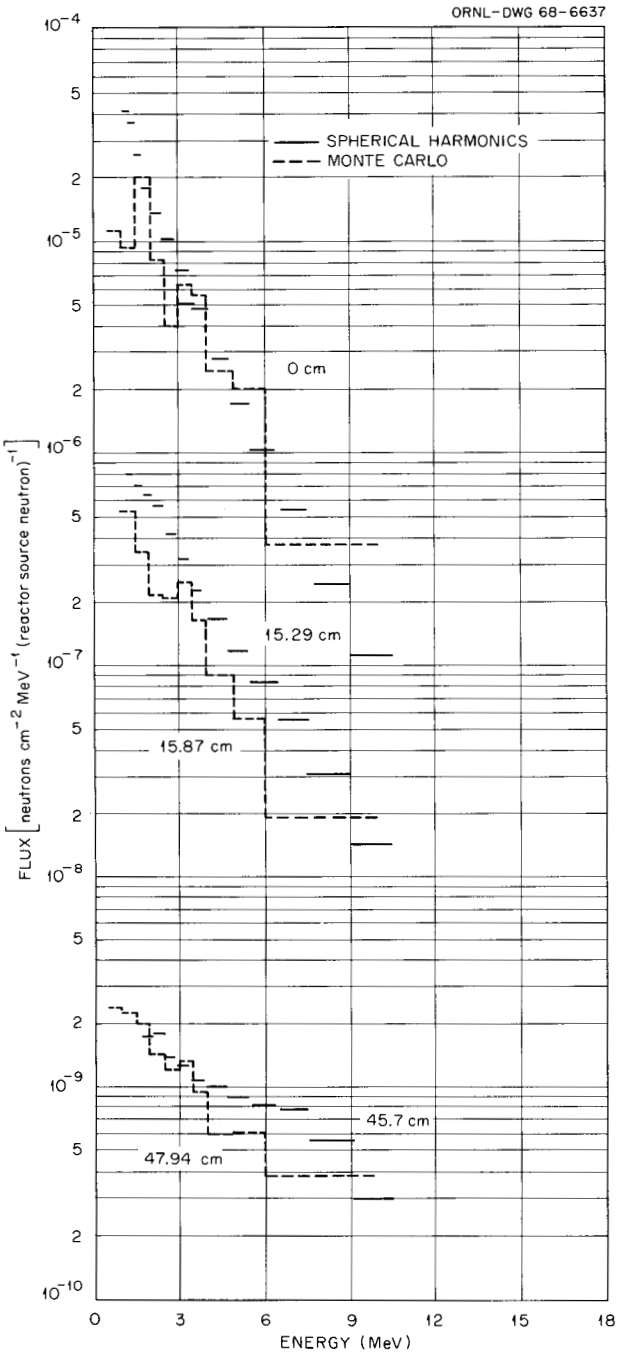

Fig. 3.11.1. Comparison of Neutron Spectra Calculated by Monte Carlo Method with Those Calculated by Spherical Harmonics Method.

Table 3.11.1 compares the fission spectrum and the source energy spectra for the spherical harmonics and Monte Carlo calculations; the source for the measurement is assumed to be a fission spectrum.[5] The source spectra are normalized in the 6- to 10-MeV interval.

From the preliminary calculations it is concluded that the energy spectra transmitted through several thicknesses of LiH can be calculated simultaneously providing that the importance-sampling parameters do not vary significantly. In addition, it is concluded that the present source tape is not adequate for determining the penetration of thin LiH slabs due to the undersampling of low-energy source neutrons.

Table 3.11.1. Comparison of Spectra Normalized to Fission Spectrum in the 6- to 10-MeV Range

Energy (MeV)	Fission Spectrum $\Delta F(E)/\Delta E$ (Ref. 5)	Hehn (Ref. 4)	Our Calculations
0.5–1.0	0.354		0.170
1.0–1.5	0.324	0.68	0.143
1.5–2.0	0.268	0.334	0.310
2.0–2.5	0.212	0.2475	0.128
2.5–3.0	0.160	0.185	0.062
3.0–3.5	0.119	0.1095	0.096
3.5–4.0	0.087	0.1095	0.087
4.0–5.0	0.0538	0.0439	0.0372
5.0–6.0	0.0268	0.010	0.03
6.0–10.0	0.00582		0.00582
10.0–18.0	0.00013		0.000142

References

[1]Institut für Kernenergetick, Universität Stuttgart, Germany; work funded by Bundesministerium fur wissenschaftliche Forschung, Germany.

[2]R. S. Hubner, *Methods for Calculating Fast-Neutron Leakage from the SNAP-TSF Reactor and Preliminary Results*, ORNL-TM-1666 (October 1967).

[3]S. G. Wogulis and K. L. Rooney, *Experimental Studies of Neutron Attenuation in Natural Lithium Hydride Shields*, NAA-SR-9364 (1964).

[4]G. Hehn, Institut für Kernenergetick, Stuttgart, Germany, unpublished report.

[5]H. Goldstein, p. 19 in "Shielding," Vol. III, Part B, of *Reactor Handbook*, 2d ed., edited by E. P. Blizard and L. S. Abbott, Interscience, New York, 1962.

3.12 MEASUREMENT OF THE ABSOLUTE POWER AND FISSION DISTRIBUTION IN THE TSF-SNAP REACTOR AND COMPARISON WITH MONTE CARLO AND DISCRETE ORDINATES CALCULATIONS [1]

E. A. Straker
T. V. Blosser
L. B. Holland
F. J. Muckenthaler
V. R. Cain
F. R. Mynatt[2]
J. J. Manning
J. L. Hull

The relative power distribution in the TSF-SNAP reactor was determined by scanning individual fuel elements for fission-product gammas, and the absolute fission rate was determined from uranium foil activation. Numerical integration of the fission density over the core volume gave an absolute power calibration for detectors and foils external to the core. Calculations of both the axial and radial power distributions by Monte Carlo and discrete ordinates methods were in excellent agreement with the measured distributions.

References

[1]Abstract of ORNL-TM-2265 (to be published).

[2]Computing Technology Center, Union Carbide Corporation, Oak Ridge, Tennessee.

3.13 MEASUREMENT OF THE ENERGY SPECTRA OF NEUTRONS ABOVE 1 MeV LEAKING FROM THE TSF-SNAP REACTOR

F. J. Muckenthaler
K. M. Henry
J. J. Manning
J. L. Hull
R. M. Freestone, Jr.

The energy distribution of neutrons emerging from the bottom of the TSF-SNAP reactor was measured in order to provide results for comparison with calculations. A 2- by 2-in. NE-213 organic scintillator was used to measure neutron energies from about 0.8 to 14 MeV, and a $1/E$ detector developed by T. V. Blosser will be used for measurements in the low-energy region up to about 10 keV.

A schematic diagram of one of the reactor-detector geometries is shown in Fig. 3.13.1. The cylindrical reactor was suspended vertically from a boom so that the reactor could be rotated about its own axis and be lowered or raised through a distance of 36 in. The boom could be rotated about its pivot point, permitting movement of the reactor through an arc greater than 180°. The reactor, NaK coolant system, and beryllium control drums were placed inside a heat-and-weather shield of stainless steel; the pressure vessel was also inside the shield, but its bottom portion was left exposed to the atmosphere. The experimental arrangement is shown in Fig. 3.13.2.

The NE-213 scintillator was placed inside a lead-water shield 48 in. in diameter and 59 in. long which was mounted on a support mechanism that permitted the shield to be rotated in a vertical plane about the horizontal axis of the detector and to move in a line passing through and perpendicular to the vertical axis of the reactor. The collimator in the shield was designed through Monte Carlo calculations[1] to limit the contribution from neutrons scattered by the walls of the collimator to less than 5%. The opening of the collimator was square in cross section of the shape and size shown in Fig. 3.13.3. When the vertical axis of the reactor coincided with the axis of the collimator, the center of the bottom of the reactor pressure vessel was 56 in. from the center of the detector. In this configuration the end of the collimator was 11.7 in. from the reactor vessel and the detector viewed 10% of the area of the bottom of the pressure vessel.

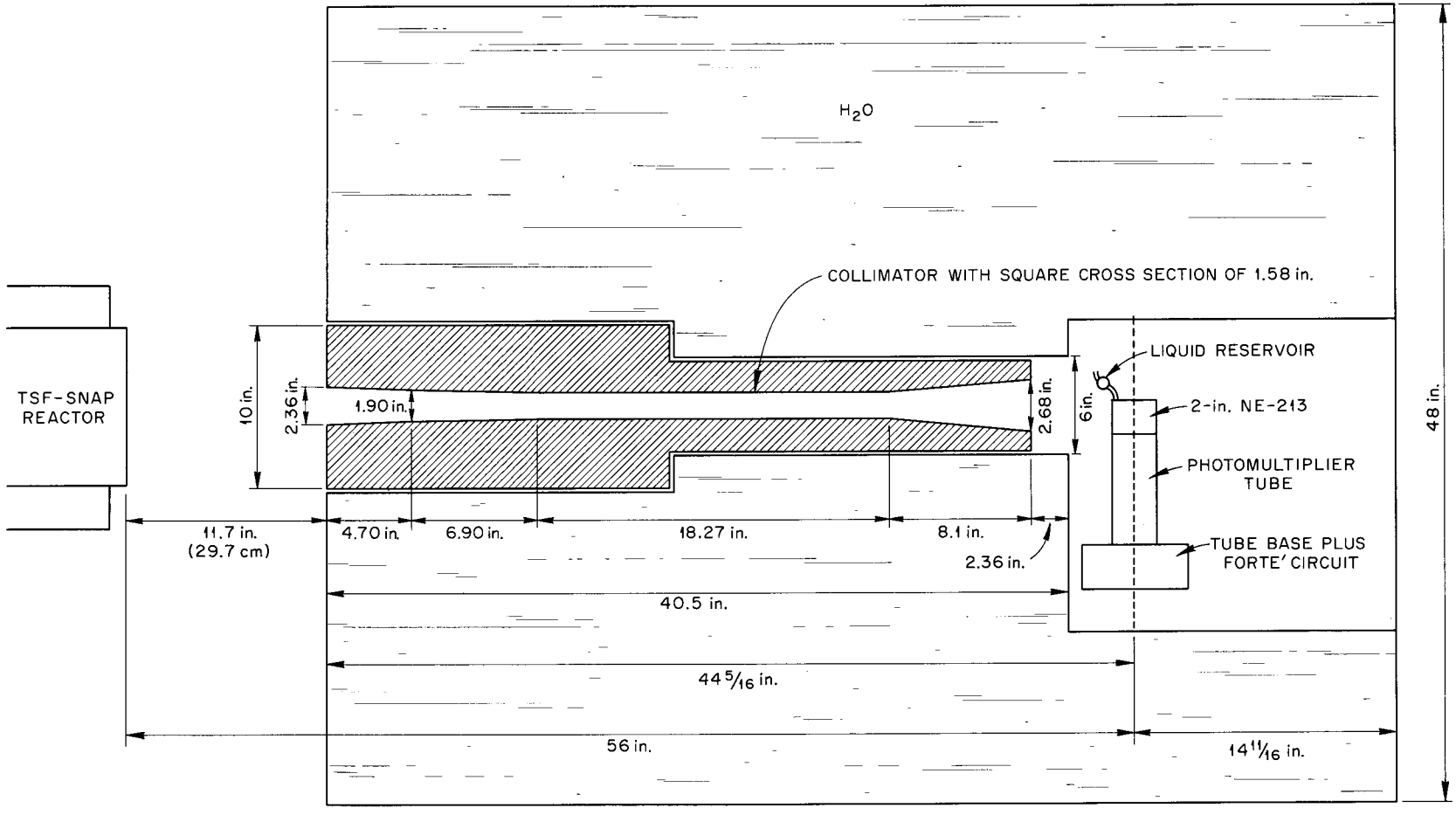

Fig. 3.13.1. Schematic Diagram of Geometry for Measurement of the Neutron Leakage Spectrum from the TSF- SNAP Reactor.

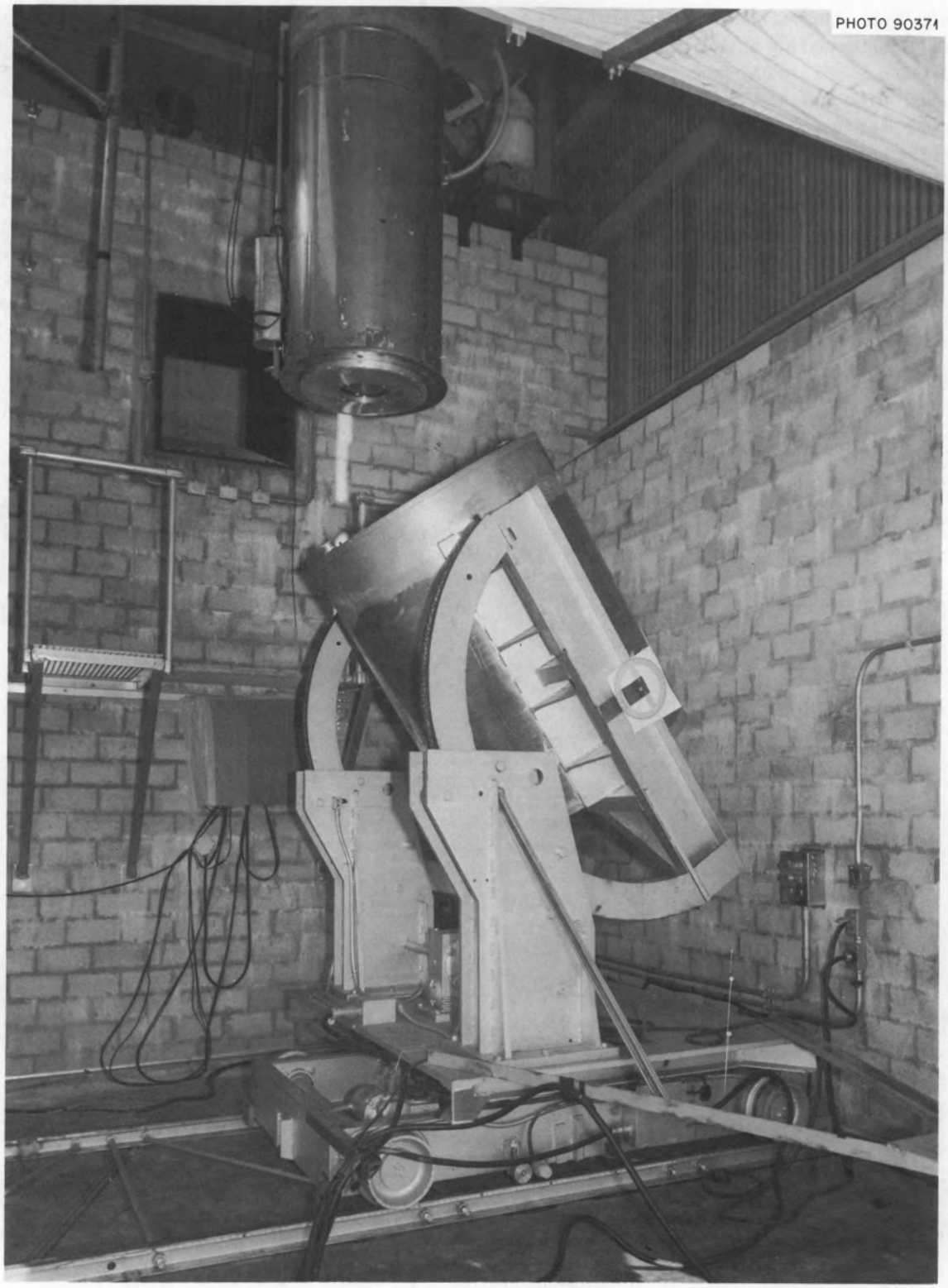

Fig. 3.13.2. Photograph of Experimental Arrangement.

Spectra were obtained with the axis of the detector collimator making angles of 0°, 18° 12′′, 25° 50′′, and 36° 52′′ with respect to the vertical axis of the reactor. The detector collimator was then moved horizontally so that the axis of the collimator looked at points 2.756 and 5.512 in. along the radius of the reactor, and measurements were repeated for the above four angles. For all the measurements the detector, looking along the axis of the collimator insert, was always 56 in. from a horizontal line passing through the bottom of the reactor pressure vessel at the axis of the reactor.

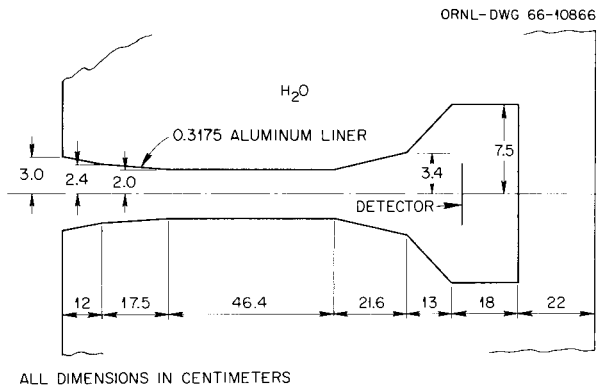

Fig. 3.13.3. Collimator Opening.

Preliminary analysis of the results and comparison with calculations by Cain *et al.*[2] have been completed. A comparison is shown in Fig. 3.13.4 for the configuration in which the detector is looking vertically at the center of the reactor. The agreement between calculations and experiment was good in all cases except when the detector was viewing the reactor through structural materials that were not included in the calculational model.

References

[1]E. A. Straker and M. B. Emmett, *Neutron Phys. Div. Ann. Progr. Rept. May 31, 1967,* ORNL-4134, p. 76.

[2]V. R. Cain and K. D. Franz, *Neutron Phys. Div. Ann. Progr. Rept. May 31, 1967,* ORNL-4134, p. 75.

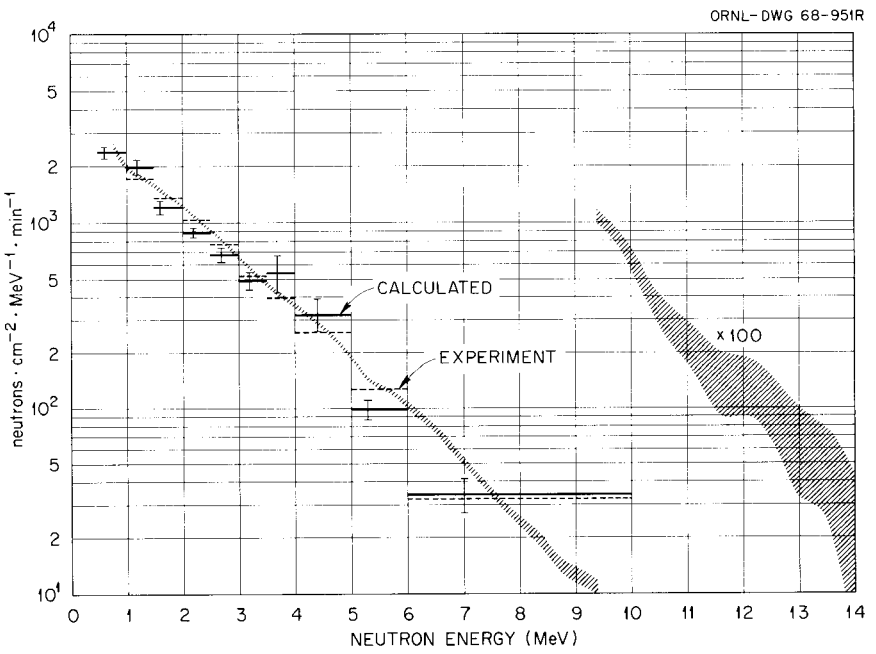

Fig. 3.13.4 TSF-SNAP Core Leakage Spectrum (Detector No. 1; Center Core, cos U = 1). The hatched area represents the 68% confidence region for the continuous spectrum. The histogram marked "Experiment" represents the continuous spectrum quantized for comparison with calculation.

3.14 USE OF SPACE-ENERGY-TIME KERNELS FOR STUDYING NEUTRON TRANSPORT PROBLEMS[1]

N. Cramer[2] P. N. Stevens[3] E. A. Straker

An analytic time-dependent kernel for neutron transport in air has been derived from an energy-dependent P_1 approximation of the Boltzmann transport equation. The model assumes continuous slowing down of the neutrons in an infinite homogeneous medium with constant cross sections and isotropic elastic scattering in the center-of-mass system. This solution gives the spatial distribution of neutron flux for any time-energy combination and describes the neutron wavefront as it moves outward from the impulse source. The wavefront has a continuously decreasing speed of propagation, as would be required by the continuous slowing-down assumption.

The analytic model is being evaluated by comparison with time-integrated Monte Carlo results for neutron transport in an infinite air medium. The preliminary results from these comparisons are encouraging. The extension of this method to a broader (less restrictive) class of problems and the practical considerations involved will also be considered.

A kernel based on this solution can be used as a Monte Carlo "estimator" from collisions in the keV and eV energy ranges for neutron transport in air. At these energies, the elastic scatterings are isotropic, the scattering cross sections for oxygen and nitrogen may vary very slowly, and absorptions are negligible. It is these conditions which make the analytical solution possible but cause a Monte Carlo solution to require excessive computer time.

References

[1]Work partly funded by the Defense Atomic Support Agency under DASA Task No. RRP-5037.

[2]University of Tennessee, Knoxville.

[3]Consultant, University of Tennessee, Knoxville.

3.15 NEUTRON TRANSPORT IN THE ATMOSPHERE[1]

E. A. Straker R. J. Rodgers[2]

In many shelter design problems it is necessary for the radiation field incident on the shield to be completely defined – that is, that the free-field radiation from a weapon burst be defined as a function of space, energy, and angle and in some instances time. In the past the problem has been treated in three different ways: the free field has been measured experimentally, the free field has been calculated in infinite air and then modified in some way to account for the effect of the ground, or Monte Carlo calculations have been made without approximating the geometrical description of the problem. Each approach has been very useful in providing the information needed for shelter design but not complete enough. We have solved the transport problem by utilizing the two-dimensional, anisotropic-scattering, discrete ordinates code DOT.[3] In order to determine the capabilities of a code of this complexity, results of calculations have to be compared with measurements and with other calculational methods.

Cylindrical geometry is used in the calculation, with the source located on the z axis at a given height z_s above the ground. The geometry must be finite and in our problems the cylinder has a radius of 1500 m and a height of 750 m. To reduce the effect of the finite geometry on the results, neutrons are returned isotropically at the outer boundaries in proportion to calculated albedos. Although the energy-angular spectra are determined at each of the approximately 3000 spatial mesh points, we are primarily interested in the results near the air-ground interface. Thus the albedo boundary condition in the upper surface at 750 m has a small effect on the results of interest. A P_3 expansion of the cross section and an S_8 angular quadrature (48 angles in two dimensions) were used in the calculations.

To determine the adequacy of these two-dimensional discrete ordinates calculations, a comparison was made with the experimental data measured during Operation BREN,[4] in which some of the measurements were of neutron dose on the interface due to a bare uranium reactor operating at various heights above the ground.

The reactor leakage spectrum has been measured and is essentially a Godiva type of spectrum slightly softer than a Cranberg fission spectrum. Figure 3.15.1 shows a comparison of the calculations with the experiment.[5,6] The solid line represents the first DOT calculations, which agree quite well with the experimental data even in the prediction of the peak at about 40 m. The histogram is the result of a Monte Carlo calculation and does not indicate the existence of a peak there. The peak in the DOT calculations was found to result from ray effects in the calculation that were due to the discrete angular quadrature since there are then some spatial mesh points which cannot see the point source. At deeper penetration (several mean free paths) the effect of the discrete angular quadrature becomes washed out because of redistribution of neutrons through scattering.

Increasing the angular quadrature would remove the ray effect, but would increase the computer time. Alternatively, the source description could be changed to a distributed first-collision source. The dashed line in Fig. 3.15.1 is the result of using a first-collision source in DOT. The DOT results agree very well with the Monte Carlo results in this spatial range but disagree with some of the experimental data. However, there are experimental data points on both sides of the calculated curve in this region. Thus it appears that

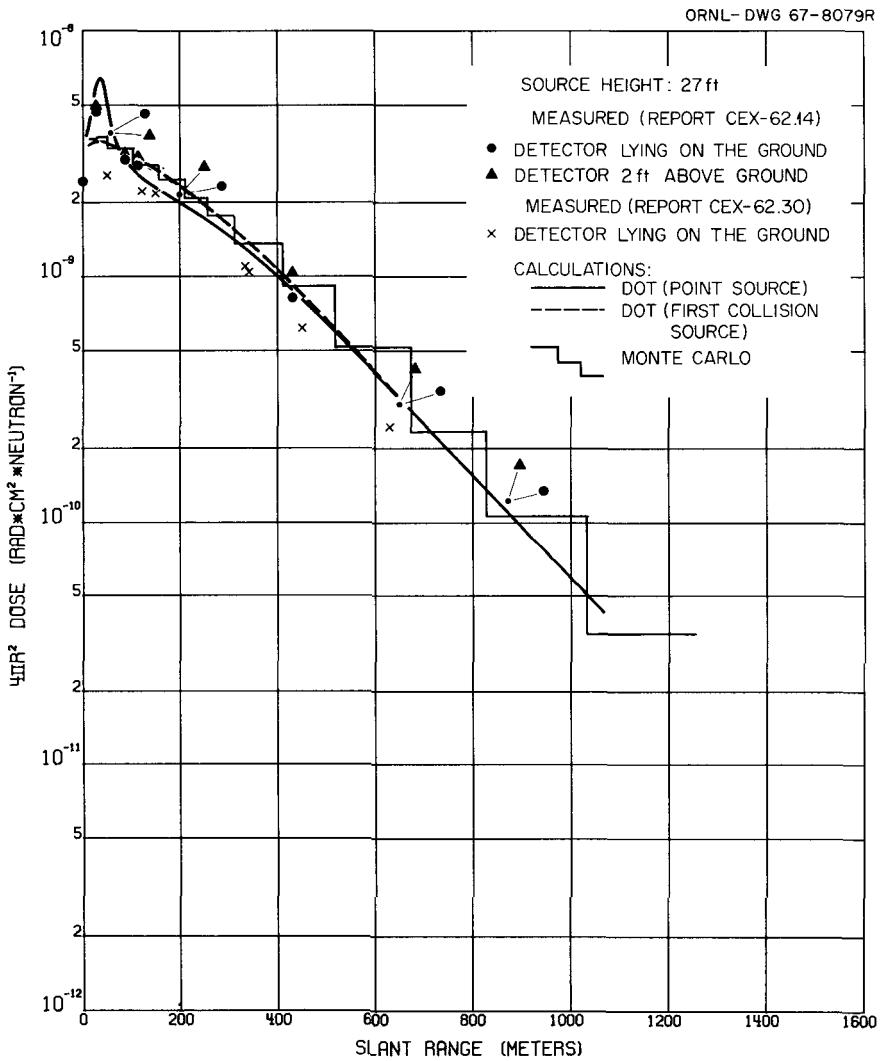

Fig. 3.15.1 Comparison of Calculation and Measurement of $4\pi R^2$ Dose vs Slant Range for a Godiva Spectrum Source 27 ft Above the Ground.

the first-collision source essentially removes the dominant ray effects.

To illustrate the detail that can be calculated, the angular distribution of the fast dose at a slant range of 258 m is shown in Fig. 3.15.2. The figure at the top illustrates the 50 solid-angle directions in which the flux is calculated. At the bottom of the figure the dose in a given polar angle (curves 1–8) is plotted as a function of the cosine of the azimuthal angle. It can be seen that the dose is peaked away from the source, curve 5 for azimuthal cosines near 1, and is nearly isotropic in returning from the ground, curves 1–4.

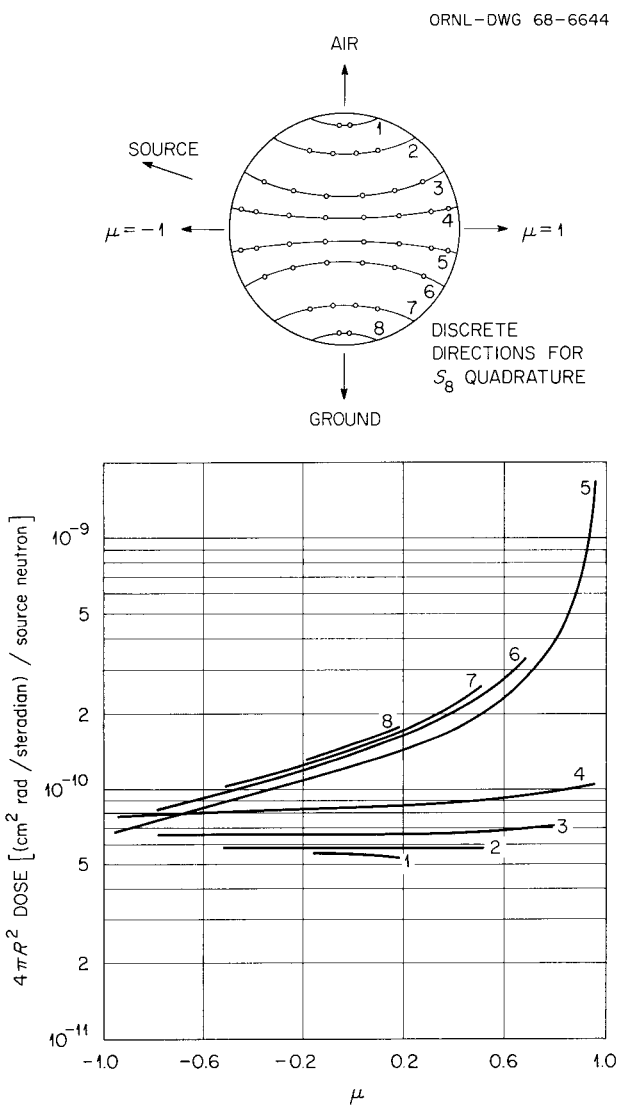

Fig. 3.15.2. $4\pi R^2$ Dose vs Angle at a Slant Range of 258 m Calculated for a Godiva Spectrum Source 27 ft Above the Ground.

The good agreement between measured and calculated results for Operation BREN provides a substantial degree of confidence in the results of two-dimensional discrete ordinates calculations. By using a first-collision source, ray effects have been minimized and good agreement with Monte Carlo calculations is obtained. The energy-angular distributions at the interface illustrate a strong dependence on angle, and it is now feasible to determine the complete energy-angular description of the radiation field.

References

[1]Work funded by Defense Atomic Support Agency under DASA Task No. RRP-2050.

[2]Computing Technology Center, Union Carbide Corporation, Oak Ridge, Tennessee.

[3]F. R. Mynatt, *A User's Manual for DOT, a Two-Dimensional Discrete Ordinates Transport Code with Anisotropic Scattering,* K-1694 (to be published).

[4]J. A. Auxier, F. F. Haywood, and L. W. Gilley, *General Correlative Studies – Operation BREN,* CEX 62.03 (1963).

[5]F. J. Muckenthaler *et al., An Evaluation of Simple Iron Water Radiation Shields and Radiation Measurement within Concrete-Lined and Capped Pits,* CEX 62.30 (1964).

[6]F. F. Haywood, J. A. Auxier, and E. T. Loy, *An Experimental Investigation of the Spatial Distribution of Dose in an Air-Over-Ground Geometry,* CEX 62.14 (1964).

3.16 CALCULATIONS OF NEUTRON TRANSPORT IN THE ATMOSPHERE AND THE EFFECT OF INPUT CROSS SECTIONS[1]

E. A. Straker N. M. Greene[2] R. J. Rodgers[2]

The sensitivity of calculations of dose and thermal flux to the energy group structure and type of weighting of multigroup cross sections was investigated for fission and 14-MeV sources in an infinite air medium. The discrete ordinates code ANISN was used to determine the differences resulting from the use of GAM and ENDF/B cross sections and from the number of energy groups used in the calculations. ENDF/B cross sections were reduced to a 104 fine-group set with the

group structure chosen to fit the structure in the total cross section. This fine-group set was then reduced to 33, 22, and 14 groups using both zone and infinite medium spectra weighting. Results with infinite-medium-weighted cross sections in 22 energy groups were essentially the same as a 104-group calculation. Excellent agreement for the calculation of dose from a fission source was obtained with Monte Carlo out to a range of 2400 m in standard air when the same basic cross sections were used.

References

[1]Abstract of p. 155 in *A Review of the Discrete Ordinates S_n Method for Radiation Transport Calculations,* ORNL-RSIC-19 (March 1968); work funded by Defense Atomic Support Agency under DASA Task No. RRP-2050.

[2]Computing Technology Center, Union Carbide Corporation, Oak Ridge, Tennessee.

3.17 TIME-DEPENDENT NEUTRON AND SECONDARY GAMMA-RAY TRANSPORT IN AN AIR-OVER-GROUND GEOMETRY[1]

E. A. Straker R. J. Rodgers[2]
F. R. Mynatt[2] M. B. Emmett[3]
C. L. Thompson[3]

The time, energy, and spatial distribution of fast neutrons and their secondary gammas has been calculated by Monte Carlo for a point isotropic source at a height of 50 ft above the ground. In addition, discrete ordinates calculations of the steady-state angular distribution of fast and thermal neutrons as well as the secondary gammas have also been made. The neutron source was uniform over each energy interval, and calculations were made for eight different energy intervals; therefore results for any desired spectrum may be approximated by weighted sums of the individual calculations. Except for the time dependence of low-energy neutrons and the secondary gammas from these neutrons, the calculations serve to define the radiation field at the air-ground interface.

Time-dependent versions of the 05R[4] and OGRE[5] Monte Carlo codes were used to obtain the time-dependent histories of the neutrons and secondary gammas. Importance-sampling schemes included the exponential transform, source angle biasing, and Russian roulette and splitting. Secondary gammas from inelastic scattering and fast-neutron capture in both the air and the ground were included in the Monte Carlo calculations.

The two-dimensional code DOT[6] was used for the discrete ordinates calculations. A first-collision source routine virtually eliminated all ray effects which had appeared in previous calculations.[7] A fine-group structure was chosen so that the minima in the total cross section of air would be adequately represented; neutron cross sections for this group structure were obtained with CSP-I.[8]

Neutron cross sections were taken from the ENDF/B library, and the secondary gamma production cross sections were compiled from many sources. Figure 3.17.1 shows the neutron dose (Henderson's[9] flux-to-dose conversion factors) and the secondary gamma-ray dose due to a source uniform in energy between 12.2 and 15

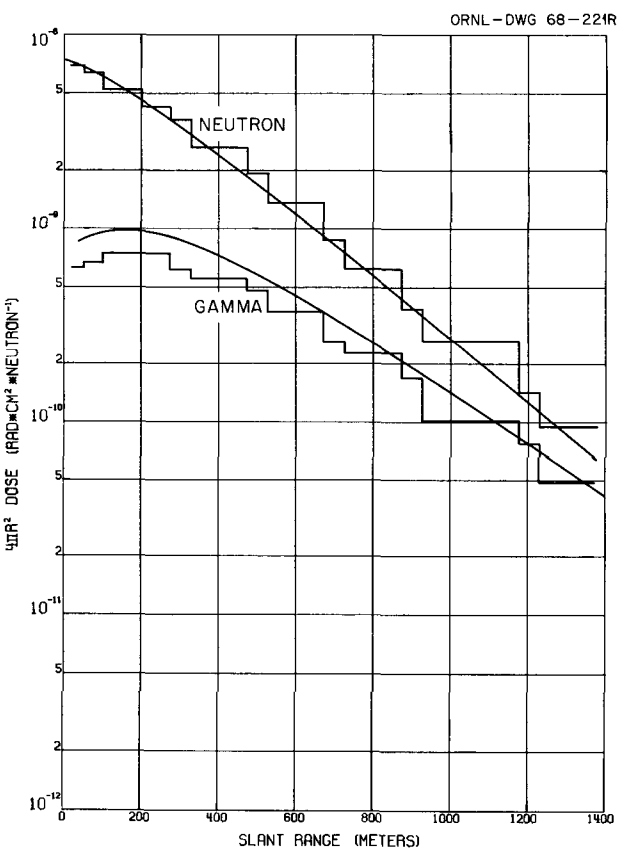

Fig. 3.17.1. $4\pi R^2$ Dose vs Slant Range for Neutron Source Energies Between 12.2 and 15 MeV.

MeV. The air density was 1.1 mg/cc and the dose is plotted as a function of slant range. The histogram is the result of the Monte Carlo calculations, and the solid line is the result of the discrete ordinates calculation. The same basic cross sections were used in both codes with the exception that the secondary gamma-ray source in the discrete ordinates calculation included thermal-capture gammas as well as fast-capture and inelastic gammas. This should account for the differences in the gamma-ray dose as calculated by the two methods.

Figure 3.17.2 shows the dose rate vs time for nominal slant ranges of 300 and 900 m for both neutrons and gamma rays. At 300 m the neutron dose rate is larger but of shorter duration than the secondary gamma pulse; at 900 m, however, the secondary gamma-ray pulse is slightly larger but of shorter duration. The decay of the neutron dose rate may be approximated by $D = Ct^{-2}$, where D is the dose rate, t is time, and C is a constant which depends on range. The long-time gamma-ray decay (for times longer than the peak neutron dose rate time) may be approximated by $D = Bt^{-3.6}$. The short-time gamma-ray dose rate behavior appears to be strongly dependent on the range.

Contributions to the secondary gamma-ray dose due to thermal captures would occur for times greater than approximately 50 to 100 μsec and would therefore modify the long-time behavior of the gamma-ray dose rate. However, from Fig. 3.17.1 it is noted that for this high-energy source, thermal-capture gammas in both the air and ground contribute at most 25% of the total gamma-ray dose; thus, thermal-capture gammas should be

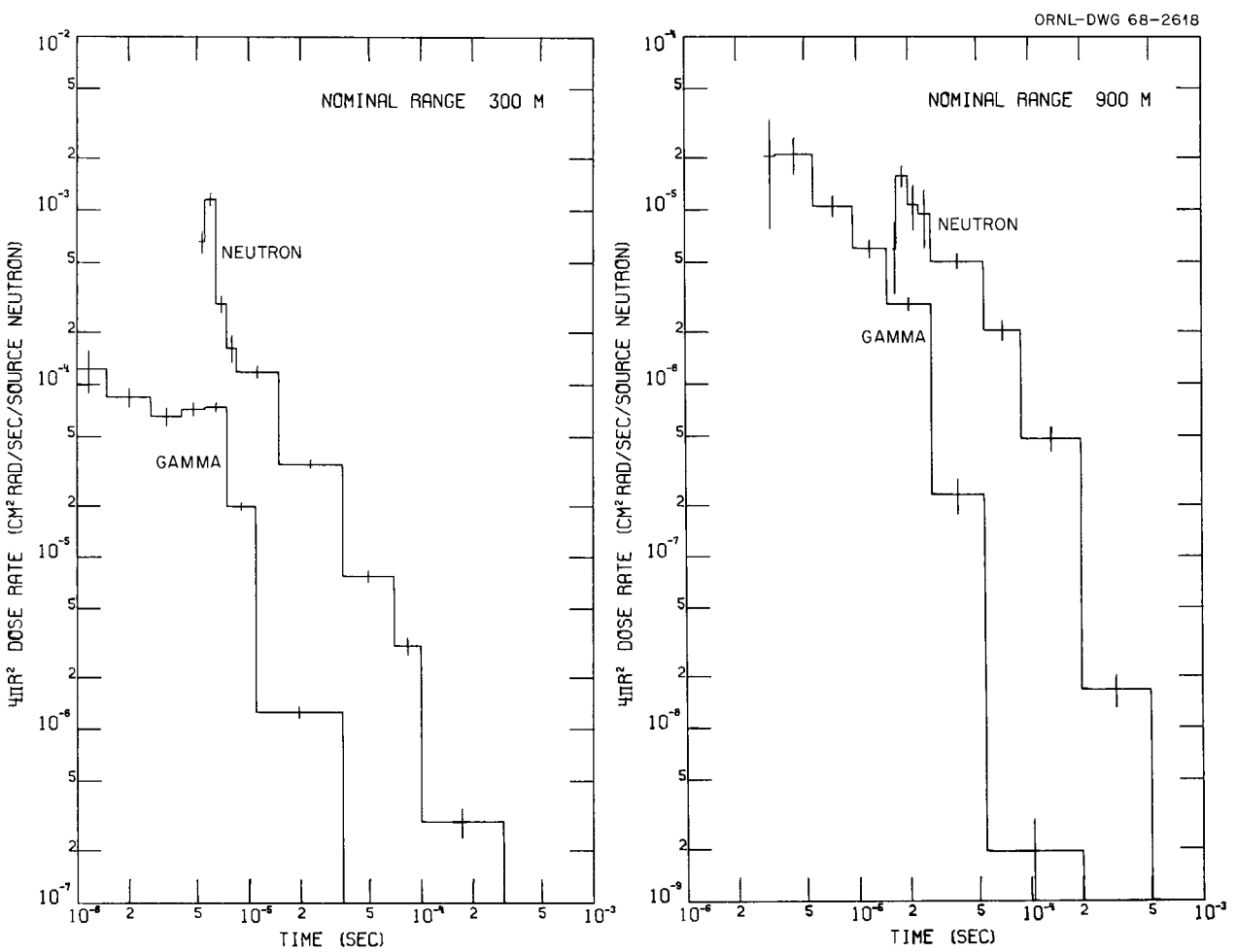

Fig. 3.17.2. $4\pi R^2$ Dose Rate vs Time for Detectors at 300 and 900 m.

negligible in the time region of peak dose rates shown in Fig. 3.17.2.

References

[1]Summary of paper to be presented at the Fourteenth Annual Meeting of the American Nuclear Society, Toronto, Ontario, Canada, June 9–13, 1968, and to be published in *Trans. Am. Nucl. Soc.*, Vol. 11, No. I (1968); work funded by the Defense Atomic Support Agency under DASA Task No. RRP-2050.

[2]Computing Technology Center, Union Carbide Corporation, Oak Ridge, Tennessee.

[3]Mathematics Division.

[4]D. C. Irving *et al.*, *05R, A General Purpose Monte Carlo Neutron Transport Code*, ORNL-3622 (1965).

[5]S. K. Penny, D. K. Trubey, and M. B. Emmett, *OGRE, A Monte Carlo System for Gamma-Ray Transport Studies, Including an Example (OGRE-P1) for Transmission Through Laminated Slabs*, ORNL-3805 (1966).

[6]F. R. Mynatt, *A User's Manual for DOT, a Two-Dimensional Discrete Ordinates Transport Code with Anisotropic Scattering*, K-1694 (to be published).

[7]E. A. Straker and F. R. Mynatt, *Calculations of the Effect of the Air-Ground Interface on the Transport of Fission Neutrons Through the Atmosphere*, ORNL TM-1819 (1967).

[8]K. J. Yost and N. M. Greene, *CSP-I: A Neutron Cross-Section Averaging Package for Use with the 05R Data Tape*, ORNL-4130 (1967).

[9]B. J. Henderson, *Conversion of Neutron and Gamma-Ray Flux to Absorbed Dose Rate*, XDC 59-8-179 (1959).

3.18 *WEAPONS RADIATION SHIELDING HANDBOOK:* STATUS REPORT

L. S. Abbott, H. C. Claiborne, and
C. E. Clifford, Editors

Substantial progress was made toward complete publication of the *Weapons Radiation Shielding Handbook*. The first seven chapters, which were designated in the initial scope of the Handbook, have been completed in either published or review form. Plans are being formulated for an eighth chapter, "Shielding Effectiveness of Above-Ground Structures Against Initial Radiation."

Chapter 3, "Methods for Calculating Neutron and Gamma-Ray Attenuation," by P. N. Stevens and D. K. Trubey has been published as DASA-1892-3. Chapters 4 and 5, which were published in 1967 as DASA-1892-1 and -2, have also been issued as ORNL-RSIC-20 and -21. Chapter 1, "Introduction and Basic Considerations," by P. N. Stevens; Chapter 2, "Radiation Environment for Nuclear Weapons," by W. E. Selph and M. B. Wells; Chapter 6, "Engineering Methods for Hardened Shelter Design Against Initial Radiation," by L. G. Mooney, M. B. Wells, and H. C. Claiborne; and Chapter 7, "Engineering Method for Calculating Structure Shielding Against Fallout Radiation," by R. L. French have been issued in draft form and sent for review to those designated by the Defense Atomic Support Agency.

Chapter 2 is in the final stages of revision and editing prior to its publication.

3.19 THERMAL-NEUTRON FLUXES WITHIN A LARGE DUCTED CONCRETE ROOM[1]

R. E. Maerker

One of the major problems in the design of large shelters, whether for military or civilian use, is the prediction of neutron-induced dose levels at various locations within a large underground room, access to which is afforded by a man-sized passageway consisting of several tortuous bends. The AMC[2] code was developed for just such a problem, and some useful results are reported here.

Previous studies[3] have shown that the major part of the dose arising deep inside a multibend

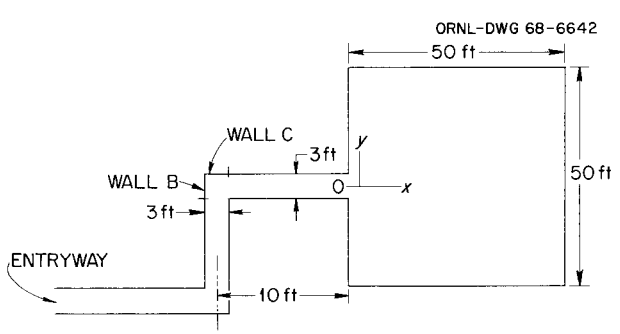

Fig. 3.19.1. Room and Passageway Geometry. The passageway and enclosed room are 7 ft high.

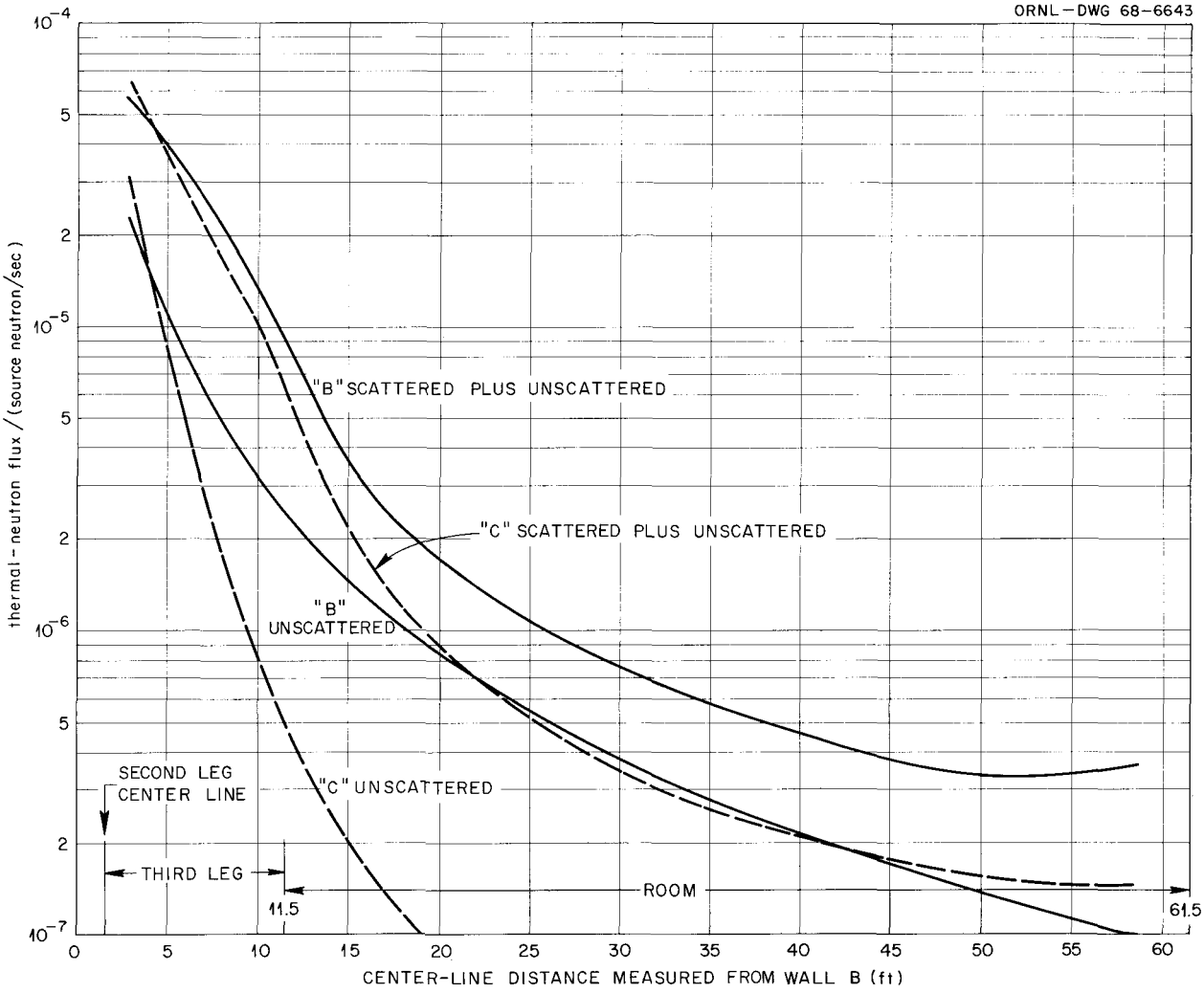

Fig. 3.19.2. Comparison of Center-Line Fluxes Due to Source B and Source C.

concrete duct from radiation penetrating the entryway is due to thermalized neutrons and the accompanying wall-capture secondary gamma rays. Thus, for the geometry depicted in Fig. 3.19.1, a good approximation to the dose levels in the room that result from passageway transmission is made by assuming that only a thermal-neutron source exists on walls B and C. Because the geometric dissimilarities of these pseudo-plane sources affect the flux levels within the room, problems were run for each source location.

Sources B and C were each normalized to 1 neutron/sec spread uniformly over the plane area at the bend as indicated in Fig. 3.19.1, and each was assumed to emit with a cosine angular distribution with respect to the normal to the plane on which it lay.

Figure 3.19.2 illustrates the behavior of the center-line fluxes along the third leg and into the room for each of the two sources. It should be noted that, due to solid angle effects, the unscattered component of the flux from source C falls off closely as the cube of the center-line distance, whereas that from source B falls off closely as the square of the center-line distance. Since the scattered components from the two sources are closely the same, however, the sums of the scattered and unscattered fluxes for each source are within a factor of 2 of each other.

Table 3.19.1 illustrates the off-center-line fluxes in the room for each source. The detectors were all located 3.5 ft from the floor (i.e., in a horizontal plane midway between the floor and

Table 3.19.1. Comparison of Total Fluxes Per Source Neutron Per Second at Off-Center-Line Detectors Within the Room

$z = 3.5$ ft

x (ft)	y (ft)	Flux		x (ft)	y (ft)	Flux
		Source B	Source C			Source C
		$\times 10^{-7}$	$\times 10^{-7}$			$\times 10^{-7}$
3	3.5	7.91	6.03	3	−3.5	5.76
	8.5	2.29	1.66		−8.5	1.67
	13.5	1.38	1.08		−13.5	1.10
	18.5	1.17	0.87		−18.5	0.88
	23.5	0.99	0.88		−23.5	0.80
10	3.5	7.06[a]	4.46	10	−3.5	6.52
	8.5	2.65	2.05		−8.5	1.99
	13.5	1.69	1.31		−13.5	1.33
	18.5	1.34	1.03		−18.5	1.05
	23.5	1.02	0.88		−23.5	0.96
17.5	3.5	5.50[a]	2.81	17.5	−3.5	3.82[a]
	8.5	2.30	1.83		−8.5	1.71
	13.5	1.73	1.30		−13.5	1.27
	18.5	1.38	1.07		−18.5	1.02
	23.5	1.24	0.94		−23.5	0.96
25	3.5	4.23[a]	1.96	25	−3.5	2.55[a]
	8.5	2.07	1.56		−8.5	1.96[a]
	13.5	1.63	1.23		−13.5	1.15
	18.5	1.40	1.05		−18.5	1.01
	23.5	1.39	0.95		−23.5	0.98
35	3.5	3.20[a]	1.47	35	−3.5	1.77[a]
	8.5	2.13[a]	1.24		−8.5	1.70[a]
	13.5	1.47	1.09		−13.5	1.12[a]
	18.5	1.27	0.95		−18.5	0.95
	23.5	1.23	0.90		−23.5	0.92
47	3.5	3.30[a]	1.31	47	−3.5	1.66[a]
	8.5	2.20[a]	1.15		−8.5	1.77[a]
	13.5	1.42[a]	1.02		−13.5	1.51[a]
	18.5	1.13	0.95		−18.5	0.94
	23.5	0.93	0.79		−23.5	0.80

[a]Includes the unscattered component.

ceiling). In the table, the x coordinate is measured from the plane defining the left side of the room and the y coordinate from the center line (see Fig. 3.19.1). The symmetry of source B with respect to y precludes the necessity of any calculations in the half-space defined by negative y. The percent standard deviation for these results is ±10%.

From the results presented in Table 3.19.1 it is clear that the y asymmetry in the case of source C is totally due to the unscattered component. When this component is absent, the results for (x, y) are the same as for $(x, -y)$. Further, the flux at detectors in the room invisible to both sources is approximately the same for each source. Flux levels for a given source vary in the

room by a factor of about 30, and at those detectors which are invisible to the source the levels vary by a factor of 8. The lowest flux levels lie in the vicinity of the corners $y = \pm 25$, $x = 0, 50$, although the x variation is weak at these locations.

The scattered flux from source C may be broken up into two parts: a component which reflects from wall B and a component that does not. An analysis of the results presented in Fig. 3.19.2 and Table 3.19.1 indicates that this scattered component, C_{scat}, may be decomposed into

$$C_{scat} = (0.18\ B_{unscat} + 0.32\ B_{scat}) + 0.41\ B_{scat}\ ,$$

where the values in parentheses represent the contribution from at least one reflection from wall B and the remainder the contribution from neutrons that have been reflected elsewhere. Thus, roughly half of the scattered flux from the source C is reflected from wall B, and this component dominates the flux from source C at large center-line distances into the room, since under these conditions $B_{unscat} >> B_{scat}$.

These results may be normalized to 1 neutron/sec incident at the entryway by the use of the formulas developed in Section 3.20.

References

[1]Work funded by Defense Atomic Support Agency under DASA Task No. RRP-5037.

[2]R. E. Maerker and V. R. Cain, *AMC: A Monte Carlo Code Utilizing the Albedo Approach for Calculating Neutron and Capture Gamma-Ray Distributions in Rectangular Concrete Ducts*, ORNL-3964 (1967).

[3]R. E. Maerker and F. J. Muckenthaler, *Nucl. Sci. Eng.* **30**, 340 (1967).

3.20 SEMIEMPIRICAL EQUATIONS FOR NEUTRON-INDUCED DOSES WITHIN RECTANGULAR CONCRETE DUCTS[1]

R. E. Maerker

In order to generalize the expressions originally generated for an Engineering Compendium article[2] and to provide data for use in Chapter 6 of the *Weapons Radiation Shielding Handbook*, a series of calculations was performed using the AMC code[3] to determine neutron-induced center-line doses within rectangular concrete ducts. Semiempirical expressions for the doses were then deduced as functions of the duct dimensions which agreed within the statistics of the Monte Carlo calculations and which could be used as an interpolative device over the range of duct dimensions investigated.

Specifically, multicollision (absorbed) dose rates along the center lines of two-legged rectangular ducts (containing one right-angled bend) resulting from a cosine current angular distribution of neutrons incident upon the plane of the duct mouth were calculated. The incident epicadmium energy distribution (given in Table 3.20.1) was assumed to come from a point fission source moderated by 1500 m of air.[4]

The duct is of uniform cross section $W \times H$, with the aspect ratio A defined as H/W. The length of the first leg is L_1 (center-line distance from mouth to intersection with the second leg center line), and the detector is located at X_1 along the first-leg center line from the mouth. The first-leg doses are given for

$$\alpha \leq \frac{X_1}{W} \leq \frac{L_1}{W} + \frac{1}{2},$$

which carries the detector to the plane of the second-leg opening (see Fig. 3.20.1). The length of the

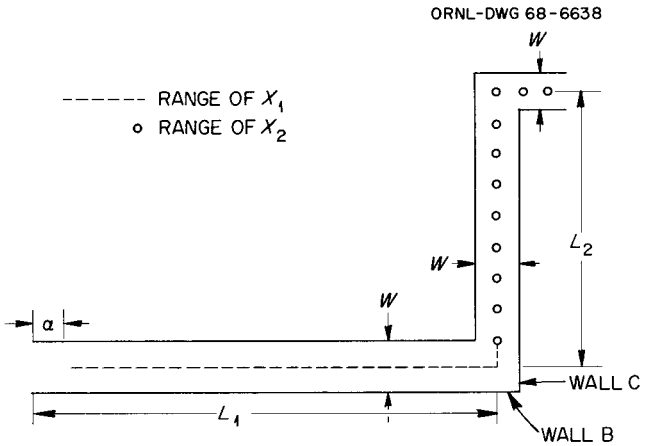

Fig. 3.20.1. Duct Notation.

Table 3.20.1. Assumed Incident Epicadmium Energy Spectrum

ΔE_0	Relative Number of Neutrons	ΔE_0	Relative Number of Neutrons
0.5–1.8 eV	0.0792	15–55 keV	0.0792
1.7–6.6	0.0792	55–200	0.0792
6.6–24	0.0792	0.2–0.75 MeV	0.121
24–87	0.0792	0.75–1.5	0.049
87–320	0.0792	1.5–3.0	0.032
0.32–1.2 keV	0.0792	3.0–4.0	0.002
1.2–4.2	0.0792	4.0–6.0	0.003
4.2–15	0.0792	>6.0	0.001

second leg is L_2 (center-line distance along the second leg from the intersection with the first-leg center line to the intersection with a third-leg center line), and the detector is located at a distance X_2 along the second leg measured from the same origin as L_2. The second-leg doses are given for

$$\frac{1}{2} < \frac{X_2}{W} \leq \frac{L_2}{W} + \frac{1}{2},$$

so that they start at the point where the first-leg doses end and continue to the plane of the third-leg opening. The dose expressions have an estimated inaccuracy of less than ±20% over the ranges

$$3 \leq \frac{L_1}{W} \leq 12\,, \quad 3 \leq \frac{L_2}{W} \leq 9\,, \quad 1 \leq A \leq \frac{7}{3}.$$

The following expressions are for multicollision (absorbed) dose rates per incident neutron current of specified energy range, in units of rads/incident neutron/cm^2.

Let D_F = dose rate above 200 keV per incident current above 200 keV. Then

$$D_F\left(\frac{X_1}{W}, \frac{L_1}{W}, A\right) = \left\{3.8 \times 10^{-9} \tan^{-1}\left[\frac{A\left(\frac{W}{2X_1}\right)^2}{\sqrt{1 + \frac{A^2+1}{4}\left(\frac{W}{X_1}\right)^2}}\right]\right\}\left(1 + \frac{X_1}{W}\, e^{-0.39X_1/W}\right)$$

$$\times\left[1 + (A-1)\left(-0.19 + 0.04\,\frac{X_1}{W}\right)\right]\left[1 + 0.09\, e^{-(L_1 - X_1)/W}\right],$$

with $\alpha = 0.2$. The expression in the braces represents $D_{\text{func}}\left(\frac{X_1}{W}, A\right)$, the uncollided dose rate above 200 keV.

$$D_F\left(\frac{X_2}{W}, \frac{L_1}{W}, \frac{L_2}{W}, A\right) = \frac{2}{\pi}\Bigg(\Bigg\{0.27\, D_{\text{func}}\left(\frac{L_1}{W}, A\right)\frac{W}{2L_1}$$

$$+ [0.0125 + 0.0022\,(A-1)]\, D_{\text{func}}\left(\frac{L_1}{W} + \frac{1}{2}, A\right)\Bigg\}$$

$$\times\left\{1 + 0.32\left(\frac{L_1}{W}\right)^2 e^{-0.039(L_1/W)^2}\right\}\left\{2\tan^{-1}\frac{A}{4\left(\frac{X_2}{W}+\frac{1}{2}\right)^2\sqrt{1+\frac{A^2+1}{4\left(\frac{X_2}{W}+\frac{1}{2}\right)^2}}}\right\}$$

$$\times\left\{1 + 0.5\left(\frac{X_2}{W}+\frac{1}{2}\right)\exp\left[-0.39\left(\frac{X_2}{W}+\frac{1}{2}\right)\right]\right\}\times\left\{1 + (A-1)\left[-0.19 + 0.02\left(\frac{X_2}{W}+\frac{1}{2}\right)\right]\right\}$$

$$+\left\{0.250\, D_{\text{func}}\left(\frac{L_1}{W}+\frac{1}{2}, A\right)\right\}\times\left\{2.1 + 0.056\left(\frac{L_1}{W} - 10.67\right)^2\right\}$$

$$\times\left\{\tan^{-1}\frac{A}{\sqrt{1+\frac{A^2+1}{4\left(\frac{X_2}{W}+\frac{1}{2}\right)^2}}} - \tan^{-1}\frac{A}{\sqrt{1+\frac{A^2+1}{4\left(\frac{X_2}{W}-\frac{1}{2}\right)^2}}}\right\}\left\{1 + 0.5\frac{X_2}{W}e^{-0.39X_2/W}\right\}$$

$$\times\left\{1 + (A-1)\left(-0.19 + 0.02\frac{X_2}{W}\right)\right\}\Bigg)\times\left[1 + 0.09\, e^{-(L_2 - X_2)/W}\right].$$

As in the succeeding expressions, the terms enclosed in the first five pairs of braces represent the contribution from wall B (see Fig. 3.20.1), and those in the remaining five pairs of braces represent the contribution from wall C.

Let D_I = dose rate between 0.5 eV and 200 keV per incident current above 0.5 eV. Then

$$D_I\left(\frac{X_1}{W}, \frac{L_1}{W}, A\right) = \left[7.1\times 10^{-10}\tan^{-1}\frac{A\left(\frac{W}{2X_1}\right)^2}{\sqrt{1+\frac{A^2+1}{4}\left(\frac{W}{X_1}\right)^2}}\right]\left(1 + 2.2\frac{X_1}{W}e^{-0.39X_1/W}\right)$$

$$\times \left[1 + (A-1)\left(-0.09 + 0.032\frac{X_1}{W}\right)\right]\left[1 + 0.033\frac{L_1}{W}e^{-(L_1 - X_1)/W}\right],$$

with $\alpha = 0.2$. The expression in the first pair of brackets represents $D_{\text{Iunc}}\left(\frac{X_1}{W}, A\right)$, the uncollided dose rate lying between 0.5 eV and 200 keV per incident current above 0.5 eV.

$$D_I\left(\frac{X_2}{W}, \frac{L_1}{W}, \frac{L_2}{W}, A\right) = \frac{2}{\pi}\left(\left\{0.40\, D_{\text{Iunc}}\left(\frac{L_1}{W}, A\right)\frac{W}{2L_1} + [0.0423 + 0.0074(A-1)]\right.\right.$$

$$\left.\times D_{\text{Iunc}}\left(\frac{L_1}{W} + \frac{1}{2}, A\right)\right\}\left\{1 + 1.05\left(\frac{L_1}{W}\right)^2 e^{-0.054(L_1/W)^2}\right\}$$

$$\times\left\{2\tan^{-1}\frac{A}{4\left(\frac{X_2}{W} + \frac{1}{2}\right)^2\sqrt{1 + \frac{A^2+1}{4\left(\frac{X_2}{W} + \frac{1}{2}\right)^2}}}\right\}\left\{1 + 1.2\left(\frac{X_2}{W} + \frac{1}{2}\right)\exp\left[-0.39\left(\frac{X_2}{W} + \frac{1}{2}\right)\right]\right\}$$

$$\times\left\{1 + (A-1)\left[-0.09 + 0.032\left(\frac{X_2}{W} + \frac{1}{2}\right)\right]\right\} + \left\{0.46\, D_{\text{Iunc}}\left(\frac{L_1}{W} + \frac{1}{2}, A\right)\right\}$$

$$\times\left\{3.6 + 0.13\left(\frac{L_1}{W} - 9.67\right)^2\right\}\left\{\tan^{-1}\frac{A}{\sqrt{1 + \frac{A^2+1}{4\left(\frac{X_2}{W} + \frac{1}{2}\right)^2}}} - \tan^{-1}\frac{A}{\sqrt{1 + \frac{A^2+1}{4\left(\frac{X_2}{W} - \frac{1}{2}\right)^2}}}\right\}$$

$$\left.\times\left\{1 + 1.2\left(\frac{X_2}{W}\right)e^{-0.39X_2/W}\right\}\left\{1 + (A-1)\left(-0.09 + 0.032\frac{X_2}{W}\right)\right\}\right)\left[1 + 0.033\frac{L_2}{W}e^{-(L_2 - X_2)/W}\right].$$

Let D_E = thermal-neutron dose rate arising as a consequence of slowing down per incident neutron current above 0.5 eV. Then

$$D_E\left(\frac{X_1}{W}, \frac{L_1}{W}, A\right) = \frac{1.8 \times 10^{-10}\, e^{-0.33 X_1/W}}{X_1/W} \left\{1 + \left[0.22 + 0.0064\left(\frac{L_1}{W} - 3\right)^2\right] \times e^{-(L_1 - X_1)/W}\right\} \left[1 + 0.22(A - 1)\frac{X_1}{W}\right] ,$$

with $\alpha = 1.5$, and

$$D_E\left(\frac{X_2}{W}, \frac{L_1}{W}, \frac{L_2}{W}, A\right) = \frac{1.35\, D_E\left(\frac{L_1}{W}, \frac{L_1}{W}, A\right) \exp\left[-0.39\left(\frac{X_2}{W} + \frac{1}{2}\right)\right]}{\frac{X_2}{W} + \frac{1}{2}} \times \left[1 + 0.125(A - 1)\left(\frac{X_2}{W} - \frac{1}{2}\right)\right]\left[1 + 0.045\frac{L_2}{W} e^{-(L_2 - X_2)/W}\right] .$$

Let $D_{\gamma E}$ = wall capture secondary gamma-ray dose rate per incident neutron current above 0.5 eV. Then

$$D_{\gamma E}\left(\frac{X_1}{W}, \frac{L_1}{W}, A\right) = 1.1\, D_E\left(\frac{X_1}{W}, \frac{L_1}{W}, A\right) ,$$

with $\alpha = 1.5$, and

$$D_{\gamma E}\left(\frac{X_2}{W}, \frac{L_1}{W}, \frac{L_2}{W}, A\right) = \left[1.05 - \frac{0.20\left(\frac{X_2}{W} - 1.2\right)}{\frac{X_2}{W} + \frac{1}{2}}\right] D_E\left(\frac{X_2}{W}, \frac{L_1}{W}, \frac{L_2}{W}, A\right) .$$

Let D_{th} = thermal-neutron dose rate per incident thermal-neutron current. Then

$$D_{\text{th}}\left(\frac{X_1}{W}, \frac{L_1}{W}, A\right) = \left[4.1 \times 10^{-10} \tan^{-1} \frac{A\left(\frac{W}{2X_1}\right)^2}{\sqrt{1 + \frac{A^2 + 1}{4}\left(\frac{W}{X_1}\right)^2}}\right]\left(1 + 3.5\frac{X_1}{W} e^{-0.33 X_1/W}\right) \times \left[1 + (A - 1)\left(-0.19 + 0.047\frac{X_1}{W}\right)\right]\left[1 + 0.033\frac{L_1}{W} e^{-(L_1 - X_1)/W}\right] ,$$

with $\alpha = 1.5$, and

$$D_{th}\left(\frac{X_2}{W}, \frac{L_1}{W}, \frac{L_2}{W}, A\right) = 0.89\, D_{th}\left(\frac{L_1}{W}, \frac{L_1}{W}, A\right) \left[1 + 0.18(A-1)\left(\frac{X_2}{W} - \frac{1}{2}\right)\right]$$

$$\times \exp\left\{-\left[0.42 + 0.01\left(\frac{L_1}{W} - 3\right)\left(1 - \frac{1.67}{\frac{X_2}{W} + \frac{1}{2}}\right)\right]\left(\frac{X_2}{W} + \frac{1}{2}\right)\right\}\left[1 + 0.033\,\frac{L_2}{W}\, e^{-(L_2 - X_2)/W}\right] .$$

Finally, let $D_{\gamma th}$ = wall capture secondary gamma-ray dose rate per incident thermal-neutron current. Then

$$D_{\gamma th}\left(\frac{X_1}{W}, \frac{L_1}{W}, A\right) = 0.60\, D_{th}\left(\frac{X_1}{W}, \frac{L_1}{W}, A\right) ,$$

with $\alpha = 1.5$, and

$$D_{\gamma th}\left(\frac{X_2}{W}, \frac{L_1}{W}, \frac{L_2}{W}, A\right) = 0.84\, D_{th}\left(\frac{X_2}{W}, \frac{L_1}{W}, \frac{L_2}{W}, A\right) .$$

References

[1]Work funded by Defense Atomic Support Agency under DASA Task No. RRP-5037.

[2]R. E. Maerker, H. C. Claiborne, and C. E. Clifford, "Neutron Streaming in Rectangular Ducts," *Engineering Compendium on Radiation Shielding*, Springer-Verlag, Berlin (to be published).

[3]R. E. Maerker and V. R. Cain, *AMC: A Monte Carlo Code Utilizing the Albedo Approach for Calculating Neutron and Capture Gamma-Ray Distributions in Rectangular Concrete Ducts*, ORNL-3964 (1967).

[4]E. A. Straker, private communication.

3.21 NEUTRON FLUXES IN CONCRETE DUCTS ARISING FROM INCIDENT THERMAL NEUTRONS: CALCULATION AND EXPERIMENT[1]

R. E. Maerker F. J. Muckenthaler

Monte Carlo calculations, employing the albedo concept, have been carried out to determine the thermal-neutron flux distributions along the center lines of a straight, a two-legged, and a three-legged square open concrete duct for a particularly demanding source geometry. The neutrons entering the duct were of thermal energy. The calculations used differential angular albedo data for concrete which have been reported previously. A comparison of the results of the calculations with those from a geometrically similar experiment conducted at the Tower Shielding Facility shows good agreement and places on a firm foundation the concept of treating the thermal-neutron duct transmission problem as a reflection phenomenon at a point that is describable by the differential albedo properties of the walls.

Reference

[1]Abstract of *Nucl. Sci. Eng.* **29**, 444–454 (1967); work funded by Defense Atomic Support Agency under DASA Task No. RRP-5037.

3.22 NEUTRON FLUXES IN CONCRETE DUCTS ARISING FROM INCIDENT EPICADMIUM NEUTRONS: CALCULATIONS AND EXPERIMENTS[1]

R. E. Maerker F. J. Muckenthaler

Monte Carlo calculations, using the albedo concept, have been carried out to determine subcadmium and epicadmium neutron flux distributions along the center line of a straight, a two-legged, and a three-legged square concrete duct arising from the slowing down of incident epicadmium neutrons for a particularly demanding source geometry and spectrum. The calculations used albedo data differential both in the reflected angles and reflected energy which have been reported previously for concrete. A comparison of the results of these calculations with those from a geometrically similar experiment conducted at the Tower Shielding Facility shows good agreement and places on a firm foundation the concept of treating neutron slowing down in a concrete duct as a reflection phenomenon at a point which is describable by the differential albedo properties of the walls The conclusion is also reached that the dose rates arising from the subcadmium neutrons (whether due to an epicadmium source or a subcadmium source) and associated secondary wall-capture gamma rays can comprise a very important part of the total absorbed dose rate in tissue deep inside a multilegged duct.

Reference

[1] Abstract of *Nucl. Sci. Eng.* **30**, 340–354 (1967); work funded by Defense Atomic Support Agency under DASA Task No. RRP-5037.

3.23 ANGLE-DEPENDENT NEUTRON SPECTRA EMERGENT FROM SLAB SHIELDS: COMPARISON OF TWO-DIMENSIONAL DISCRETE ORDINATES CALCULATIONS WITH EXPERIMENT[1]

F. R. Mynatt[2] F. J. Muckenthaler
P. N. Stevens[3]

An experiment has been performed at the ORNL Tower Shielding Facility to provide data for comparison with transport calculations. The emphasis in the experiment was in the measurement of angle-dependent fast-neutron leakage spectra in a clean geometry suitable for direct comparison with calculation. Of primary interest was the comparison with the two-dimensional, anisotropic, discrete ordinates transport code DOT.[4] This comparison with experiment provided a check on accuracy as well as data for testing the selection of the computational options.

A drawing of the experimental configuration is shown in Fig. 3.23.1. The neutron source was the TSR-II, and the highly collimated neutron beam was directed normal to large slab shield samples. The slabs were backed with an 8-in.-thick lead collar so that double albedo effects could be calculated if necessary.

Detailed measurements were made of the incident beam, including neutron spectra and angle dependence and radial and axial dose distributions. These data are required as input to describe the source in the calculations which are thus normalized only to the absolute magnitude of the source. Measurements were made of angle-dependent fast-neutron spectra emergent from lead, polyethylene, depleted uranium, and laminated lead and polyethylene slabs. The spectra were measured at a radius of 27.4 ft from the slab, at angles of 0, 13, 30, 47, and 65° with a collimator that viewed the entire exit face of the slab. Fast-neutron dose distributions were measured at several distances from the slabs with an uncollimated detector.

All fast-neutron spectral measurements were made with the NE-213 liquid organic scintillator – FERD unfolding code system.[5,6] The neutron dose measurements were made with a Hurst fast-neutron dosimeter.

The DOT calculations for this system were performed by representing the slabs as right circular cylinders. The phase space mesh consisted of 675 spacial points, S_{10} (70 angles) quadrature, and 30 energy groups above 0.7 MeV for the fast spectra, or 38 energy groups for dose and fission distribution calculations. The calculations were made using GAM-II,[7] AWRE, and ENDF/B cross-section data with anisotropic scattering representations (in DOT) from P_3 to P_8. The model has several representations of the source, including an analytic first-collision source and a zone-of-interest convergence criteria. Two methods were used for obtaining the flux in space external to the calculated system: a surface integration of the angular flux and a volume integration using a calculated last flight importance function.

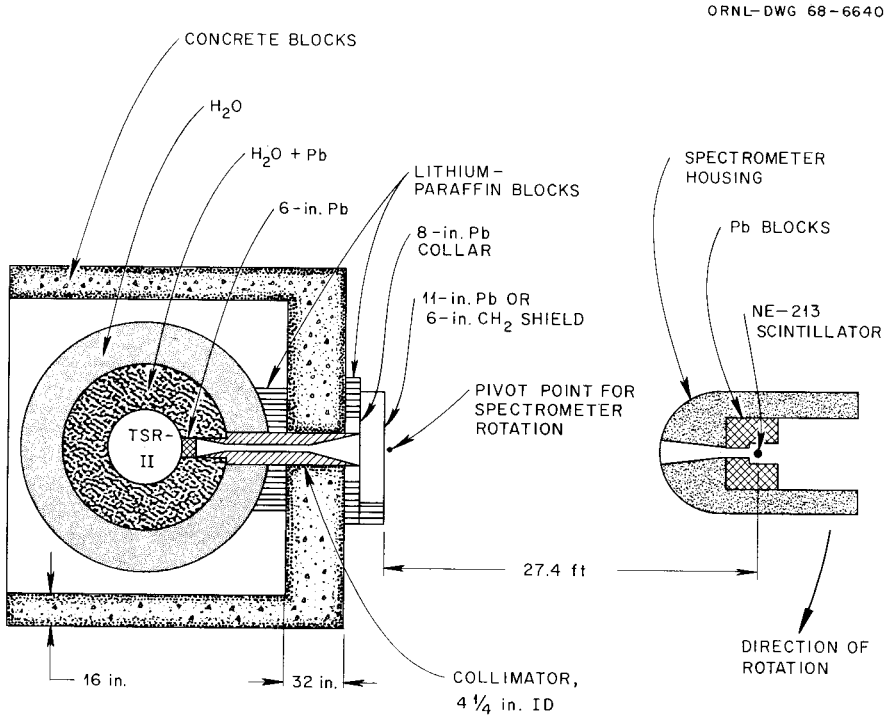

Fig. 3.23.1. Experimental Configuration at the Tower Shielding Facility.

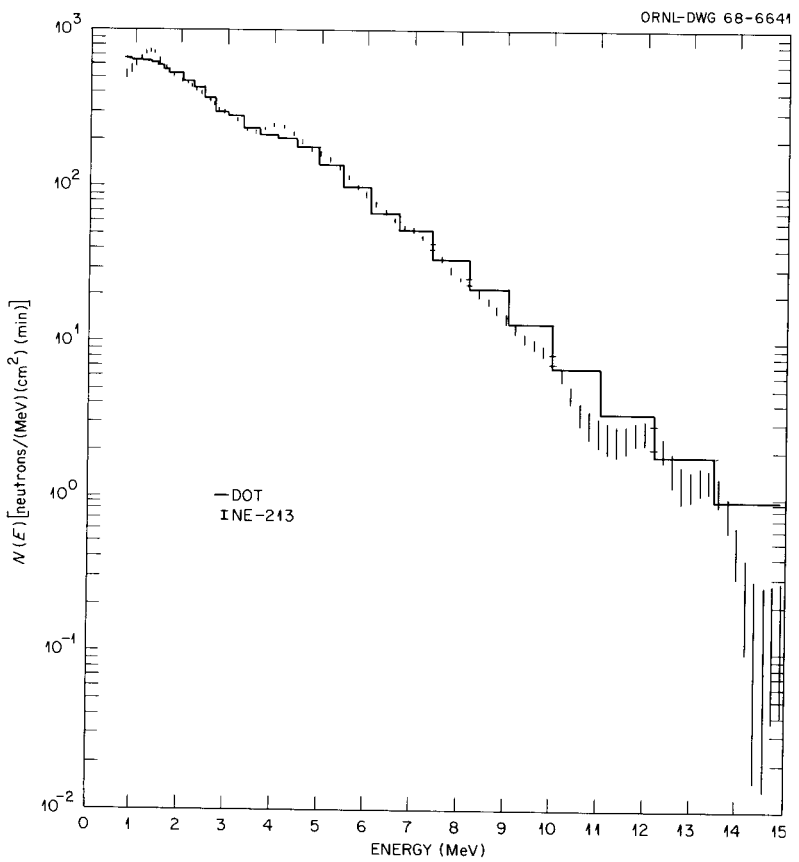

Fig. 3.23.2. Comparison Between Calculation and Experiment for Angle-Dependent Neutron Spectra from 6-in. Polyethylene Slab at 30°.

Figure 3.23.2 shows a comparison of calculation and experiment at 30° for a 6-in. polyethylene slab. The calculation used GAM-II cross sections with P_3 scattering, an analytic first-collision source, and surface integration of the angular flux. The agreement in intensity and shape is considered quite good.

References

[1]Summary of paper to be presented at the Fourteenth Annual Meeting of the American Nuclear Society, Toronto, Ontario, Canada, June 9–13, 1968, and to be published in *Trans. Am. Nucl. Soc.*, vol. 11, No. 1 (1968); work funded by Defense Atomic Support Agency under DASA Task No. RRP-5037.

[2]Computing Technology Center, Union Carbide Corporation, Oak Ridge, Tennessee.

[3]Consultant from the University of Tennessee, Knoxville.

[4]F. R. Mynatt, *A User's Manual for DOT – A Two-Dimensional Discrete Ordinates Transport Code with Anisotropic Scattering*, K-1694 (to be published).

[5]W. R. Burrus and V. V. Verbinski, p. 148 in *Proceedings of Special Session, Fast Neutron Spectroscopy, 1964 Winter Meeting of the American Nuclear Society, San Francisco, Calif.*, ANS-SD-2 (1965).

[6]W. R. Burrus, *Utilization of A Priori Information by Means of Mathematical Programming in the Statistical Interpretation of Measured Distributions*, ORNL-3743 (1964).

[7]G. D. Joanou and J. S. Dudek, *GAM-II: A B_3 Code for the Calculation of Fast Neutron Spectra and Associated Multigroup Constants*, GA-4265 (1963).

3.24 DISCRETE ORDINATES CALCULATIONS OF ANGLE-DEPENDENT NEUTRON SPECTRA IN ONE-DIMENSIONAL POLYETHYLENE AND GRAPHITE SPHERES[1]

F. R. Mynatt[2] L. R. Williams[2]
D. H. Wallace[2]

In order to demonstrate and verify the accuracy of the discrete ordinates transport method and to determine the usefulness of angle-dependent neutron-spectra measurements in evaluating cross-section data, selected experiments performed at the Gulf General Atomic Linac facility[3,4] have been analyzed using the ANISN[5] code.

The first experiment to be analyzed was for neutron transport in a paraffin sphere[3] for which previously reported calculations had shown unsatisfactory results, primarily due to insufficient capacity of the transport codes and computers that were used. The geometry of the ANISN calculation was composed of concentric spheres with dimensions given in Table 3.24.1. A unit source with a photofission spectrum was distributed in a 1-cm sphere about the origin. GAM-II[6] cross sections were used with 99 energy groups from 14.9 MeV to 0.414 eV and one thermal group for neutrons below 0.414 eV. The elastic scattering was represented by a P_3 Legendre polynomial in the laboratory system, while all nonelastic scatterings were assumed to be isotropic. An S_{48} full-range Gaussian angular quadrature was used in order to obtain an angular resolution equal to or better than the experiment for all detection angles. The running time on the IBM 360-75 computer for the ANISN calculation which converged each group to a maximum pointwise error of 10^{-4} was ~40 min.

Figure 3.24.1 shows a comparison of calculation and experiment for the straightahead (0°) angle at the surface of the sphere. Both the experiment and

Table 3.24.1. Geometry of Concentric Spheres

External Radius (cm) of Spherical Zone	Composition (atoms/cm^3) of Zone	Number of Intervals
3.81	^{235}U: 0.010406×10^{24} ^{238}U: 0.036894×10^{24}	14
3.85	Cu: 0.05512×10^{24} Ni: 0.03143×10^{24}	2
4.05	H: 0.0669×10^{24} O: 0.0334×10^{24}	2
4.13	Cr: 0.01574×10^{24} Mn: 0.00166×10^{24} Fe: 0.05717×10^{24} Ni: 0.00829×10^{24}	2
7.62	Void	7
38.1	H: 0.07798×10^{24} C: 0.03859×10^{24}	61

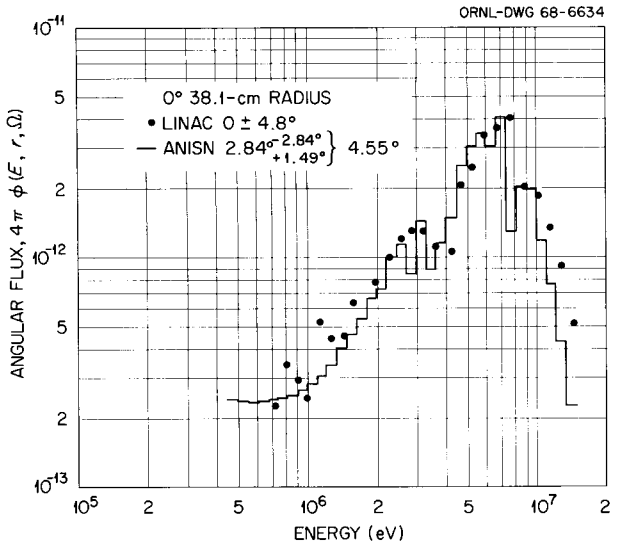

Fig. 3.24.1. Comparison Between Experiment and Calculation of Angle-Dependent Neutron Spectra for Paraffin Sphere at 0°.

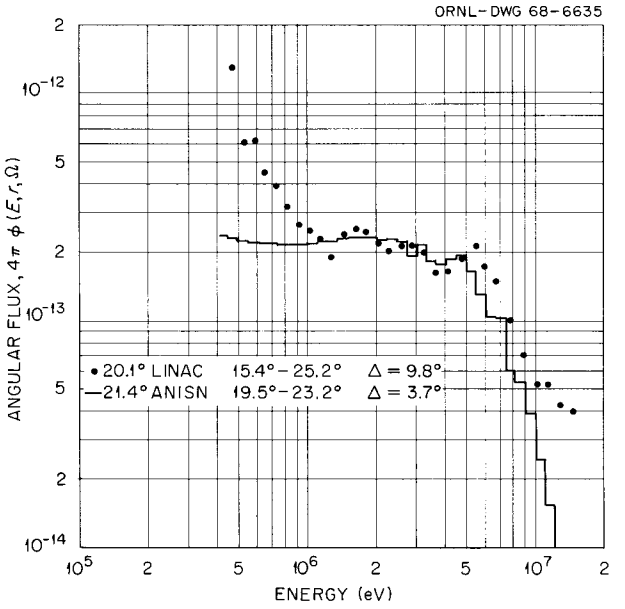

Fig. 3.24.2. Comparison Between Experiment and Calculation of Angle-Dependent Neutron Spectra for Paraffin Sphere at 20°.

calculation are normalized to 1 source particle/sec. Although the calculation extended to thermal, only the high-energy portion is shown in these comparisons. The agreement is good and the detail is adequate for the verification of the transport code. For a detailed study of cross sections, better resolution in the energy regions showing structure would be desirable. The high angular quadrature (S_{48}) was required in order to obtain sufficient resolution for the 0° measurement. An S_{16} quadrature is sufficient for the transport inasmuch as the scalar fluxes and angular moments of the flux agree with the S_{48} calculation.

Figure 3.24.2 shows the comparison for the 20° measurement. Experimental difficulties make this comparison valid only over the energy range from 1 to about 8 MeV.

A similar and somewhat more detailed study has been carried out for the infinite graphite experiment.[4] Since beam ports were used to obtain the flux at a specific angle and position in the interior of the graphite assembly, spherical symmetry may be assumed. The geometry of the ANISN calculation was composed of concentric spheres as in the paraffin calculation. The zones in the target assembly (up to the void) were the same as before. In this case the void was only 0.32 cm in width and contained only one interval. The graphite zone in the calculation extended from 4.45 cm to 96.5 cm

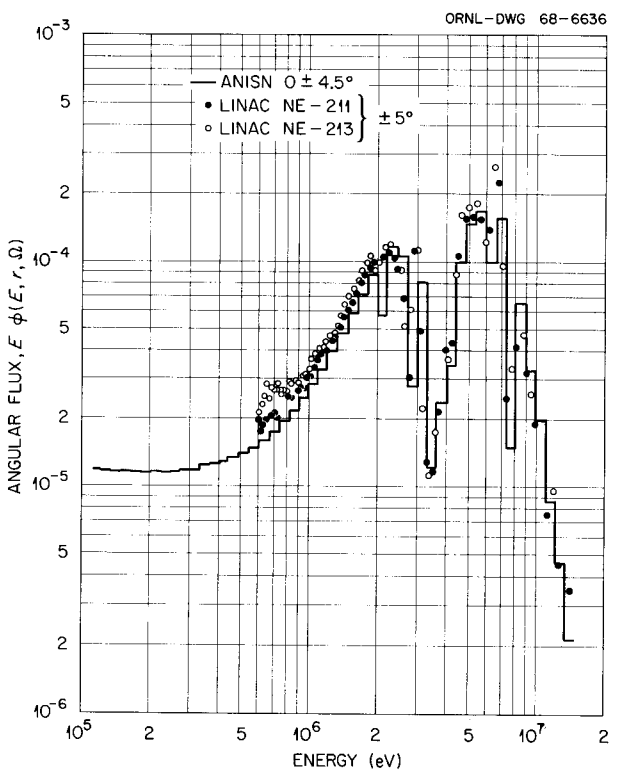

Fig. 3.24.3. Comparison Between Experiment and Calculation of Angle-Dependent Neutron Spectra for Graphite Configuration at 0°.

radius and contained 91 intervals. The density of carbon was 0.0828×10^{24} atoms/cm^3. The same source and 100 energy group structure was used as in the previous case.

Several calculations were performed using both GAM-II and ENDF/B cross sections for carbon. Figure 3.24.3 shows a comparison of experiment and an ANISN calculation using ENDF/B cross sections with a P_7 expansion for the elastic scattering. The agreement is remarkably good. A P_3 calculation with the same cross sections also varies only a few percent from the experimental data so that the selection of angular quadrature above P_3 cannot be shown to be more accurate. A calculation with GAM-II cross sections, however, is high by a factor of 1.5 above 9 MeV and in the 3.5-MeV valley and is low in all other energy regions by about 20%. The experiment is normalized to the calculation using a suggested[7] scale factor of 2.6×10^{-19}.

Work on these and other one-dimensional comparisons is continuing as new experimental data and cross-section improvements become available. The accuracy of the one-dimensional discrete ordinates code ANISN has been established; therefore, further experiments and comparisons of this type will serve only as good transport evaluation of cross-section data.

References

[1]Work funded by Defense Atomic Support Agency under DASA Task No. RRP-5037.

[2]Computing Technology Center, Union Carbide Corporation, Oak Ridge, Tennessee.

[3]A. E. Profio, *Comparison of Discrete Ordinates and Monte Carlo Calculations with Measurements of Fast-Neutron Spectra in Paraffin Shields,* AFWL-TR-66-153 (March 1967).

[4]A. E. Profio *et al., Measurements of the Neutron Angular Flux Spectrum in Graphite – Annual Report,* GA-7470 (October 1966).

[5]W. W. Engle, Jr., *A Users Manual for ANISN, A One-Dimensional Discrete Ordinates Transport Code with Anisotropic Scattering,* K-1693 (March 1967).

[6]G. D. Joanou and J. S. Dudek, *GAM-II: A B_3 Code for the Calculation of Fast-Neutron Spectra and Associated Multigroup Constants,* GA-4265 (1963).

[7]A. E. Profio, private communication.

3.25 DIFFERENTIAL NEUTRON AND GAMMA CURRENT ALBEDOS FOR CONCRETE[1]

R. J. Rodgers[2] F. R. Mynatt[2]

A unique version of DOT[3] has been developed for calculating neutron and gamma current albedos which are doubly differential in angle. The discrete-ordinates transport difference equations that were solved explicitly impose periodic top and bottom boundary requirements. Therefore for this particular application an infinite monodirectional parallel beam source on a concrete wall was simulated. The advantage realized by performing the calculation under these requirements is that the DOT[3] calculations can be immediately recognized as being one-dimensional in space, thereby significantly reducing the computing time for such problems.

DOT calculations were made of the energy and angle distribution of neutrons and gammas, emating from a 9-in.-thick steel-reinforced concrete slab for 5 incident source angles and for 21 incident neutron energy groups with a range of 15 MeV to thermal. The gamma distributions on the source surface resulted from the capture-gamma production in the concrete. The gamma energy groups ranged from 10 to 0.01 MeV and totaled 15 in number.

The reflected angular distributions are given in 30 discrete angles, which is typical of S_{10} discrete ordinates calculations, and the incident directions in polar angles of 17, 33, 47, 59, and 77° with reference to the normal of the concrete slab.

Comparisons of DOT calculations with 05R Monte Carlo results, reported by Coleman, Maerker, and Muckenthaler,[4] are shown in Figs. 3.25.1–3.25.3.

The energy group limits and the angles used in the DOT and 05R calculations are not identical; however, they are essentially of like structure and the results can be reasonably compared – e.g., compare the group limits of the source, the incident polar angles of the source, and the exit angles for the DOT and Monte Carlo exit energy distributions shown in Fig. 3.25.1. The polar angle was measured with respect to an inward normal to the slab, with the azimuthal angle being such that an exactly backward scattering of slant incident particle represents a ϕ_{out} of 180°.

Figures 3.25.2 and 3.25.3 show the resultant angular distributions after the incident neutrons in the same energy groups as in Fig. 3.25.1 have undergone energy degradation. It should be noted

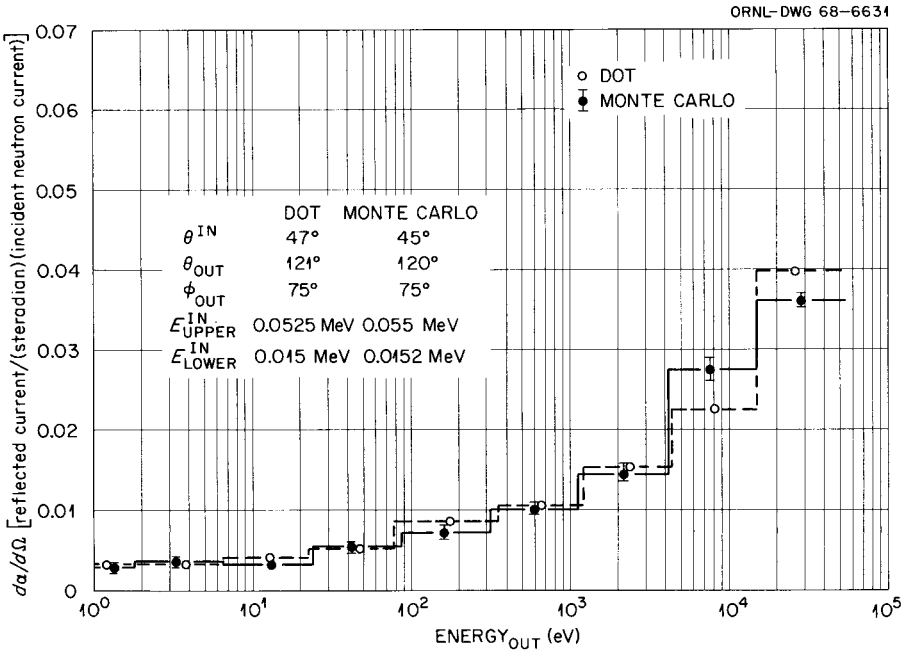

Fig. 3.25.1. Doubly Differential Angular Albedo vs Exit Energy for 9-in. Concrete Slab.

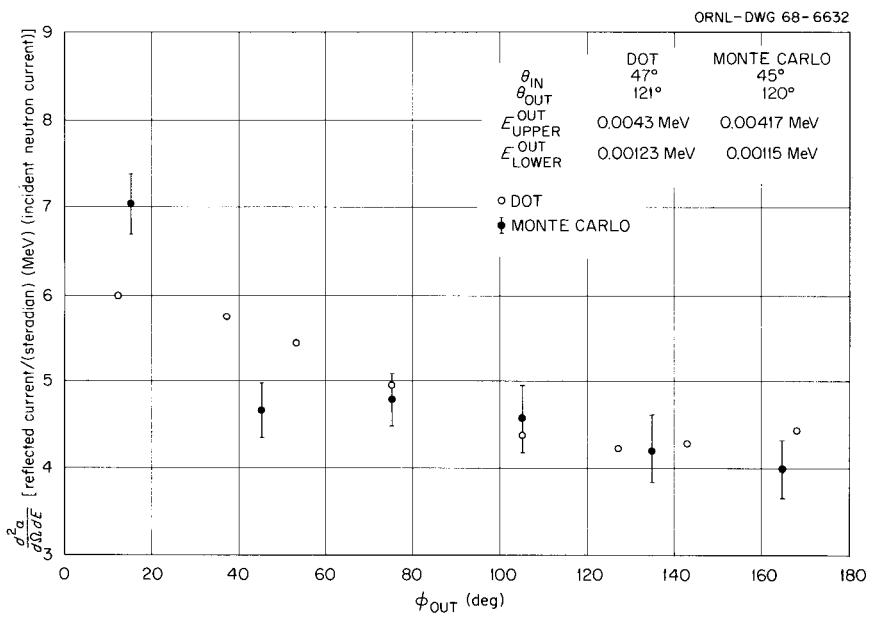

Fig. 3.25.2. Doubly Differential Angular Albedo vs Azimuthal Angle for 9-in. Concrete Slab.

that DOT does not lend itself readily to θ distributions for a given ϕ; hence only three DOT data points could be obtained for Fig. 3.25.3. The data are included merely for illustration in the comparison with Monte Carlo results, which are given with their standard deviation. The composition of the concrete is that given by Coleman, Maerker, and Muckenthaler.

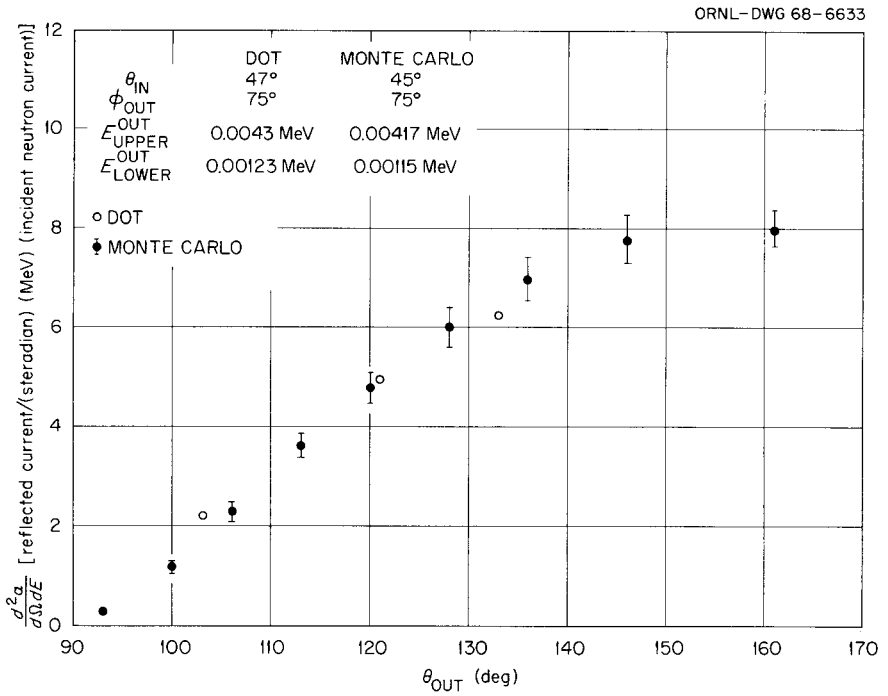

Fig. 3.25.3. Doubly Differential Angular Albedo vs Polar Angle for 9-in. Concrete Slab.

References

[1]Work funded by Defense Atomic Support Agency under DASA Task No. RRP-5037.

[2]Computing Technology Center, Union Carbide Corporation, Oak Ridge, Tennessee.

[3]F. R. Mynatt, *A User's Manual for DOT – A Two-Dimensional Discrete Ordinates Transport Code with Anisotropic Scattering*, K-1694 (to be published).

[4]W. A. Coleman, R. E. Maerker, and F. J. Muckenthaler, *Differential Neutron Current Albedos for Concrete in the Incident Energy Range 0.5 eV to 200 keV*, ORNL-3967 (1967).

3.26 DEVELOPMENT AND APPLICATION OF THE DISCRETE ORDINATES METHOD – MISCELLANEOUS PROJECTS[1]

F. R. Mynatt[2] L. R. Williams[2]
R. J. Rodgers[2] D. H. Wallace[2]

Analytic First-Collision Source for DOT[3]

The ray effect anomaly in two-dimensional discrete ordinates calculations has caused some concern[2] (Sect. 3.15, this report). In cylindrical *r-z* geometry irregular flux distributions are caused by preferential streaming along paths coincident with discrete η levels, where η is the direction cosine between the flux angles and the cylinder axis. The discrete angle sets are grouped in η levels, within which for several angles, η remains constant while the other direction cosines vary.

Although ray effects are always present to some degree, they are unimportant except when the source is highly localized (not distributed evenly throughout the system) and the mean free path (mfp) is long compared with the space mesh. The situation is at its worst for a point source in a void or low-density medium such as the atmosphere. An analytic first-collision source will thus help considerably. For points within 1 mfp of the source the analytic uncollided flux will dominate, and for points beyond 1 mfp the flux will be mainly due to neutrons that have suffered one or more collisions. Hence in both cases ray effects will be greatly reduced.

An analytic first-collision source technique has been developed for the two-dimensional code DOT. At present only point sources and monodirectional sources parallel with the *z* axis can be used. The

procedure of the technique is as follows:

1. The problem is described with the same space mesh and material zones as for the DOT problem.

2. The uncollided angular flux (magnitude and angle) is calculated for each space point and energy group.

3. The source array S, a function of radial interval I, axial interval J, moment L, and group G, is calculated with the expression

$$S(I,J,L,G) = \sum_{G'=1}^{G} \Sigma^l(G' \longrightarrow G)\, \phi_u(I,J,G')$$

$$\times P_l^m(\mu) \sqrt{2} \left[\frac{(l-m)!}{(l+m)!}\right]^{1/2} \cos(m\psi) ,$$

where $\Sigma^l(G' \rightarrow G)$ is the lth moment of the scattering cross section from group G' to G, ϕ_u is the magnitude of the uncollided flux, μ is the direction cosine with respect to the radius for the uncollided flux angle, $\cos(m\psi)$ is -1 for downward angles and $+1$ for upward angles, and L corresponds to a particular pair of indices l and m.

4. The source array S and scalar uncollided flux ϕ_u are written on magnetic tape.

5. DOT has been modified to use, as option, the anisotropic source array S as the fixed source. The result of such a calculation is collided flux distribution $\phi_c(I,J,G,D)$, where the arguments are as before except that D, for angle, is added. At the end of the calculation the scalar uncollided flux is added to the scalar collided flux, so that the total flux is printed in the DOT output.

The use of the analytic first-collision source technique has improved the results for point source problems (Sect. 3.15, this report) and has increased our understanding of ray effects.

Parametric Study of Simple Shadow Shields for SNAP Reactors

During the early part of the report year, prior to the development of a workable shield optimization code, a sequence of parametric calculations for simple shadow shields was performed. The shields were simplified right circular cylinder shadow shields with a diameter somewhat larger than the reactor diameter. The set of calculations were performed with the two-dimensional discrete ordinates code DOT and included two reactor core compositions and four core sizes for each composition. The shields consisted of four zones: 1 in. of tungsten followed by a thickness t_1 of lithium hydride followed by a thickness t_2 of tungsten followed by 12 in. of lithium hydride. The thickness t_1 was 9, 12, and 15 in., while t_2 was $3\frac{1}{2}$, $4\frac{1}{2}$, and $5\frac{1}{2}$ in., giving nine shields for each reactor type and size.

Thus 72 calculations were possible; however, early results indicated that many calculations could be omitted by using answers scaled from similar calculations. The study required more than 30 full calculations (30 neutron and 30 gamma). Each calculation contained 1500 to 2500 space points, used S_{10} (70 angles) quadrature, and included 21 energy groups for neutron cases or 18 groups for the gamma cases. For each calculation the total dose was calculated at four different gallery distances. The results of the study have been used to indicate the effect of reactor type and size on shield requirements and for gross optimization of the shields.

Calculations in Support of the NERVA Program

A study is in progress to determine the feasibility of using two-dimensional discrete ordinates calculations in the analysis of radiation transport problems for flight systems including a NERVA propulsion reactor and propellant tank. The study thus far has included calculation of the reactor power distribution, neutron transport, and primary and reactor secondary gamma-ray transport for the reactor-propellant tank assembly. Emphasis has been placed on investigating methods of coupling calculations for the reactor to calculations for the propellant tank.

References

[1]Work partly funded by Defense Atomic Support Agency under DASA Task No. RRP-5037.

[2]Computing Technology Center, Union Carbide Corporation, Oak Ridge, Tennessee.

[3]F. R. Mynatt, *A User's Manual for DOT – A Two-Dimensional Discrete Ordinates Code with Anistropic Scattering*, K-1694 (to be published).

3.27 THE DISCRETE ORDINATES METHOD – PROBLEMS INVOLVING DEEP PENETRATIONS[1]

F. R. Mynatt[2]

A generalized development of the discrete ordinates method is considered as a numerical technique for approximately determining a solution of the linear, energy-dependent, Boltzmann transport equation. Emphasis is directed toward time-independent problems involving deeply penetrating radiation, either neutron or gamma ray. The multigroup anisotropic discrete ordinates equation is derived from the analytic Boltzmann equation. A precise definition of the multigroup constants is presented, and the commonly used difference schemes are discussed. A general discussion is given on the applicability of the method and the behavior of the inner iteration process for deep-penetration problems. Two of the early checkout problems are presented, along with comparisons with moments method and Monte Carlo solutions. The first problem includes both one- and two-dimensional calculations of the fast-neutron dose in infinite water with a fission plate source. The second is a one-dimensional calculation of fast-neutron dose in a lithium hydride sphere with a point fission source.

References

[1]Abstract of p. 25 in *A Review of the Discrete Ordinates S_n Method for Radiation Transport Calculations*, ORNL-RSIC-19 (March 1968); work partly funded by Defense Atomic Support Agency under DASA Task No. RRP-5037.

[2]Computing Technology Center, Union Carbide Corporation, Oak Ridge, Tennessee.

3.28 COMPARISON OF TWO METHODS OF INNER-ITERATION CONVERGENCE ACCELERATION IN DISCRETE ORDINATES CODES[1]

W. W. Engle, Jr.[2] F. R. Mynatt[2]

Experience in using the discrete ordinates method, particularly in deep-penetration calculations, has demonstrated that the rate of convergence of the inner iterations is primarily dependent on two factors, the size of the nonsource region and the dominance ratio of the individual energy groups. A nonsource region is one containing no external source and no fission source. In general, the flux converges in a few iterations in or near source regions but, depending on the dominance ratio, may require several hundred iterations to converge at a point many mean free paths from the source. The dominance ratio may be expressed as the ratio of the number of particles which collide in the nth iteration to the number which collide in the $(n-1)$th iteration. As this ratio approaches unity, the rate of convergence decreases rapidly. The two effects are obviously coupled and indicate the desirability of a space-dependent acceleration technique.

In the usual discrete ordinates inner iteration the flux matrix is scaled by a single factor which effectively removes the within-group scatter error. Consider the following balance equation which is applicable to any group after n iterations:

$$L\phi^n + \Sigma_s\phi^n = S + \Sigma_s\phi^{n-1} , \tag{1}$$

where $L\phi$ is the loss rate, $\Sigma_s\phi$ is the within-group scatter rate, and S includes all sources external to the group. A single scale factor f is desired so that the following equation is satisfied:

$$f(L\phi^n) = S . \tag{2}$$

From Eqs. (1) and (2)

$$f = \frac{S}{S + \Sigma_s(\phi^{n-1} - \phi^n)} . \tag{3}$$

A more general approach is to seek a separate scale factor for each space interval. Restricting Eq. (1) to the ith interval yields

$$L\phi_i^n + \Sigma_s\phi_i^n = S_i + LL_i + LR_i + \Sigma_s\phi_i^{n-1} , \tag{4}$$

where LL is leakage into interval i across the left boundary and LR is leakage into interval i across the right boundary. Given a scale factor for each interval, the desired balance is described by

$$f_i(L\phi_i^n) = S_i + f_{i-1}LL_i + f_{i+1}LR_i . \tag{5}$$

Combining Eqs. (4) and (5) yields

$$-f_{i-1}LL_i + (S_i + LL_i + LR_i + \Sigma_s\phi_i^{n-1} - \Sigma_s\phi_i^n)\, f_i - f_{i+1}LR_i = S_i . \tag{6}$$

Writing Eq. (6) for each interval and applying appropriate boundary conditions leads to a tri-diagonal matrix equation which is readily solved for all f_i. In a modified inner iteration the flux in each interval is then scaled by the corresponding f.

As an alternative, the Chebyshev acceleration method[3] appears to be attractive since, as will be shown, the extrapolation factor depends on the dominance ratio. After each inner iteration the flux in each interval is extrapolated according to Eq. (7):

$$\phi'^{n} = \frac{2T_{n-1}}{\lambda T_n}(\phi^n - \phi^{n-2}) + \phi^{n-2}, \qquad (7)$$

where λ is the fundamental eigenvalue and the T's are Chebyshev polynomials.[3] In the discrete ordinates method the dominance ratio may be used as a first approximation to the eigenvalue λ.

Space-dependent scaling and Chebyshev acceleration were separately implemented in the ANISN[4] code. In the Chebyshev technique the effect of varying λ was studied, and in general it was found that the dominance ratio was within 3% of the optimum λ. In the cases studied use of the optimum λ resulted in a maximum of 10% fewer iterations when the dominance ratio was used.

Table 3.28.1 shows the results of an ANISN adjoint flux calculation through 3000 m of air using

Table 3.28.1. ANISN Adjoint Flux Calculation

Group	Dominance Ratio	Inner Iterations		Space-Dependent Scaling
		Standard	Chebyshev Acceleration	
1	0.850	254	121	40
2	0.856	241	116	15
3	0.887	294	123	16
4	0.862	140	70	11
5	0.890	266	115	13
6	0.922	357	122	20
7	0.922	328	114	17
8	0.909	256	99	17
9	0.932	270	89	32
10	0.897	146	58	34
11	0.707	29	20	9
12	0.671	36	24	15
13	0.425	13	11	9
14	0.473	18	15	9
15	0.423	13	11	8
16	0.399	14	13	9
17	0.429	17	14	9
18	0.393	15	13	7
19	0.332	9	9	7
20	0.344	10	9	8
21	0.416	16	14	9
22	0.428	17	14	9
23	0.417	16	13	9
24	0.319	13	12	7
25	0.320	14	13	7
26	0.380	17	15	8
		2819	1247	354
	Running time:	50.07 min	24.53 min	6.91 min

the standard iteration, Chebyshev acceleration, and space-dependent scaling. It should be noted that the flux in some groups decreased by more than 10^{30} between the source and the system boundary. Although this problem is unusually severe, it demonstrates the effectiveness of space-dependent scaling. Other problems with high dominance ratios and irregular flux shapes have been investigated and show similar results.

References

[1]Summary of paper to be presented at the Fourteenth Annual Meeting of the American Nuclear Society, Toronto, Ontario, Canada, June 9–13, 1968, and to be published in *Trans. Am. Nucl. Soc.* vol. II, No. 1 (1968); work partly funded by Defense Atomic Support Agency under DASA Task No. RRP-5037.

[2]Computing Technology Center, Union Carbide Corporation, Oak Ridge, Tennessee.

[3]L. A. Hageman, *The Chebyshev Polynomial Method of Iteration*, WAPD-TM-537 (January 1967).

[4]W. W. Engle, Jr., *A Users Manual for ANISN*, K-1693 (Mar. 30, 1967).

3.29 CSP-I: A NEUTRON CROSS-SECTION AVERAGING PACKAGE FOR USE WITH THE O5R DATA TAPE[1]

K. J. Yost N. M. Greene[2]

A code package, identified as CSP-I, has been developed for averaging cross-section data to be used as input to the S_n radiation transport codes. The code, designed to work from the O5R and ENDF/B data tapes, allows up to 200 energy groups with arbitrary boundaries and can accommodate up to a P_{15} approximation to elastic-scattering distributions.

References

[1]Abstract of ORNL-3140 (1967).

[2]Computing Technology Center, Union Carbide Corporation, Oak Ridge, Tennessee.

3.30 SHIELD ANALYSIS AND DESIGN SERVICE

H. C. Claiborne E. Solomito

The function of the Shield Design and Analysis Group is to give assistance in the design of radiation shields, either by solving specific problems or by recommending methods of solution. This has led to the development of new computer codes for use in design and to the improvement of these codes. (An example of the latter is the modification of the Los Alamos point-kernel code QAD-P5A.) In addition, close interaction with the developers of shielding codes is maintained in order to make them more aware of the user's problems and also so that new techniques can be applied to design problems with no delay. Such assistance in the past year has been given to a number of reactor and weapons projects at the Laboratory and at six other government agencies and contractors.

3.31 MODIFICATIONS OF THE POINT-KERNEL CODE QAD-P5A: CONVERSION TO THE IBM-360 COMPUTER AND INCORPORATION OF ADDITIONAL GEOMETRY ROUTINES[1]

E. Solomito J. Stockton[2]

The point-kernel code QAD-P5A, used for both neutron and gamma-ray shield penetration calculations, has been converted to FORTRAN IV language for use on the IBM 360/75 computer. The code has also been modified to use the generalized geometry subroutines of the O5R code, as well as special O5R subroutines for cylindrical and spherical geometries. With the increased speed of the IBM-360 computer and the ability of the generalized geometry to describe arbitrary shapes, the versatility of the code has been increased. Another modification has been the addition of a lithium hydride kernel for use in neutron calculations; the kernel was obtained from moments method calculations.

References

[1]Abstract of ORNL-4181 (in press).

[2]Mathematics Division.

3.32 CALCULATIONS OF NEUTRON FLUENCE-TO-KERMA FACTORS FOR THE HUMAN BODY[1]

J. J. Ritts[2] E. Solomito
P. N. Stevens[3]

Fluence-to-kerma factors (where fluence is the time-integrated neutron flux and kerma is equal to the total *k*inetic energy *r*eleased in *m*aterials by charged particles resulting from direct neutron interaction per unit mass of the irradiated medium) were calculated at discrete neutron energies from 0.045 eV to 15 MeV for various compositions in the human body – tissue, muscle, bone, lung, brain, red marrow, and the "standard man" composition. The calculations applied the latest cross sections for the 11 most common elements in man. A number of reactions were included which were not considered in previously reported work, namely, an anisotropic elastic-scattering correction, inelastic scattering, $(n,2n)$ reactions, $(n$, charged particle) reactions, and beta or positron emissions from these reactions. These calculations are improvements in the 10- to 15-MeV and 2- to 100-eV ranges over the neutron first-collision flux-to-dose conversion factors previously reported by Snyder.

References

[1]Abstract of ORNL-TM-2079 (Jan. 19, 1968).
[2]University of Tennessee, Knoxville (now with ORNL Reactor Division).
[3]Consultant from University of Tennessee, Knoxville.

3.33 CURRENT-TO-DOSE CONVERSION FACTORS FOR NEUTRONS INCIDENT ON PHANTOMS WITH ENERGIES OF 0.5 TO 13.5 MeV

J. J. Ritts[1] E. Solomito
P. N. Stevens[2]

Current-to-dose conversion factors for neutrons incident on various tissue phantoms have been calculated. Three phantom types have been considered: the 30-cm slab made up of an average tissue composition; the sphere representing the human skull, including brain, bone, tissue, and skin; and the cylinder representing the upper torso, including lung, bone, red marrow, tissue, and skin.

The calculations were performed using the S_n method to obtain the neutron and secondary gamma-ray flux distribution within the phantoms. The latest available cross-section data were used in the calculation, with particular attention given to the calculation of the secondary gamma-ray source and the subsequent gamma-ray transport. The calculations were performed for monoenergetic incident neutrons with energies in the range 0.5 to 13.5 MeV. Both isotropic and beam sources were considered in each calculation.

Analysis of the data for the spherical and cylindrical phantoms is under way. The data for the tissue slab have been analyzed and prepared as a series of graphs as typified in Figs. 3.33.1 and 3.33.2. In these figures the current-to-dose conversion factors for a 13.6- and 5-MeV neutron beam sources are shown as a function of depth in the tissue slab.

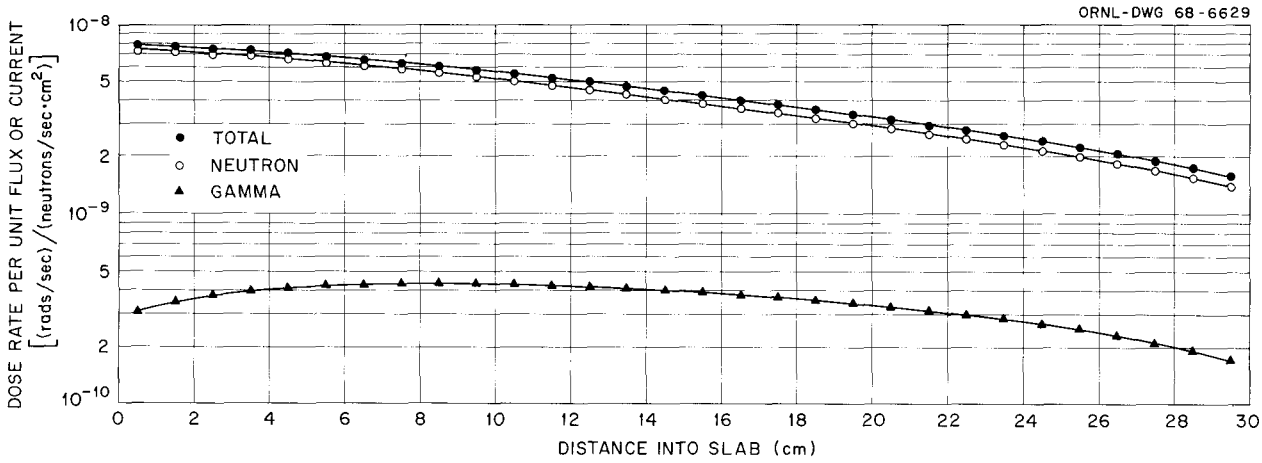

Fig. 3.33.1. Neutron Current-to-Dose Rate Conversion Factors for 13.6-MeV Beam Source.

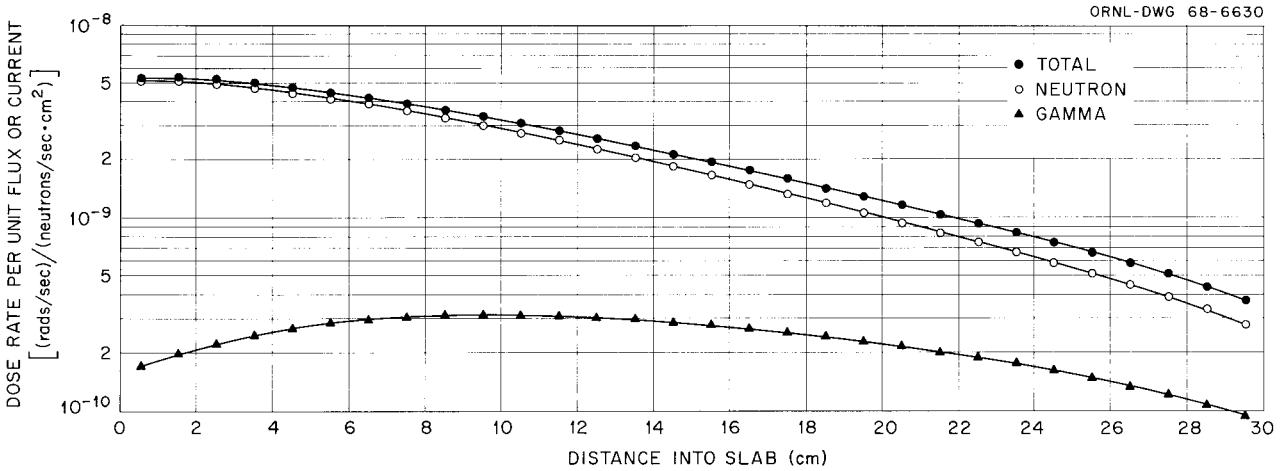

Fig. 3.33.2. Neutron Current-to-Dose Rate Conversion Factors for 5.0-MeV Beam Source.

References

[1]University of Tennessee, Knoxville (now with ORNL Reactor Division).

[2]Consultant from University of Tennessee, Knoxville.

3.34 SHIPPING CASK SHIELDING REQUIREMENTS

E. Solomito H. C. Claiborne

It has been found that the previously reported[1] point kernel technique using infinite-medium build-up factors for calculating the dose rate away from the surface of a shipping cask for radioactive materials is too far removed from the infinite-medium condition to give good results, since the detector actually sees the entire surface as a source. For calculating surface doses, however, this method gives good results because the infinite-medium condition applies approximately, particularly in the case of a lead shield for which backscattering will be small.

For calculations away from the surface, a method is required that will give not only the magnitude of the flux on the surface but also the angular distribution. At present, it seems that these requirements can be met quite well by using the S_n codes ANISN[1] and DOT[2] to calculate angular fluxes on the surface and the code SPACETRAN[3] to project the fluxes to points away from the surface. However, this procedure requires too much effort for survey calculations.

A proposed simpler method is to relate the dose away from the surface to the dose on the surface by means of a series of curves for various assumed angular distributions of the flux, the proper distribution being determined by experiment and/or theoretical studies. Curves for projecting the dose from cylindrical, circular, and rectangular surfaces are shown in Figs. 3.34.1–3.34.3. With the data obtained from the curves for a particular angular distribution, the dose at points away from the surface can be calculated if the dose on the surface is known. Angular distribution of the flux from the isotropic to the highly forwardly peaked $\cos^6 \theta$ has been calculated. Work is under way to determine the most appropriate distribution as a function of cask geometry and thickness.

As part of this program both the AARR and TREAT shipping cask designs have been evaluated for shielding effectiveness using the point kernel code QAD.[4]

References

[1]E. Solomito and H. C. Claiborne, *Neutron Phys. Div. Ann. Progr. Rept. May 31, 1967,* ORNL-4134, p. 73.

[2]W. W. Engle, *A User's Manual for ANISN,* K-1693 (Mar. 30, 1967).

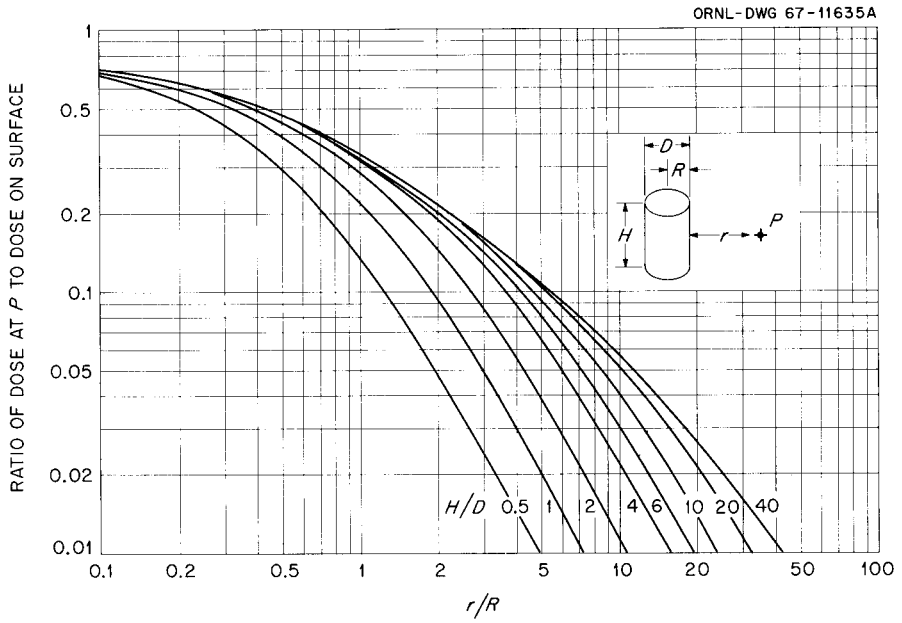

Fig. 3.34.1. Ratio of Dose at P to Dose on the Surface Based on Isotropic Flux Distribution on Surface.

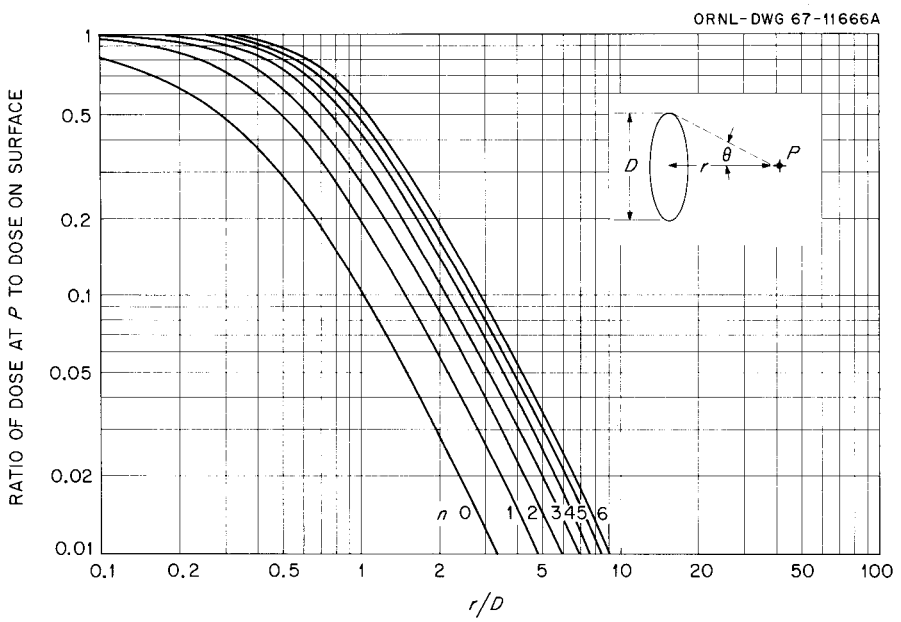

Fig. 3.34.2. Ratio of Dose at P to Dose on the Surface Based on $\cos^n$ Flux Distribution on Surface.

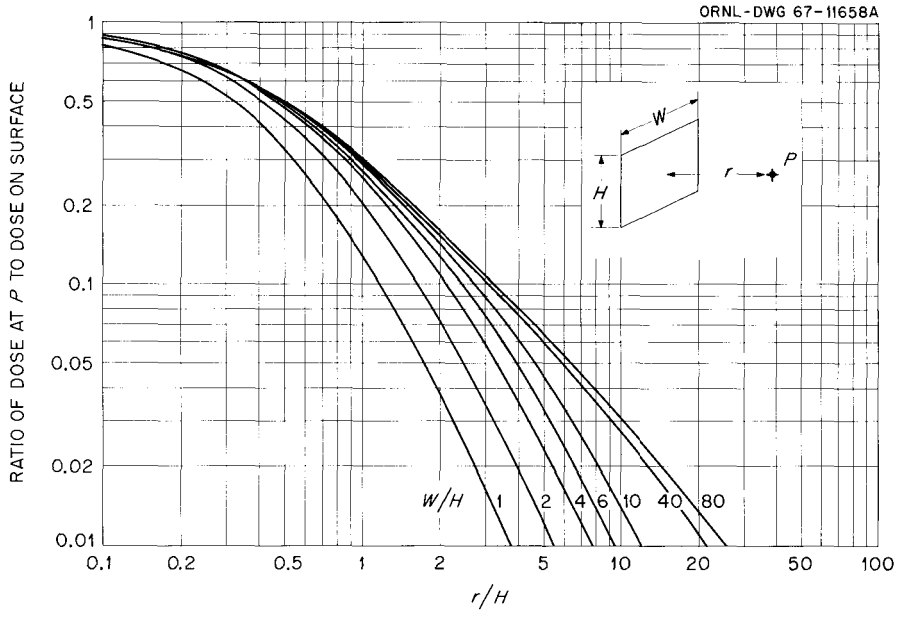

Fig. 3.34.3. *Ratio of Dose at P to Dose on the Surface Based on Isotropic Flux Distribution on Surface.*

[3]F. R. Mynatt, *A User's Code for DOT – A Two-Dimensional Discrete Ordinates Code with Anisotropic Scattering,* K-1694 (to be published).

[4]S. N. Cramer and E. Solomito, SPACETRAN, unpublished code.

[5]E. Solomito and J. Stockton, *Modifications of the Point-Kernel Code QAD-P5A: Conversion to the IBM-360 Computer and Incorporation of Additional Geometry Routine,* ORNL-4181 (in press); see also Sect. 3.31.

3.35 COMPARISON OF THE BUILDING PROTECTION FACTOR CODES CAPS-2 AND PF-COMP

M. L. Gritzner[1] P. N. Stevens[2]
H. C. Claiborne

The relative merits of computer codes PF-COMP and CAPS-2, which calculate radiation fallout protection factors for shelter areas, have been evaluated. Protection factors for various detector positions within five building designs of varying complexity were hand-calculated by the *Engineering Manual* method as outlined in the most recent revision. These results were then compared with machine-calculated protection factors using the PF-COMP and CAPS-2 programs.

As a result of the comparisons, some program errors were found in PF-COMP. They were corrected by the authors of the code, and the cases were recalculated. The PF-COMP code calculated protection factors in the 1 to 100 range for the five building designs to within about ±15% of the hand-calculated values. The protection factors calculated with the CAPS-2 code tended to be high and were within −44 to +90% of the hand-calculated values. For protection factors above 100, the PF-COMP code gave results that tended to be conservative and were within −41 to +36% of the hand-calculated values. In contrast, CAPS-2 results were found generally not be conservative, with the percentage error being anywhere from −10 to +58%.

Based on these considerations PF-COMP is judged to be the better of the two codes.

References

[1]University of Tennessee, Knoxville.

[2]Consultant from University of Tennessee, Knoxville.

3.36 SPECTRUM OF GAMMA RAYS EMITTED BY A STAINLESS-STEEL-CLAD POOL-TYPE REACTOR (BSR-II)[1]

G. T. Chapman W. R. Burrus[2]

Measurements of the pulse-height distribution of gamma rays observed as a function of position and

angle in the water shield of the Bulk Shielding Reactor II, a water-moderated and water-cooled pool-type reactor with stainless-steel-clad fuel plates, have been transformed to gamma-ray energy flux spectra by a computer program which removed the effects of the spectrometer's nonunique pulse-height response and accounted for the energy variation of the spectrometer's efficiency. The results show that photons above 5 MeV originate primarily from thermal-neutron capture in the components of the stainless steel. Gamma rays due to the ^{57}Fe component were identified as those known to be at 5.91, 6.02, and 7.6 MeV. Others were due to ^{58}Fe at 10.16 MeV, to ^{54}Cr at 8.88 and 9.72 MeV, and to ^{59}Ni at 8.53 and 8.99 MeV. Below 5 MeV the spectra consist of a strong contribution at 2.2 MeV from thermal-neutron capture in the hydrogen of the pool water, combined with a continuum presumably composed of prompt and delayed gamma rays following fission, lower energy components in the capture spectra from the stainless steel, scattering in the reactor or shield, and other lesser sources.

References

[1]Abstract of paper to be submitted to *Nuclear Science and Engineering* and to be published as ORNL-TM-1284.

[2]Present address: Tennecomp, Inc., P.O. Box J, Oak Ridge, Tennessee.

3.37 THE SPECTRUM OF PROMPT GAMMA RAYS ABOVE 1.5 MeV FROM FISSION OF ^{235}U[1]

R. W. Peelle W. Zobel
F. C. Maienschein

An extensive effort was made prior to 1962 to provide a definitive spectrum for the prompt gamma rays from fission of ^{235}U by thermal neutrons. The resulting spectrum above about 0.4 MeV was presented after a quick analysis,[2] while the spectrum later presented[3] for lower energies was merely the slightly modified pulse-height spectrum from a rather small NaI(Tl) scintillator. Spectral results are presented here for gamma rays above 1.5 MeV, within about 50 nsec of fission, corresponding to data obtained with the scintillation pair spectrometer described in ref. 2.

Altogether, about 45 pair spectrometer pulse spectra from fission and 10 from random background were combined, with their small gain differences taken into account, and their internal consistency was established. About three-fourths of this data was obtained after preparation of the 1958 paper,[2] but only a fraction of the data was obtained with a gain which allowed observation of gamma rays of over 5 MeV. A very careful study of the absolute pair spectrometer response was performed, and an interpolation formula was determined by least-squares fitting which adequately represented the observed pulse-height spectra for the available monoenergetic sources.[4]

The current work has included a careful recheck of the data handling and integration of the old response interpolation formula to yield the response functions for each of the final data pulse-height bins (44) as a function of gamma-ray energy (152 points). These response or bin sensitivity functions were used in the FERD unscrambling code of Burrus.[5] The code estimates outer limits to the two-thirds confidence intervals for the integral of the underlying gamma spectrum over any specified window functions.

Figure 3.37.1 shows the confidence intervals found for the high-energy regions of the spectrum, overlaid upon a smoothed version of the earlier[2] spectrum. The agreement is closer than had been expected, probably because of skillful (or lucky) guesses in the earlier analysis. The windows used for Fig. 3.37.1 were intended to duplicate closely the inherent line breadth of the pair spectrometer, but in some cases the confidence intervals will be narrowed by use of windows that adhere more faithfully to the line shape. At high energies the natural instrument resolution has been broadened by the combination of several pulse-height channels into bins; in general the resolution is about 1.4 times the spacing of the plotted points. The confidence intervals shown are largely statistically independent, but there is in addition a systematic uncertainty of $\sim$3% in corrections to the pulse spectrum and an incompletely evaluated uncertainty propagating from the absolute instrument response. The results shown for energies above about 2.5 MeV are final except for possible reduction of the window-fitting uncertainties and possible inclusion of response function uncertainties. For energies below 2.5 MeV the final results should be influenced by the analysis of the experimental pulse-height spectra from the Compton spectrometer.

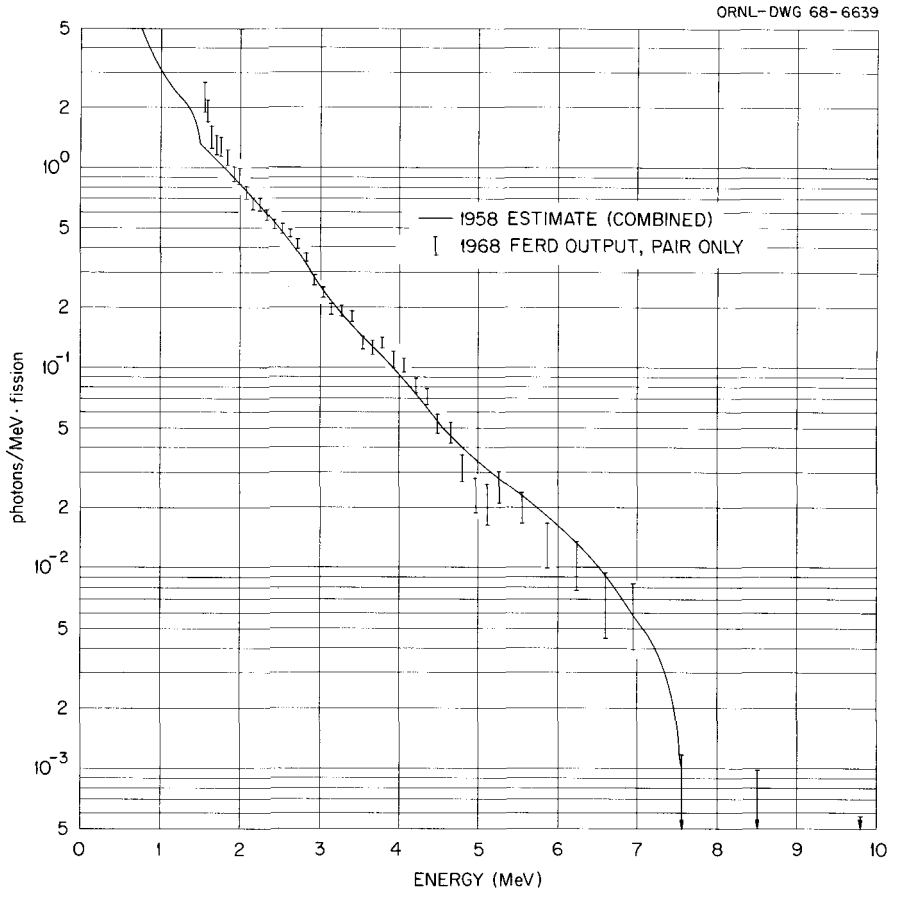

Fig. 3.37.1. Spectrum above 1.5 MeV of Prompt Gamma Rays from Thermal Neutron Fission of ^{235}U.

References

[1]Work funded through Los Alamos Scientific Laboratory.

[2]F. C. Maienschein *et al.*, *Proc. U.N. Intern. Conf. Peaceful Uses At. Energy, 2nd, Geneva, 1958* **15**, 366 (1958).

[3]R. W. Peelle *et al.*, p. 273 in *Pile Neutron Research in Physics,* International Atomic Energy Agency, Vienna, 1962.

[4]F. C. Maienschein and R. W. Peelle, *Neutron Phys. Div. Ann. Progr. Rept. Sept. 1, 1960,* ORNL-3016, p. 82.

[5]W. R. Burrus, *Utilization of A Priori Information by Means of Mathematical Programming in the Statistical Interpretation of Measured Distributions,* ORNL-3743 (June 1965); W. R. Burrus *et al., Neutron Phys. Div. Ann. Progr. Rept. May 31, 1966,* ORNL-3973, vol. 1, p. 61.

4. Radiation Shielding Information Center

4.1 RECENT DEVELOPMENTS IN RSIC OPERATIONS

D. K. Trubey Betty F. Maskewitz

The Radiation Shielding Information Center continues to serve the technical community engaged in radiation shielding research and development.[1] This community represents a wide variety of interests, as indicated by the fact that RSIC is supported by three agencies: the Atomic Energy Commission, the National Aeronautics and Space Administration, and the Defense Atomic Support Agency. The people served by RSIC generally have interests in parallel with or are doing work for one of those agencies.

The internal operation of the Center has changed markedly because of personnel reorganization. Until this year most of the computer code work, pertaining to both the code collection and information retrieval, was accomplished through contract services of the Union Carbide Computing Technology Center (CTC) at Oak Ridge. To effect more efficient operation and to cope with the constantly increasing load, four employees who had been doing RSIC work at CTC were transferred to ORNL. Three part-time information specialists have also been added to the staff. Two of them had formerly been performing such work under contract.

Evaluated Nuclear Data File

An important adjunct to any radiation transport computer code is the associated nuclear cross-section library. Unless continually updated and expanded, the library and hence the code which uses it tend to become obsolescent since improved cross-section data are constantly becoming available. Thus RSIC has been very interested, since the beginning, in the work of the Cross Section Evaluation Working Group (CSEWG) to provide evaluated data for neutron calculations for a generally accepted computer-oriented file. In 1967 a shielding subcommittee was formed. The work of this committee resulted in an extension of the format to provide for photon production and interaction cross sections[2] and the submission of several sets of data for the ENDF/B file. The work of the subcommittee is being continued, and is reported from time to time in the RSIC newsletter. It is anticipated that RSIC will work closely with the National Neutron Cross section Center at Brookhaven National Laboratory so that cross sections adequate for shielding calculations will be widely available in the shortest possible time.

Discrete Ordinates (S_n) Seminar-Workshop

A seminar-workshop, attended by approximately 100 specialists in radiation transport, was held at Oak Ridge in August 1967. The three-day meeting was co-sponsored by RSIC and CTC. Invited speakers included Bengt Carlson, Los Alamos Scientific Laboratory, Kaye D. Lathrop, Gulf General Atomic, and F. R. Mynatt, CTC. Other speakers from many laboratories also presented contributed papers, which were published in an RSIC report.[3] The first half of the meeting was used to evaluate the state-of-the-art of the discrete ordinates method for calculating radiation transport and the remaining time was used for a workshop in the use of the ANISN code, developed by CTC for the ORNL Neutron Physics Division and now available from RSIC.

DASA Shielding Handbook

The Defense Atomic Support Agency (DASA) gave permission for RSIC to reprint the first two

DASA Weapons Radiation Shielding Handbook chapters.[4–5] These reports are of general interest and merited a wide distribution. The third chapter,[6] co-authored by an RSIC staff member, was distributed by RSIC to its reactor-weapons shielding distribution.

Russian Shielding Review

In spite of a time lag and communication barrier it is apparent that a great deal of good shielding work is being done in the Soviet Union. In order to acquire an overall picture of this work RSIC undertook the task of reviewing the available Russian work since the last Geneva Conference (see Sect. 4.3). A development of special interest to RSIC is that a group in the Information Center on Nuclear Data at Obninsk produces shielding review articles for the Bulletin of the Center. Unfortunately, this section of the Bulletin is not routinely translated.

Literature Store

The three sets of literature files, reactor-weapons, space-accelerator, and computer codes, have continued to increase. The bibliography of computer code literature[7] was reissued. The space-accelerator indexed bibliography was also reissued[8] and the loose-leaf abstracts were updated.

European-American Committee on Reactor Physics Questionnaires

Questionnaires distributed on an international basis by the European-American Committee on Reactor Physics have been given to RSIC for collation and publication. Two types of data were collected: tests of reactor shields and experimental shielding facilities. The report is planned for issue in the third quarter of 1968 as ORNL-RSIC-24.

Code Center Operations

The computer codes collection[7,9,10] has continued to grow. As of April 30, 1968, nineteen additional programs have been processed, bringing the collection to 100 code packages ready for distribution. Approximately 12 more programs are in various stages of checkout and packaging.

The Center continues to provide computer tools directly to the individual scientist who performs radiation transport calculations.[10] Shipments to code users are averaging 1.3 packages per working day. Other information services connected with computer codes are performed at the rate of almost three per day. An analysis of the acquisitions and services of the Codes Center shows that most persons in need of RSIC services are engaged in government-connected work. Universities and foreign scientists also participate substantially in the information exchange.

RSIC continues to encourage participation in the codes section work by interested members of the shielding community. Eight individuals made several visits to the Codes Center to assist in checking out specific computer codes in which they were interested. Three individuals made visits to work with RSIC staff members to learn how to use a code.

Individual scientists at the contributing installations continue to assist RSIC in the acquisition of new programs. Members of the RSIC staff participated in a workshop-in-depth on seven specific codes at the originating installation.

RSIC is receiving increasing evidence of user support. Codes distributed by RSIC are often made compatible with computers other than those for which they were designed, and the new version is returned to be added to the code package. Interesting modifications to a specific code or errors discovered in usage are called to the attention of the RSIC staff. The concept of the "live" code package is basic to the RSIC philosophy of serving the shielding community. When a code is packaged, lines of communication are kept open with the contributor and with users. Proposed corrections, after being verified by the original contributor, and additions and modifications are made to the code package as long as the program is of interest.

References

[1]D. K. Trubey, Nuclear News **10**(1), 24–25 (1967).

[2]D. J. Dudziak, *ENDF/B Format Requirements for Shielding Applications,* LA-3801 (December 1967).

[3]D. K. Trubey and Betty F. Maskewitz, Editors, *A Review of the Discrete Ordinates S_n Method for Radiation Transport Calculations,* ORNL-RSIC-19 (March 1968).

[4]W. E. Selph and H. C. Claiborne, *Methods for Calculating Effects of Ducts, Access Ways, and Holes in Radiation Shields,* ORNL-RSIC-20 (DASA-1892-1) (January 1968).

[5]W. E. Selph, *Neutron and Gamma-Ray Albedos,* ORNL-RSIC-21 (DASA-1892-2) (February 1968).

[6]P. N. Stevens and D. K. Trubey, *Methods for Calculating Neutron and Gamma-Ray Attenuation,* DASA-1892-3 (March 1968).

[7]B. F. Maskewitz, V. Z. Jacobs, and J. Gurney, *Bibliography of the Computer Codes Literature Examined by the Radiation Shielding Information Center,* ORNL-RSIC-15 Rev. (July 1967).

[8]M. P. Guthrie, R. G. Alsmiller, and J. Gurney, *Bibliography, Subject Index, and Author Index of the Literature Examined by Radiation Shielding Information Center, Space and Accelerator Shielding,* ORNL-RSIC-11 (Rev. 1) (September 1967).

[9]B. F. Maskewitz, *Abstracts of Digital Computer Code Packages Assembled by the Radiation Shielding Information Center,* ORNL-RSIC-13, Vols. I and II (January 1968).

[10]B. F. Maskewitz and D. K. Trubey, *The Radiation Shielding Information Center Computer Codes Collection 1963–1967,* ORNL-TM-1956 (September 1967).

4.2 USE OF ICRU UNITS IN SHIELDING[1]

D. K. Trubey

The International Commission on Radiological Units and Measurements (ICRU) and the International Organization for Standardization (ISO) have offered definitions and made recommendations concerning nomenclature that should be adopted to the greatest extent possible in the shielding community. Because of the nuclear engineering context for shielding calculations and design, special problems have arisen. In order to help alleviate some of these problems, a review is presented along with recommendations. Some of these recomendations are controversial and do not represent a consensus of the many reviewers who have contributed to this work. These cases are identified.

Discussions are given of terms such as flux, density, dose, kerma, energy deposition coefficient, response functions, and buildup factors.

Reference

[1]Abstract of revised draft of ORNL-RSIC-16 (in press).

4.3 A SURVEY OF RECENT SOVIET RADIATION SHIELDING WORK[1]

J. Lewin J. Gurney

A literature survey of Soviet radiation shielding work is presented based on extraction from the RSIC reactor-weapons and space-accelerator literature files. These files have recently been supplemented with accessions from the Soviet literature. The publication period covered is the interval from 1964 through 1967, including the Third Geneva Conference of 1964. Based on the RSIC subject categories, compilations are presented of contributing authors, their publications, and abstracts. Selected extracts from recent publications are also included to illustrate the wide scope of Soviet work in shielding.

Reference

[1]Abstract of ORNL-RSIC-23 (in press).

4.4 COMPARISONS OF RESULTS OBTAINED WITH SEVERAL PROTON PENETRATION CODES – PART II[1]

W. Wayne Scott[2] R. G. Alsmiller, Jr.

Comparisons of the results obtained for a hypothetical problem with four different proton penetration codes have previously been presented in ORNL-RSIC-17. In this report, similar comparisons obtained with two additional proton penetration codes, CHARGE, written by J. R. Lilley and W. R. Yucker, and ASTROS, written by R. Wallace, P. G. Steward, and C. Sondhaus, which have been added to the code collection of the Radiation Shielding Information Center are presented. The hypothetical problem considered is to find the dose as a function of depth in tissue when a typical solar-flare proton spectrum is incident on a semi-infinite slab of aluminum followed by tissue and to find the dose as a function of depth when monoenergetic protons are incident on a semi-infinite slab of tissue.

References

[1]Abstract of ORNL-RSIC-22 (in press); work funded by the National Aeronautics and Space Administration under NASA Orders R-104 (10).

[2]Associate Professor of Physics at Chattanooga State Technical Institute and Consultant to RSIC.

4.5 ENERGY AND DOSE BUILDUP FACTORS FOR VARIOUS CONCRETES[1]

F. H. Clark D. K. Trubey

Buildup factors have been determined by moments method calculations for ordinary, magnetite, and barytes concretes. They agree well with approximate evaluations in the range 3 to 6 MeV. Outside that range, there is noticeable disagreement.

Reference

[1]Abstract of *Nucl. Appl.* **4**(1), 37–41 (1968).

4.6 COMMENTS ON BENCHMARKS, MILESTONES, AND TESTING IN THE AREA OF RADIATION TRANSPORT[1]

E. A. Straker D. K. Trubey

Several committees have been appointed to select benchmark problems to be used as standards in the area of radiation transport. A discussion of the aims of these committees is given in relation to proposed testing models. It is recommended that milestones representing the current state-of-art be identified from which, with further testing, benchmarks may be selected.

Reference

[1]Abstract of ORNL-TM-2148 (Mar. 22, 1968).

5. Radiation Detection and Data-Handling Techniques

5.0 INTRODUCTION

The Neutron Physics Division in carrying out its programs of experimental research has frequently been required to develop new instruments and methods of measurement. The papers in this section describe such investigations. (See footnotes 1–8 for specific section references.)

One search of long standing has been for a workable neutron spectrometer for determining energy spectra from shields in the fission range, that is, from ~1 to ~14 MeV. A bulk organic scintillator which combines moderate energy resolution, high sensitivity, and relative freedom from gamma-ray background has become a "standard" instrument for this purpose. Further development of this instrument continues,[1] and a new and promising method of discrimination against gamma rays has been investigated.[2] This scintillator is also useful as a detecting element in neutron time-of-flight systems. Use of this type of pulse-height spectrometer requires that the measured pulse-height spectra be converted to the desired energy spectra, a process which continues to demand attention.[3]

Nuclear physics experiments and shield spectral measurements have increased in sophistication so that they now almost universally demand complex data-handling systems centered about digital computers. The small computer forms the basic element for acquiring data from experiments at the cyclotron[4] and at the Van de Graaff.[5] A larger data-handling system[6] has been obtained for use with the new linear accelerator facility (ORELA) designed to produce pulsed neutrons for cross-section measurements using the time-of-flight technique. The laboratory part of this facility is literally centered about this data-handling equipment. The most massive of the many detectors to be used at the new facility is a liquid scintillation tank,[7] which will be used to detect the gamma radiation resulting from neutron capture or from neutron-induced fission. The use of photomultipliers as part of this detector requires a magnetic-field compensation system.[8]

References

[1]Sections 5.3, 5.4, 5.6, and 5.11.
[2]Section 5.5.
[3]Sections 5.7 and 5.8.
[4]Sections 5.9, 5.14, and 5.15.
[5]Section 5.13.
[6]Section 5.18.
[7]Section 5.17.
[8]Section 5.16.

5.1 RESPONSE FUNCTIONS FOR A 5- × 5-in. NaI(Tl) DETECTOR INSIDE A SIMPLE COLLIMATOR[1]

R. E. Maerker

An analysis of the data described in Section 5.2 was performed in order to obtain response functions for each of eight different source energies. The procedure involved the following steps:

1. matching up accurately the peaks that appeared in both the bare and cadmium-covered foreground counting rates,
2. interpolating the cadmium-covered foreground counting rates so that the interpolated values lie at mean energies deposited in the crystal that correspond exactly to the energies represented in the bare foreground run,
3. performing a point by point determination of the quantity

$$\text{net}\,(x) = (\text{counting rate})_{\text{bare}}\,(x) - 1.014\,(\text{counting rate})_{\text{Cd}}\,[x + y(x)]\,,$$

where x is the integral channel number for the bare foreground run $40 \leq x \leq 511$ and $y(x)$ is the channel shift between the cadmium-covered and bare runs, and which is in general of either sign and nonintegral,

4. determining the gain G as a function of x and the channel x_0 corresponding to zero energy by recognizing the peaks in the quantity calculated in step 3 and obtaining the best fit to $E(x) = G(x)\,(x + x_0)$,
5. repeating steps 1–4 for the background runs,
6. plotting the quantities calculated in step 3 as a function of E for both foreground and background runs, and interpolating the background counting rates so that they correspond to the same E values as the foreground counting rates,
7. obtaining a point by point value of the quantity net foreground (E) – net background (E).

For the 2.22-, 7.38-, 9.30-, and 10.83-MeV runs (the air "slab" was effectively 41 in. thick), the number of unscattered gamma rays incident upon the crystal was calculated by

$$N(E_0) = S(E_0)\,\Delta\Omega\, e^{-M(E_0)} \int\int_{\text{slab}} j_{\text{th}}(x,y)\, dx\, dy\ ,$$

where

$N(E_0)$ = incident gamma-ray current integrated over the front face of the crystal per 100 kw per 200 min,

$S(E_0) = \dfrac{I_\gamma(E_0)}{4\pi} \int_{\text{slab}} \Sigma_{n\gamma}\, \Phi_{\text{th}}(z)\, dz$, the number of secondary gamma rays of energy E_0 generated in the slab per steradian per incident thermal-neutron current, and in which

$I_\gamma(E_0)$ = probability of emission of gamma ray of energy E_0 per capture in the slab,

$\Sigma_{n\gamma}$ = Maxwellian-averaged macroscopic cross section for radiative capture in the slab at a temperature corresponding to a peak energy of 0.030 eV, in cm^{-1},

$\Phi_{\text{th}}(z)$ = thermal-neutron flux within the slab per incident thermal-neutron current,

$M(E_0)$ = mean free path of gamma rays of energy E_0 between the point of birth of the gamma ray and the front face of the crystal, $\int\int_{\text{slab}} j_{\text{th}}(x,y)\, dx\, dy$

= number of thermal neutrons incident on the slab per 100 kw per 200 min

$= 8.46 \times 10^{13}$,

$\Delta\Omega$ = the solid angle subtended by the front face of the crystal from the center of the slab

$= 3.41 \times 10^{-4}$ steradian.

Thus,

$$N(E_0) = 2.30 \times 10^9\, I_\gamma(E_0)\, e^{-M(E_0)} \times \int_{\text{slab}} \Sigma_{n\gamma}\, \Phi_{\text{th}}(z)\, dz\ .$$

A Monte carlo program was written to evaluate the integral appearing in $N(E_0)$. For the thin slabs used here, radiative capture of the unscattered thermal neutrons contributed approximately 80% of the total integral.

For the 1.37- and 2.76-MeV runs, $N(E_0)$ was calculated from the known decay rate of the ^{24}Na source and the decay scheme:

$$N(E_0) = 4.22 \times 10^6 \text{ photons of each energy per 200 min}\ .$$

To determine the absolute response functions in units of counts MeV^{-1} (incident unscattered photon)$^{-1}$, the values calculated in step 7 were divided by $N(E_0)\,\bar{G}(x)$, where $\bar{G}(x)$ is the gain averaged over all channels in MeV/channel.

Calculations of the absolute response functions were performed using a Monte Carlo code written by Zerby and Moran,[2] in which the 5-in. crystal was necessarily assumed to be suspended in space, so that collimator and polyethylene scattering effects were absent. Comparisons of the experimentally deduced response functions with the response functions calculated by the Zerby-Moran code may be summarized by referring to Fig. 5.1.1. In the low-energy Compton tail region the experimental responses are higher by factors of 2 to 8, presumably due to collimator and polyethylene scattering. In the vicinity of $E_0 = 2.76$ MeV the valley between the total absorption and first escape peaks is *lower* experimentally, which is probably due to inaccuracies in the code. Similarly, in the vicinity of $E_0 =$ 7 MeV, the second escape peak is overestimated by the Zerby-Moran code, again throwing doubt on the bremsstrahlung approximations used in the code. However, in general, the agreement in the vicinity of the total absorption and the first escape peaks

is remarkably good. In particular, as can be at least partially seen from Fig. 5.1.1, the absolute magnitude of the peaks agrees within ±10% for all six energies previously mentioned.

Since the first two peaks agreed so well, the relative response functions for 6.13 and 4.43 MeV (the latter had to be modified somewhat to account for less polyethylene scattering since it was experimentally determined using 10 in. instead of 2 in.) were normalized to the calculated values at the total absorption peak.

Figure 5.1.2 presents the response functions finally obtained. Some amount of guessing had to be done in the Compton tails for $E_0 = 7.38$ and 9.30 MeV, since the gamma rays due to incident epicadmium-neutron interactions dominated the low-energy region from 1 to 3 MeV in the case of lead, and other thermal-neutron capture gamma rays dominated the region below 8 MeV in the case of iron.

The response functions for source energies other than those shown in Fig. 5.1.2 may be obtained by an interpolation scheme identical to the one discussed last year for a 3- × 3-in. crystal.[3] The scheme is based on the fact that the response at $E_1 = E_0 - \Delta E$ is a slowly varying function of E_0 for a fixed ΔE, and may be calculated sufficiently accurately by interpolating between the values for the closest values of E_0 appearing in Fig. 5.1.2. This scheme suggests itself because the loci of the total absorption peaks, the valleys, the first escape peaks, and the second escape peaks all lie on curves that are slowly varying with energy. Thus, for example,

$$R(E_0 = 3.50,\ E_1 = 2.00) \cong \frac{0.74}{1.67} R(E_0 = 4.43,\ E_1 = 2.93) + \frac{0.93}{1.67} R(E_0 = 2.76,\ E_1 = 1.26)\ ,$$

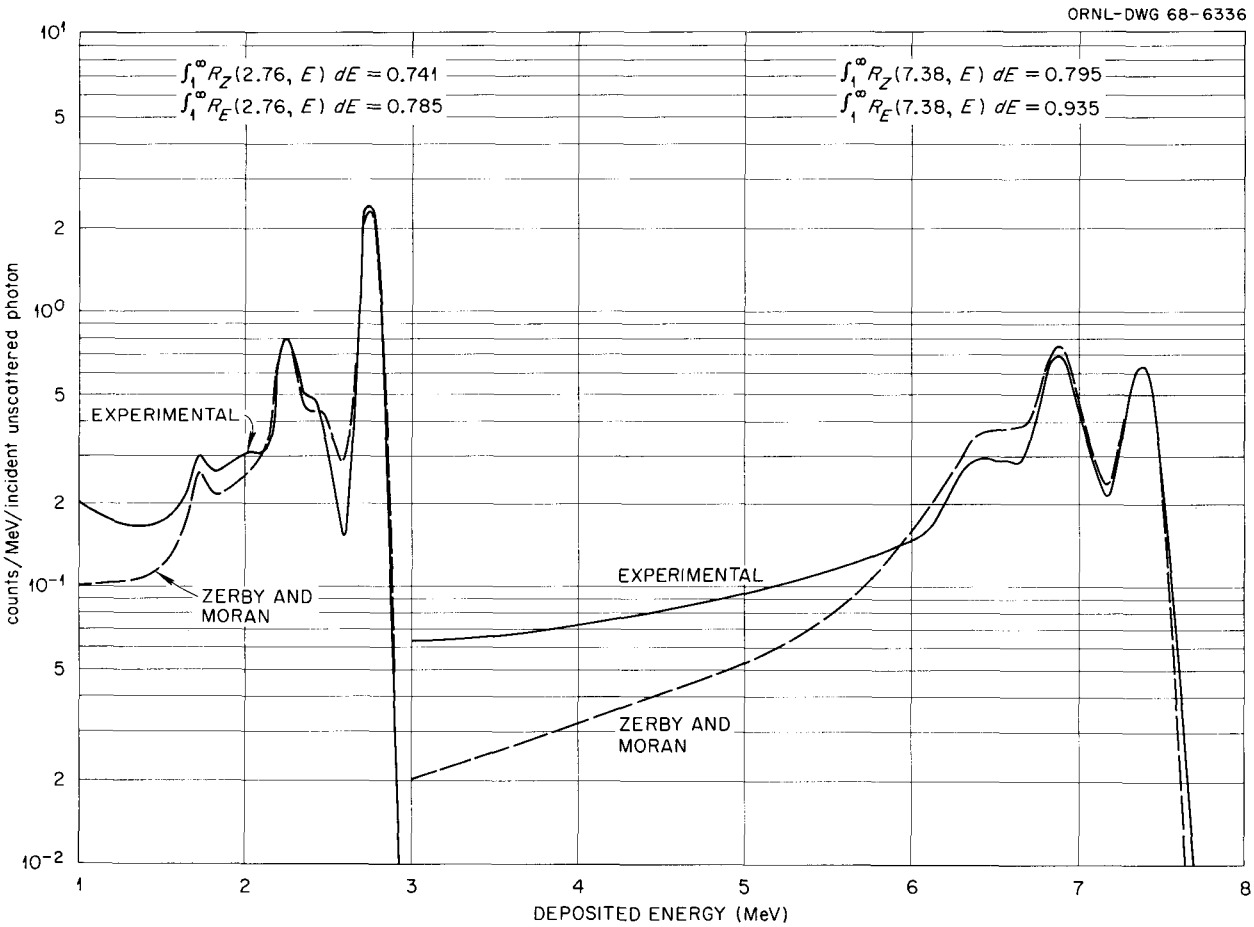

Fig. 5.1.1. Comparison of Experimental Responses for 7.38 and 2.76 MeV with Calculated Responses of Zerby and Moran (ref. 2).

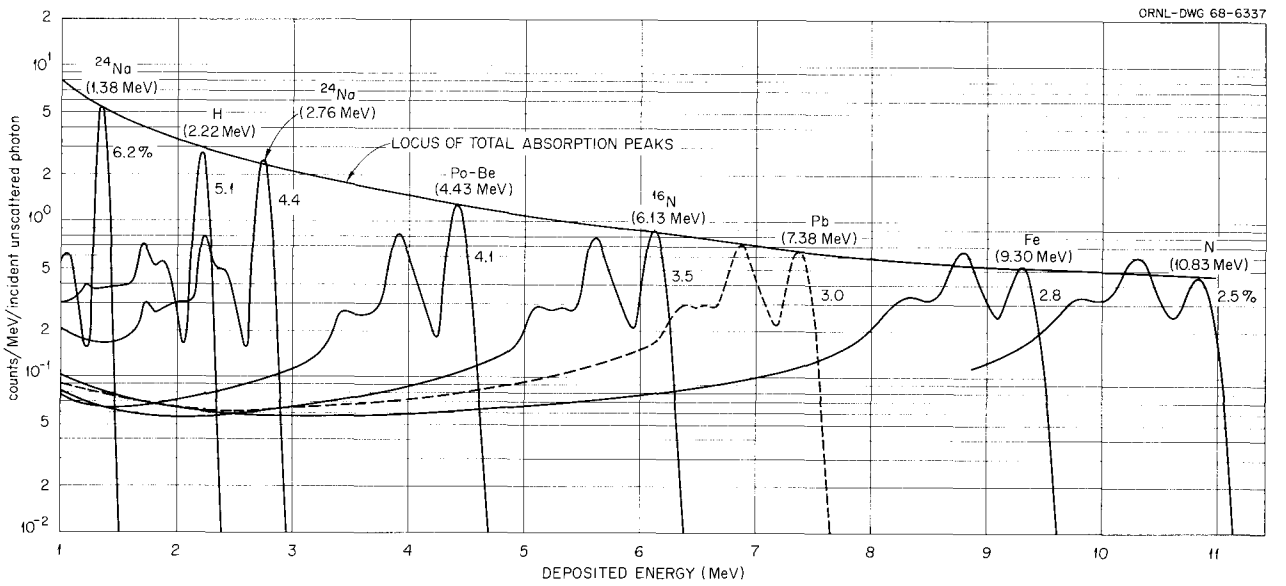

Fig. 5.1.2. Responses for a 5- × 5-in. NaI Crystal Preceded by 2-in. Borated Polyethylene in a Simple Collimator.

or, again,

$$R(E_0 = 7.72,\ E_1 = 7.00) \cong \frac{0.34}{1.92} R(E_0 = 9.30,\ E_1 = 8.58) + \frac{1.58}{1.92} R(E_0 = 7.38,\ E_1 = 6.66)\ .$$

It is believed that the response functions thus obtained have an accuracy of ±10%, except in the low-energy end of the Compton tail for $E_0 > \sim 7$ MeV, where they are not particularly important. Because of the nature of the interpolation scheme the response function for 1.38 MeV had to be extended down to $E_1 = 0.14$ MeV; and to include source energies between 1.0 and 1.38 MeV, a ninth response function for $E_0 = 1.0$ MeV starting at $E_1 = 0.62$ MeV was generated by the Zerby code and approximately corrected for collimator and polyethylene scattering effects.

A rigorous test of the response functions of Fig. 5.1.2 and the interpolation scheme just described is to compare the experimental response to a reasonably well-known complex spectrum with one calculated by folding the spectrum with the individual response functions. Such a spectrum is the one arising from thermal-neutron capture in iron or in nitrogen.

Both spectra were obtained, and we present here the results for iron. Figure 5.1.3 shows a comparison of the experimental response to two calculated responses. (The calibration peak at 9.30 MeV was omitted from this figure.) The first calculated response used a spectrum that is a compromise between the results of Bartholomew *et al.*[4] and of Orphan and Rasmussen.[5] This spectrum accounts for 93% of the binding energy in iron above 1.2 MeV, and 96% overall. The agreement between the calculated and measured responses is within ±10% almost everywhere, and except in the vicinity of 2.4 MeV the shapes are remarkably consistent. From this, together with a similar agreement for nitrogen, it is concluded that the response functions are sufficiently accurate for the spectral intensities lying within 0.5-MeV intervals to be deduced to within ±10%.

In Fig. 5.1.3 the second calculated response used a revised spectrum that best fits the experimental data. In general, only minor revisions in the original spectral intensities were necessary. The revised spectrum accounts for 95% of the binding energy in iron above 1.2 MeV, and 98% overall.

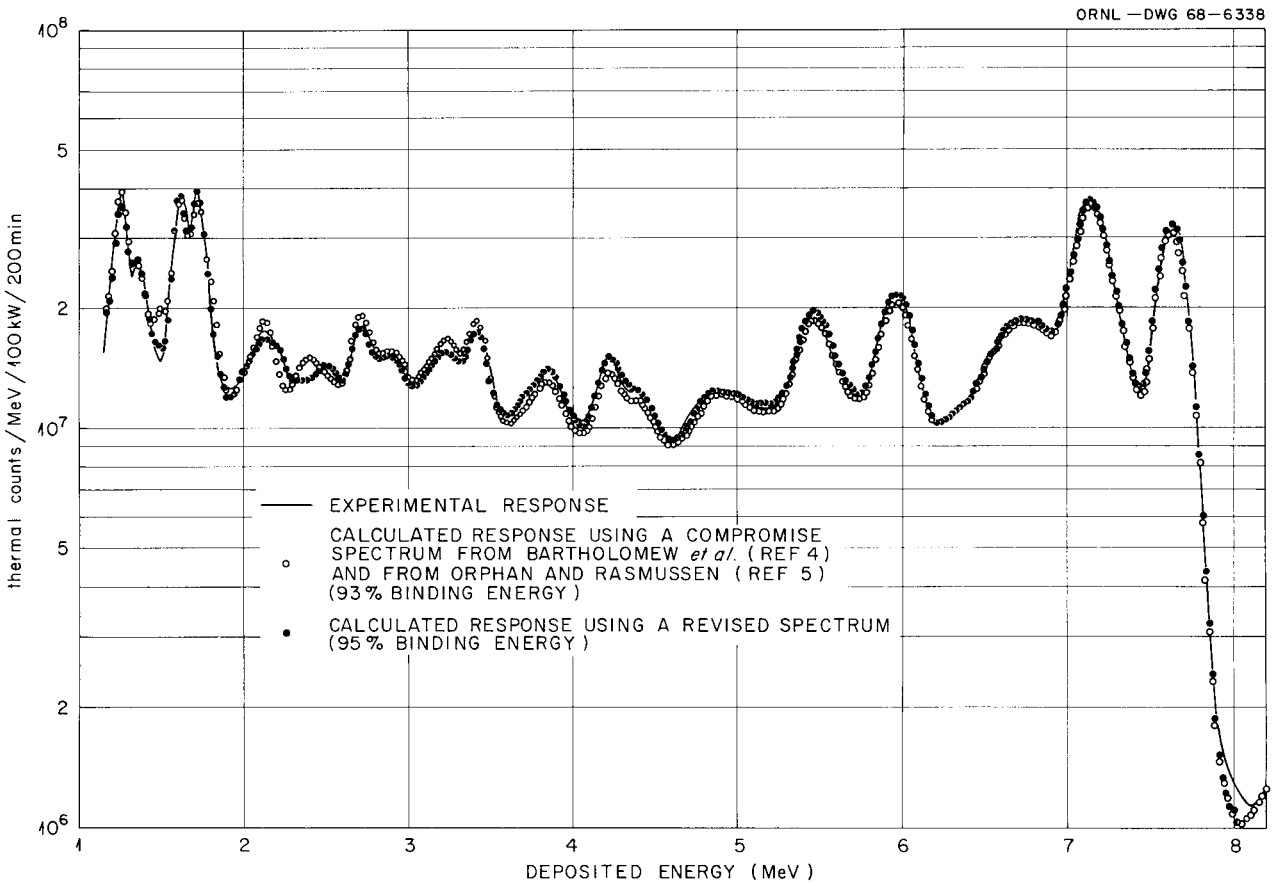

Fig. 5.1.3. Comparison of Experimental Response from $\frac{1}{16}$-in. Fe with Calculated Response Assuming a Compromise Spectrum from Bartholomew *et al.* (ref. 4) and from Orphan and Rasmussen (ref. 5) and Assuming a Revised Spectrum That Best Fits the Experimental Response.

References

[1]Work funded by Defense Atomic Support Agency under DASA Task No. RRP-5037.

[2]C. D. Zerby and H. S. Moran, *Calculation of the Pulse-Height Response of NaI(Tl) Scintillation Counters,* ORNL-3169 (1961).

[3]R. E. Maerker, *Neutron Phys. Div. Ann. Progr. Rept. May 31, 1967,* ORNL-4134, p. 68.

[4]As reported by G. A. Bartholomew *et al., Nucl. Data* **3A**, 367-650 (1967).

[5]V. J. Orphan and N. C. Rasmussen, *Study of Thermal Neutron Capture Gamma Rays Using a Lithium-Drifted Germanium Spectrometer,* AFCRL-67-0104 (1967).

5.2 DETERMINATION OF RESPONSE FUNCTIONS OF A 5-in. NAI CRYSTAL TO GAMMA RAYS WITH ENERGIES ABOVE 1 MeV[1]

F. J. Muckenthaler
J. L. Hull
J. J. Manning
K. M. Henry

A program has been initiated at the Tower Shielding Facility to determine experimentally a series of response functions for a collimated 5- by 5-in. NaI crystal exposed to single-energy gamma rays between 1 and 11 MeV. Gamma rays from radioisotopes and thermal-neutron capture in various slabs of material exposed to a collimated beam from the TSR-II were used as sources. Where possible, ma-

terials were chosen (1) to provide a single-energy gamma ray (due to thermal-neutron capture) so that these results could be used to accumulate a series of response functions, (2) to have a known cross section for the interaction, (3) to have a known number of gamma rays emitted per thermal-neutron capture, and (4) to provide a range of gamma-ray energies sufficient to provide extrapolated response functions needed. Other materials will be chosen to test the response functions and verify their validity.

The TSR-II was placed inside a spherical lead-water beam shield to provide a convenient means of collimating the neutron beam and at the same time to reduce the background as shown in Fig. 5.2.1. The collimator consisted of a cylindrical section $4\frac{1}{4}$ in. in inside diameter and 24 in. long attached to a conical section, $19\frac{1}{2}$ in. long on the reactor end of the collimator, which reduced neutron scattering in the collimator. The face of the reactor shield and the inside of the cylindrical section of the collimator were lined with cadmium to eliminate thermal-neutron scattering along the collimator walls and to reduce the number of thermal neutrons diffusing through the shield and reaching the sample. A 2-in.-thick lead disk was inserted in the collimator adjacent to the reactor vessel to reduce the gamma-ray intensity scattered by a sample of material placed in the beam. A 36- by 30-in. lead collar 8 in. thick and containing a 15-in.-diam hole was placed around the collimator opening to prevent capture gamma rays in the cadmium from reaching the detector. The thin slab sample of material was placed in the beam at an angle of 45° to the beam center line in the horizontal plane.

ORNL-DWG 68-6627

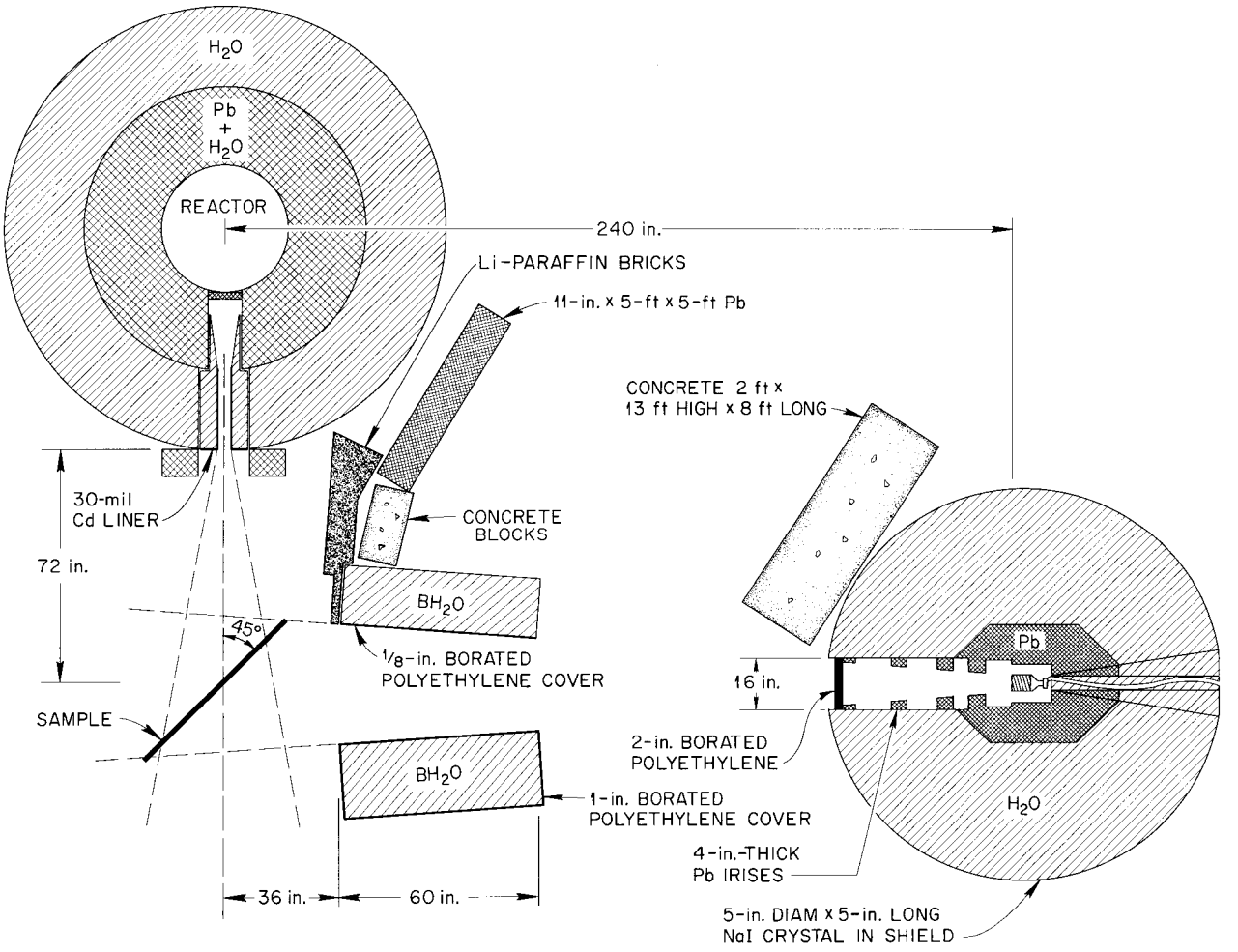

Fig. 5.2.1. Schematic Diagram of Geometry for Thermal-Neutron Capture Gamma-Ray Experiment.

A 5-in.-diam by 5-in.-long NaI crystal was located inside a spherical lead-water shield placed at an angle of 90° to the reactor beam center line (45° with respect to the slab normal) so that the detector looked at the beam emergent side of the slab. This geometry was chosen to minimize incidence of reactor capture and fission gamma rays on the crystal and to reduce to 0.5 MeV or less the energy of those gamma rays scattered by the sample to the crystal. The collimator consisted of a series of four 4-in.-thick lead irises spaced out to a distance of 51 in. from the crystal. The inside edges of the irises were beveled to provide a conical-shaped collimator, 5 in. in diameter at the crystal surface and 12.3 in. in diameter at the outer edge of the last iris. A 2-in.-thick borated (5.9 wt %) polyethylene slab was placed against the iris farthest from the crystal to minimize the thermal-neutron intensity incident on the crystal. The axis of the detector collimator intersected the axis of the center line of the reactor beam at a point 6 ft from the edge of the reactor shield. In this geometry the detector was 20 ft from the reactor beam center line, permitting the crystal to view the full width of a 5-ft-slab sample placed at the 6-ft point at an angle of 45° to the reactor beam center line (see Fig. 5.2.2). For measurements using air as the sample, two aluminum-walled tanks whose outer surfaces were covered with a 1-in.-thickness of borated (5.9%) polyethylene and filled with borated water. These tanks were placed on each side of the collimator cone, defined by the lead irises, between the detector shield and the nearest edge of the neutron beam profile. This substantially reduced the penumbra formed by the collimator and crystal and thus clearly defined that volume of air from which air-capture gamma rays reached the crystal with equal probability.

The profile of the thermal-neutron flux incident on the slab was mapped using a bare and a cad-

Fig. 5.2.2. Photograph of Experimental Arrangement.

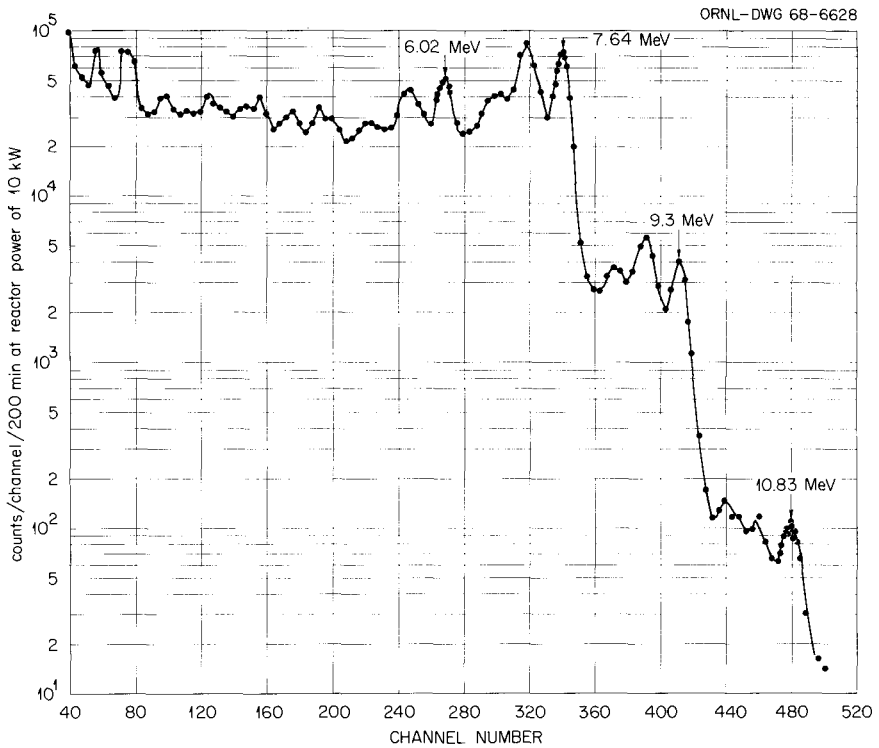

Fig. 5.2.3. Thermal-Neutron Capture Gamma-Ray Pulse-Height Spectrum for $\frac{1}{16}$-in. Iron Slab Sample.

mium-covered spherical BF_3 counter. Traverses were made perpendicular to the beam at the sample location, 6 ft from the end of the reactor collimator, in both the horizontal and vertical direction through the beam center line, and the intensity (bare-counter reading minus cadmium-covered-counter reading) under this profile was determined through integration. The profile of the beam was sufficiently collimated that it was completely intercepted by the slab oriented at 45°.

The relative response functions for the crystal were obtained using a Po-Be source (4.43 MeV) and the gamma ray from the decay of ^{16}N (6.13 MeV) in the reactor water. The energy scale of the pulse-height spectra was checked several times daily through the use of the 4.43-MeV gamma ray from the Po-Be source. The absolute response functions were determined using the decay gamma rays from ^{24}Na, and the thermal-neutron-capture gamma rays from hydrogen (2.23 MeV), lead (7.38 MeV), iron (9.30 MeV), and nitrogen (10.83 MeV).

Spectral measurements were obtained for slabs of $\frac{1}{4}$-in.-thick lead, $\frac{1}{16}$-in.-thick iron, and $\frac{1}{32}$-in.-thick polyethylene placed in the beam. The nitrogen gamma-ray data were obtained from the volume of air seen by both the reactor collimator and the detector collimator. To determine the pulse-height spectra due to thermal-neutron capture only, data were obtained with and without cadmium over the reactor collimator, with the samples in (foreground) and with the samples out (background) of the beam. In the case of nitrogen a background was taken with 8 in. of Li-paraffin followed by 8 in. of lead between the water tanks. A proper sequence of subtractions provided spectra of the gamma rays due to incident thermal-neutron captures only.

A typical pulse-height spectrum obtained from thermal-neutron capture in iron is shown in Fig. 5.2.3.

Reference

[1]Work funded by Defense Atomic Support Agency under DASA Task No. RRP-5037.

5.3 CALIBRATION OF AN ORGANIC SCINTILLATOR FOR NEUTRON SPECTROMETRY[1]

V. V. Verbinski[2] W. Zobel
W. R. Burrus[3] N. W. Hill[4]
T. A. Love R. Textor[5]

The absolute differential efficiency of a 4.60- by 4.65-cm-diam liquid organic scintillator, NE-213, was determined for nearly monoenergetic neutrons at 20 energies between 0.2 and 22 MeV incident on the curved side of the detector. These calibrations are shown to apply to an NE-211 scintillator as well. A 5-MeV Van de Graaff generator provided 2-nsec pulses of neutrons by means of $T(p,n)^3He$, $D(d,n)^3He$ (gas target), and $T(d,n)^4He$ reactions. With the aid of time-of-flight techniques and pulse-shape discrimination to eliminate spurious neutron and gamma-ray events, reliable pulse-height spectra were obtained for monoenergetic neutrons. The spectra were normalized to Monte Carlo calculations of absolute differential efficiency by utilizing the proton-recoil plateau. The accuracy of the Monte Carlo calculation was verified in the region of the proton-recoil plateau by absolute experimental calibrations carried out at neutron energies of 2.66 and 14.43 MeV and by using a scintillator geometry more suitable for such tests.

References

[1]Abstract of paper submitted to *Nuclear Instruments and Methods* and to be published as ORNL-TM-2183; work partly funded by the National Aeronautics and Space Administration under NASA Orders R-104(1) and L-12,186 and partly funded by the Defense Atomic Support Agency under DASA Task No. 06.515.

[2]Present address: Gulf General Atomic, P.O. Box 608, San Diego, California.

[3]Present address: Tennecomp, Inc., P.O. Box J, Oak Ridge, Tennessee.

[4]Instrumentation and Controls Division.

[5]Computing Technology Center, Union Carbide Corporation, Oak Ridge, Tennessee.

5.4 FAST-NEUTRON SPECTROSCOPY WITH THICK ORGANIC SCINTILLATORS[1]

W. R. Burrus[2] V. V. Verbinski[3]

A neutron spectrometer which utilizes a 4.60- by 4.65-cm-diam NE-213 liquid organic scintillator is described. Pulses due to gamma radiation are eliminated by the use of a modified Forté-type pulse-shape discriminator circuit. The FERDoR unfolding method and code are used to transform the measured pulse-height distribution into a neutron spectrum. This code produces an estimate of the neutron spectrum with a rigorous confidence interval. The effects of nonlinear scintillation characteristics, multiple scattering, and charged-particle reactions are all taken into account. The code is based on constrained minimization and utilizes the known nonnegativity of the neutron spectrum in obtaining the confidence intervals. The scintillator arrangement, the electronic circuit, and the FERDoR code are described. Typical results obtained by unfolding continuous and discrete line spectra are given. Satisfactory overall results were obtained with neutrons from 0.5 to over 16 MeV in a gamma-ray background of $\sim$5 mr/hr.

References

[1]Abstract of ORNL-TM-2225 (in press) and of paper to be submitted for publication in *Nuclear Instruments and Methods*; work partly funded by the National Aeronautics and Space Administration under NASA Orders R-104(1) and L-12,186 and partly funded by the Defense Atomic Support Agency under DASA Task No. 06.515.

[2]Present address: Tennecomp, Inc., P.O. Box J, Oak Ridge, Tennessee.

[3]Present address: Gulf General Atomic, P.O. Box 608, San Diego, California.

5.5 A PULSE-SHAPE DISCRIMINATION SYSTEM FOR USE WITH NE-213 ORGANIC SCINTILLATOR IN NEUTRON FLIGHT-TIME SPECTROSCOPY[1]

W. A. Gibson[2] R. T. Santoro

The problem of detecting neutrons in the presence of a gamma-ray background when using organic scintillators has received considerable investigation, and many techniques have been proposed for discriminating between the neutron and gamma-ray events in the detector. A brief discussion of some of these methods is given in a recent article by Johnson.[3] We have developed a pulse-shape discrimination system for use with organic scintillators which has the principal advantages of wide dynamic range, relatively simple operation, and visual "yes-no" display to indicate operation.[4]

The liquid organic scintillator NE-213 exhibits a difference in the time behavior of the light through two components with different decay times, both of which are approximately exponential and are produced by electrons, low-energy neutrons (through recoil protons), and alpha particles. These components are characterized by a fast component with a decay time of about 3 nsec and a slow component with a decay time of a few hundred nanoseconds. Love *et al.*[5] measured the fraction of the slow-to-total light for NE-213 as a function of detector bias and have shown that the fraction of slow light is typically 5% for electrons and ~20% for protons for detector bias values ~100-keV electron equivalent energy. The circuit described here performs discrimination by separately integrating the total-light pulse and its slow component and identifies the neutron or gamma-ray according to the slow-to-total light ratio.

Figure 5.5.1 is a block diagram of the instrumentation required for the pulse-shape discriminator. Radiation incident on the NE-213 produces light which is viewed by an RCA 6810 photomultiplier tube. (Any 12- to 14-stage fast photomultiplier tube with the earlier dynodes accessible will also work.) The pulse from the 14th dynode is detected by a fast discriminator which is set to detect low-level pulses from the photomultiplier tube and

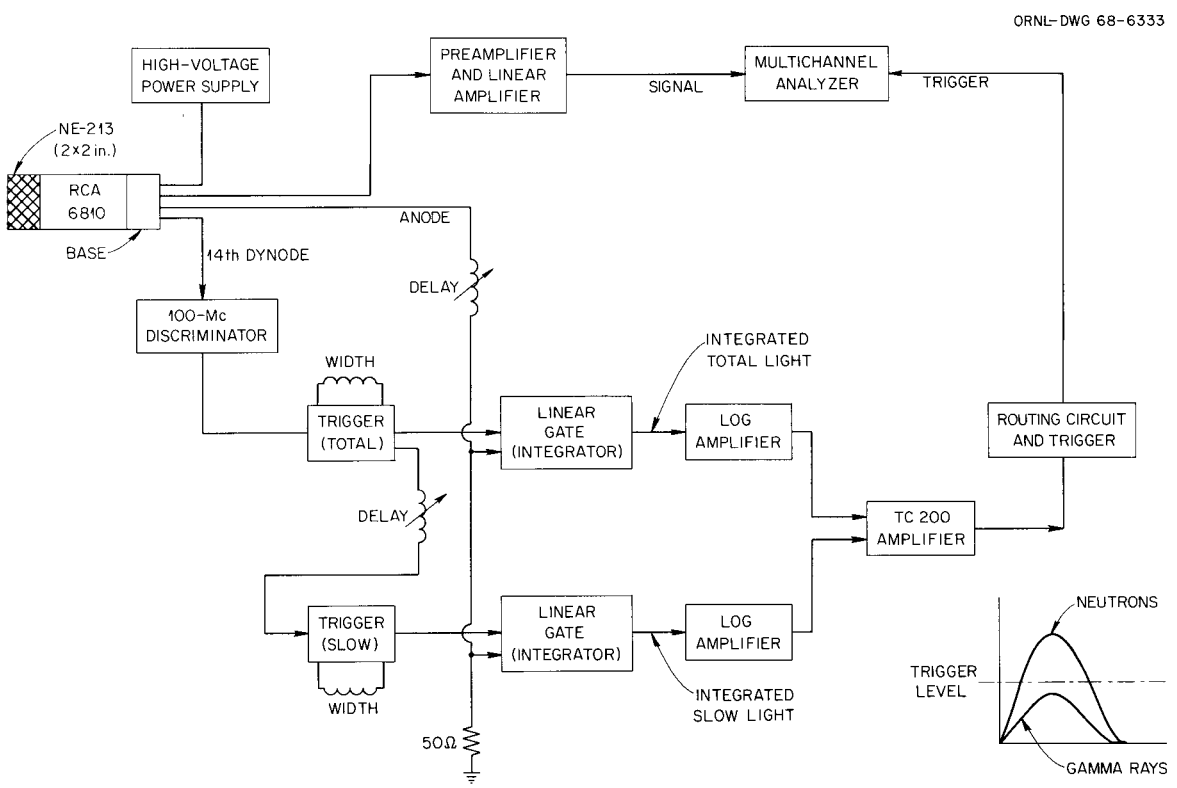

Fig. 5.5.1. Simplified Block Diagram of Pulse-Shape Discriminator.

whose logic level output is fed to a pair of trigger circuits. One circuit is adjusted to give an output pulse ~650 nsec wide, corresponding approximately to the time duration for 90% of the total-light pulse. The signal to the second trigger circuit is delayed by the time which gives optimum performance (~100 nsec), and the output pulse is adjusted to terminate in time with the pulse from the total-light trigger (~550 nsec). The outputs from these instruments are each used as gating inputs to a pair of Tennelec integrating linear gates,[6] which operate for the duration of these pulse widths. Simultaneously, the anode current pulse is delayed, split, and fed to the inputs of the gates. The first gate is opened before arrival of the anode pulse, permitting integration of the total-light pulse. Opening of the second gate is delayed, which prevents integration of the fast-light component but allows integration of the slow-light component. The outputs of two gates are the integral of the total and slow light. These signals are each fed to LASL four-decade logarithmic amplifiers.[7] The slow-to-total light ratios are obtained by taking the difference of the logarithmic signals at the differential input of a Tennelec TC-200 linear amplifier. Typical output pulses from the summing amplifier are shown in the inset of Fig. 5.5.1. These signals are fed to a differential discriminator and the pulses which exceed a trigger level set just between the distribution, as shown in the inset, are identified as neutrons. The relative amplitudes of these pulses are approximately 2:1, which is consistent with the values computed from the slow-to-total light ratios. Also shown in the block diagram is the linear channel circuitry used to obtain the pulse-height spectrum. Not shown, however, are the components used to obtain routing of the neutron and gamma-ray portions of the pulse-shape-discriminator output for gating the pulse-height analyzer.

The circuit has been tested extensively using neutrons and gamma rays from Am-Be sources and from the $T(d,n)^4He$ reaction. The results of these investigations are still being analyzed. However, the following data indicate the performance which has been observed.

Figure 5.5.2 shows the results obtained using 14-MeV neutrons incident on a 2- × 2-in. cylindrical scintillator in which the photomultiplier voltage was 1850 V. The ratio of neutrons to gamma rays (~4:1) is consistent with the data obtained using

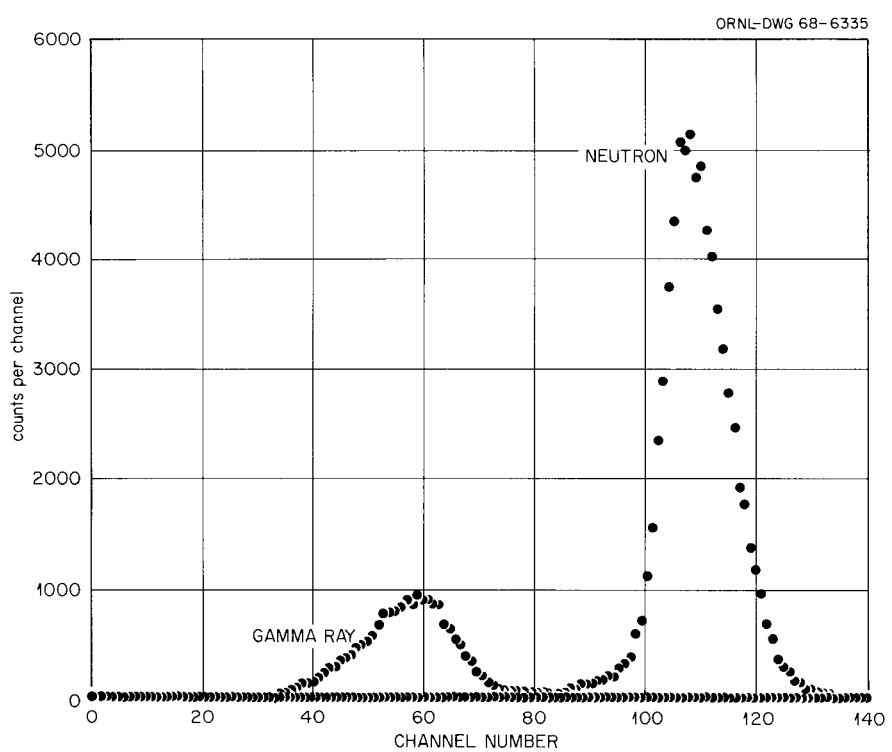

Fig. 5.5.2. Distribution of Pulses at the Output of Pulse-Shape Discriminator Circuit for 14-MeV Neutrons.

other pulse-shape discriminators.[8] What is of principal interest, however, is the wide separation between the peaks. For a bias setting midway beween the two peaks, the fraction of neutrons that can be confused with gamma rays is 0.5% or less. The wide separation also allows some uncertainty in the bias setting with only a slight change in performance. For this test, the dynamic range was measured to be ~50:1 for a lower threshold setting of ~180 keV electron equivalent. This preliminary analysis also indicates that good separation at much higher dynamic ranges can be effected.

References

[1]Work funded by the National Aeronautics and Space Administration under NASA Orders R-104(1) and L-12,186.

[2]Present address: Tennecomp, Inc., P.O. Box J, Oak Ridge, Tennessee.

[3]F. A. Johnson, *Nucl. Instr. Methods* **18**, 134 (1968).

[4]Mention is made of a somewhat similar system by M. G. Schomberg *et al.* in Paper SM-101/41 in *IAEA Symposium on Fast Reactor Physics and Related Safety Problems, October 30–November 3, 1967, Karlsruhe, Germany* (to be published).

[5]T. A. Love, R. W. Peelle, and N. W. Hill, *Neutron Phys. Div. Ann. Progr. Rept. May 31, 1967,* ORNL-4134, p. 96.

[6]We wish to thank Mr. Rainer Kurz of the Tennelec Instrument Company for suggesting the modification to the linear gates for conversion to integrators.

[7]We wish to thank Dr. B. Diven of the Los Alamos Scientific Laboratory for providing the logarithmic amplifiers. These instruments are described by J. S. Lunsford in *Rev. Sci. Instr.* **36**, 461 (1965).

[8]T. A. Love, private communication.

5.6 MONTE CARLO CALCULATION OF THE GAMMA-RAY RESPONSE OF AN NE-213 LIQUID SCINTILLATOR COUNTER[1]

V. R. Cain E. A. Straker
C. Y. Fu[2] P. N. Stevens[3]
F. J. Muckenthaler

The OGRE-G[4] Monte Carlo computer code has been modified to calculate the response of an NE-213 liquid scintillator to gamma rays. Photon histories are followed as in OGRE-G, and side trips are made to estimate the electron leakage spectra. Electron transport from the scintillator to the glass wall is calculated by a code provided by Moran.[5] Contribution to the scintillations process by electrons originated in the wall is estimated using the empirical formula of Mar[6] for electron energy transmission through slabs.

The liquid scintillator was assumed to be contained in a glass bottle of square-cylindrical shape, and the other assumptions used in the calculation were the following:

1. The response of the crystal was proportional to the energy deposited. The calculations were first carried out as if the crystal produced a sharp line in response to the energy deposition and the response spectrum was subsequently spread out by a Gaussian broadening. The energy dependence of the width of the Gaussian broadening was determined empirically from the present work.

2. In the transport of photons through the scintillator only Compton scattering takes place. Photoelectric events were highly improbable because photons escaped from the system before they were degraded to the energy range in which photoelectric events were significant. Pair production was ignored because it would at best contribute only a few percent of the total energy deposition even for source energies as high as 10 MeV.

3. In the transport of electrons through the detector, electrons do not cross the glass-liquid boundary more than one time. Actually an electron travels in a devious path and could cross the interface more than once. However, since the effects of these multiple crossings tend to cancel each other as far as energy deposition is concerned, this assumption should produce little error.

Figures 5.6.1 through 5.6.3 show comparisons of the calculated responses with the experimental data of Muckenthaler[7] for source energies from 0.66 to 6.13 MeV. The experimental data for ^{137}Cs, ^{60}Co, and ^{24}Na gamma-ray sources are presented in their absolute magnitudes. The source strengths of the 4.43- and 6.13-MeV gamma rays were not determined during the experiments. Therefore the response spectrum from 4.43-MeV gamma rays was adjusted to fit the magnitude of the computational results at the Compton edge (note that the calculated response spectrum was first broadened to give the same slope as the experimental data at the Compton edge). The experimental response spec-

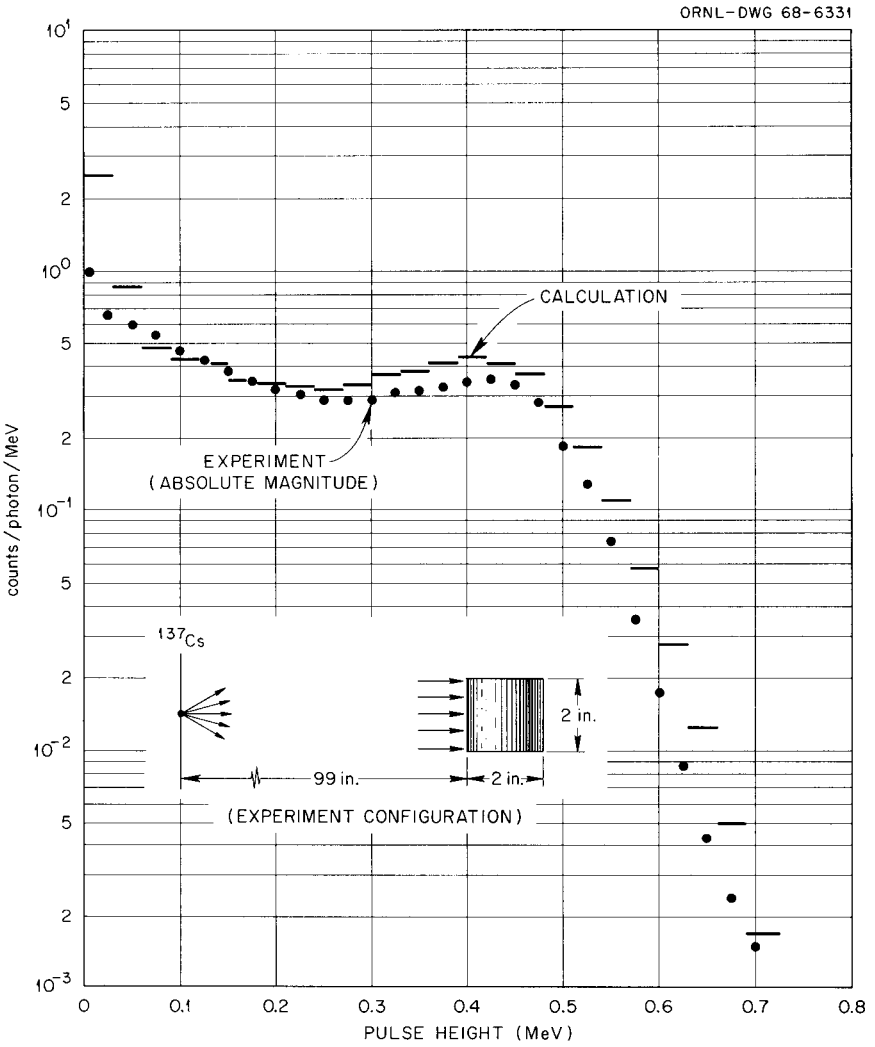

Fig. 5.6.1. Response Spectrum of NE-213 Scintillator Exposed to 0.66-MeV Gamma Rays.

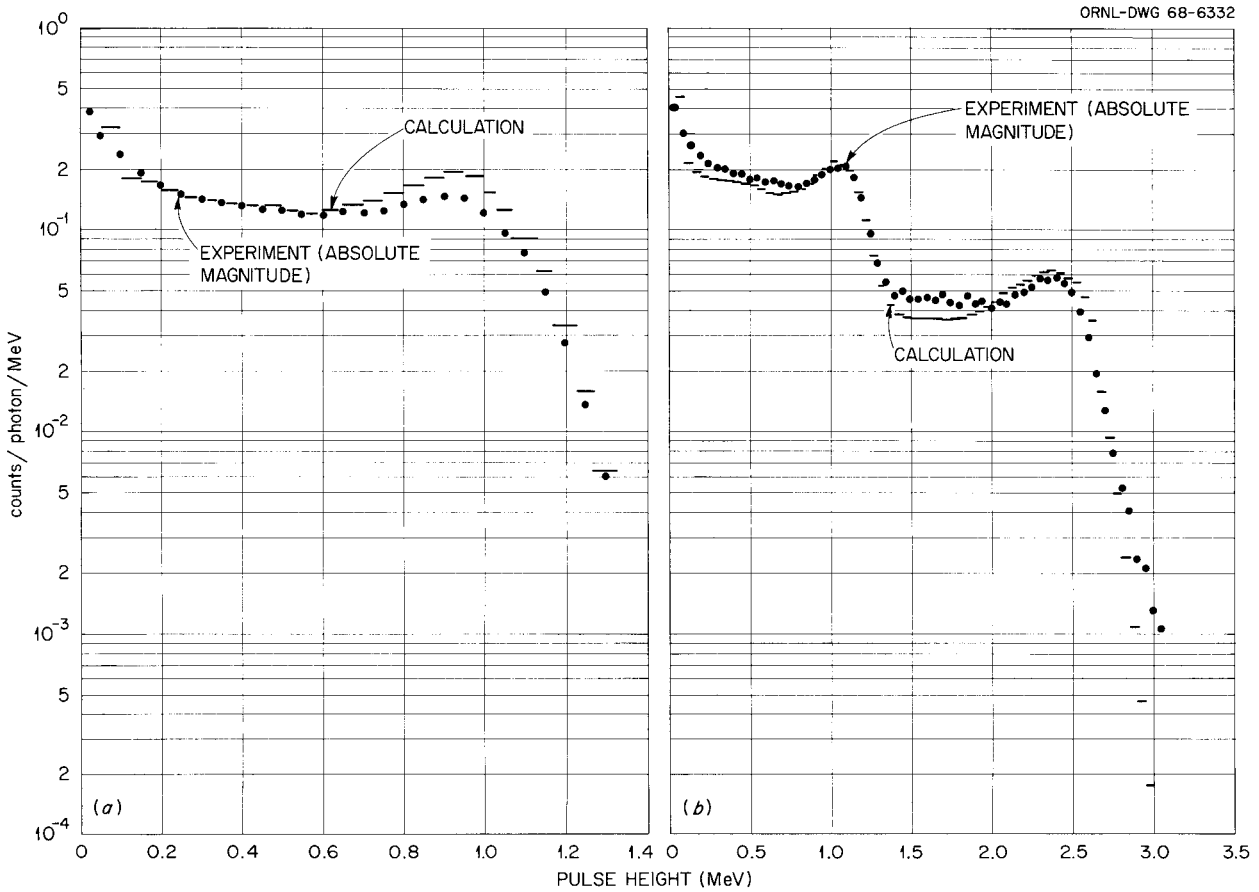

Fig. 5.6.2. Response Spectrum of NE-213 Scintillator Exposed (*a*) to ^{60}Co Gamma Rays and (*b*) to ^{24}Na Gamma Rays.

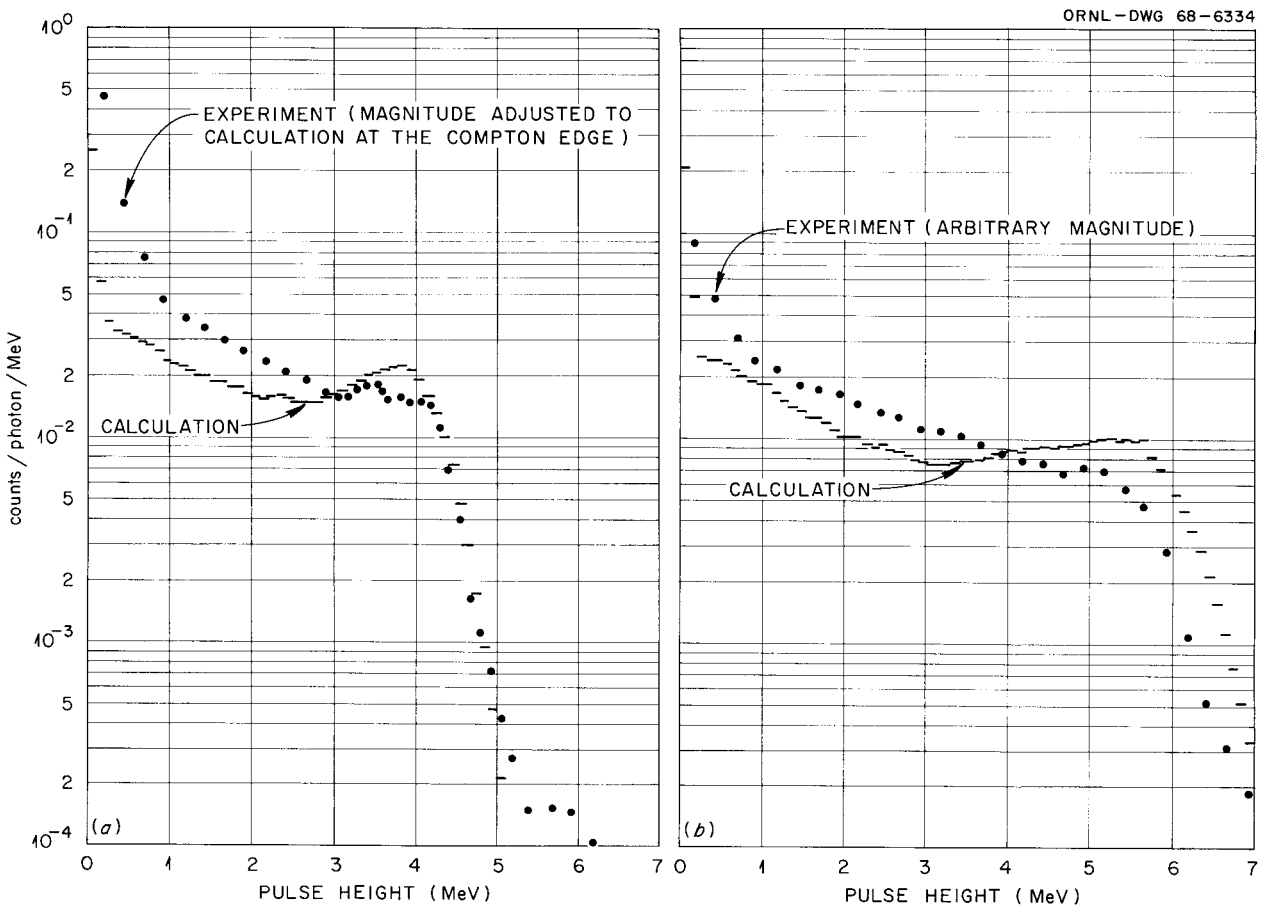

Fig. 5.6.3. Response Spectrum of NE-213 Scintillator Exposed (*a*) to 4.43-MeV Gamma Rays and (*b*) to 6.13-MeV Gamma Rays.

trum from the 6.13-MeV gamma rays was plotted with an arbitrary magnitude. Adjusting the experimental data to the calculated data at the Compton edge would have raised its Compton peak higher than that of the calculation, which would be unacceptable on a physical basis. Note also that the calculated response spectrum for the ^{60}Co source has been adjusted slightly to account for the contributions from two gamma-ray energies, 1.17 and 1.33 MeV.

The comparisons seem to be good for the ^{137}Cs, ^{60}Co, and ^{24}Na sources, but are open to question for the other two cases. Deviations between calculations and experiments in the valley of two peaks (Fig. 5.6.2*b*) and in the region of low pulse heights may be attributed to background effects in the experiments. The difference at the Compton edges from the 0.66- and 6.13-MeV sources indicates that the phosphor response of the scintillator may be nonlinear, but more data are needed to confirm this.

Present efforts are concerned with the formulation of a source-energy-dependent correction factor which would bring the calculated responses into better agreement with all the experimental data.

References

[1]Work partly funded by Defense Atomic Support Agency under DASA Task No. RRP-5037.

[2]University of Tennessee, Knoxville.

[3]Consultant, University of Tennessee, Knoxville.

[4]D. K. Trubey and M. B. Emmett, *OGRE-G, An OGRE Monte Carlo Code for the Calculation of Gamma-Ray Dose Rate at Arbitrary Points in an Arbitrary Geometry*, ORNL-TM-1212 (1966).

[5]H. S. Moran, private communication.

[6]B. W. Mar, *Nucl. Sci. Eng.* **24**, 193 (1966).

[7]F. J. Muckenthaler, private communication.

5.7 A DIGITAL FILTER FOR UNFOLDING PULSE-HEIGHT DISTRIBUTIONS[1]

Myron H. Young[2] W. R. Burrus[3]

A computer program has been developed which acts as a digital filter to remove undesired spurious features (such as Compton tails, escape peaks, etc.) from the response of a scintillation spectrometer. The input to the filter is the digital representation of the pulse-height distribution, and the output consists of a digital representation of the desired unfolded spectrum. A relatively clean Gaussian line is obtained from the filter. The filtering procedure is simple enough that small computers have been used on-line (or built-in circuitry can be used) to give rapid unscrambled results. Thus far we have demonstrated the capabilities of the filter up to 4 MeV both with a 3- by 3-in. NaI(Tl) gamma spectrometer (using data of Russel Heath) and with an 8- by 12-in. NaI(Tl) total-absorption gamma spectrometer. The program, written in FORTRAN-4 language, includes nonlinearity corrections and rigorous error estimates. The filter has been extensively simulated on off-line computers (IBM 7090 and CDC 1604), and we have a simplified working version for the PDP-8. The execution time for 128 channels for the IBM 7090 version is about 1 sec, and for the PDP-8 version is about 6 sec.

References

[1]Abstract of paper to be published in *Nuclear Instruments and Methods;* work partly funded by National Aeronautics and Space Administration under NASA Orders R-104(1) and L-12,186.

[2]Present address: Louisiana State University, Baton Rouge.

[3]Present address: Tennecomp, Inc., P.O. Box J, Oak Ridge, Tennessee.

5.8 SEGO, A COMPUTER CODE FOR UNFOLDING EXPERIMENTAL PULSE-HEIGHT DISTRIBUTIONS[1]

W. R. Burrus[2]

A mathematical unfolding procedure is described for unfolding scintillation pulse-height spectra to obtain an estimate of the incident energy spectra. The method reduces the amount of arithmetic required (compared with conventional matrix inversion) and simplifies the problem of constructing a model for the response of the spectrometer.

References

[1]Abstract of ORNL-TM-2172 (to be published).

[2]Present address: Tennecomp, Inc., P.O. Box J, Oak Ridge, Tennessee.

5.9 COUNTING TECHNIQUES FOR SMALL COMPUTERS[1]

B. W. Rust[2] W. R. Burrus[2]

This paper considers alternate strategies for accumulating nuclear counting data on small computers. Computers limited to short words do not provide enough capacity for a one-word-per-channel scheme and higher precision is wasteful of storage. Alternatives include storing differences between channels, treating overflows dynamically, and incrementing stochastically. Programming and display techniques are considered.

References

[1]Abstract of *IEEE Trans. Nucl. Sci.* NS-15(1), 117 (1968); work funded by the National Aeronautics and Space Administration under NASA Orders R-104(1) and L-12,186.

[2]Present address: Tennecomp, Inc., P.O. Box J, Oak Ridge, Tennessee.

5.10 A PROTON MICROSTRUCTURE MONITOR FOR NEUTRON MEASUREMENTS AT ORIC[1]

R. T. Santoro T. A. Love
J. W. Wachter J. K. Millard[2]
C. O. McNew[2]

A series of experiments are to be conducted at the Oak Ridge Isochronous Cyclotron to measure the yield and angular distributions of secondary neutrons produced from the interactions of 25-60 MeV protons with nuclei (Sect. 7.6, this report). A time-of-flight spectrometer will be used in obtaining the neutron data. To determine the overall timing resolution of the spectrometer, the average time distribution of the protons incident on the target must be known. These data, along with instrumental timing errors, define the energy resolution for each path length. A proton microstructure monitor has been developed to measure this distribution for approximately 60-MeV protons and will be used to monitor the burst width in subsequent experiments.

Figure 5.10.1 is a simplified block diagram showing the instrumentation used in the measurement. Protons are injected into the ion optic system from the cyclotron at a repetition rate, f_{rf}, corresponding to the rf acceleration frequency. To increase the time between bursts and thereby extend the range of neutron flight times having no time overlap for a given flight path, a beam deflection apparatus is employed.[3] The deflector consists of a pair of plates 1 in. wide and 3 ft long on which an rf voltage is applied at one-seventh of the fundamental frequency.[4] The low frequency signal is phased with f_{rf} so that one beam burst in seven is allowed to pass through a collimator slit on the node of the deflector rf signal. In this test the undeflected proton burst passed through a 153° analyzing magnet and was incident on a 6-mil-thick aluminum foil at the terminus of the beam pipe. A timing signal was established by forming a coincidence between the pulses derived from the "fast" and "slow" rf frequencies.

Protons scattered from the aluminum foil were intercepted by a 0.5-cm-diam by 1-cm-thick plastic scintillator viewed by an RCA C-70045 photomultiplier tube. For these measurements the detector was placed at an angle of 20° ~15 cm from the aluminum foil. At this angle the differential elastic-scattering cross section for protons on aluminum is $\sim 10^3$ mb/steradian. The anode signal of the photomultiplier tube was fed to a pair of fast discriminators. One is a differential discriminator adjusted so that a window is set over the elastic peak of the scattered proton spectrum. The other is an integral discriminator which fires at ~50 mV on the leading edge of the anode pulse. The outputs from these instruments were placed in coincidence with the integral discriminator gating, and the resulting signal was used as the start pulse for a time-to-amplitude converter (TAC). The TAC stop signal was derived from the fast-slow coincidence, with the timing delays adjusted so that the start-stop pulse pair was related to the same rf burst.

The time distribution of seven adjacent proton bursts corresponding to extraction on each cycle of the 22.4-Mc fundamental frequency was studied. These data were obtained with no driving voltage on the beam-sweeper deflector plates. Since the frequency of the slow rf signal was one-seventh of the fundamental frequency, the time between stop signals was 308 nsec (the time between bursts was 44 nsec, corresponding to $1/f_{rf}$). After the proton time distribution was obtained with a driving voltage of 14 kV applied to the deflector; only one burst in seven was undeflected, as was expected. The width of the distribution was observed to be

~500 psec. In addition to gaining essential information on the width of the burst, the fraction of protons from the deflected bursts which leaked through the collimator slits was also determined. This fraction was found to be typically 0.2% of the undeflected proton burst. These data were obtained with the window of the differential discriminator set tightly over the elastic proton peak. Measurements with this instrument used in the integral mode showed no significant change in the apparent burst width.

The jitter between consecutive rf time fiducial signals was measured by feeding the fast-slow signal to both the start and stop input of the TAC with the start signal appropriately delayed. The biased amplifier on the output of the TAC was tuned for maximum sensitivity. The FWHM of the time distribution of the fiducial signal was observed to be as low as 25 psec, which implies a very small time jitter since this is of the order of the time resolution of the TAC.

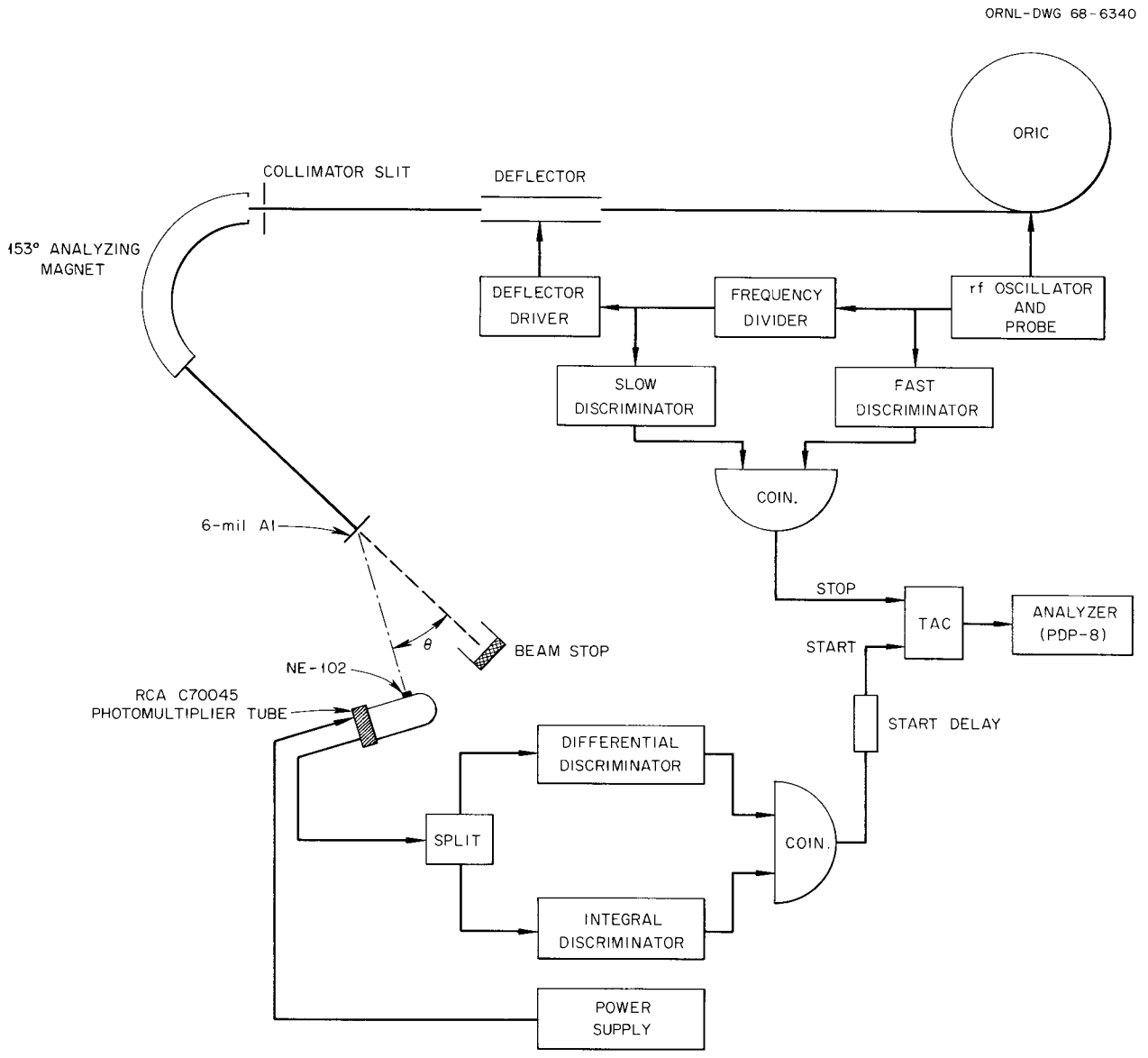

Fig. 5.10.1. Simplified Block Diagram of Proton Microstructure Monitor.

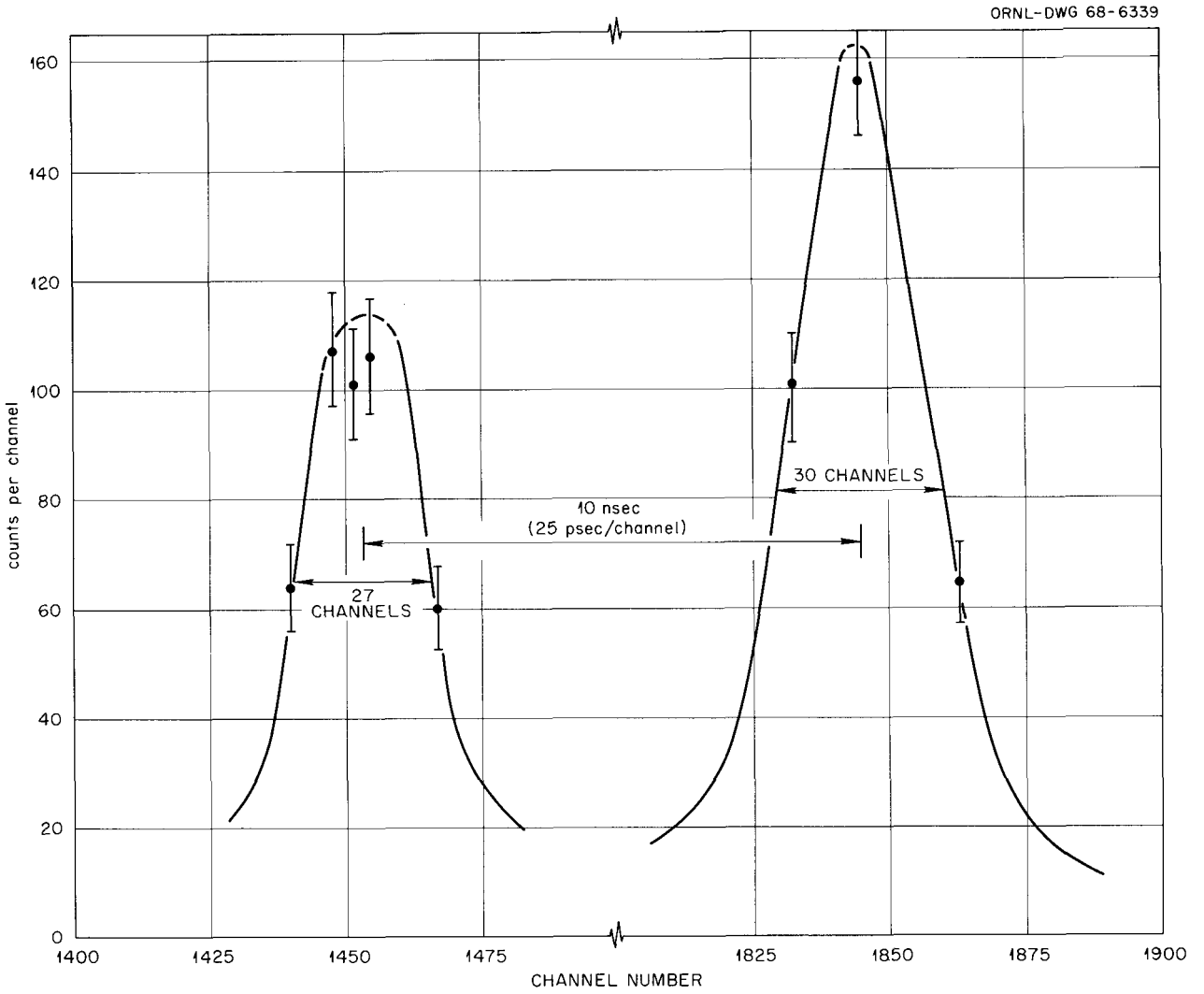

Fig. 5.10.2. Proton Burst Width for ORIC Proton Beam for f_{rf} = 22.4 Mc. The two peaks were obtained for two values of the start delay which were different by 10 nsec.

The burst width was also determined by measuring the variation in time between protons in successive bursts. This was done by using the scattered proton pulses to provide both the start and stop signal. A proton scattered from one burst produced the start signal, while the stop pulse was produced by the following burst provided that the adjacent bursts each yielded a proton which was intercepted by the detector. If the second burst did not yield a detected proton, then the TAC stayed on for a time exceeding 308 nsec. For these cases the TAC reset itself and the next scattered proton initiated the start signal. The resulting time spectra are shown in Fig. 5.10.2. The two peaks correspond to two separate runs obtained with a difference of 10 nsec in the start delay, which was necessary to calibrate the multichannel analyzer. A proton at the leading portion of one burst could start the TAC, while a proton from the trailing edge of the next burst could provide the stop signal. The resulting distribution represents a convolution of the two adjacent bursts. Correcting for this effect, the FWHM of the distribution is ~500 nsec.

References

[1]Work funded by the National Aeronautics and Space Administration under NASA orders R-104(1) and L-12,186.

[2]Instrumentation and Controls Division.

[3]F. E. Bertrand *et al.*, *Differential Cross-Sections for the Charged Particles Produced by 60-MeV Protons on Carbon, Iron, and Bismuth*, ORNL-4274 (in press).

[4]Selecting the deflector frequency of one-seventh of the fundamental is somewhat arbitrary. It is the largest value which is easiest to obtain in terms of sustained deflector operation and which increases the time between bursts to a satisfactory extent for the intended experiment.

5.11 DORO 2: AN ORGANIC SCINTILLATOR PULSE-HEIGHT ANALYSIS CODE[1]

R. M. Freestone, Jr.

A number of methods presently exist for the unscrambling or unfolding of pulse-height spectra obtained through the use of an organic scintillator spectrometer system. Most of them suffer from the requirement of large computer capacity, and thus are not adaptable to small computer on-line or almost-on-line unscrambling, a desirable feature in the control of experiments. An unscrambling code, DORO-2, has been written which produces at the remote terminal at the experimental facility an unscrambled spectrum within minutes of the conclusion of an experimental run, although it is not as precise as the spectra obtained with more elegant (and much more time-consuming) methods. DORO-2, which incorporates many of the ideas and approximations of G. G. Doroshenko and co-workers in the USSR, is written in CAL language for the time-shared SDS-940 computer of the Com-Share system at Ann Arbor, Michigan. Experimental data concerning the proton light vs energy curve for the currently used scintillator, NE-213, have been utilized.

Several comparisons of DORO-2 results with results from a more sophisticated code are presented, and an appendix contains a listing of the code and the input and output of a typical run.

Reference

[1]Abstract of ORNL-TM-2112 (Feb. 9, 1968).

5.12 REJECTION OF PILEUP PULSES IN PULSE-HEIGHT SPECTROMETRY BY USE OF ASSOCIATED FAST TIMING SIGNALS[1]

R. W. Peelle T. A. Love
F. E. Bertrand

In a recent semiconductor telescope experiment (see Sects. 7.1-7.4, 1.21, and 1.22) designed to observe charged particles from incident 60-MeV protons, the resolution of pulse-height groups was sufficiently narrow that efforts were required to minimize spectrum distortion from pulse pileup effects. In this experiment up to three analyzed pulse heights were summed to obtain the particle energy, so a pileup distortion in any one of the three detector-analyzer systems could affect the final result. The use in some cases of a plastic anticoincidence collimator to define the detector aperture resulted in only a small fraction of the pulses at the analyzer input terminals being appropriate for analysis as determined by an external triggering arrangement. The logic system for the telescope included fast timing pulses from each of the detectors, so we used the timing information to reject digitized events likely to be distorted by pileup.

The summary presented here contains test information corresponding to a single detector-analyzer channel. The recent paper of Blatt *et al.*[2] is concerned with a similar use of timing information for rejection of pileup effects but concentrates on a particular amplitude relation between the pulse of interest and the interfering pulses. Both systems are concerned with interfering pulses in the near time zone of event spacings, in which the amplitude from a single interfering pulse is enough to cause amplitude distortion in the pulse of interest and for which baseline restorers are not generally effective. Williams[3] has reported similar results using a symmetric protection interval around the pulse of interest. These systems relate to the experimental circumstance that not all pulses are of the class to be analyzed, since otherwise the analyzer dead time would help to protect the recorded spectrum against pileup distortion.

If the event producing the pulse of interest occurs at time zero, the recorded amplitude may be distorted by another pulse from any event in the time range $-t_- \leq t \leq t_+$. The interval t_- represents the time required for the linear amplifier output pulse to approach the baseline within a fraction

of the instrument resolution, and is typically several microseconds. The interval t_+ depends on the time delay after triggering before the analyzer input gate (or its equivalent) is closed, typically 1 to 4 μsec. The amount of resulting amplitude distortion depends on the relative amplitude and timing of the pulse of interest and the interfering pulse. Some efficiency of operation is gained by recognizing the nonequality of t_- and t_+.

Figure 5.12.1 shows a logic diagram equivalent to the rejection system used for the tests and nearly equivalent to that used for the charged-particle experiment. Synchronizing delays are not shown. All events of the class to be analyzed are digitized if the pulse-height analyzer is not "busy," but the system rejects storage of the event if the "inhibit storage" signal appears. The univibrator of period t_+ in the trigger logic chain may be any unit having moderate dead time, since its recovery is allowed by the digitizing time of the pulse-height analyzer. The fast logic signal train at the input to the pileup gate is assumed to include a signal for each pulse of interest. (The larger unit with the dotted perimeter may either be an EG & G[4] pileup gate or be composed of more standard logic units as shown.) A pileup level appears at the output of this gate whenever a pulse at its input is preceded by another within the interval t_-, and the level remains for at least t_-. At high rates, since an integrating or extending univibrator is used, it is more helpful to state that a pileup level becomes absent when a gap in the pulse train of length t_- is established and reappears for at least a period t_- when the second of two pulses again follows its earlier neighbor by an interval less than t_-. If a pulse normally of interest does have a neighbor at the relative time $-t_- \leq t \leq t_+$, storage will be inhibited by use of the output of the arrangement of Fig. 5.12.1. The only pileup events which evade the system are those arising from such closely spaced pulse pairs that the pileup gate cannot recognize that two events have occurred, because of the recovery time of the detectors, the circuitry preceding the pileup gate, or the pileup gate itself. Also, if any truly isolated event of interest should through some malfunction produce a pair of logic pulses at the input to the pileup gate, storage of this pulse, too, will unfortunately be re-

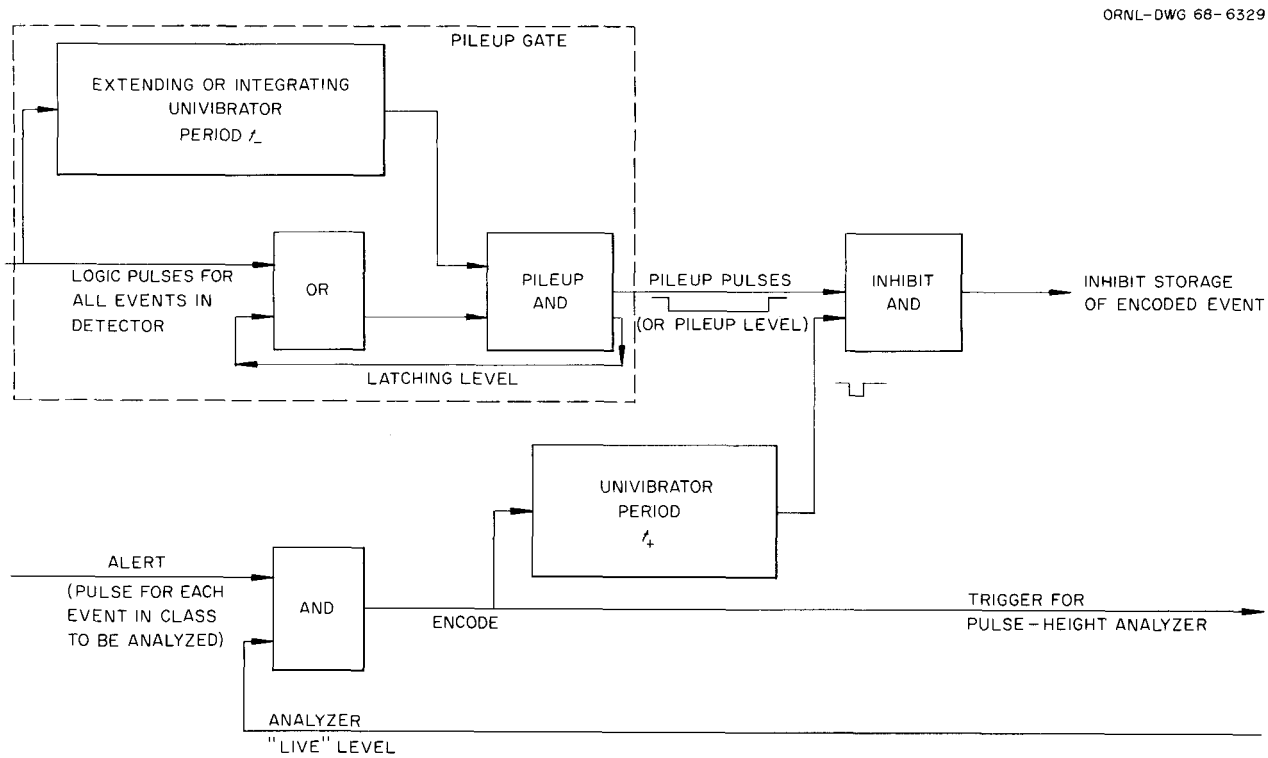

Fig. 5.12.1. Block Diagram of Pileup-Pulse-Rejection System.

jected. Thus, fast timing information can be used to purge pileup noise from the result only to the extent that the fast timing signals themselves are clean and sharp.

The system of Fig. 5.12.1 was tested in several ways, but the clearest results were obtained by mixing logic and linear signals from a 53-Hz mercury-switch pulser and a random pulser, the random pulser providing signals of nearly constant amplitude.[5] The pulses of interest were taken to be those from the 53-Hz pulser, while the random pulses were timed by a radioactive source and an organic scintillation counter. Although the events contained in the random pulse train were no closer together than 40 nsec, this disadvantage did not relate to the timing between pulses from the two different pulsers. All pulses appeared to be identical in shape at the output of the Tennelec TC-200 which was used with double 0.8-μsec clipping and 0.8-μsec integrating time.

Figure 5.12.2 shows the discarded spectrum and the retained spectrum for a random counting rate of 6.53×10^4 counts/sec with $t_- = 15$ μsec and $t_+ = 3.3$ μsec. The fraction of counts in the retained spectrum (29%) suggests a total protected interval of 19 μsec rather than the indicated 18.3 μsec. The random pulses had just less than half the amplitude of the pulses of interest. The retained spectrum consists of a nearly unbroadened line, together with a small sum peak arising from the dead period of the pileup gate. The rejected spectrum contains first-, second-, and a few third-order pileup events; the shape of the rejected spectrum reflects the output pulse shape of the TC-200 amplifier. Note that very little area is contained in the far-flung tails of the rejected spectrum. The data displayed in Fig.

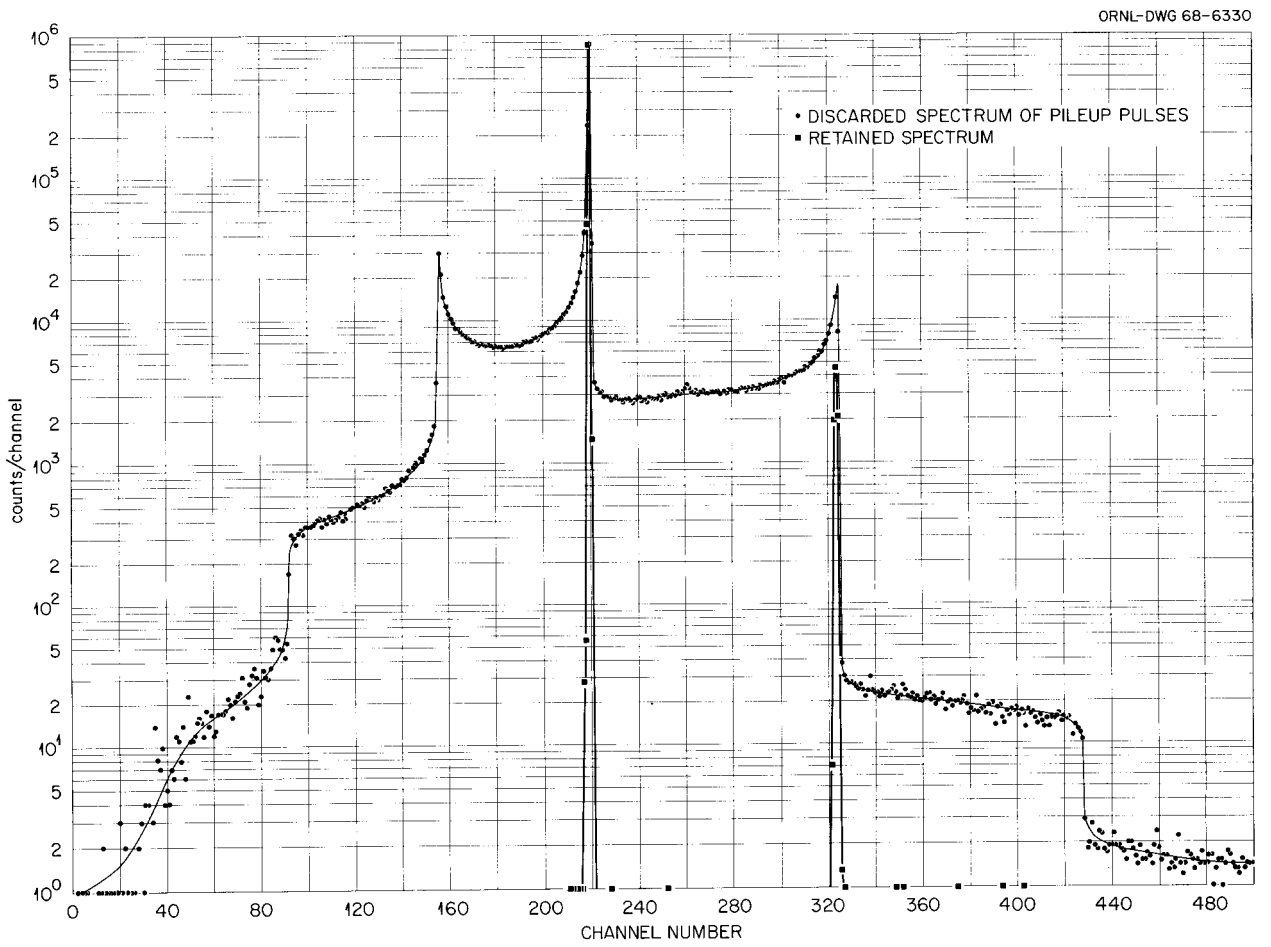

Fig. 5.12.2. Pileup Test Spectra for Random Interfering Pulses of Constant Amplitude.

5.12.2 were obtained using standard coincidence circuits and an R 303 "integrating one-shot"[6] to form the pileup gate. Observations during the test indicated a dead time of 70 nsec, while the results in the figure give a spurious peak with area corresponding to a dead time of 73 nsec. For this test the diode restorer was removed from the input of the analyzer.

In practical cases additional complications arise. For instance, when all amplitudes are present in the random source, the sensitivity of the fast threshold affects the line breadth of retained events, since elimination of an interfering event depends on its recognition by the logic circuitry. In the multidetector system referred to above, the "all events in detector" signal was replaced with the logical "OR" of similar signals from all three detectors.

As shown in Fig. 5.12.2, many rejected pulses were very close to the correct amplitude. This occurred because t_- was set to an unnecessarily large value. In practice unnecessary rejection has been common because, for very small pulses, t_- would not need to be nearly as long as for pulses of maximum amplitude. The chief difficulty in using the inexpensive R 303 unit is that the delay between triggering and the output pulse is long and is a function of the counting rate. (It shifted from 200 to 150 nsec between zero rate and the rate corresponding to the illustrated measurements.) In a very similar test the EG & G pileup gate performed with a conveniently small delay and a measured dead time of 18 nsec.

References

[1]Work funded by the National Aeronautics and Space Administration under NASA Orders R-104(1) and L-12,186.

[2]S. L. Blatt *et al.*, *Nucl. Instr. Meth.* **60**, 221 (1968).

[3]C. W. Williams, *IEEE Trans.* Nucl. Sci. **NS-15**, 297 (1968).

[4]Edgerton, Germeshausen and Grier, Inc., Salem, Massachusetts.

[5]The random pulser was conceptually the same as that described by C. W. Williams (ref. 4) but for each scintillator pulse a constant current was dumped for a few nanoseconds from a standard 100-MHz discriminator into the input of an EG & G stretcher amplifier set for ~200-μsec decay period.

[6]Digital Equipment Corp., Maynard, Massachusetts.

5.13 FLOTSAM – A TWO-PARAMETER ON-LINE DATA ACQUISITION PROGRAM FOR THE PDP-7[1]

A. L. Marusak[2]

FLOTSAM is a program for the PDP-7, designed to accept one- and/or two-parameter data from experiments. This report describes the particular two-parameter program used for measuring neutron cross sections by the time-of-flight technique from (d,n), (n,n'), and (p,n) reactions. Sufficient versatility is included so that conversion to one-parameter 4096-channel data acquisition or other configurations is, with some study of the program, easy, and has been done. The data from analog-to-digital converters are fed directly into the computer into one of two 64-word temporary buffers. While one buffer is being filled with data, events in the other are being analyzed and stored. A bank of six scalers can be read into the computer and stored. A continuous oscilloscope display of all or some of the data is provided, with three modes (linear, log, and square root) available for the y coordinate (number of counts in a channel). Light pen routines enable peak information to be extracted from either old data stored on magnetic tape or from data as they are taken. Permanent storage of data is on IBM-compatible magnetic tape; the data can also be typed out or plotted on a CALCOMP plotter. The report includes a general description of the program, some flow charts, operating instructions, and the complete annotated listing of the program itself.

References

[1]Abstract of ORNL-4299 (to be published).

[2]Oak Ridge Graduate Fellow from the University of Tennessee, Knoxville, under appointment from the Oak Ridge Associated Universities, Inc.

5.14 A PDP-8 INTERFACE FOR A CHARGED-PARTICLE NUCLEAR PHYSICS EXPERIMENT[1]

W. R. Burrus[2] C. O. McNew[3]
E. Madden[3] R. W. Peelle

An interface has been constructed for use between a PDP-8 computer and a charged-particle

spectrometer employing three solid-state detectors and flight-time analysis. Up to 48 bits from each randomly occurring event are transferred through the data (break) channel to a hardware-selected buffer region in the core of a PDP-8 computer. Designed for use as a magnetic tape analyzer for the most complex cases, the system assumes that the 48 bits originate in flag bits set by fast logic and in amplitude digitizers (four at present), all of which are assumed to contain information for the same event. The system includes some limited capability for controlling the course of the experiment and provides for readout through the computer of a series of external fast counters. This report summarizes the design concepts, shows schematic flow diagrams, defines the computer instructions associated with the interface system, and gives simple model programs to illustrate methods of application.

References

[1]Abstract of ORNL-TM-2013 (Oct. 4, 1967); work funded by the National Aeronautics and Space Administration under NASA Orders R-104(1) and L-12,186.

[2]Present address: Tennecomp, Inc., P.O. Box J, Oak Ridge, Tennessee.

[3]Instrumentation and Controls Division.

5.15 PDP-8 PROGRAM DEVELOPMENT FOR INTERACTIVE ANALYSIS OF DATA FROM CHARGED-PARTICLE EXPERIMENTS[1]

R. W. Peelle D. I. Putzulu[2]
F. E. Bertrand

Two data analysis programs have been written for the PDP-8 computer (8K, 12-bit words) originally employed to facilitate event-by-event recording of the data from the same charged-particle experiment (Sects. 7.1–7.4). The serial tapes were sorted by an IBM 360/75 computer, and data in a form suitable for analyses were in turn written on magnetic tape by the large machine for use by the PDP-8. For large data sets, use of the small machine with its oscilloscope and light "pen" is extremely advantageous whenever the experimenter must study graphical data and subsequently supply graphically expressed judgments which will affect the output analyzed data after the judgments are converted to numeric form. Such needs are not rare, but they are often sidestepped because of the great difficulties involved when appropriate facilities are not available.

Data tapes from the subject experiment were analyzed with the IBM 360/75 to obtain detailed energy spectra for the more energetic emerging particles separated according to particle type using a $\Delta E \times E$ identification system. Flight-time information was utilized to sort the lower energy particles according to energy and "mass" as represented in Fig. 5.15.1. In the figure the average blackness of a symbol represents the number of events in a Δmass $\times \Delta E$ bin. From run to run, timing and bias drifts caused the dense regions like those in Fig. 5.15.1 to shift slightly, so the "discrimination lines" used to separate the regions corresponding to particles of various masses need to be rechecked for each set of data. The PDP-8 program TOF displays a mesh of up to 2560 points, one-quarter of the region shown in Fig. 5.15.1, each point having a brightness (intensity) which depends on the number of counts in the corresponding mass-energy bin. At least low intensity is produced when the number of counts in a bin is greater than an adjustable threshold, while medium and high intensities have thresholds automatically 4 and 16 times as large as that for low intensity. As the experimental data are examined with the aid of the intensity threshold, up to seven sets of discrimination lines corresponding to seven different particle masses are stored in the computer memory as they are drawn with a light pen. When the discrimination lines appear to be satisfactory, the count distributions are summed over the mass interval between each pair of lines, and the resultant energy spectra are printed (and punched) while the next set of data is examined.

Nearly every spectrum (out of a total of about a thousand) of the higher energy particles contains a series of particle groups at near-elastic energies, as seen elsewhere (Sect. 1.21). Though the 360/75 program contains a simple peak-search feature, graphs of all peaks in the pulse-height spectra must be examined to assure that the count spectrum is properly interpreted and that any background "underneath" the peak in the pulse spectrum has been properly subtracted. This function is handled by a peak-stripping program on the PDP-8 which is rather similar to others previously described.[3] The (1264-channel) raw spectrum can be examined on the PDP-8 display at any of three horizontal mag-

nifications; the light pen is used to choose the regions to be more closely examined. The estimated background is drawn into the display with the light pen, and on demand the program computes the output cross section, Q value, and statistical uncertainty for the particle group under examination. This program is now being modified to allow the spectra from carbon to be subtracted from data obtained for oxygen by using mylar or cellulose foils. To facilitate scaling of the display and computation of output quantities, the program contains a low-precision (and therefore fast) floating-point arithmetic subroutine package using a 12-bit unsigned mantissa. Included with the basic package are simple (sine, square root, etc.) functions, a general output format controller, and a teletype command program which allows simple computation at the console.

Programming time has tended to be long for this work on the PDP-8, although efficiency should improve on any future programs because of overlaps. Most errors have been in the floating-point and output packages and in the logical handling of the various controls and displays. Floating-point computation of results, which might be programmable in FORTRAN on another machine, has not been bothersome in any case.

We have arrived at a few judgments on the types of displays and controls which are easiest to use:

1. For use with the light pen, a simple four-point symmetric tracking cross has been found most satisfactory, with the diameter of the cross a few percent of the screen size. This open cross often allows the data point at the cross location to be seen. After the four points have been intensified, the displacements from the central location are averaged, and if a net displacement is required, the central location is shifted one-fourth the radius of the cross in the indicated direction. Two manual control switches are required for a cross, one to disable motion so that the pen can be removed from the screen without shifting the cross and the other to enable "drawing" into the appropriate storage buffer. A button on the pen is used for the latter. We allow teletype printout of the cross location, in appropriate units, on demand.

2. Utilization of the variable intensity level has been the most desirable way to acknowledge contact of the light pen with a control "light button," to indicate which part of a spectrum is to be expanded, to distinguish between two ar-

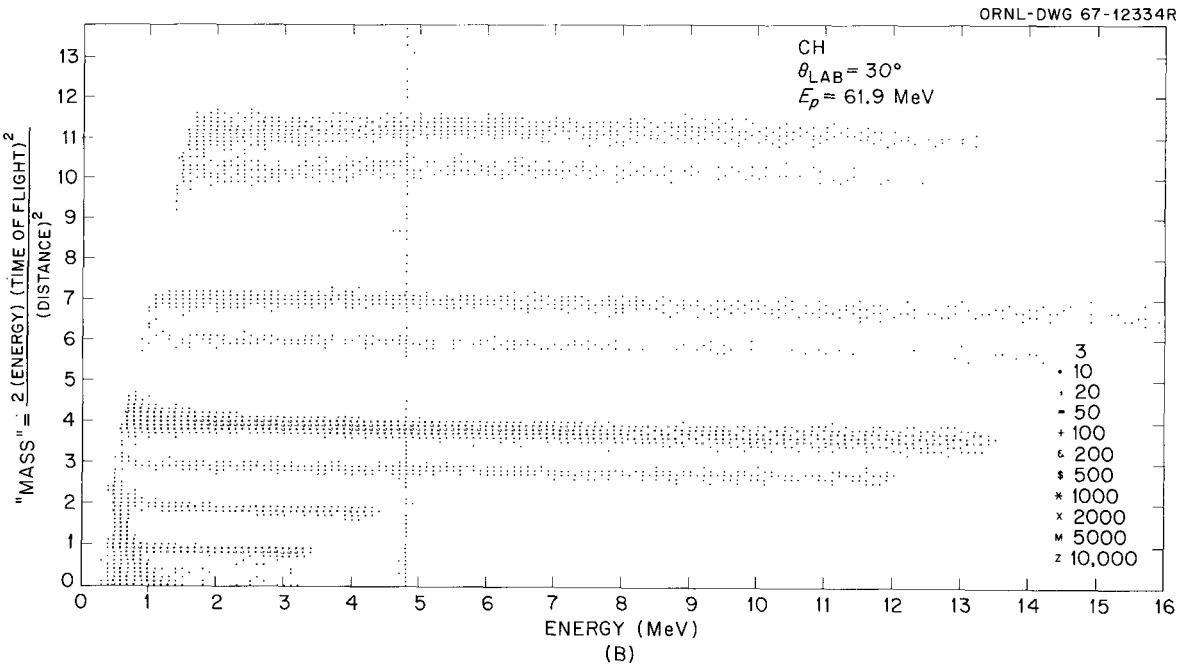

Fig. 5.15.1. Raw Data Map for Time-of-Flight Identification System.

rays simultaneously plotted, and to represent the number of counts in a two-dimensional bin.

3. Decimal thumbwheels provided for entry of data into the program have been found useful, but not mandatory. A set of control switches other than the teletype has been found to be very useful, and the ability to determine for a given program whether these should set toggles or give program interrupts has proved invaluable (Sect. 5.14).
4. When the discrimination lines separating the various mass regions have been set into the TOF program, it is necessary to check them against a displayed data set, which is sometimes confused and dense. Satisfactory examination can be made if the line is flashed each time a switch is depressed. We suspect but have not proved that this method allows better perception than an automatically flashing line.
5. A large screen (10 × 10 in.) with slow display has been utilized with the peak-stripping program. Programmed delays have been satisfactory to allow settling of the spot position. Although the large display has rather low quality, users report that it is less tiring to study than the sharper 4-in. display oscilloscope.

References

[1]Work funded by the National Aeronautics and Space Administration under NASA Orders R-104(1) and L-12,186.

[2]Now at Virginia Polytechnic Institute, Blacksburg.

[3]J. A. Biggerstaff *et al.*, *Neutron Phys. Div. Ann. Progr. Rept. May 31, 1967,* ORNL-4134, p. 102.

5.16 MAGNETIC-FIELD COMPENSATION WITH PAIRS OF RECTANGULAR COILS[1]

E. G. Silver

FORTRAN programs have been written for determining the magnetic fields generated by rectangular pairs of current-carrying coils. One of the programs calculates the optimum separation distance between the pair of coils for producing a field constant to second order at the center of symmetry of the coil pair. Another program calculates the currents required to compensate for any arbitrary external field at the center of symmetry of any coil pair and obtains the resultant of the external field and the fields of three mutually orthogonal pairs of compensating coils. Another version of this program calculates a set of 19 by 19 field values in any plane normal to one of the coordinate axes with adjustable mesh-point separations.

Examples of results are given.

Reference

[1]Abstract of ORNL-TM-2129 (Mar. 1, 1968)

5.17 STATUS OF DESIGN AND CONSTRUCTION OF ORELAST (ORELA SCINTILLATOR TANK)

E. G. Silver J. Lewin
J. Todd[1]

A large scintillator tank is under construction at ORNL for the detection of gamma rays in a variety of experiments dealing with neutron fission and capture events.

As the result of extensive calculations for determining the effects of tank volume and tank shape on the gamma-ray detection efficiency, the final design calls for a tank consisting of a central cylinder and two truncated-cone sections, with a total volume of approximately 800 gal. The system is sketched in Fig. 5.17.1. A major design criterion has been to make the facility as flexible as possible for future experiments. For example, the shape and size of the beam tube along the axis of the tank can be chosen by the experimenter to suit his particular needs. Large access hatches are provided at the sides of the tank to permit mounting of auxiliary detectors.

The choice of the scintillator fluid was partly determined by the need for fire safety in the presence of the large amount of organic liquid together with quantities of plutonium or other dangerous targets in the tank. Hence NE-224, a scintillator based on the high-flash-point liquid 1,2,4-trimethylbenzene (pseudocumene), was chosen. This type of scintillator has been used successfully in other tanks at ORNL. In order to suppress the gamma rays from neutron capture in hydrogen, the scintillator fluid will be mixed with trimethylborate in the ratio of one part to three parts NE-224. Experiments on the compatibility and performance of

ORNL-DWG 68-6645

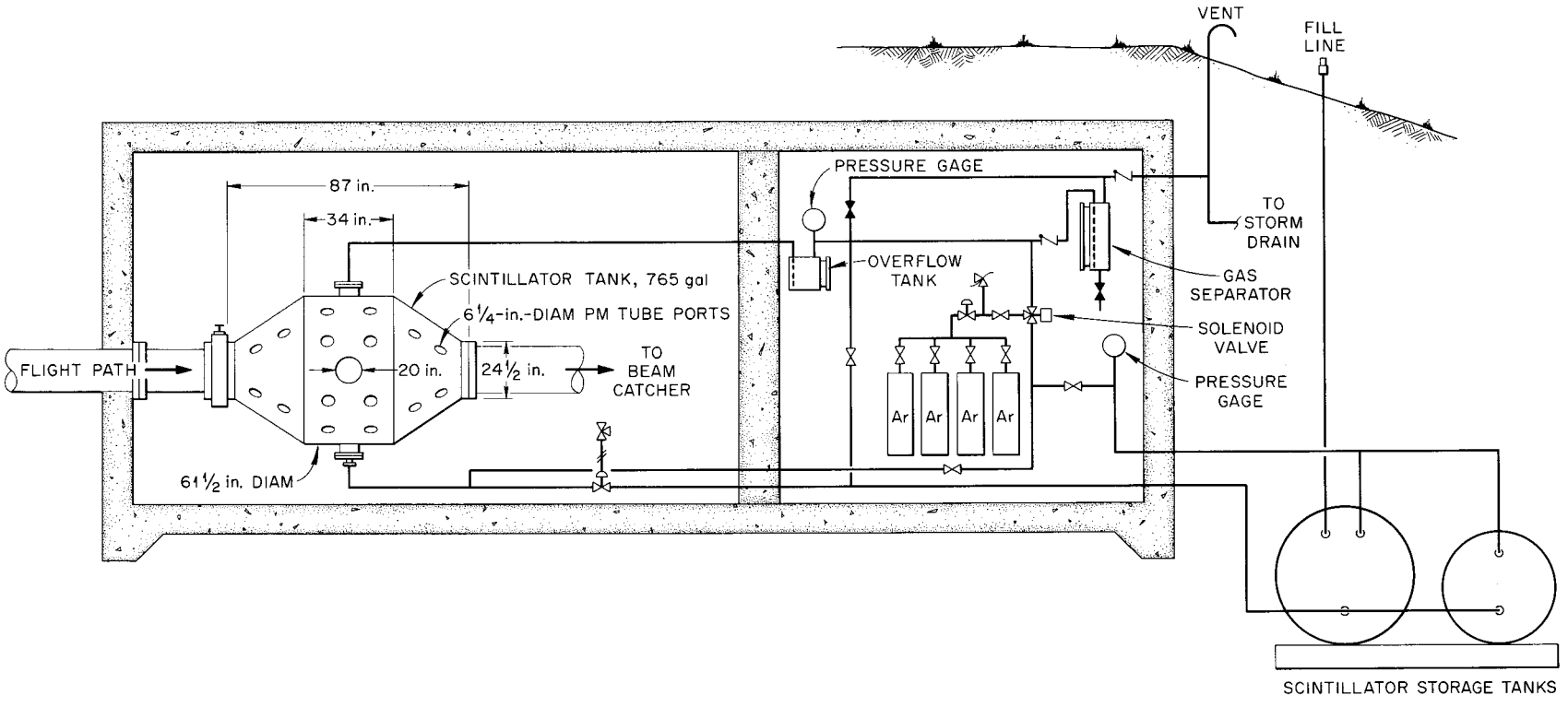

Fig. 5.17.1. Sketch of ORELAST and Scintillator Transfer and Storage System.

these two materials showed that the light output is reduced only proportionately to the reduction of scintillator volume fraction. It is hoped that by adjusting the secondary and tertiary solute concentrations the output of the mixture can be somewhat increased. The transparency of the mixture was tested at various wavelengths over a 4-ft path length and was found to be at least 95% of that of pure NE-224.

Experiments have also been performed to find a satisfactory surface treatment of the tank interior that will produce a durable finish with good light reflection. The reflectivity, relative to that of alumina, was measured in contact with the scintillator for a number of surfaces both for normal and oblique reflection. While no other surface proved to have as high a reflectivity as alumina, a surface treatment consisting of sandblasting followed by pickling in a hot solution of nitric and phosphoric acids, yielded a diffusely reflecting surface with about 65% of the reflectivity of alumina at 45° and probably considerably better than that at normal incidence.

The use of alumina has presented problems in the past because the coating tends to be poorly bonded. With repeated filling and draining of the tank there would be danger of detachment of pieces of the coating and partial obscuring of the lower photomultipliers with the debris. Hence, the pickled surface will be employed in the ORELAST. Should the reflectivity prove too low, painting with an AlO_2 coating could still be done.

Extensive experimental work was performed to select the most suitable type of photomultipliers. Since it was desired that as much of the tank wall be covered with effective photocathode surface as possible and since fast pulse rise-time is necessary, only large-diameter, fast-timing tubes were considered. The types tested were Amperex 58-AVP and 60-AVP and RCA 4522 tubes. The main effort consisted in determining the uniformity of the cathode surface response by means of a flying-spot scan method. Since the RCA 4522 tube was much superior in this regard and also had good timing characteristics, it was selected. The ORELAST will use 32 tubes located so as to have three normal planes of symmetry through the tank center, allowing front-back, top-bottom, and left-right separation of the emitted radiation if suitable optical separators are installed.

Each tube will be preassembled into a fixture designed to combine the functions of a support, light shield, and safety envelope. The fixtures are entirely interchangeable in the 32 tube ports. Once mounted on the scintillator tank, each fixture will be filled with an inert gas, which will prevent fire if the tube glass should break.

A study of the degradation of the performance of the tubes due to the presence of magnetic fields in various directions resulted in the decision to install a square-coil Helmholtz coil system around the ORELAST to compensate for the vertical component of the earth's field. Also, cylindrical passive shields will be available for use with those tubes whose axes are nearly vertical.

Some evidence has been collected, using several 58-AVP photomultiplier tubes and a scintillation tank at Building 5500, on the effect of multiplicity of tubes on both resolution and timing. It appeared that the resolution improved by a factor of about 3 in going from one detector to five, and then improved slowly up to the maximum of eight tubes tested. The timing improved slightly from about 5.5 nsec with one tube to 4.7 nsec with four tubes. However, the final characteristics of the ORELAST are difficult to predict on the basis of such experiments.

The scintillator liquid will be stored in a pair of underground tanks and will be transferred to the ORELAST by means of argon gas pressure. The scintillator will be maintained under inert gas at all times, and it is possible to sparge with argon gas at either location. The liquid can also be filtered during transfer. With this system the tank may be conveniently emptied to allow work such as photomultiplier-tube exchanges and similar manipulations.

The present status of the project is as follows: The tank itself and the tank cradle have been fabricated, but the surface has not yet been treated. The scintillator tubes have been ordered and will be delivered soon. The detail design and construction of the tube bases and the electronics will be based on tests to be performed with tubes as they arrive. Design has been completed on the transfer system and on the Helmholtz coil system, and construction is about to start. ORELAST is expected to be ready by the time a beam is available from the accelerator.

Reference

[1]Instrumentation and Controls Division.

5.18 ORELA DATA-HANDLING SYSTEM

J. W. Reynolds[1] N. A. Betz[2]
D. R. Winkler[2]

The ORELA data-handling system consists of a series of computers for real-time data acquisition and on-line analysis of the acquired data.

An interim system for Phase 1 has been installed to allow systems program checkout. The final Phase-1 equipment, shown in Fig. 5.18.1 as it will be installed in September 1968, will be used for collection and storage of large data sets. Special fixed head disks (4×10^5 and 8×10^5 words of 16 bits each) are used for data storage. The theoretical data rate is 11,500 events per second, which allows approximately 50 computer instructions to be executed for preliminary sorting of each event. The peripheral equipment (card reader, plotter, and magnetic tapes) is concentrated on data acquisition computer No. 2 (DAC2) with access by all experimenters through interprocessor communication. The interfaces for several experiments have been proposed, with construction to be completed by fall of 1968.

Software for the ORELA Phase-1 data-handling system is under development. One data acquisition computer system (DAC1), consisting of a System Engineering Laboratory 810B computer, a special fixed head disk (4×10^5 words), teletype, and experimental interface, was simulated on the IBM 360/75. The monitor system which dynamically allocates memory, both protected and unprotected, and dynamically loads routines from the disk when they are called has been programmed and checked out on the simulator. The design of the monitor system was approved by the experimenters before it was programmed. A general data acquisition package for the Phase-1 system is being designed and will be submitted to the experimenters for approval.

Specifications for the Immediate Analysis and Coordinating Computer (IACC) have been completed with a scheduled delivery of June 1969. It is a display-oriented time-sharing computer system with

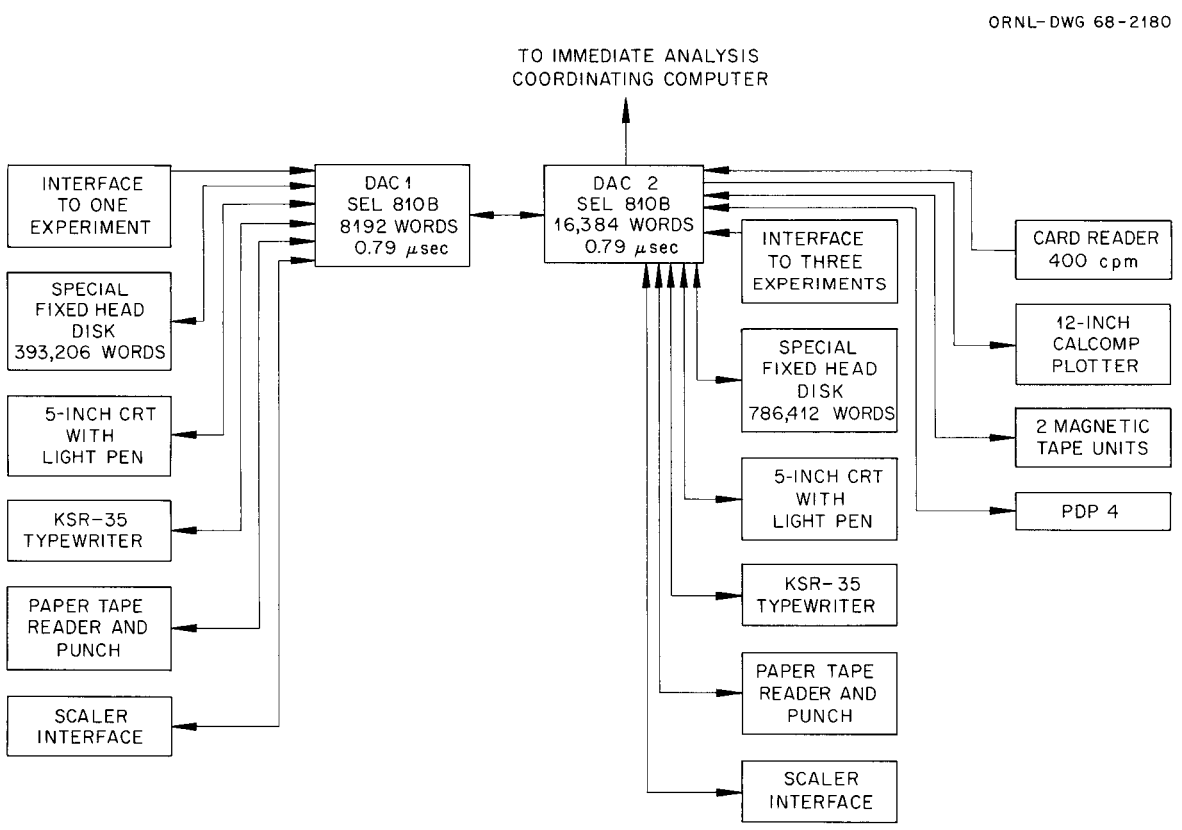

Fig. 5.18.1. Phase-1 Equipment for ORELA Data-Handling System.

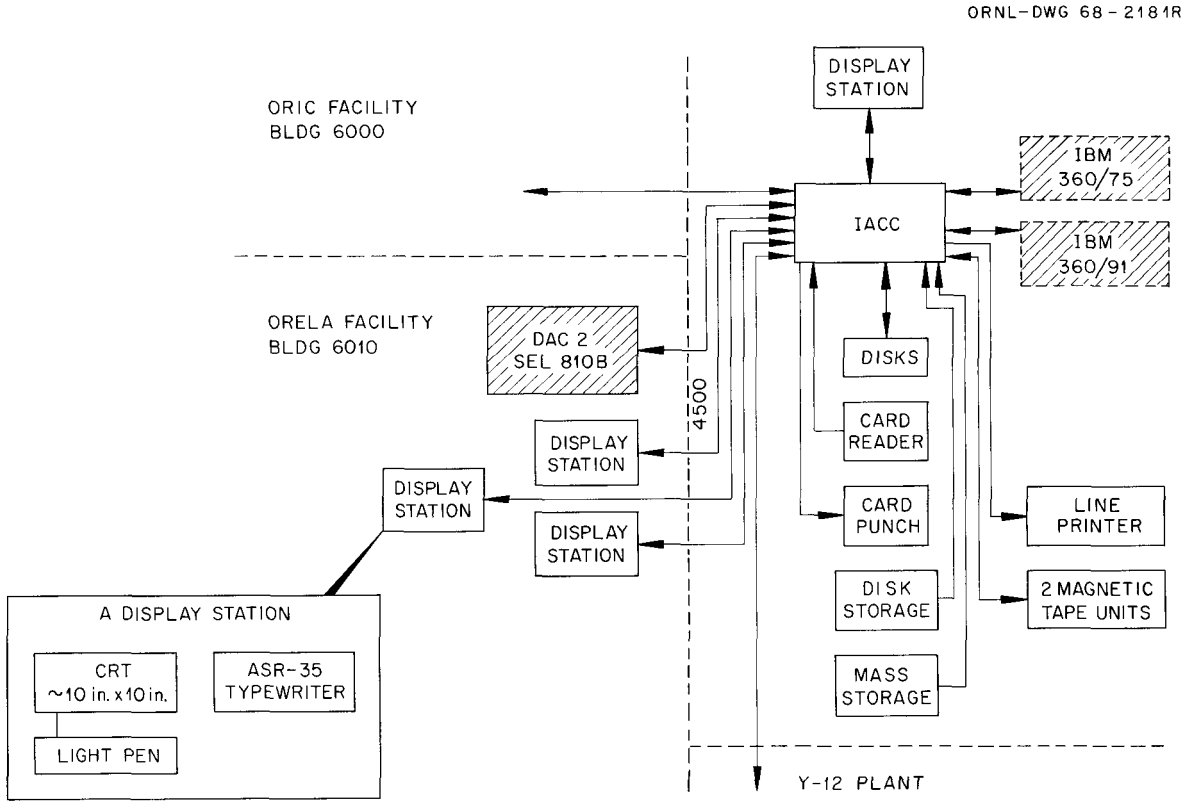

Fig. 5.18.2. Block Diagram of Immediate Analysis and Coordinating Computer (IACC).

a response time of less than 1 sec to user requests via the display console. A block diagram of the proposed system is shown in Fig. 5.18.2. Final analysis of the data will be accomplished by the IBM 360/75, since the computing time for the IACC would be excessive. As may be seen from Fig. 5.18.2, this system provides connections to the major nuclear physics facilities at ORNL. It will be operated by the Mathematics Division.

References

[1]Instrumentation and Controls Division.
[2]Mathematics Division.

5.19 SIGNIFICANCE ARITHMETIC BASED ON A RANDOM COMPUTER[1]

C. M. Schneeberger[2] W. R. Burrus[3]

Errors occur in a computer calculation because of the finite number of bits used to represent numbers, for example, errors on input and output, in the arithmetic operations, and in the library functions (such as SQRT). In many problems the loss of significance is crucial and the user does not know how many significant digits he has in his results. We have programmed a scheme in which computer operations of input, addition, multiplication, and division are given random perturbations at each step, with the sample variance of several runs indicating the significance. Its advantages over other significance systems are that the correlation between pairs of numbers is not lost, it yields as many or more significant digits, and *a priori* analysis may be used on some types of errors. Disadvantages are the length of time used to make several runs and the difficulty of guaranteeing the indicated significance. Some numerical examples are given to illustrate the performance.

References

[1]Abstract of ORNL-TM-2255 (in press).
[2]Summer employee; present address: University of Michigan, Ann Arbor.
[3]Present address: Tennecomp, Inc., P.O. Box J, Oak Ridge, Tennessee.

6. Theoretical Studies for Medium- and High-Energy Radiation Shielding

6.0 INTRODUCTION

Theoretical studies of medium- and high-energy radiation transport are pursued on a continuing basis. The purpose of the program is to provide basic data and to study transport methods that are applicable to the shielding of manned space vehicles and high-energy accelerators. While many of the problems involved in the shielding of manned spacecraft are quite different from those involved in shielding high-energy accelerators, the two disciplines have a sufficient area of overlap that it is efficient for them to be considered under the same general program.

One of the fundamental difficulties in the study of medium- and high-energy radiation transport has always been the lack of information concerning particle production from nucleon-nucleus collisions, and therefore a substantial portion of the program is devoted to the calculation of such particle-production cross sections. Because of the very large amount of data required, a reliance on experimental information is not practical, but efforts are continually made to obtain experimental verification of the theoretical cross sections by comparing with available experimental data.

Using these theoretical cross sections, transport methods are studied and their validity is confirmed by comparisons with experimental data. The purpose of this portion of the program is not only to devise elaborate transport methods that yield results of high accuracy but also to devise approximation methods that are sufficiently accurate and easily applicable to be suitable for routine shield design.

A substantial portion of the program is also directed toward using the best available transport methods to provide design data as required by those groups presently engaged in designing particular shields. Also, the transport methods that are developed as part of the shielding program are useful in areas that are only peripherally related to shielding. A small part of the program is directed toward these other applications which are of interest to the National Aeronautics and Space Administration and to the U.S. Atomic Energy Commission.

Examples of the work conducted during the past year in all these areas are described in the pages following.

6.1 CALCULATION OF THE CAPTURE OF NEGATIVE PIONS IN LIGHT ELEMENTS AND COMPARISON WITH EXPERIMENT[1]

M. P. Guthrie H. W. Bertini
R. G. Alsmiller, Jr.

Reactions resulting from the capture of π^- mesons in carbon, nitrogen, oxygen, and aluminum are being studied using Bertini's[2] low-energy intranuclear cascade code. The purpose of the study is twofold: to compare calculated data with experimental data on π^- capture and to provide data for studies of the effectiveness of beams of π^- mesons in cancer radiotherapy.

In order to use Bertini's code without modification, the absorption of pions from a mesonic orbit about the nucleus is approximated by assuming a parallel beam of 1-MeV negative pions. The pion is absorbed by a two-particle cluster in the nucleus. Whether the pion is absorbed by proton-proton cluster or a deuteron is determined statistically in the code from the number of possible pairs of each type in the nucleus. The two nucleons released by the capture reaction share the rest-mass energy of the pion and are assumed to be emitted isotropically in the center-of-mass

system. The two nucleons either initiate cascade reactions within the nucleus, escape from the nucleus, or contribute to the excitation energy of the nucleus as a whole.

At the completion of the cascade, an evaporation code is used to determine the energy spectra and multiplicities of particles "boiled off" from the excited cascade residual nucleus. The evaporation code used by Bertini has been modified to include the effects of the recoil kinetic energy of the cascade residual nucleus and the recoil kinetic energy of the nucleus after a particle is evaporated. The kinetic energies and excitation energies of the residual nuclei, after particle emission is no longer possible, are tabulated, and the energy distributions of the most numerous residual nuclei are obtained.

The results of the calculation have been compared with the experimental results of Fowler,[3] Fowler and Mayes,[4] and Anderson *et al.*[5] By varying the water content in photographic emulsions, Fowler and Mayes were able to determine the effects of π^- capture in oxygen and other light elements. They presented tables of multiplicities and mean kinetic energies of protons, neutrons, alpha particles, and recoil nuclei from π^- capture in oxygen, carbon, and emulsion nuclei. A comparison of the calculated values with the data obtained by Fowler and Mayes for oxygen is shown in Table 6.1.1. Similar comparisons have been made for carbon. In both cases reasonable agreement with experiment for the yields and kinetic energies of neutrons, protons, and alpha particles has been obtained. For the recoil nuclei, both the calculated yields and the calculated kinetic energies are too low. The sum of the calculated yields for alpha particles and recoil nuclei agrees well with the experimental sum for both elements, and similarly, the sums of the kinetic energies per π^- capture are in good agreement. Since a similar amount of biological damage is caused by alpha particles and by heavier nuclei, the discrepancies we have noted are probably not significant in the determination of the effectiveness of π^- mesons in radiotherapy.

Comparisons have also been made between the calculated energy spectra for various types of

Table 6.1.1. Multiplicities and Energy Partition from π^- Capture in $^{16}_{8}O$

Particle Type	Calculation: Number per π^- Capture		Calculation: Kinetic Energy per π^- Capture (MeV)		Experiment[a]: Number per π^- Capture	Experiment[a]: Kinetic Energy per π^- Capture (MeV)
Neutron	2.94		60.35		2.7 ± 0.15	69 ± 7
Proton	1.23		20.04		0.95 ± 0.05	15.2 ± 1.0
Deuteron	0.242		2.48			
Triton	0.055		0.57			
^{3}He	0.029		0.29			
Alpha	1.084		10.48		0.99 ± 0.07	7.8 ± 0.7
Li[b]	0.152		0.330			
Be[b]	0.024		0.090			
B[b]	0.096	0.545	0.243	1.39	0.78 ± 0.03	4.4 ± 0.3
C[b]	0.185		0.591			
N[b]	0.088		0.136			
Average excitation energy of residual nuclei per capture			2.31			
Total energy			97.91			96.4

[a]H. W. Bertini, *Phys. Rev.* **131**, 1801 (1963).

[b]Both stable and unstable isotopes.

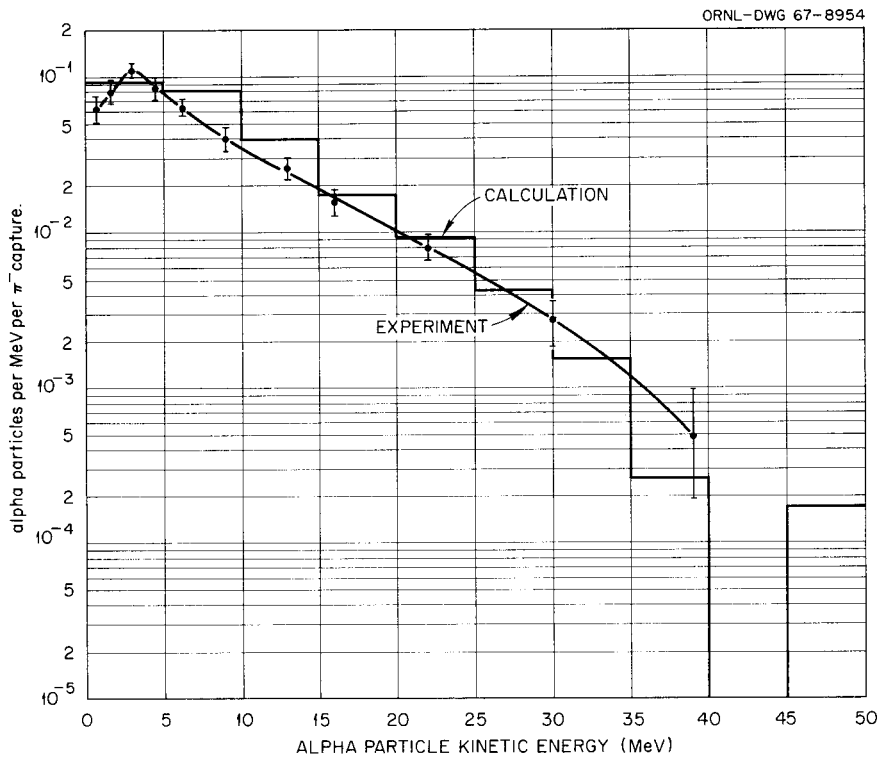

Fig. 6.1.1. Energy Spectrum of Alpha Particles from π^- Capture in $^{16}_{8}O$.

emitted particles and the experimental spectra of Fowler and Mayes and of Anderson *et al.* Reasonable agreement was obtained between Anderson's neutron energy spectra and the calculated spectra from π^- capture in carbon and aluminum. Above 10 MeV, the calculated values are somewhat lower than the experimental values. For aluminum, very good agreement is obtained below 10 MeV; for carbon, the calculated values are too high in this low-energy region. Using Fowler's data, the calculated and experimental proton spectra from π^- capture in oxygen are in good agreement above 10 MeV. Again, the calculation overestimates the experimental data at low energies. The alpha-particle distributions are in very good agreement, as shown in Fig. 6.1.1. The energy spectra of the heavy recoil nuclei from π^- capture in oxygen are also in agreement. The calculated spectra of the sum of lithium, boron, carbon, and nitrogen recoils are within the experimental error over most of the energy range.

References

[1]Work partly funded by National Aeronautics and Space Administration under NASA Orders R-104(1) and H-38280A.

[2]H. W. Bertini, *Phys. Rev.* **131**, 1801 (1963).

[3]P. H. Fowler, *Proc. Phys. Soc.* **85**, 1051 (1965).

[4]P. H. Fowler and V. M. Mayes, *Proc. Phys. Soc.* **92**, 377 (1967).

[5]H. L. Anderson *et al.*, *Phys. Rev.* **133**, B392 (1964).

6.2 NUCLEON EMISSION SPECTRA FROM HIGH-ENERGY PHOTON-NUCLEUS COLLISIONS

T. A. Gabriel[1] R. G. Alsmiller, Jr.

Through the combined use of the quasi-deuteron model of Levinger,[2] which defines the initial interaction, and the medium-energy cascade code of

Bertini,[3] which gives subsequent particle-particle interactions, Monte Carlo calculations on high-energy photon-nuclear interactions are being obtained. While there have been several theoretical papers[2,4–7] in which the quasi-deuteron model is used to obtain the energy and angular distribution of emergent nucleons from complex nuclei, the secondary particle-particle collisions which are important in large nuclei have not previously been taken into account in a systematic manner.

In the quasi-deuteron model the incident photon is absorbed by a neutron-proton pair within the nucleus. Levinger related the probability for this event to the photodisintegration cross section of the deuteron, and obtained the relation

$$\sigma_{\mathrm{Q.D.}} = \frac{L}{A}\sigma_D , \qquad (1)$$

where A is the atomic mass number, σ_D is the (experimental) value of the photo-deuteron cross section, and L is a constant independent of the atomic mass number and photon energy. The best value of L will be obtained by comparing the calculated results with several experiments and, once determined, will remain that value for all future calculations.

Since photon absorption by a proton-neutron pair within a nucleus and photodisintegration of the deuteron are not on the same energy shell, we calculate the center-of-mass emergent angle of the proton from the differential deuteron cross section corresponding to a "pseudo-photon" energy. The pseudo-photon energy is obtained through the requirement that the total energy in the center-of-mass system associated with each process mentioned above be the same. For pseudo-photon energies below 140 MeV the theoretical differential cross sections for photodeuteron disintegration obtained by Partovi[8] are being used, and above 140 MeV the experimental differential cross sections obtained by Keck and Tollestrup[9] are used. Also taken into account in the calculations is the exclusion principle. It is required that all final state energies of primary as well as secondary cascading nucleons be above the appropriate Fermi energy.

Since most of the data is produced by bremsstrahlung photons or bremsstrahlung difference photons, the cascade calculations use the theoretical bremsstrahlung spectrum obtained by Schiff.[10] However, calculations with monoenergetic photons can also be obtained.

The calculations should be valid for photon energies from ~50 MeV up to ~180 MeV, where pion production becomes significant. Even though calculations with photon energies below 50 MeV can be done, it is not yet possible to determine photon energy below which the quasi-deuteron process ceases to be the major mechanism of interaction.

Further calculations incorporating in the initial interaction single pion production as well as the quasi-deuteron process are in progress. In these calculations the pion is assumed to be formed via the (3/2,3/2) isobaric state, i.e.,

photon + nucleon ⟶ isobar ⟶ nucleon + pion;

it is also assumed that the isobar decays isotropically in its rest system. With the addition of single pion production the energy range in which the calculations should be valid is extended to ~300 MeV.

Figure 6.2.1, which shows the energy spectrum of emergent neutrons at 67.5° from Cu, gives a

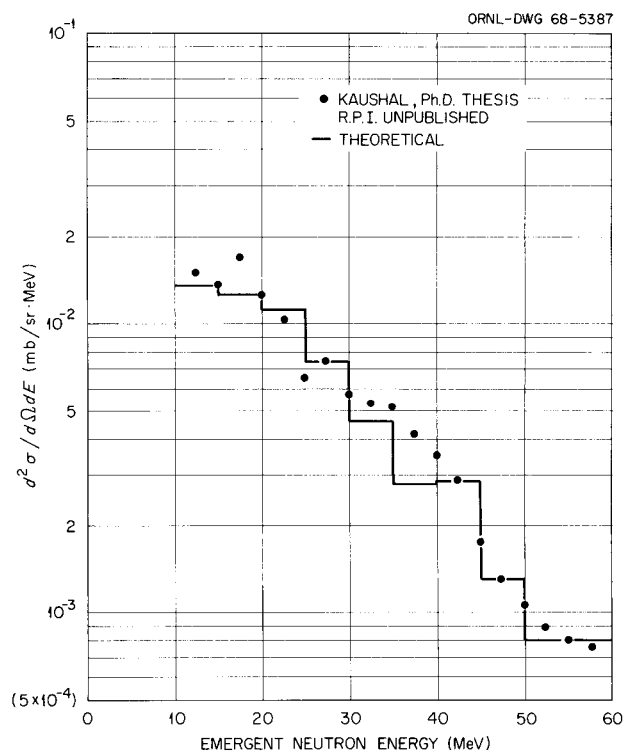

Fig. 6.2.1. Emergent Neutrons at 67.5° from ^{63}Cu. The photons result from a 55-, 85-MeV bremsstrahlung difference spectrum. Errors are of the order of 20 to 30% for both experimental and theoretical values.

comparison between the Monte Carlo cascade calculations and the experimental results of Kaushal.[11] The photons producing the neutron spectrum resulted from the difference of two bremsstrahlung spectra with maximum photon energies of 85 and 55 MeV.

References

[1]Oak Ridge Graduate Fellow from the University of Tennessee under appointment from the Oak Ridge Associated Universities, Inc.

[2]J. S. Levinger, *Phys. Rev.* **84**, 43 (1951).

[3]H. W. Bertini, *Phys. Rev.* **131**, 1801 (1963), and *Monte Carlo Calculations on Intranuclear Cascades*, ORNL-3383 (1963).

[4]K. G. Dedrick, *Phys. Rev.* **100**, 58 (1955).

[5]K. Gottfried, *Nucl. Phys.* **5**, 557 (1958).

[6]J. L. Matthews, Ph.D. thesis, MIT, 1967.

[7]S. Fujii, *Nuovo Cimento* **XXV**, 3403 (1962).

[8]F. Partovi, *Ann. Phys. (N.Y.)* **27**, 79 (1964).

[9]J. C. Keck and A. V. Tollestrup, *Phys. Rev.* **101**, 360 (1956).

[10]L. I. Schiff, *Phys. Rev.* **83**, 252 (1951).

[11]N. N. Kaushal, Ph.D. thesis, RPI, 1967.

6.3 VARIATION OF THE NEUTRON SPECTRUM IN THE FORWARD DIRECTION WITH CHANGES IN THE NUCLEAR DENSITY DISTRIBUTION USED IN THE INTRANUCLEAR CASCADE CALCULATION[1]

Hugo W. Bertini

A discrepancy between the calculated and experimental neutron spectrum at 2° from 140-MeV protons on aluminum has been observed and discussed previously.[2] The cascade model that was used in the calculation is described briefly in Section 6.5, this report. The only difference is that meson production was ignored for the present work. The discrepancy is in the failure of the calculation to predict as many neutrons emitted with energies between 20 and 100 MeV as are observed, while at the same time a much sharper "quasi-elastic" peak is predicted compared with the observed peak; i.e., the calculation predicts a greater peak-to-valley ratio than is measured. An attempt was made to reduce the discrepancy by altering the density distribution of nuclear matter vs nuclear radius in the calculation to determine whether the discrepancy is really inherent in the model.

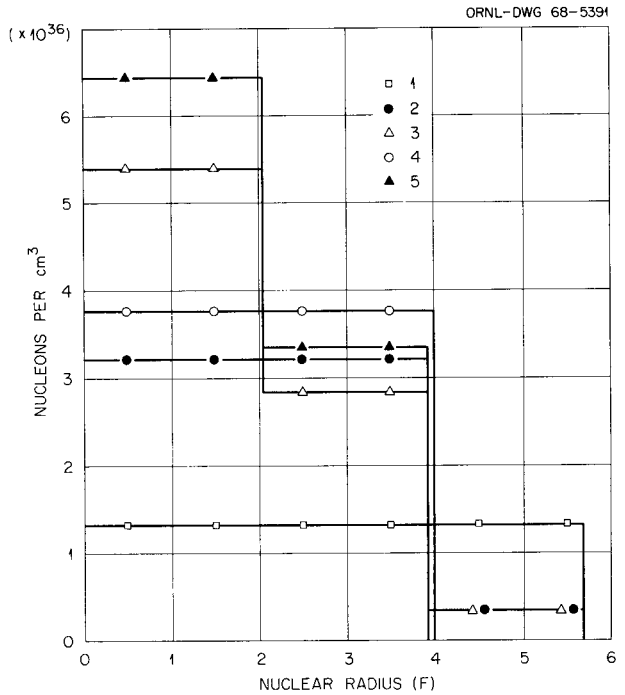

Fig. 6.3.1. The Various Nucleon Density Distributions vs Nuclear Radius Used in the Calculation of the Neutron Spectrum.

In describing the various distributions, the following terminology is adopted: The central region of the three-region nucleus is called the core; the next region, the spherical annulus surrounding the core, is called the skin; and the outermost region is called the mantle. The various density distributions are shown in Fig. 6.3.1. Distribution No. 1 is a uniform distribution throughout with a large radius. Number 2 consists of a uniform skin and core with the standard mantle. Number 3 is the standard three-region configuration, which is used in most of our calculations. Number 4 is a uniform distribution throughout, but with an outer radius (smaller than No. 1) such that this distribution has the same rms value as the standard configuration, No. 3. Number 5 has almost the same radius as No. 4, but the density of the core is greater than that of the skin.

All the distributions illustrated were normalized so that the integral of the density over the nuclear volume was 1. The proton and neutron densities that were used in the calculation were obtained by multiplying the densities illustrated by the

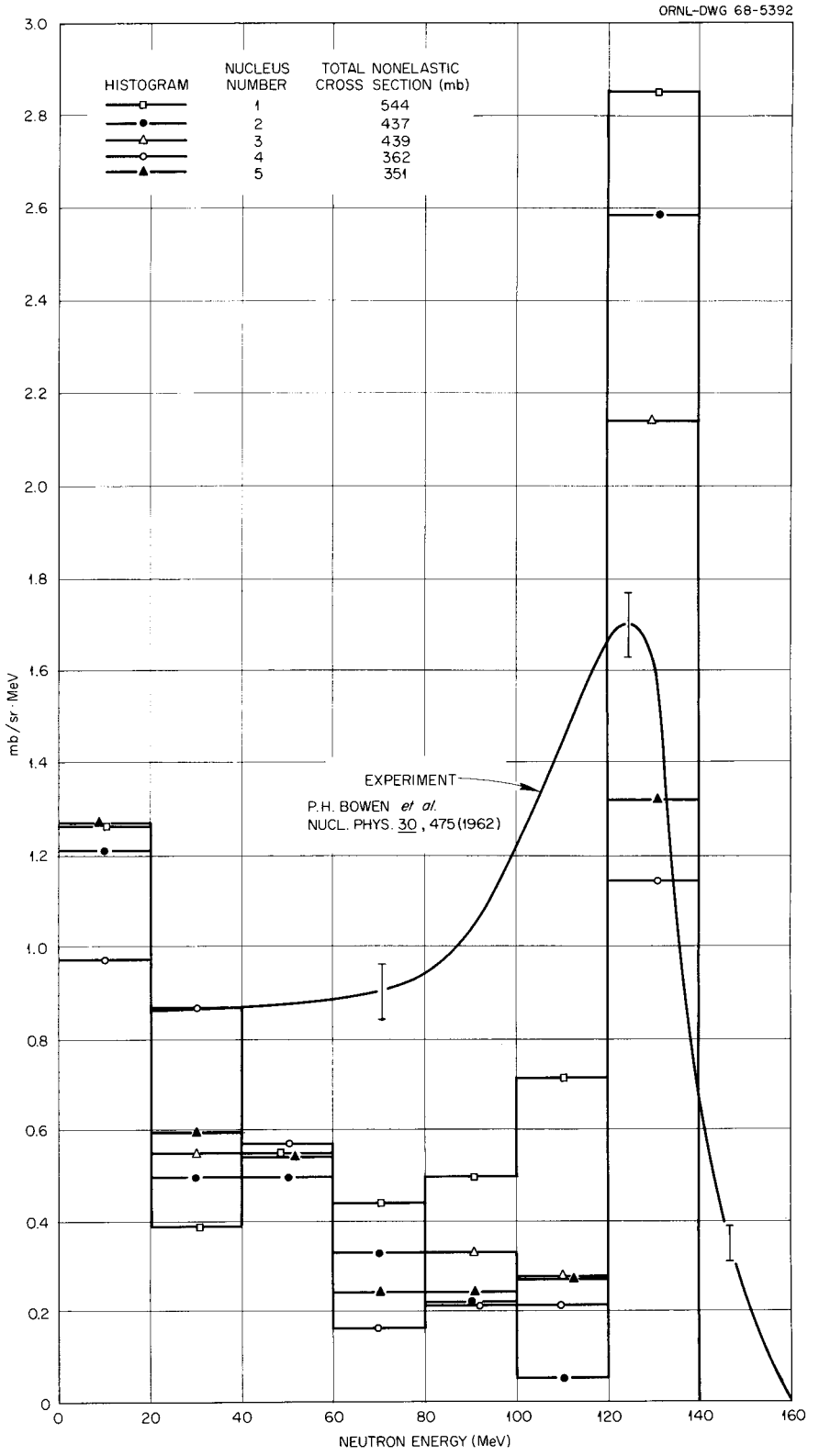

Fig. 6.3.2. Neutron Energy Spectrum at 2° from 143-MeV Protons on Aluminum. The smooth curve with error bars represents the experimental data of Ref. 2. The histograms are the calculated neutron spectra for neutrons emitted into the angular interval 0–7° from 140-MeV incident protons where each density distribution of Fig. 6.3.1 has been used for the target.

number of protons and the number of neutrons in the aluminum nucleus.

The neutron spectrum in the forward direction from each of the distributions is illustrated in Fig. 6.3.2. The experimental data are also shown.[3]

All the distributions fail to improve the discrepancy in the middle of the energy range. The only distribution that shows some promise in this respect is No. 1, but the peak from this distribution is considerably higher than the measured peak, while the total nonelastic cross section (tabulated in the figure) has increased significantly. When reflection and refraction are included in the calculation, the discrepancy persists.[4]

One can conclude, with little reservation, that the cascade model is incapable of providing the values of the spectrum in the middle of the energy range that correspond to existing experiments for neutrons emitted at small forward angles in the reaction described.

A calculation is in progress that will compare the neutron spectrum from the breakup reaction of protons on deuterium with that for protons on free neutrons. The latter process will yield a peak that is similar to the calculated peak in Fig. 6.3.2, while the former may provide a means of inducing the emission of forward-moving neutrons with the required energies.

References

[1]Work partly funded by National Aeronautics and Space Administration under NASA Orders R-104 (1) and H-38280A.

[2]H. W. Bertini, *Phys. Rev.* **162**, 976 (1967).

[3]P. H. Bowen *et al.*, *Nucl. Phys.* **30**, 475 (1962).

[4]J. M. Miller, Columbia University; private communication. For a description of this calculation and for a comparison of the calculated and measured neutron spectrum at 2° for a lead target, where the same type of discrepancy exists, see K. Chen *et al.*, *Phys. Rev.* **166**, 949 (1968).

6.4 SPECTRA FROM INTRANUCLEAR-CASCADE CALCULATIONS USING THREE ISOLATED REGIONS OF THE NUCLEUS FOR 200-MeV PROTONS ON COPPER[1]

Hugo W. Bertini

With a small modification in the program for the calculation of intranuclear cascades, the target nucleus was made to consist of only one region at a time out of the three regions normally used.[2] The object of this investigation was to try to determine what nuclear region, if any, was the main contributor to the various channels available in the final state for nuclear reactions of a few hundred MeV. The reaction discussed here is for 200-MeV protons on copper, and the channels investigated are those leading to secondary proton emission at a few angles.

Spectra were calculated when the nucleus consisted of only the central (and most dense) region, called the core; when it consisted of only the next surrounding spherical annulus (with a smaller density), called the skin; and when it consisted of only the outermost (and least dense) surrounding annulus, called the mantle. For example, when the nucleus consisted of the mantle only, the density of the skin and core was set equal to zero.

Clearly, no separation of the various contributions is possible by this method when a reaction channel is made up of successive interactions that have taken place from region to region. On the surface, the secondary proton spectrum between 0 and 10°, illustrated in Fig. 6.4.1, might appear to be such a channel, but Figs. 6.4.2 and 6.4.3, which illustrate the proton spectra at wider angles, show a distinct separation. It is readily apparent that at the wider angles the secondary particle spectra consist almost entirely of reactions that have taken place in the nuclear skin.

For the spectra in the forward direction illustrated in Fig. 6.4.1, one can estimate the contribution to the high-energy peak from the skin and mantle (the contribution from the core is seen to be small) by the following considerations: In order to contribute to the peak, the scattered proton must come out approximately along the same line as the incident proton. Subtract from the mantle's contribution those protons which must have passed through the skin and core. This fraction of the total contribution is estimated to be proportional to the fraction of the total cross-sectional area made up of the skin and core. Similarly, subtract from the contribution of the skin those protons which must have passed through the core. In this manner, admittedly crude, one finds that about one-third of the total contribution to the peak comes from the mantle and that the remainder comes from the skin.

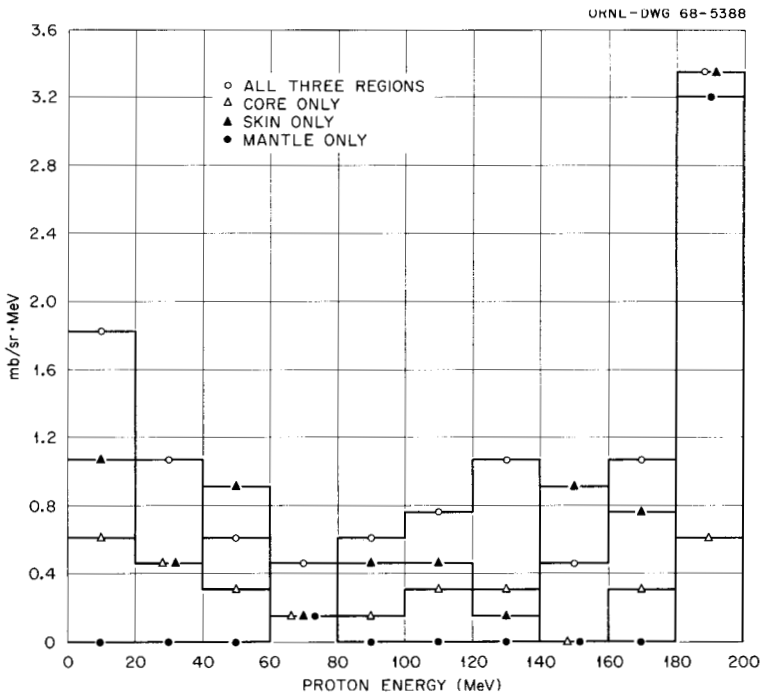

Fig. 6.4.1. Energy Spectra of Secondary Protons Emitted into the Angular Interval 0 to 10° from 200-MeV Protons on Copper. The artificial nuclear density distributions used for the target nucleus are described in the text.

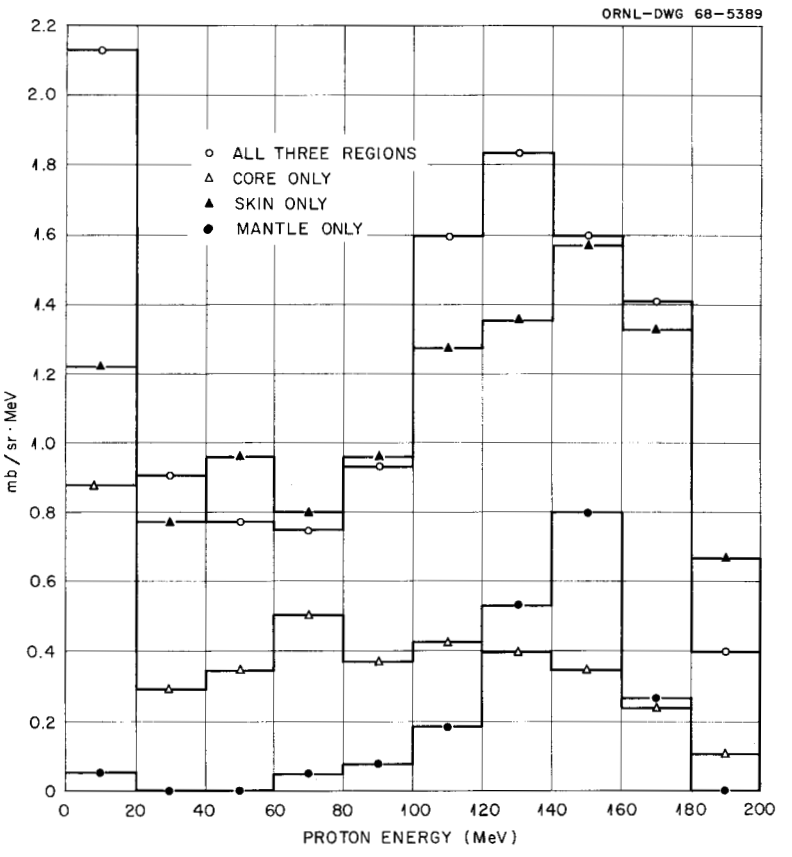

Fig. 6.4.2. Energy Spectra of Secondary Protons Emitted into the Angular Interval 25 to 35°. See text for description of density distribution of target.

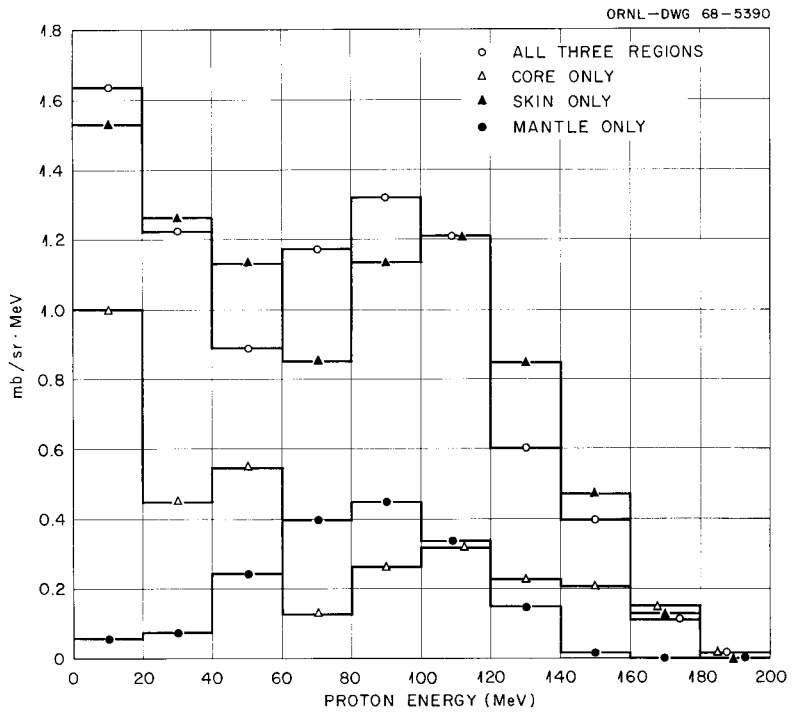

Fig. 6.4.3. Energy Spectra of Secondary Protons Emitted into the Angular Interval 40 to 50°. See text for description of density distribution of target.

The contribution from each nuclear region to other reaction channels is under investigation.

References

[1]Work partly funded by National Aeronautics and Space Administration under NASA Orders R-104(1) and H-38280A.

[2]H. W. Bertini, *Phys. Rev.* **131**, 1801 (1963). See Section 6.5, this report, for a brief description of the calculation, which in the present case does not include meson production, and Section 6.3 for a description of the three regions normally used.

6.5 SECONDARY PARTICLE SPECTRA FROM THE INTERACTION OF 450-MeV PROTONS ON COMPLEX NUCLEI[1]

H. W. Bertini J. W. Wachter

The intranuclear cascade approach was used in the calculation of the neutron and proton spectra from 450-MeV protons on aluminum and bismuth. This means that the calculated spectra consist of particles that have escaped from the nucleus at some stage of the cascade, which is initiated by the incident particle striking one of the nucleons inside the nucleus and which is generated by the collision of the reaction products from this collision with other nucleons in the nucleus, etc. The individual particle-particle reactions that take place within the nucleus are assumed to be free-particle reactions, and the free-particle scattering and π-meson production cross sections are used to determine the types of reactions. The free-particle differential cross sections were used to determine the scattering angles (and thereby the energies) of the scattered particles, while the Lindenbaum-Sternheimer[2] isobar model was used to determine the energies, charges, and directions of the particles emanating from π-meson production reactions. In this calculation the angular distribution of the isobar was assumed to be 50% isotropic, 25% forward, and 25% backward. The isobar was made to decay isotropically in its own

rest system. The diffuseness of the nuclear surface of the target nucleus was accounted for by making a three-step approximation to Hofstadter's nuclear charge density vs nuclear radius.[3] Other details of the target configuration are described elsewhere.[4]

Comparisons of the calculated proton and neutron spectra at several angles from 450-MeV protons on aluminum with the experimental data of Wachter, Burrus, and Gibson[5] are shown in Figs. 6.5.1 and 6.5.2.

The comparisons with the proton spectra, shown in Fig. 6.5.1, indicate a fairly reasonable agreement. There is a discrepancy in the neutron spectrum at 20°, shown in Fig. 6.5.2, where the calculated "quasi-elastic" peak appears at a higher energy than is indicated by the experiments. The position and magnitude of the calculated peak are about where they would be expected to be from the "quasi-free" scattering of a proton by a bound nucleon in the nucleus. Hence the discrepancy is unexplained.

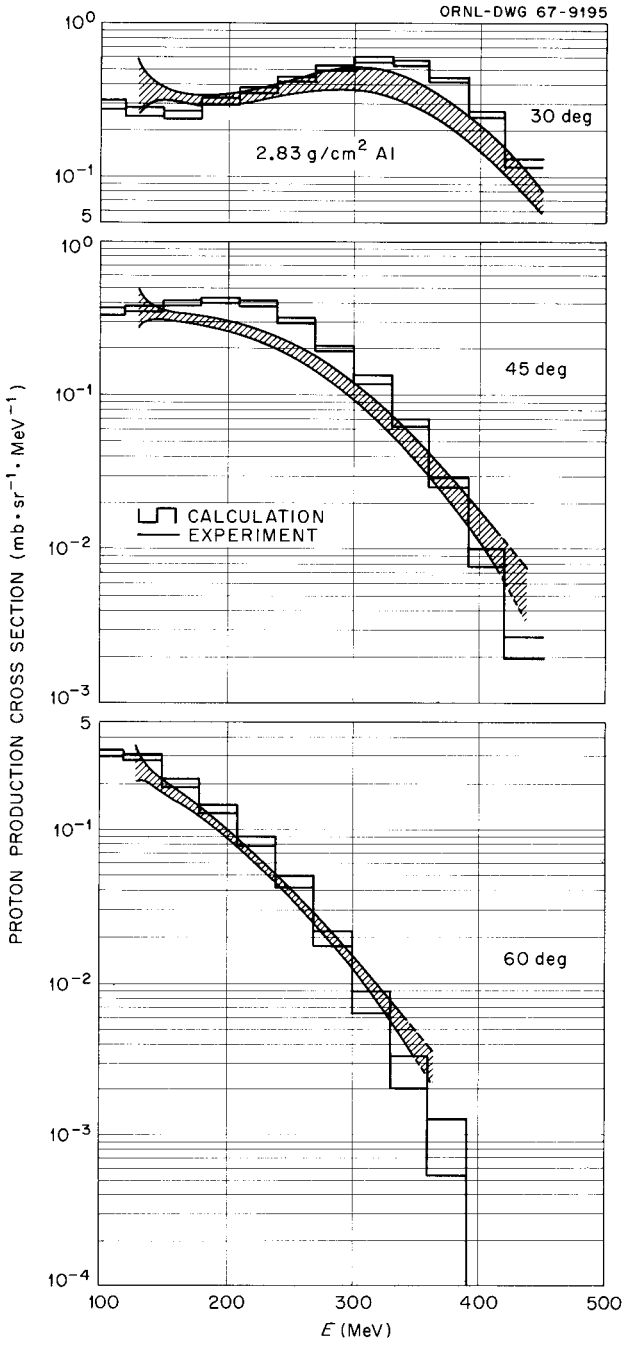

Fig. 6.5.1. Secondary Proton Spectra from 450-MeV Protons on Aluminum. The hatched area indicates the 68% confidence interval of the experimental data. The calculated data has been "smeared" (by the authors of Ref. 4) to correspond to the same response function of the experimental instruments.

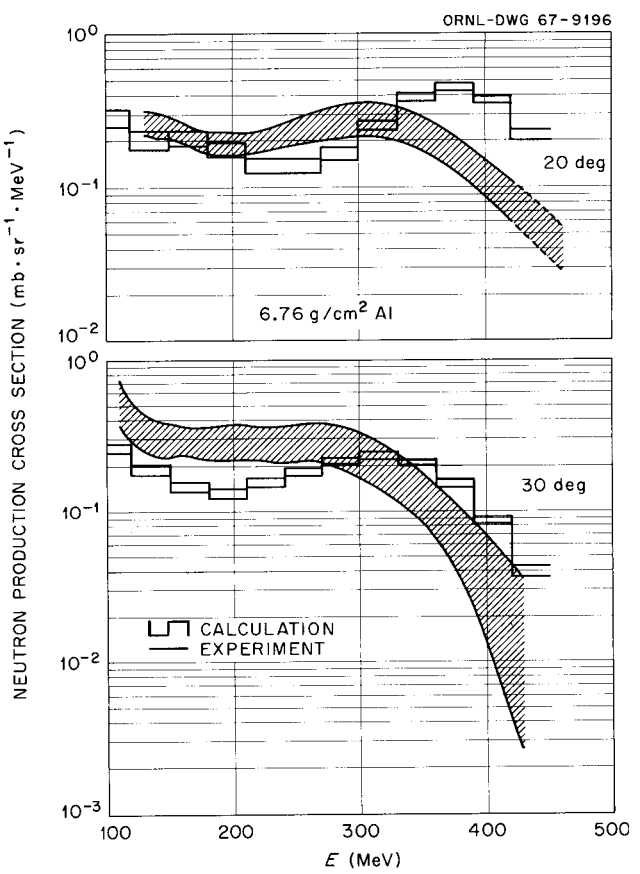

Fig. 6.5.2. Secondary Neutron Spectra from 450-MeV Protons on Aluminum. See Fig. 6.5.1 for comments on the experimental and calculated data.

A comparison of the proton spectra at a few angles from 450-MeV protons on bismuth is shown in Fig. 6.5.3. The agreement is excellent.

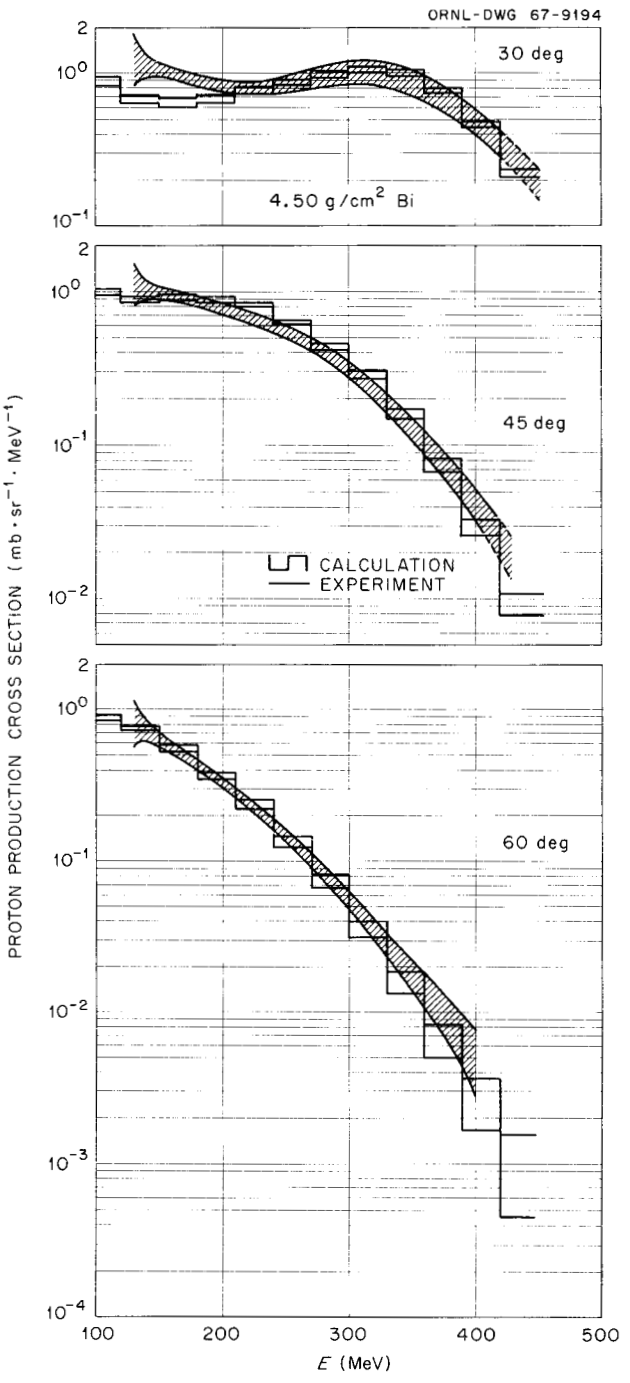

Fig. 6.5.3. Secondary Proton Spectra from 450-MeV Protons on Bismuth. See Fig. 6.5.1 for comments on the experimental and calculated data.

References

[1]Work partly funded by National Aeronautics and Space Administration under NASA Orders R-104(1) and H-38280A.

[2]R. M. Sternheimer and S. J. Lindebaum, *Phys. Rev.* **123**, 333 (1961); *Phys. Rev.* **109**, 1723 (1958); *Phys. Rev.* **105**, 1874 (1957).

[3]R. Hofstadter, *Revs. Mod. Phys.* **28**, 214 (1956).

[4]Hugo W. Bertini, *Phys. Rev.* **131**, 1801 (1963).

[5]J. W. Wachter, W. R. Burrus, and W. A. Gibson, *Neutron Phys. Div. Ann. Progr. Rept. Aug. 1, 1965*, ORNL-3858, Vol. II, p 88.

6.6 PROTON SPECTRA FROM 2.7-GeV PROTONS ON Ag, Br NUCLEI[1]

D. T. King[2]

Despite the long-established availability of monoenergetic particle beams of sufficient energy to ensure complete nuclear spallation ($\gtrsim$2 GeV), there has been remarkably little published[3] regarding the particle spectra produced by collisions of such beams with complex nuclei. Most of the experimental work has been directed toward the production characteristics of pions and strange particles. With the development of computer programs written to reproduce the intranuclear-cascade process, however, a theoretical model has become available by which the observations of nuclear spallation can be interpreted and compared. For these reasons the recent appearance of a paper[4] giving extensive results on particle spectra produced by the bombardment of Be and Pt by 2.9-GeV protons is of great interest.

A notable characteristic of these published results is found in the momentum spectra of the emergent protons at both 13 and 93°. These spectra show a pronounced maximum, at ~0.7 GeV/c for 13° and at ~0.35 GeV/c for 93°, regardless of the target. Since this aspect of the proton spectrum is contrary to our experience and also in disagreement with preliminary results from the Monte Carlo program, it was decided to carry out further measurements on emergent protons with energies between 80 and 850 MeV in an attempt to resolve this point. We had in the laboratory some old nuclear emulsions which had been exposed to the 2.7-GeV internal circulating proton beam of the Brookhaven Cosmotron. These

ten plates, each 2 in. × 3 in., were Ilford-G5 emulsions each 400 μ thick, with the proton beam parallel to the emulsion plane. In preceding studies the energies of the beam protons in the emulsion had been verified both by multiple-scattering measurements[5] and by kinematic analysis of those two-prong stars which satisfied the coplanarity requirement for elastic proton-proton collisions.[6]

The nuclear interactions caused by beam particles in 5.0 cm^3 of the emulsion were examined closely. From previous studies in which beam-particle collisions were found by following beam tracks, the cross section for collision by 2.7-GeV protons in all emulsion nuclei was determined to be 1070 ± 110 mb. Taking into account the emulsion composition,[7] the cross section for collision in Ag and Br nuclei was then 740 ± 100 mb. In the same study it was also possible to identify the collisions in Ag and Br as those which showed five or more heavily ionized prongs. In the 5.0 cm^3 of emulsion examined, we recorded 3565 examples of beam collisions which satisfied this criterion of a medium-weight nuclear target and which, in addition, were located more than 30 μ from an emulsion interface. The emergent tracks from these collisions were subjected to close scrutiny.

An ionization calibration experiment has determined that in this emulsion stack the values of track grain density in the range 23–80 grains/100 μ correspond to singly charged particle velocities between 0.85 and 0.39 c. For protons this range of ionization therefore represents the kinetic energy interval 850–80 MeV. Emergent tracks from Ag, Br stars with ionization in this range and of track length exceeding 3.0 mm were therefore recorded. The length requirement was imposed both as a means of applying a geometric correction for tracks lost through large angles of dip and also afforded a method for distinguishing charged pions from the emergent protons through observation of the multiple Coulomb scattering.[8] After exclusion of the charged-pion tracks we found 646 long tracks of protons emergent with kinetic energies between 80 and 850 MeV from 3565 collisions of 2.7-GeV protons in Ag and Br.

The projection on the emulsion plane of the polar angle of emission was determined for each of these 646 proton tracks of visible length exceeding 3.0 mm. A 10° interval in the projected polar angle then corresponds to an emission solid angle 2 × 0.023 = 0.046 sr. For emission polar angles increasing from 0° through 90° and thence to 180°, it then becomes necessary to apply a geometric correction factor varying from 2.01 through 23.5 and thence back to 2.01 in order to take account of tracks emitted at sufficiently large dip angles that the visible track length is less than 3.0 mm. The angular distribution for the observed and corrected proton emission is given in Table 6.6.1. From these data it is seen that the 646 proton tracks of visible length exceeding 3.0 mm correspond to a total emission of 7259 proton tracks from the 3565 Ag, Br stars. Taking the average Ag, Br collision cross section to be 740 ± 100 mb, it is then deduced that the total emission cross section for protons in the interval 80–850 MeV is 1500 ± 200 mb, corresponding to 2.04 cascade protons (within this energy range) from each Ag, Br collision of a 2.7-GeV proton.

The intranuclear-cascade program has been employed in making a prediction of the emission of protons with kinetic energies between 80 and 850 MeV from ^{100}Ru bombarded by 2.7-GeV protons.[9] The angular distribution results from 5000 histories are shown in Fig. 6.6.1, together with

Table 6.6.1. Observed and Corrected Proton Emission Angular Distributions

$\Delta\theta_{proj}$ (deg)	N_{obs}	N_{corr}
0–10	146	293
10–20	125	760
20–30	85	840
30–40	62	848
40–50	34	567
50–60	42	814
60–70	33	706
70–80	32	729
80–90	24	564
90–100	14	329
100–110	11	251
110–120	11	235
120–130	8	155
130–140	1	17
140–150	4	55
150–160	6	59
160–170	5	30
170–180	3	6.0

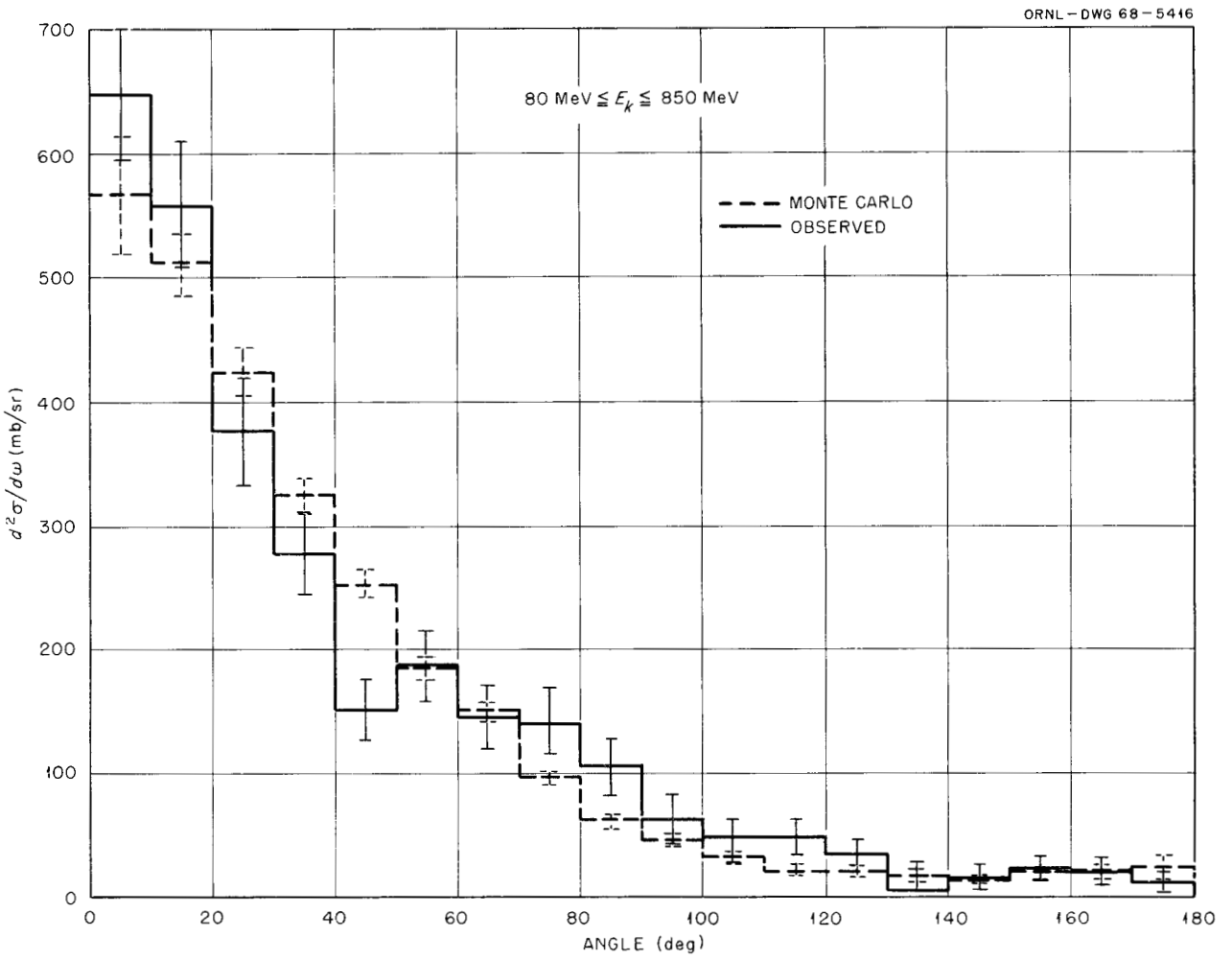

Fig. 6.6.1. Cascade Protons from 2.7-GeV Protons on Ag, Br: Angular Distribution.

the results of this experiment. The agreement appears satisfactory.

In order to make a more detailed examination of the proton emission spectra, it is necessary to concentrate attention on the data within a limited range of polar angle and to study the energy distribution of this material after appropriate geometric correction.

We have derived the proton spectrum at forward angles from our observations on 356 proton tracks emitted at polar angles $<30°$. Similarly, the proton spectrum at large angles is based on 86 tracks with polar angles between 70 and 110°. The proton energy distribution is extracted in intervals of varying width so that the statistical significance in each interval is approximately uniform. In Fig. 6.6.2 the 80- to 850-MeV proton spectral results of this experiment are compared with the corresponding predictions of the intranuclear-cascade program for 2.7-GeV protons on ^{100}Ru. At forward angles, $<30°$, the agreement is evidently close, while at large angles, 70–110°, the observed spectrum appears to rise rather more steeply toward lower proton energies than that calculated by the cascade program. Our experimental spectra are in substantial agreement with the Monte Carlo calculations with regard to the monotonic increase in proton intensity toward lower energies. In particular, we find no evidence for a spectral maximum in the 250- to 300-MeV region at forward angles. For contrast with our results, the proton spectrum at 13° from 2.9-GeV protons on Pt, from Ref. 4, has been included in Fig. 6.6.2.[10]

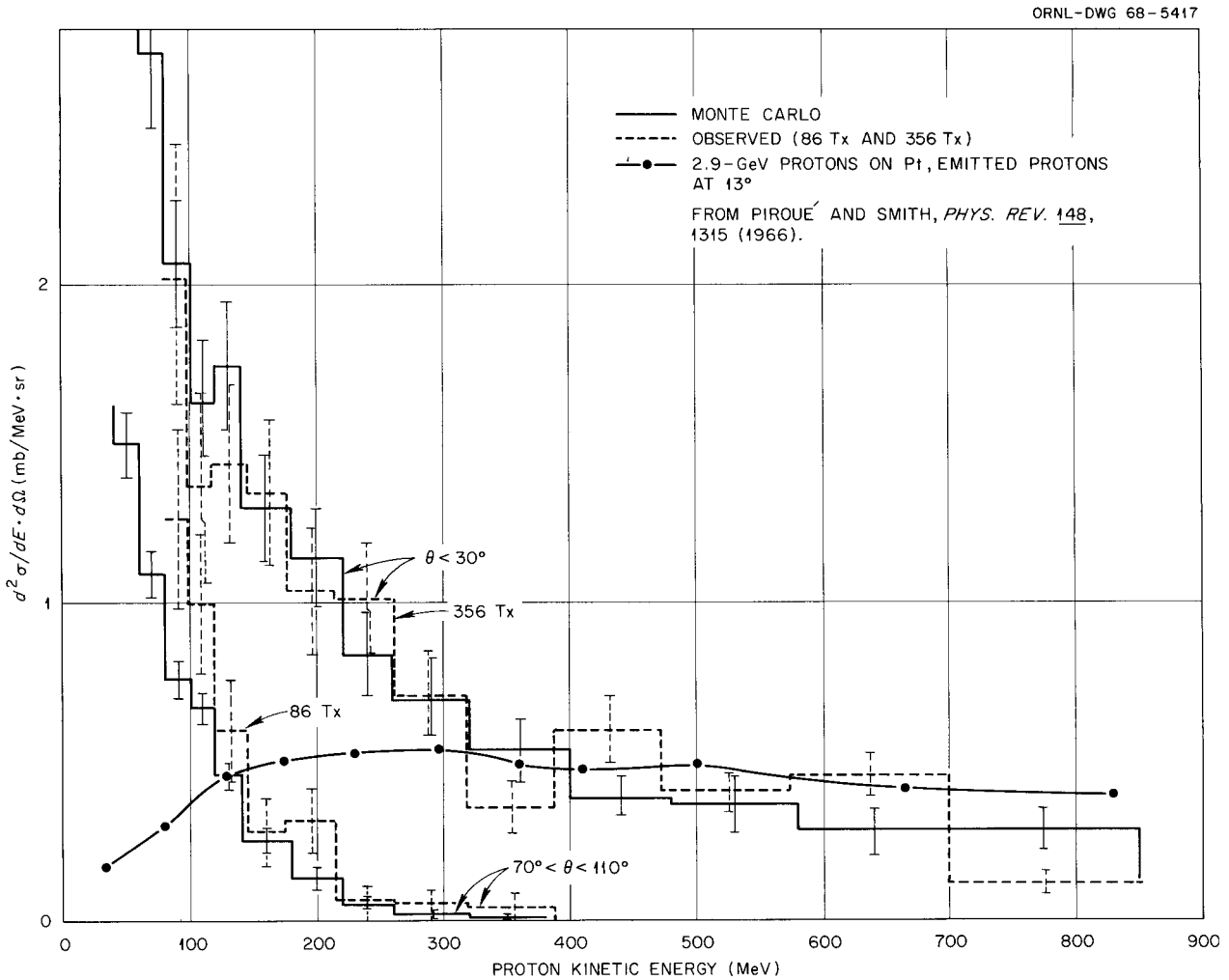

Fig. 6.6.2. Cascade Protons from 2.7-GeV Protons on Ag, Br.

References

[1]Work partly funded by National Aeronautics and Space Administration under NASA Orders R-104(1) and H-38280A.

[2]Consultant from the University of Tennessee, Knoxville.

[3]W. B. Fowler *et al.*, *Phys. Rev.* **91**, 479 (1953).

[4]P. A. Piroué and A. J. Smith, *Phys. Rev.* **148**, 1315 (1966).

[5]L. Voyvodic and E. Pickup, *Phys. Rev.* **85**, 91 (1952).

[6]R. Cester, T. F. Hoang, and A. Kernan, *Phys. Rev.* **103**, 1443 (1956).

[7]W. H. Barkas, *Nuclear Research Emulsions*, p. 74, Vol. 1, Academic Press, New York, 1963.

[8]The multiple scattering observations were insufficiently accurate to ensure discrimination of either charged kaons or deuterons. It is expected that this source of error is smaller than 2% in any interval.

[9]H. W. Bertini, *Neutron Phys. Div. Ann. Progr. Rept. May 31, 1967*, ORNL-4134, p. 113.

[10]These results have been communicated to Professor Piroué, and he feels that because of energy losses in his target his low-energy results are not comparable to those presented here.

6.7 PION-NUCLEON DIFFERENTIAL CROSS SECTIONS IN THE 0 TO 700-MeV ENERGY REGION IN TERMS OF THE COULOMB SCATTERING AMPLITUDE, COULOMB PHASE SHIFTS, AND NUCLEAR PHASE SHIFTS UP TO $l = 4$[1]

Hugo W. Bertini

A derivation of the expression for the pion-nucleon differential scattering cross section in terms of the nuclear phase shifts is presented. It follows that of Ashkin. The method for altering this expression in order to obtain the cross section for all charge states of the pion and nucleon is described where simple isotopic spin analysis is employed. Coulomb and absorption effects are incorporated in the manner described by Roper, Wright, and Feld. A detailed and lengthy equation for the cross section in terms of the electromagnetic amplitudes, Coulomb phase shifts, and nuclear partial-wave amplitudes is presented where the multiplication of the usual series expansion for the cross section has been carried out for terms up to $l = 4$. Instructions are given for the substitution of appropriate expressions into the equation for the cross section so that it will apply to each charge state of the pion and nucleon. These expressions are functions of the nuclear phase shifts, the Coulomb phase shifts, and the absorption parameters. A table of the phase shifts and absorption parameters published by Roper *et al.* is included. The work described in this report will be utilized in an intranuclear cascade calculation for interactions up to about 3 GeV.

Reference

[1]Abstract of ORNL-4197 (in press); work partly funded by the National Aeronautics and Space Administration under NASA Orders R-104(1) and H-38280A.

6.8 EVAP-2, A MODIFIED VERSION OF THE EVAPORATION CODE EVAP[1]

Miriam Guthrie

Dresner's FORTRAN code, EVAP,[2] calculates the evaporation of particles from excited compound nuclei. Modified versions of EVAP are associated with several codes used in shielding calculations, including Bertini's intranuclear cascade codes[3] and the Nucleon Transport Code NTC.[4] The purpose of EVAP-2 is to update the nuclear masses used by EVAP and to incorporate the most desirable modifications from earlier versions into one "standard" code, which will be used with all the shielding codes.

EVAP-2 has two alternate main programs. One program is used to analyze the history tapes from Bertini's intranuclear cascade codes. The second program is to be used with EVAP-2 alone, which is the form used in association with NTC. In both cases the entire evaporation calculation is performed by a subroutine DRES and its accompanying subroutines. The main program to be used with Bertini's codes simply scans his history tapes and determines the type and excitation energy of each cascade residual nucleus. The main program to be used with EVAP-2 alone requires that the mass and charge of a target nucleus and the type and kinetic energy of an incident particle be supplied as input data. The type and excitation energy of the resulting compound nucleus are calculated, and the program then calls DRES to perform the evaporation calculation. Seven types of incident particles can be used: neutrons, protons, deuterons, tritons, helium-3 nuclei, alpha particles, and photons. The appearance of the tabulated results is identical, regardless of the main program used.

The nuclear masses used by EVAP were obtained from tables by Wapstra[5] and Huizenga.[6] Mattauch *et al.*[7] have recently published a new tabulation of mass excesses and binding energies, and these data have been used on a new data tape for the EVAP-2 code.

For nuclear masses not provided by the Mattauch tables, the EVAP program uses a semiempirical mass relationship formulated by Cameron.[8] However, no values were provided by Cameron for pairing energy parameters for nuclei with N or Z less than 10. These parameters were set equal to zero in EVAP. Peelle and Aebersold[9] determined new values for the shell-plus-pairing corrections for light nuclei. These values have been incorporated in the Cameron functions on the new data tape for EVAP-2.

In the original EVAP code no provision was made for the breakup of ^{8}Be, which tends to split into two alpha particles instead of evaporating a

lighter particle. In EVAP-2 if a nucleus that has just undergone evaporation or the original cascade residual nucleus has an A value of 8 and a Z of 4, it is assumed that two alpha particles are created. Each alpha particle has an energy equal to one-half the sum of the excitation energy of the ^{8}Be nucleus and the binding energy for the reaction. These alpha particles are then treated as evaporation particles, with no further evaporation taking place.

Because of the Monte Carlo sampling techniques used in the evaporation calculation, it is possible for the kinetic energy selected for the evaporated particle to be too high, resulting in a negative excitation energy for the evaporation residual nucleus. If this happens in EVAP-2, the calculation recycles until a physically reasonable energy is selected for the evaporated particle.

The only other major difference between the original EVAP and EVAP-2 is due to a modification made by Bertini. EVAP-2 calculates the yields, moments of energy distributions, and energy spectra of just 6 evaporated particles instead of the original 18.

References

[1]Work partly funded by National Aeronautics and Space Administration under NASA Orders R-104(1) and H-38280A.

[2]L. Dresner, *EVAP–A FORTRAN Program for Calculating the Evaporation of Various Particles from Excited Nuclei*, ORNL-TM-196 (1961).

[3]H. W. Bertini, *Phys. Rev.* **131**, 1801 (1963). Also, *Monte Carlo Calculations on Intranuclear Cascades*, ORNL-3383 (1963).

[4]W. E. Kinney, *The Nucleon Transport Code, NTC*, ORNL-3610 (1964).

[5]A. H. Wapstra, *Physica* **21**, 378 (1955).

[6]J. R. Huizenga, *Physica* **21**, 419 (1955).

[7]J. H. E. Mattauch *et al.*, *Nucl. Phys.* **67**, 1 (1965).

[8]A. G. W. Cameron, *Can. J. Phys.* **35**, 1021 (1957) and **36**, 1043 (1958).

[9]R. W. Peelle and P. M. Aebersold, *Energy Parameters for Light Nuclides in Monte Carlo Nuclear Evaporation Programs Based on EVAP*, ORNL-TM-1538 (1966).

6.9 NCDATA – NUCLEAR COLLISION DATA FOR NUCLEON-NUCLEUS COLLISIONS IN THE ENERGY RANGE 25 TO 400 MeV[1]

R. G. Alsmiller, Jr. J. Barish[2]

A computer code written in FORTRAN IV is described which interpolates between analytic fits to intranuclear-cascade data and gives for either neutrons or protons, in the energy range 25 to 400 MeV, incident on a nucleus of atomic weight A (between 12 and 238)

1. the nonelastic cross section as a function of energy,
2. the cascade neutron- and proton-emission spectra in the angular intervals 0–30°, 30–60°, 60–90°, and 90–180°,
3. the evaporation neutron- and proton-emission spectra (assumed isotropic),
4. the cascade neutron- and proton-emission spectra integrated over all angles.

In addition to numerical values for each of these quantities, the code also gives the values of the coefficients that occur in an analytic expression for each of these quantities.

References

[1]Abstract of ORNL-4220 (February 1968); work partly funded by the National Aeronautics and Space Administration under NASA Orders R-104(1) and H-38280A, partly funded by the National Aeronautics and Space Administration under Order R-104(10), and partially funded by the Atomic Energy Commission.

[2]Computing Technology Center, Union Carbide Corporation, Oak Ridge, Tennessee.

6.10 CALCULATION OF THE DOSE IN SPHERICAL PHANTOMS AND COMPARISON WITH EXPERIMENT[1]

D. C. Irving R. G. Alsmiller, Jr.
H. S. Moran

Using the Monte Carlo code NTC,[2] calculations of the dose in spherical water-filled phantoms were attempted to compare with the experiments performed by Maienschein and Blosser.[3] These experiments involved beams of 160-MeV protons

incident on various targets. Located behind the target was a spherical phantom of 1.27-cm-thick Lucite walls, 42 cm in diameter, and filled with water. An ionization chamber was used to record the dose at various locations in the phantom. The phantom was placed either in line with the incident beam or at a 45° angle from the projection of the beam through the back of the target. For the case considered here, the dose was recorded at positions along a traverse through the phantom perpendicular to the incident beam. The gas chamber of the ionization counter was a sphere of 1.72-cm radius, and the counter measured the average dose over this volume.

Monte Carlo calculations were carried out using the NTC-05R code system. Intranuclear cascades were computed by the BERT routine of Bertini, and a cutoff of 25 MeV was used in switching from the high-energy transport to the 05R portion of the calculation.[2] The neutron cross sections used below 25 MeV were taken from the 05R library. A P_1 approximation was used for the angular distribution from elastic scattering, and a version of Dresner's evaporation code[4] treated all nonelastic events in 05R. Calculations were made of the energy absorbed in a square tube, 4 cm on a side, running through the center of the phantom perpendicular to the incident beam. The tube was divided into boxes 2 cm thick along its axis. Various variance-reduction techniques were used to improve the statistics of the calculations.

The first case considered was with no target intervened between the beam and the phantom. The dose was recorded along an axis perpendicular to the beam. The primary particles did not penetrate the phantom to the depth where the dose was being obtained, and the dose was due entirely to secondary neutrons and protons. In the calculations for this case the primary protons were forced to have a pseudo collision,[2] 95% of the time with oxygen, and the proton's weight was adjusted accordingly. Whenever a particle entered the tube in which the dose was calculated, its tentative path through the tube was determined and the particle was forced with a 90% probability to have a collision inside the tube. This greatly improved the statistics of the neutron portion of the calculation, as otherwise most neutrons that entered the tube passed straight through without a collision and hence without contributing to the dose. In addition, the low-energy neutrons that

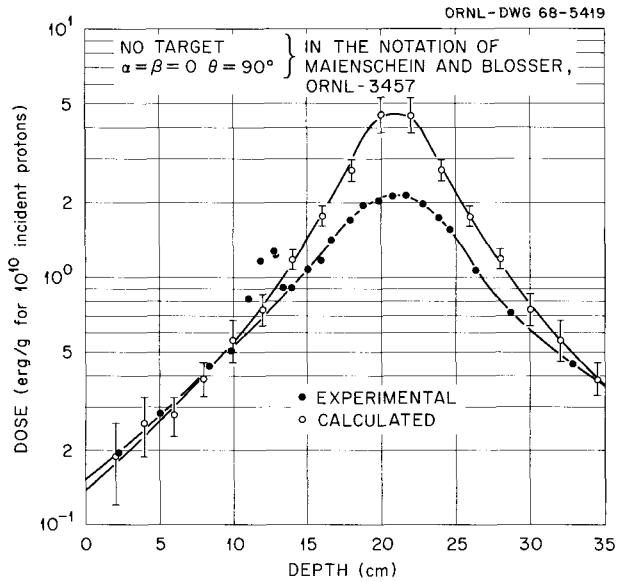

Fig. 6.10.1. Absorbed Dose vs Depth in H_2O Phantom.

were source particles for the 05R portion of the calculation were split into two particles with half the weight. The comparison between the experimental and the calculated results is shown in Fig. 6.10.1. The lines were drawn through the points solely to guide the eye – they have no other significance. The error bars represent one standard deviation in the calculation. The experimental points are as reported by Maienschein and Blosser.[3] The calculated points are a result of averaging the dose absorbed in two adjacent 2-cm-thick boxes. They thus represent the dose averaged over a volume comparable to, although slightly larger than, that of the ionization chambers used in the experiment. To reduce statistical fluctuations, advantage was taken of the symmetry of the situation to average the results from the right and left sides of the phantom. As may be seen in Fig. 6.10.1, the calculation and experiment are in good agreement away from the center but are in substantial disagreement at the peak. There is no explanation as yet for this disagreement.

References

[1]Work partly funded by the National Aeronautics and Space Administration under NASA Orders R-104(1) and H-38280A.

[2]W. E. Kinney, *The Nucleon Transport Code, NTC*, ORNL-3610 (1964).

[3]F. C. Maienschein and T. V. Blosser, *The Depth-Dose Distribution Produced in a Spherical Water-Filled Phantom by the Interactions of a 160-MeV Proton Beam*, ORNL-3457 (1963).

[4]L. Dresner, *EVAP – A FORTRAN Program for Calculating the Evaporation of Various Particles from Excited Compound Nuclei*, ORNL-TM-196 (1961).

6.11 SOLAR NEUTRON TRANSPORT IN THE EARTH'S ATMOSPHERE[1]

R. G. Alsmiller, Jr. R. T. Boughner[2]

The neutron flux per unit energy induced in the earth's atmosphere by solar neutrons has been calculated as a function of atmospheric depth for depths of less than 300 g/cm^2 (~30,000 ft). The calculated flux is compared with estimates of the cosmic-ray neutron flux per unit energy, and it is found that for many flares the solar neutron flux per unit energy is sufficiently above the cosmic-ray neutron flux per unit energy to produce a measurable effect at both balloon and aircraft altitudes.

References

[1]Abstract of ORNL-TM-2194 (in press); work partly funded by the National Aeronautics and Space Administration under NASA Orders R-104(1) and H-38280A.

[2]Mathematics Division.

6.12 THERMAL-NEUTRON FLUX GENERATION BY HIGH-ENERGY PROTONS[1]

W. A. Coleman[2]

The research for this dissertation was performed in two general phases. The first phase consisted of revising NTC, a Monte Carlo computer code that calculates a description of proton and neutron transport below ~450 MeV. Most importantly, the revision includes an extension of the valid energy range to ~3 BeV and a description of the production and transport of π and μ mesons. The basic code theory employed in NTC has been retained in the revised code NMTC. A discussion of the code theory incorporated in NMTC is given in the dissertation, with emphasis on those aspects of the code which differ from NTC.

In the second phase of work, calculations were made using NMTC, and the results were compared with experimental thermal-neutron-flux measurements to determine the validity of the code. In the experiments accelerator protons ranging from 0.54 to 2.0 BeV were used to bombard thick targets of Be, Sn, Pb, and depleted U, which were surrounded by a large water tank. The thermal-neutron flux was measured as a function of position in the water moderator. The calculated thermal-neutron flux distributions using NMTC are in quite good agreement with the experimental results.

The feasibility of producing an intense thermal-neutron flux from high-energy protons in thick targets has received considerable attention in recent years and was the motivation for the experimental measurements mentioned above with which the calculations were compared. Additional calculations have been carried out to obtain information concerning this method of thermal-neutron-flux generation which is not available experimentally. These calculations included

1. thermal-neutron-flux distribution using a Pb target and a D_2O moderator,
2. heat-producing energy release as a function of position in various targets,
3. total heat-producing energy release in the target and moderator,
4. neutron production as a function of position in a Pb target,
5. thermal-neutron-flux distributions in a D_2O moderator using Pb targets of 5- and 10.5-cm radius,
6. comparisons of thermal-neutron-flux distributions in various moderator configurations combining D_2O and H_2O, and using a Pb target.

From the data referred to in 4 and 5 above, observations are made regarding an appropriate shape for a Pb target using 900-MeV incident protons.

References

[1]Abstract of dissertation presented to the Graduate Council of the University of Tennessee, Knoxville, in partial fulfillment of the requirements

for the degree of Doctor of Philosophy and to be published as ORNL-TM-2206; work partly funded by the National Aeronautics and Space Administration under NASA Orders R-104(1) and H-38280A.

[2]Present address: 1Lt. Wayne A. Coleman, U.S. Army Nuclear Defense Laboratory, Edgewood Arsenal, Maryland, 21010.

6.13 MATHEMATICAL VERIFICATION OF A CERTAIN MONTE CARLO SAMPLING TECHNIQUE AND APPLICATIONS OF THE TECHNIQUE TO RADIATION TRANSPORT PROBLEMS[1]

W. A. Coleman[2]

Section I of this paper is a mathematical construction of a certain Monte Carlo procedure for sampling from the distribution

$$F(X) = \int_0^X \Sigma(x) \exp\left[-\int_0^x \Sigma(v)\, dv\right] dx\ ,\quad 0 \le X\ .$$

The construction begins by defining a particular random variable. The distribution function of λ is developed and found to be identical to $F(X)$. The definition of λ describes the sampling procedure. Depending on the behavior of $\Sigma(x)$, it may be more efficient to sample from $F(X)$ by obtaining realizations of λ than by the more conventional procedure described in the paper.

Section II is a discussion of applications of the technique to problems in radiation transport where $F(X)$ is frequently encountered as the distribution function for nuclear collisions. The first application is in charged particle transport where $\Sigma(x)$ is essentially a continuous function of x. An application in complex geometries where $\Sigma(x)$ is a step function and changes values numerous times over a mean path is also cited. Finally, it is pointed out that the technique has been used to improve the efficiency of estimating certain quantities, such as the number of absorptions in a material.

References

[1]Abstract of *Nucl. Sci. Eng.* **32**, 76–81 (1968).

[2]Work performed at ORNL while author was a Graduate Fellow from the Department of Nuclear Engineering, University of Tennessee, Knoxville; present address: 1Lt. Wayne A. Coleman, U.S. Army Nuclear Defense Laboratory, Edgewood Arsenal, Maryland, 21010.

6.14 MONTE CARLO CALCULATIONS OF THE NUCLEON-MESON CASCADE IN IRON INITIATED BY 1- AND 3-GeV PROTONS AND COMPARISON WITH EXPERIMENT[1]

T. W. Armstrong R. G. Alsmiller, Jr.

Results from Monte Carlo calculations of the longitudinal and lateral development of the nucleon-meson cascade in iron initiated by 1- and 3-GeV protons are presented and compared with experimental results. In general, the calculated and experimental results are in good agreement although in the 3-GeV case the calculation yields a smaller buildup of particles for the smaller penetration depths. The Monte Carlo results for the longitudinal development are also compared with available results from a calculation using the straightahead approximation, and the agreement is quite good.

Reference

[1]Abstract of ORNL-TM-2177 (Mar. 1, 1968); work partly funded by the National Aeronautics and Space Administration under NASA Orders R-104(1) and H-38280A.

6.15 RESIDUAL RADIATION LEVELS IN THE TUNNEL OF A 200-GeV PROTON ACCELERATOR AS A FUNCTION OF TIME AFTER SHUTDOWN

T. W. Armstrong R. G. Alsmiller, Jr.

Work is in progress to calculate the shielding and time after shutdown necessary to reduce the residual photon dose from the 200-GeV proton accelerator at the National Accelerator Laboratory to an acceptable level for personnel requiring entry into the accelerator tunnel. This residual radioactivity is produced by two mechanisms: the nucleon-meson cascade induced in the iron magnets and the thermal neutron capture in the concrete enclosure walls. Stray beam losses striking the magnet cavity walls, predominantly

at grazing angles, induce a nucleon-meson cascade which produces, by spallation, radioactive nuclei whose decay gives a source of photons after shutdown. For calculation purposes the magnet can be approximated as an infinite cylinder of iron ~150 g/cm^2 in radius, and the nucleon source initiating the cascade, which as used here is defined by the reaction products (protons and neutrons) of 200 GeV protons on iron, can be described as a line source of uniform strength on the axis of this cylinder. The magnet will be shielded by a layer of concrete followed by a layer of iron. An air space of ~10 ft separates the shield from the concrete tunnel wall. Neutrons escaping the shield can become thermalized and captured in the wall and thus produce radionuclides that yield a second source of residual photons.

To obtain the nucleon source description that initiates the cascade requires a knowledge of the energy and angular distribution of the reaction products from 200-GeV proton interactions, which is not, of course, well known. An empirical formula, originally proposed by Trilling and later extended by Ranft,[1] based on experimental data at lower incident energies and for small production angles is available. Application of the Ranft formula to the present problem, where the most important products are those emitted near 90°, represents a considerable extrapolation of the experimental data. However, a comparison was made of the angle and energy distribution of the reaction products for 3-GeV incident protons on iron nuclei predicted by the Ranft formula with that from the Bertini intranuclear-cascade code,[2] and reasonable agreement was obtained. Thus, in the absence of better information, the Ranft formula will be used.

Since in the present problem the most important reaction products are those emitted at angles near 90° and since the Ranft formula predicts that except at small angles these products have energies <3 GeV, the revised version, NMT,[3] of the NTC Monte Carlo program, which accommodates nucleon energies up to about 3 GeV, can be used to calculate the development of the cascade and the spatial distribution of the residual nuclei. For the transport of neutrons having energies below the energy cutoff used by NMT, the 05R code[4] will be used. With the type and spatial distribution of residual nuclei known, data from standard tables of photon production by radioactive decay can be used to obtain the photon source distribution. The OGRE-G Monte Carlo code[5] will be used to calculate the transport of the photons. From such detailed transport calculations several quantities of interest are directly available: the total photon dose as a function of time at various spatial points, the contribution of each radioisotope to the total dose, etc.

As a first step in working the above problem, calculations to evaluate the ability of the NMT code for determining the spatial distribution of residual nuclei have been carried out and compared with experiment. Experimental results on residual nuclei production in thick iron targets have been reported by Honda[6] for 3-GeV incident protons and by Shedlovsky and Rayudu[7] for 1- and 3-GeV protons. In both experiments a collimated beam of protons was incident normally at the center of one face (30 by 30 cm) of an iron block 90 cm (~700 g/cm^2) in depth, and the radial and longitudinal variations of the production of several radionuclides were measured. A

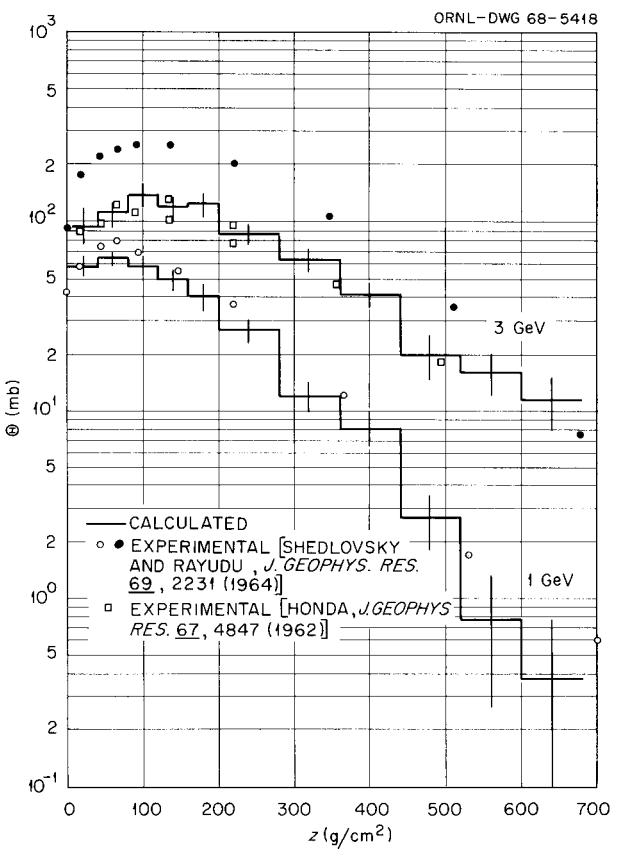

Fig. 6.15.1. Comparison of Calculated and Experimental ^{51}Cr Production from Fe.

comparison of the calculated and experimental longitudinal variation of the production of ^{51}Cr is shown in Fig. 6.15.1. The results are presented in terms of the thick target cross section:

$$\Theta(z) = \left[\sum_{j=P,N,\pi} \int dy \int dx \int_{E_c}^{E_0} dE\, \Phi_j(x,y,z,E)\, N_T \sigma_j(E) \right] \Big/ N_t \,,$$

where

P,N,π = protons, neutrons, and charged pions, respectively;

E_0 = initial proton energy;

E_c = energy below which the contribution to $\Theta(z)$ is negligible; for the results shown in Fig. 6.15.1, E_c = 25 MeV;

$\Phi_j(x,y,z,E)$ = flux of particles of type j per unit energy range per incident proton at position x, y, z;

N_t = atom density of Fe;

$\sigma_j(E)$ = microscopic cross section for the production of ^{51}Cr from Fe by a particle of type j.

The x and y integrations extend over an area defined by a radius of 15 cm about, and normal to, the beam axis. In Fig. 6.15.1 the calculated results represent averages over the depths indicated by the histogram, and the error bars are for statistical errors of one standard deviation. The reason for the discrepancy between the two experimental results in the 3-GeV case is not known; Shedlovsky and Rayudu suggest that it may be due to calibration errors in determining the primary beam strength. These comparisons indicate that the NMT code is adequate for calculating the distribution of residual nuclei in the accelerator magnet. One important advantage of this method of calculation is that explicit knowledge of the microscopic production cross sections, σ_j, is not required since, in effect, they are computed by the code in the course of the transport calculation.

References

[1]J. Ranft, *Nucl. Instr. Methods* **48**, 133 (1967).

[2]H. W. Bertini, *Preliminary Data from Intranuclear-Cascade Calculations of 0.75-, 1-, and 2-GeV Protons on Oxygen, Aluminum, and Lead, and 1-GeV Neutrons on the Same Element*, ORNL-TM-1996 (1967).

[3]W. A. Coleman, *Thermal-Neutron Flux Generation by High-Energy Protons*, dissertation presented to the Graduate Council of the University of Tennessee in partial fulfillment of the requirements for the degree of Doctor of Philosophy (to be published as ORNL-TM-2206).

[4]D. C. Irving *et al.*, *05R, A General-Purpose Monte Carlo Neutron Transport Code*, ORNL-3622 (1965).

[5]D. K. Trubey and M. B. Emmett, *OGRE-G, An OGRE System Monte Carlo Code for the Calculation of Gamma-Ray Dose Rate at Arbitrary Points in an Arbitrary Geometry*, ORNL-TM-1212 (1966).

[6]M. Honda, *J. Geophys. Res.* **67**, 4847 (1962).

[7]J. P. Shedlovsky and G. V. S. Rayudu, *J. Geophys. Res.* **69**, 2231 (1964).

6.16 HIGH-ENERGY MUON TRANSPORT AND THE MUON BACKSTOP FOR A 200-GeV ACCELERATOR

R. G. Alsmiller, Jr. M. Leimdorfer[1]
J. Barish[2]

After the high-energy proton beam interacts with the target in the proposed 200-GeV accelerator, there will be a large number of high-energy pions predominantly in the forward direction.[3] These high-energy pions will decay into high-energy muons, and to stop these muons a massive shield will be required. Muon transport calculations have been carried out to determine the size and shape of this shield.

In the calculations the target is assumed to be sufficiently small that it may be approximated by a point, and the energy and angular distribution of the pions from the target is taken from the work of Trilling.[4] From this distribution the energy, angle, and spatial distribution of the muons at the face of the shield, a distance d from the target, is calculated under the assumptions that a muon from pion decay is emitted in the

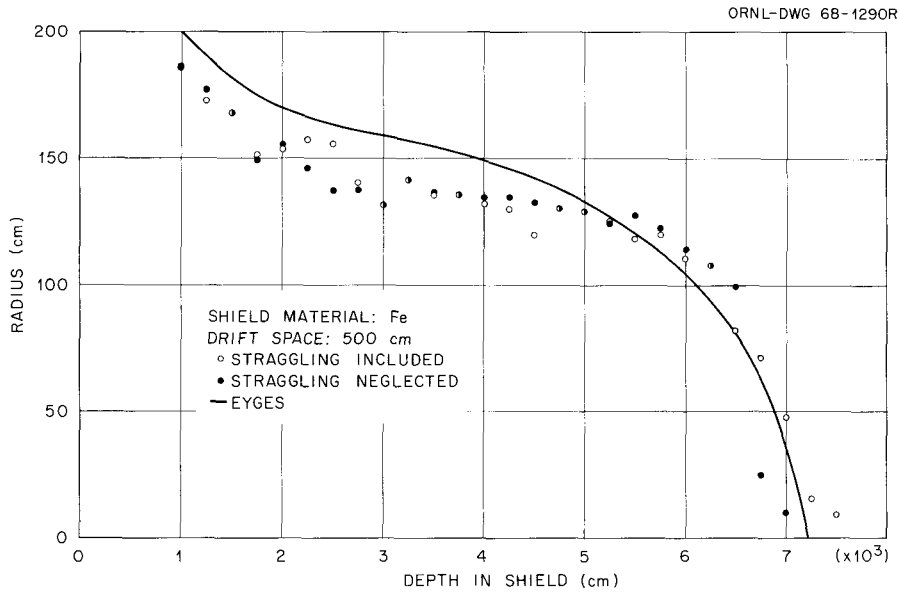

Fig. 6.16.1. Isodose Contour for a Dose of 1.5×10^{-11} MeV/g per Interacting Proton.

direction of the pion and that there is no magnetic field between the target and the shield. In calculating this distribution, muons from both positively and negatively charged pions are included. This source distribution is used in conjunction with muon transport calculations to determine the current and dose as a function of depth and radius in the shield. It is to be noted that the assumption is made that the muons produced by the strongly interacting particles in the shield may be neglected.

The transport calculations have been carried out using a modified version of PROTOS.[5] The modifications were those necessary to make the code apply to muons rather than to protons and to allow for source particles that are not incident along the axis of the cylindrical shield. This code utilizes Monte Carlo methods and includes small-angle multiple Coulomb scattering (Molière distribution[6]) and range straggling (Sternheimer formulation[7]). The stopping power as a function of muon energy was obtained from the work of R. M. Sternheimer[8] and P. J. Hayman *et al.*[9].

Calculations have been carried out for the case of an iron shield and a drift space, *d*, of 5 m. After the dose as a function of depth and radius in the shield is obtained, the radius of the shield at a given depth required to reduce the dose to a specified level is found. The radii so determined when plotted against depth form an isodose contour which represents approximately the required shape of the cylindrically symmetric shield. In Fig. 6.16.1 the calculated points of such a contour corresponding to a dose of 1.5×10^{-11} MeV/g per interacting proton in the target are shown. Calculations have been carried out with and without range straggling included, and both sets of results are shown in the figure. The fluctuations in the points arise from the statistical nature of the calculations. The inclusion of the effects of range straggling does not appreciably change the shape of the shield.

References

[1]Industri-Matematik AB, Stockholm, Sweden.

[2]Computing Technology Center, Union Carbide Corporation, Oak Ridge, Tennessee.

[3]Chapter 12, Section 2.5, in *200 Bev. Accelerator Design Study*, UCRL-16000, vols. 1 and 2, June 1965.

[4]*Ibid.*, Chapter 13, Section 1.1.

[5]C. Johansson and M. Leimdorfer, *A Monte Carlo Procedure for Calculating the Migration of Protons Taking Account Only of Electromagnetic Interactions*, Research Institute of National Defense, Stockholm, Sweden, Report A-4411-411 (January 1965).

[6]G. Molière, *Z. Naturforsch.* **3a**, 78 (1948); H. A. Bethe, *Phys. Rev.* **89**, 1256 (1953); and U. Fano, *Phys. Rev.* **93**, 117 (1954).
[7]R. M. Sternheimer, *Phys. Rev.* **117**, 485 (1960).
[8]R. M. Sternheimer, *Phys. Rev.* **115**, 137 (1959).
[9]P. J. Hayman *et al.*, *Proc. Roy. Soc. (London)* **275A**, 391 (1963).

6.17 SHIELDING CALCULATIONS FOR A 400-MeV LINEAR ELECTRON ACCELERATOR[1]

R. G. Alsmiller, Jr. R. T. Boughner[3]
J. Barish[2] W. W. Engle[4]

Shielding calculations for a linear electron accelerator may conveniently be divided into four parts: the electron-photon cascade, the photoneutron production, the particle transport through the shield, and the conversion of particle current leaving the shield to dose. Calculations in each of these categories have been carried out to aid in the design of the transverse shield of a 400-MeV linear electron accelerator. In particular, neutron-transport calculations carried out using the straightahead approximation, the straightahead approximation coupled with a low-energy discrete ordinates calculation, and the straightahead approximation coupled with a Monte Carlo calculation are presented and compared. Shields composed of silicon dioxide and silicon dioxide with 10% water by weight are considered.

References

[1]Abstract of ORNL-4211 (June 1968); work partly funded by the National Aeronautics and Space Administration under NASA Orders R-104(1) and H-38280A; also published in part in *The Discrete Ordinates Method Coupled With the Straightahead Approximation for Use in High-Energy Accelerator Shielding Studies,* ORNL-RSIC-19, p. 109.
[2]Computing Technology Center, Union Carbide Corporation, Oak Ridge, Tennessee.
[3]Mathematics Division.
[4]Instrumentation and Controls Division.

6.18 DOSE RATE FROM HIGH-ENERGY ELECTRONS AND PHOTONS[1]

R. G. Alsmiller, Jr. H. S. Moran

Electron-photon cascade calculations have been carried out, and energy deposition as a function of depth has been obtained for monoenergetic electrons (0.1 to 20 GeV) and photons (0.01 to 20 GeV) normally incident on a semi-infinite slab of water 30 cm thick. The calculated results are in approximate agreement with experimental data for the case of 5.2-GeV incident electrons.

Reference

[1]Abstract of *Nucl. Inst. Methods* **58**, 343–344 (1968).

6.19 THE ELECTRON-PHOTON CASCADE INDUCED IN LEAD BY PHOTONS IN THE ENERGY RANGE 15 TO 100 MeV[1]

R. G. Alsmiller, Jr. H. S. Moran

Electron-photon cascade calculations have been carried out for photons of energy 15, 25, 35, 45, 60, and 75 MeV incident on a semi-infinite slab of lead of 3 radiation lengths thickness and for photons of energy 100 MeV incident on a slab of lead of 15 radiation lengths thickness. The results obtained include the energy deposition as a function of depth in the slab and the energy and angular distributions of the transmitted photons and charged particles.

Reference

[1]Abstract of ORNL-4192 (January 1968); work partly funded by the National Aeronautics and Space Administration under NASA Orders R-104(1) and H-38280A.

6.20 AN ESTIMATE OF THE PROMPT PHOTON SPECTRUM ARISING FROM COSMIC-RAY BOMBARDMENT OF THE MOON[1]

T. W. Armstrong R. G. Alsmiller, Jr.

An estimate has been made of the photon leakage spectrum from the moon due to photons arising

from the capture and inelastic scattering of neutrons produced by galactic cosmic rays. The method of calculation consisted of estimating the energy and spatial distribution of the neutron flux in the moon and then using Monte Carlo methods to obtain the photon source and to perform the photon transport. While the photon production and transport are carried out with some exactitude, the results must be considered very approximate because of the approximate neutron-flux distribution that is used. In particular, no attempt is made to account for the important effect which hydrogen in the lunar composition would have on the neutron-flux distribution.

Reference

[1]Abstract of ORNL-TM-2100 (January 4, 1968); work funded by the National Aeronautics and Space Administration under NASA Orders R-104(1) and H-38280A.

7. Experimental Studies for Medium-Energy Radiation Shielding

7.0 INTRODUCTION

If reliable estimates are to be made of the effects on spacecraft occupants of secondary particles produced by medium-energy protons incident upon a spacecraft, we must be able to understand (or reproduce) the dominant behavior of the complex nuclear reactions which occur when the primary energy is a few times greater than the nucleon binding energy. Estimation of spectra of neutrons produced in the upper atmosphere and of the biological dose from medium-energy neutrons involves similar nuclear physics. The theoretical group has been able to estimate the cross sections for secondary production by using a Monte Carlo intranuclear-cascade-plus-evaporation model (Section 6, especially 6.4–6.6); one of the major tasks of the experimental group is to help define the limits of applicability of this model.

The study of secondary nucleons from 450-MeV protons on nuclei, abstracted in Section 7.7, provides a good test of the cascade theory in a favorable incident energy region. These data are compared with calculations in Section 6.5. The other papers in Section 7 deal with studies near or below the lower limit of the energy range for which the cascade model can be expected to function. The Verbinski-Burrus study of neutron spectra from 14- to 18-MeV protons, abstracted in Section 7.5, contains comparisons with the Griffin statistical model, as well as with the intranuclear-cascade-plus-evaporation model. The data in this paper have had a strong effect upon our application of this model at low energies.

This year a large contribution comes from the experiments of Bertrand *et al.*, Sections 7.1–7.4, 1.21, and 1.22. Differential cross sections were measured with good energy resolution for all charged secondaries from 60-MeV protons on a few targets; the resulting data should aid in comprehending the competition between various reaction and de-excitation mechanisms. Neutron cross sections for similar incident energies are also needed to complete the big picture of these reactions, and Section 7.6 describes preparation for the difficult experimental work required.

The emerging conclusion is that experiment supports the intranuclear-cascade-plus-evaporation model as a first-order explanation of the secondary nucleon spectra even for energies as low as 60 MeV and perhaps 14 MeV. The model is based on remarkably few assumptions; hopefully, inclusion of a few additional assumptions might allow agreement with experiment to become fully satisfactory.

A system has been devised for making balloon measurements in the upper atmosphere (Section 7.8). This new experiment is related to the others through technique and through methods of interpretation. The results should reflect the nucleonic cascades within the upper atmosphere (a shield) when it is bombarded by incident high-energy radiation.

7.1 DIFFERENTIAL CROSS SECTIONS FOR THE CHARGED PARTICLES PRODUCED BY 60-MeV PROTONS ON CARBON, IRON, AND BISMUTH[1]

F. E. Bertrand T. A. Love
R. W. Peelle N. W. Hill[2]
W. R. Burrus[3]

The differential cross sections for the production of proton, deuteron, triton, ^{3}He, and alpha particles by 60-MeV proton bombardment of ^{12}C, ^{54}Fe, and ^{209}Bi were measured over a secondary energy

range of 1 to 60 MeV. The particles were detected in an all-solid state, three-detector, total-absorption counter telescope. The system resolution was ~150 keV (FWHM). Secondary charged particles were identified by both ΔE vs E and flight-time vs E methods. Proton, deuteron, triton, ^{3}He, and alpha particles were unambiguously identified over the energy range 1 to 60 MeV. Data were obtained at 15 to 20 angles between 12 and 160°. The high-energy region of each charged-particle spectrum is dominated by elastic scattering and excitation of discrete nuclear levels, and differential cross sections are presented for 37 of the levels observed. The secondary proton spectra from ^{12}C, ^{54}Fe, and ^{209}Bi, below the region of discrete peaks, exhibit a structureless and nearly flat continuum region which at low energies merges into a peaked, nearly isotropic distribution except in the case of bismuth. The spectra of other secondaries have roughly the same continuum shape as those of the protons except that only the secondary alpha particles show a strong evaporation peak. The energy-integrated differential cross-section curves for each particle type are strongly forwardly peaked and decrease rapidly with increasing angle until they are constant for angles greater than ~120°. The ratio of protons to deuterons is ~10 to 20 : 1 and the ratio of protons to tritons is ~100 to 300 : 1.

The elastic differential cross sections were found to agree with optical-model calculations. The proton continuum spectra are compared with estimates from a Monte Carlo intranuclear-cascade-plus-evaporation calculation. For angles larger than ~70° and smaller than ~20° the observed proton cross sections are larger than the ones estimated; however, between 20 and 70° the agreement is within ±30%. The high-energy cross sections measured at back angles were larger than had been predicted. The high-energy cross sections measured at angles >120° were much higher than those calculated, especially for the heavier targets. The continuum proton spectra from the neighboring nuclides ^{54}Fe and ^{56}Fe were found to have equal shapes and cross sections in the energy region above 20 MeV, but ^{56}Fe exhibits a peaked low-energy distribution which is only ~70% as intense as the ^{54}Fe distribution.

References

[1]Abstract of ORNL-4274 (in press); work funded by the National Aeronautics and Space Administration under NASA Orders R-104(1) and L-12,186. In order to provide more information than would have been practical in this abstract of a 270-page report, phases of the work which are believed to be of particular interest are summarized in Sections 7.2 and 7.3 and in Sections 1.21 and 1.22.

[2]Instrumentation and Controls Division.

[3]Present address: Tennecomp, Inc., P. O. Box J, Oak Ridge, Tennessee.

7.2 DIFFERENTIAL CROSS SECTIONS FOR THE PROTON CONTINUUM PRODUCED BY 60-MeV PROTON BOMBARDMENT OF ^{12}C, ^{54}Fe, AND ^{209}Bi AND COMPARISON WITH INTRANUCLEAR CASCADE CALCULATIONS[1]

F. E. Bertrand R. W. Peelle

The differential cross sections for the production of secondary protons by 60-MeV proton bombardment of ^{12}C, ^{54}Fe, and ^{209}Bi were measured over a secondary energy range from ~1 to 60 MeV. Proton spectra were obtained at ~15 angles between 12 and 160°. The protons were detected and identified in an all-solid-state, three-counter, total-absorption detector telescope with an overall energy resolution of ~150 keV (FWHM). The details of the detection and analysis systems and the tabulated cross sections are reported elsewhere.[2]

Some of the many trends that were observed in the secondary-proton data above ~20 MeV are given below:

1. The spectra from each target are structureless below the region of excitation of known levels (for ^{12}C, ^{54}Fe, and ^{209}Bi below ~22, 10, and 7 MeV of excitation, respectively).
2. At the smallest angles (<25°) the spectra from each target exhibit a peak which cannot be associated with a quasi-elastic peak, since it is not located at the kinematically expected energy for quasi-elastic scattering and does not move sufficiently with changes in angle.
3. The continuum cross section increases with increasing target mass.
4. The cross sections of the high-energy regions of the spectra from each target are strongly forwardly peaked and approach zero for angles greater than ~100°.

The low-energy portions of the proton spectra from the three targets differ considerably. The

carbon and iron spectra show a low-energy distribution peaked at approximately the Coulomb barrier; however, the bismuth data show only a rapidly decreasing cross section in the low-energy regions. The low-energy peak for carbon and particularly for iron is more isotropic than any other energy region. At angles larger than ~120° the magnitude of the secondary proton spectra from each target becomes constant.

The proton spectra from the neighboring nuclides ^{54}Fe and ^{56}Fe have equal shapes and cross sections in the regions above ~20 MeV (excluding differences in peak structure caused by nuclear level differences). However, the cross section in the low-energy peak for ^{56}Fe is only ~70% as large as that for ^{54}Fe.

The low-energy cutoff to the proton data from ^{12}C and ^{54}Fe was ~1.2 MeV and was determined by foldover in the time-of-flight system. The proton output data from ^{209}Bi include all the protons emitted from the target except at the smallest angles, where a small number of protons were detected in the time-of-flight system but were obscured by large quantities of fission fragments.

Figures 7.2.1, 7.2.2, and 7.2.3 show the secondary-proton laboratory differential cross sections for ^{12}C, ^{54}Fe, and ^{209}Bi, respectively. The experimental data are shown as smooth curves from which the discrete peaks (elastic and inelastic) have been removed and the calculation is shown as a histogram. In all cases the statistical error in the experimental cross section is approximately the width of the curve.

Integration of data such as those in Figs. 7.2.1–7.2.3 over all energy (excluding elastic events) at several angles yields the cross sections shown in Fig. 7.2.4. The three curves behave in a similar manner in that each is strongly peaked at small

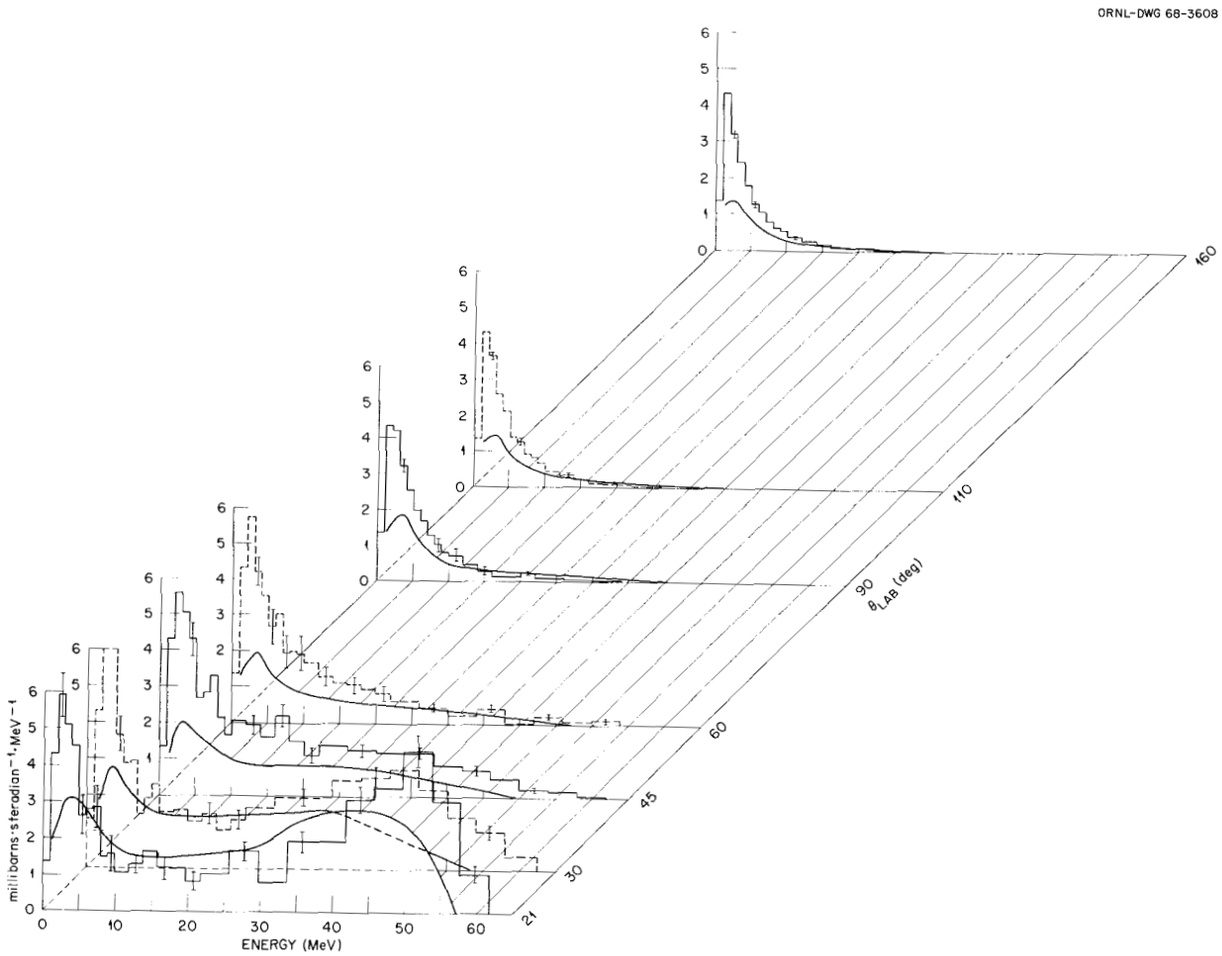

Fig. 7.2.1. Proton Continuum Spectra from ^{12}C Compared with Intranuclear Cascade Calculations.

angles and falls off rapidly with increasing angle until it reaches a nearly constant value for angles greater than ~120°. The shape of the angular distributions supports a contention that the total proton production results from a direct-interaction mechanism, which produces the forwardly peaked cross section, plus an underlying isotropic mechanism, such as a compound nuclear evaporation process. This type of double-mechanism process could describe the observed comparison between the ^{54}Fe and ^{56}Fe proton spectra. In the region above ~20 MeV, if the spectra result from a direct reaction mechanism, the equal cross sections for the neighboring nuclides would be expected. In addition, if the low-energy spectra are produced by an evaporation mechanism, the more neutron-rich nucleus, ^{56}Fe, would be expected to preferentially evaporate neutrons, thereby reducing the proton evaporation.

The proton data have been compared with the intranuclear-cascade-plus-evaporation model of Bertini,[3] although this model was designed for use at much higher energies. In all the comparisons, which are shown as histograms in Figs. 7.2.1–7.2.3, the cascade process was cut off at the Coulomb barrier corresponding to the radius of the outer region of the model nucleus.

It is seen that the agreement between the data and calculation is in general rather good, particularly between ~20 and 70°. There are, however, some consistent differences between the data and calculation:

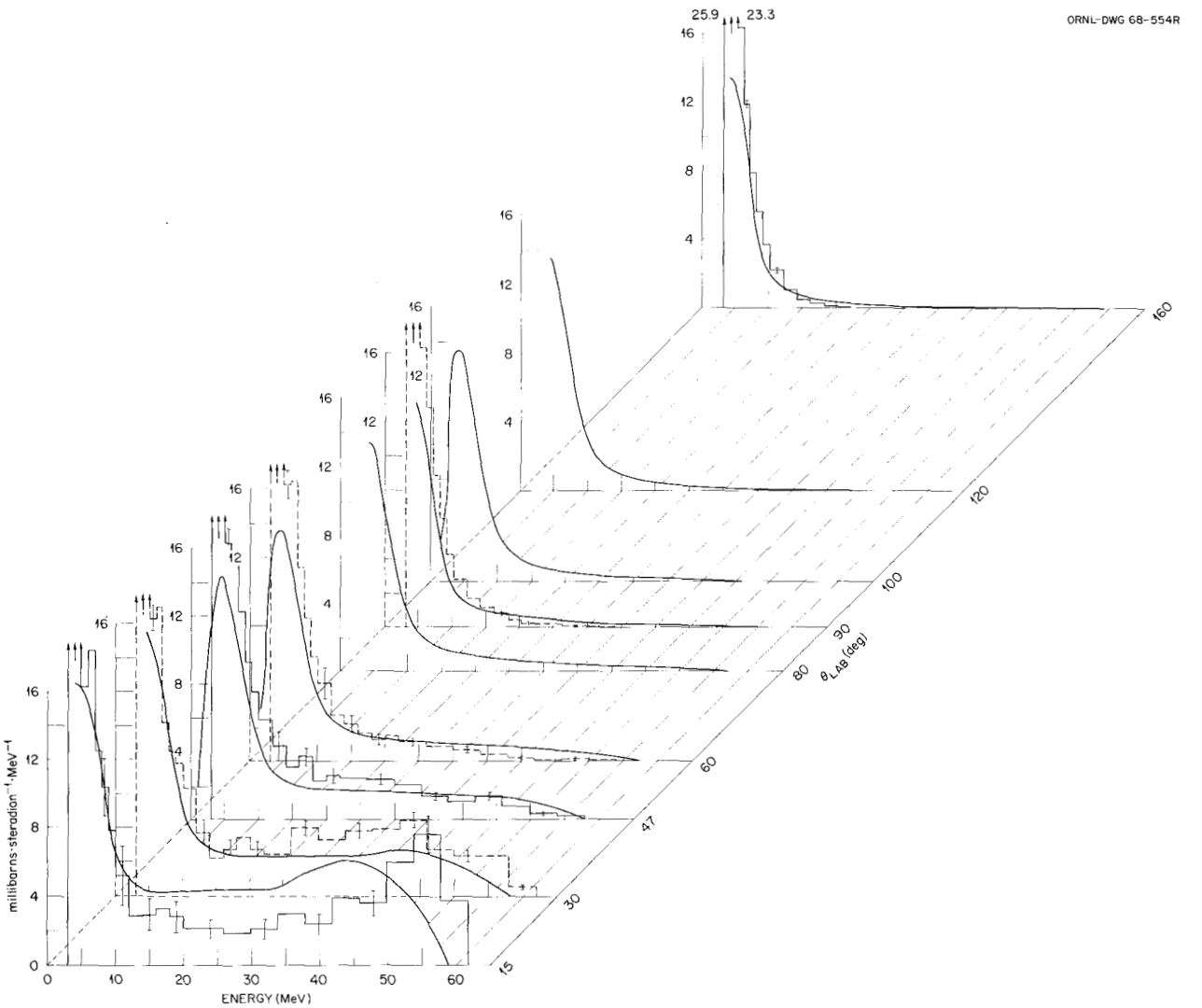

Fig. 7.2.2. Proton Continuum Spectra from ^{54}Fe Compared with Intranuclear Cascade Calculations.

1. The predicted magnitude of the evaporation peak is higher than the experimental data for the targets discussed.

2. The predicted low-energy cutoff of evaporation for ^{54}Fe and ^{209}Bi is higher than the cutoff observed. (The experimental cutoff on the ^{12}C data was too high to allow such a comparison.)

3. For angles of observation less than $\sim 15°$ the calculation considerably underestimates the total proton cross section. Also at the small angles, the calculation predicts a strong quasi-elastic peak which was not observed.

4. For angles larger than $\sim 80°$ the calculation underestimates the amount of high-energy particle production observed. This is particularly apparent at the extreme back angles, and the underestimate becomes more marked with increasing target mass.

Although there are several areas of disagreement between the intranuclear-cascade-plus-evaporation calculation and the secondary proton data, it is felt that calculation accounts for the majority of the observed energy and angle dependence and the calculation must therefore represent the dominant physical processes.

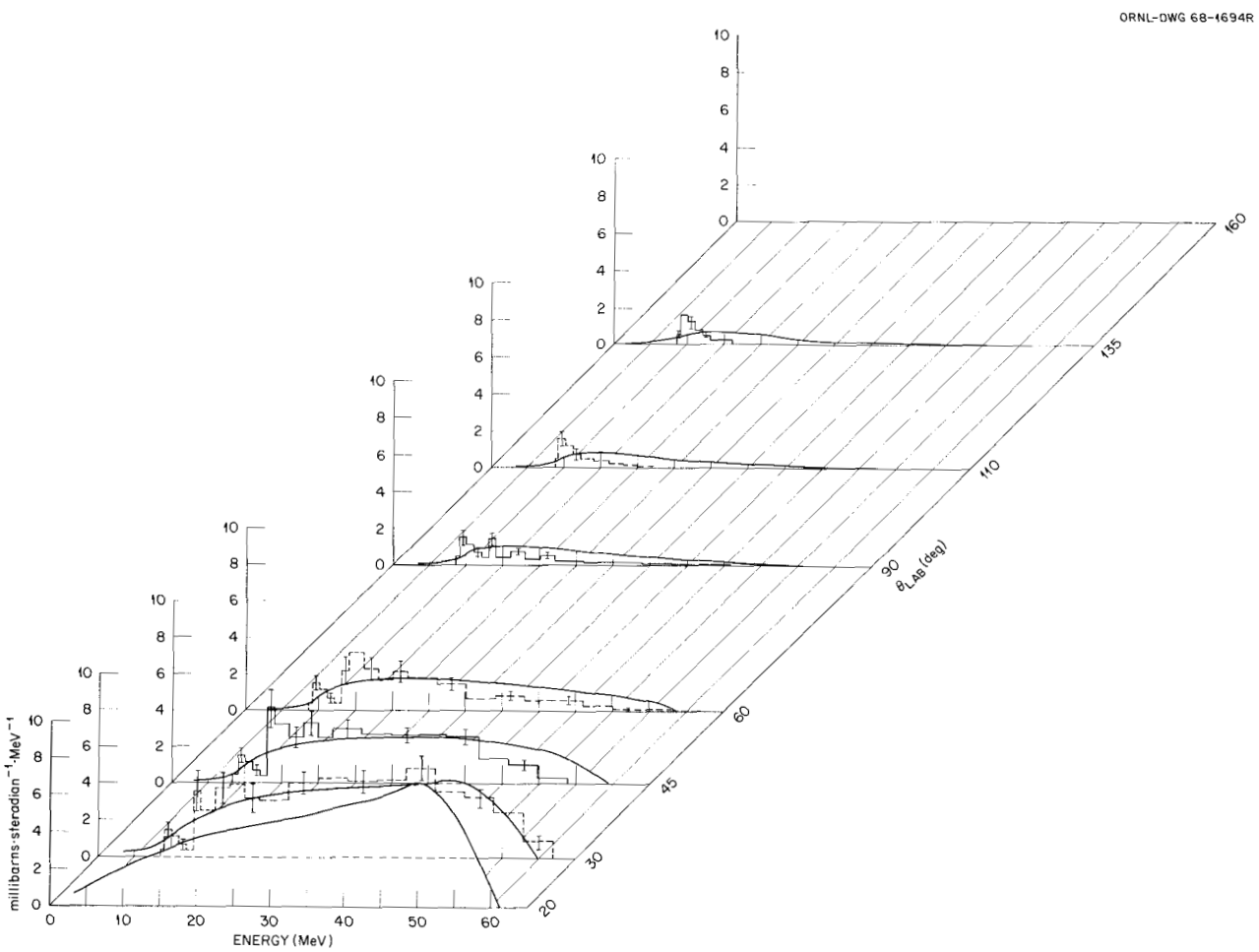

Fig. 7.2.3. Proton Continuum Spectra from ^{209}Bi Compared with Intranuclear Cascade Calculations.

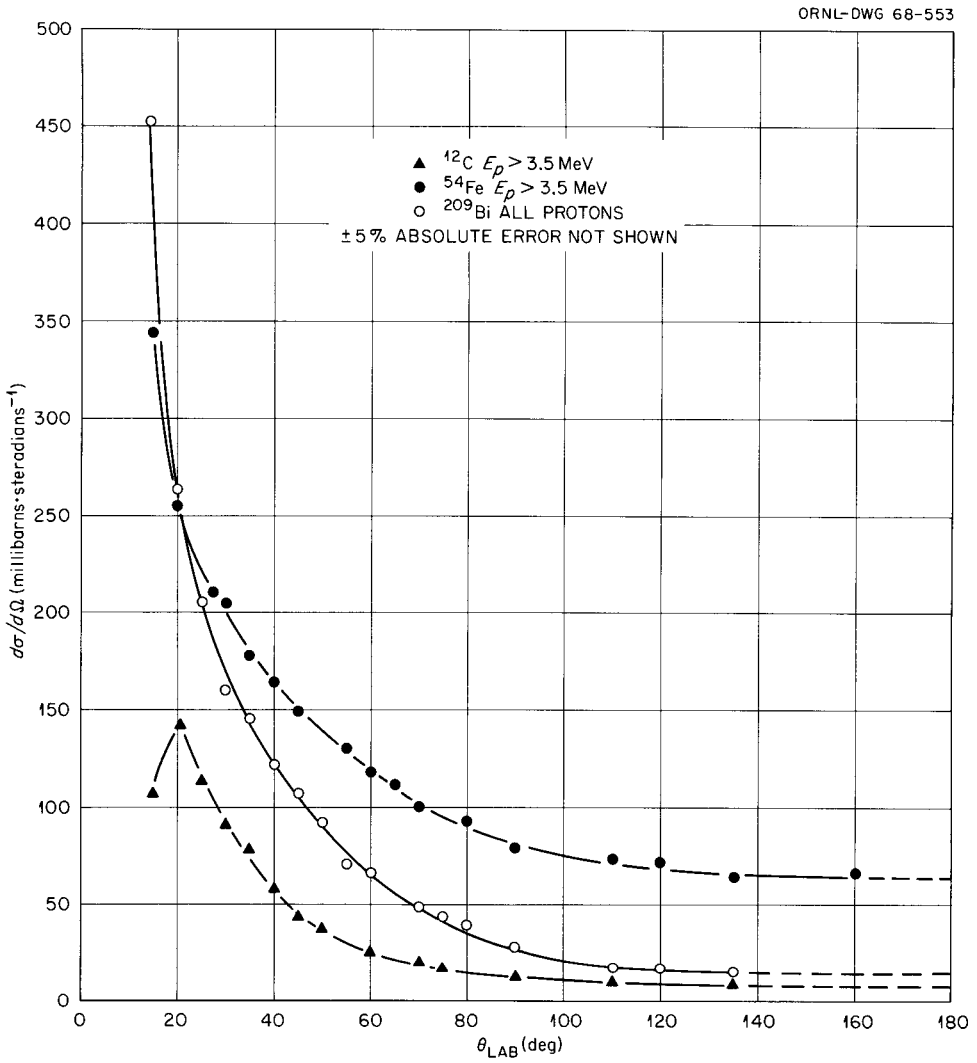

Fig. 7.2.4. Energy-Integrated Proton Differential Cross Sections (Nonelastic) for 61.7-MeV Incident Protons.

References

[1]Work funded by the National Aeronautics and Space Administration under NASA Orders R-104(1), L-12,186, and H-38280A.

[2]F. E. Bertrand *et al.*, *Differential Cross Sections for the Charged Particles Produced by 60-MeV Protons on Carbon, Iron, and Bismuth,* ORNL-4274 (in press).

[3]H. Bertini, *Phys. Rev.* **131**, 1801 (1963).

7.3 CROSS SECTIONS FOR THE PRODUCTION OF PROTON, DEUTERON, TRITON, ^{3}He, AND ALPHA PARTICLES BY 60-MeV PROTON BOMBARDMENT OF CARBON, IRON, AND BISMUTH[1]

F. E. Bertrand R. W. Peelle

Differential cross sections for the production of proton, deuteron, triton, ^{3}He, and alpha particles by 60-MeV proton bombardment of ^{12}C, ^{54}Fe, and ^{209}Bi were measured over a range of secondary energies from ~1 to 60 MeV. The particles were detected and unambiguously identified in a three-detector telescope with an overall energy resolution of ~150 keV (FWHM). The particles were identified by both ΔE vs E and time-of-flight vs E methods, and data were obtained for each target at ~20 angles between 12 and 160°. The detection and analysis systems are described in detail elsewhere,[2] along with tabulated cross sections.

The low-energy cutoff of the data was determined by several factors, including target thickness, time-of-flight foldover, and inability to distinguish ^{3}He from ^{3}H in the time-of-flight system. The cutoffs in each case are indicated by the lowest energy at which a cross section is plotted.

Figure 7.3.1 shows the spectra of deuterons from ^{209}Bi obtained at several angles. Smooth continua have been drawn under the peaks caused by excitation of discrete levels. The behavior, as a func-

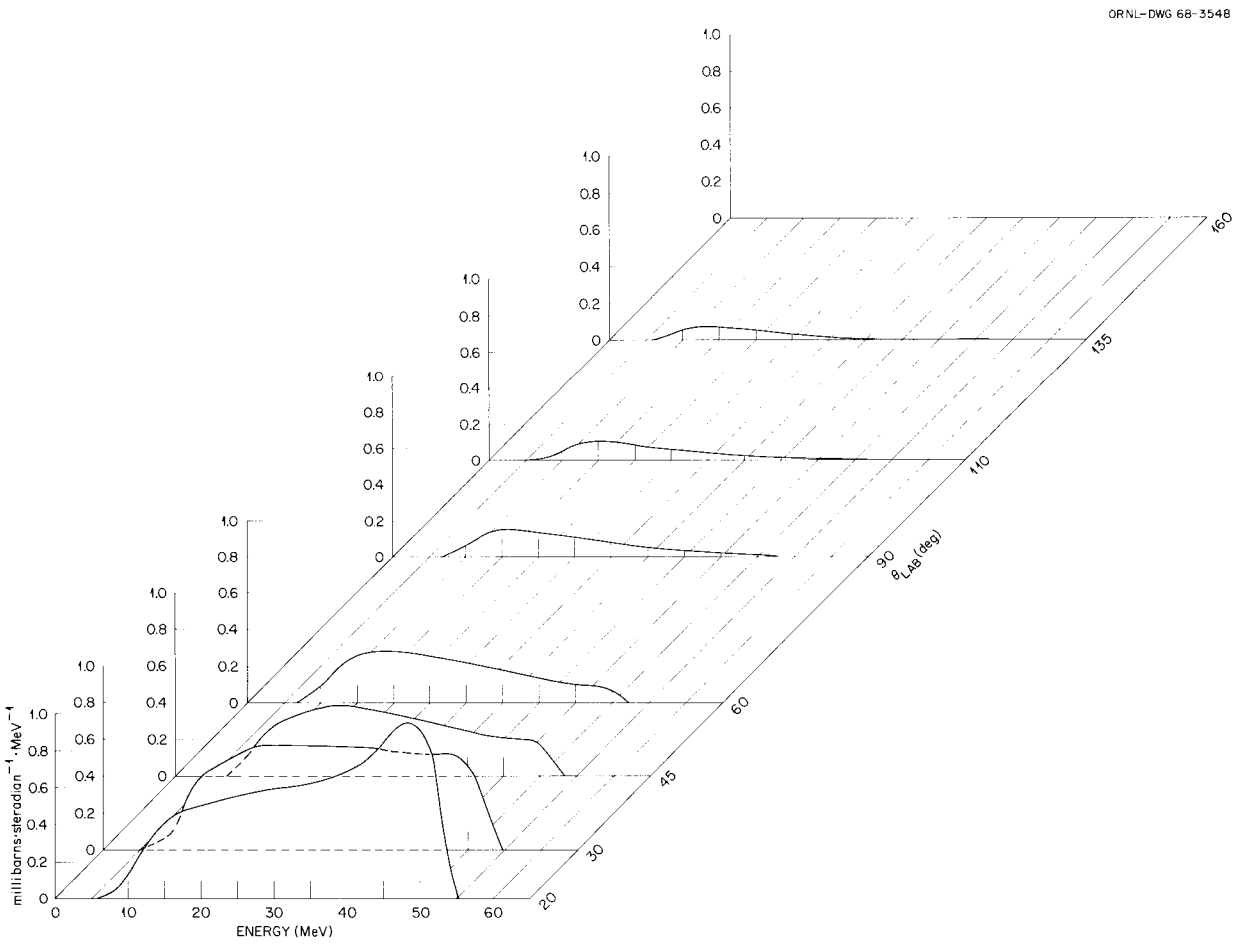

Fig. 7.3.1. Deuteron Continuum Spectra from ^{209}Bi.

tion of angle, of the deuteron cross section is typical of the behavior of all the charged-particle spectra. The high-energy cross-section curve is very forwardly peaked and approaches zero for angles larger than ~100°; however, the low-energy cross-section curve becomes constant at the back angles. It should be noted that large high-energy cross sections are observed in the spectra at angles as large as 60 to 90°. The formation of such quantities of high-energy deuterons cannot be accounted for by a direct nucleon pickup mechanism since such a pickup at, for example, 60° would require an unreasonably high momentum for the target nucleon. It is possible, however, for incident nucleons that have been scattered out of the incident direction toward larger angles by collisions with target nucleons (cascade process) to pick up a target nucleon. This indirect process[3,4] would place more reasonable momentum requirements on the target nucleon for pickup at large angles.

Figures 7.3.2, 7.3.3, and 7.3.4 show the angle-integrated spectra for all the observed particles from ^{12}C, ^{54}Fe, and ^{209}Bi. The structure seen at the high-energy end of the spectra is caused by excitation of discrete nuclear levels; however, the irregularities in the lower energy regions represent statistical fluctuation. In some regions (indicated by dashed lines) of each spectrum the data were affected by a small dead layer in the detector telescope. (A solid line is drawn through the data points for clarity only.)

Figure 7.3.5 shows the energy-integrated differential cross sections for proton, deuteron, triton, ^{3}He, and alpha particles from ^{54}Fe. The shapes of the curves are all similar in that they are peaked at small angles and decrease rapidly with increasing angle until a constant value is reached at

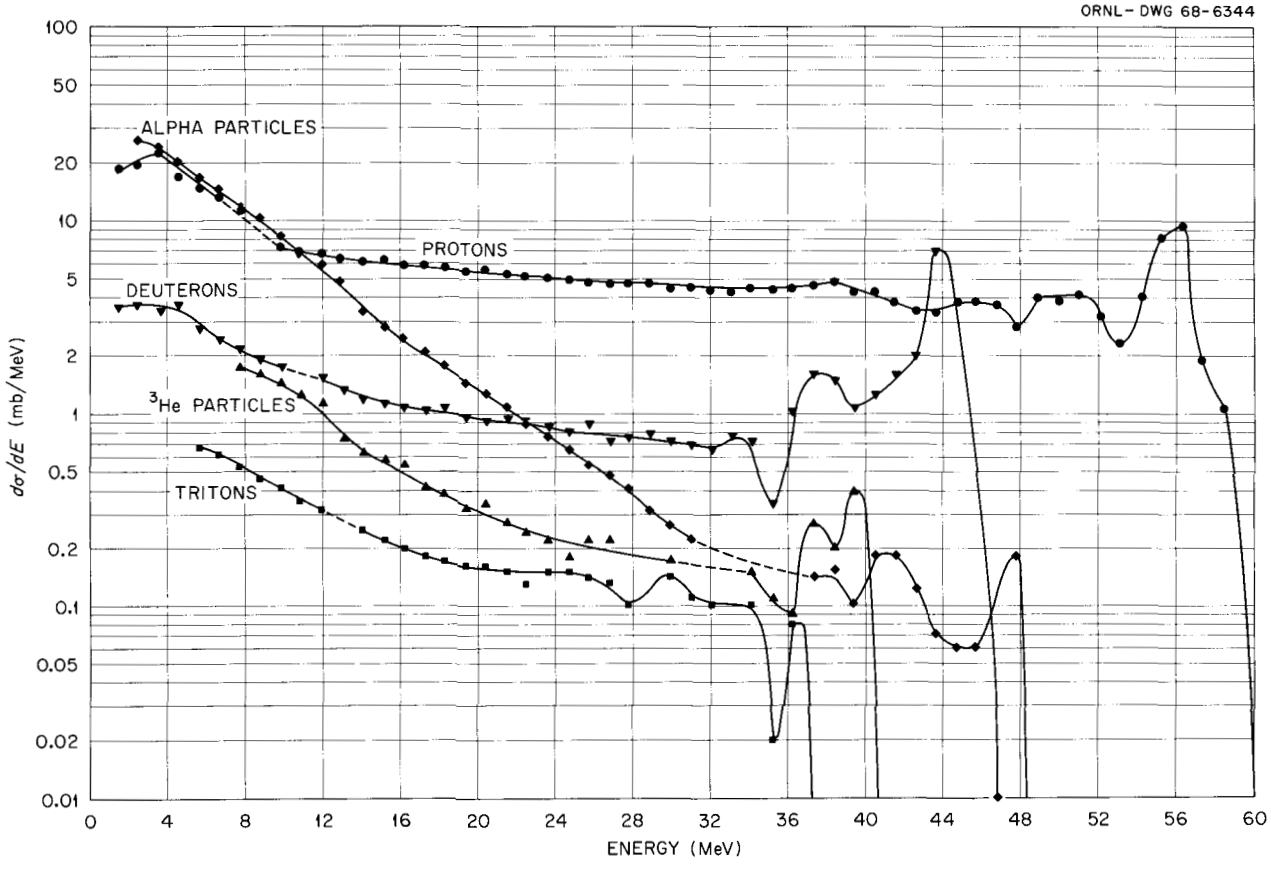

Fig. 7.3.2. Angle-Integrated Proton, Deuteron, Triton, ^{3}He, and Alpha Spectra from ^{12}C Bombarded by 62-MeV Protons.

~120°. It can be argued that the total production of each particle type results from at least two different processes: a low-order direct mechanism and an underlying, isotropic process such as compound nucleus evaporation.

Table 7.3.1 lists the total cross sections for proton, deuteron, triton, ^{3}He, and alpha particles from ^{12}C, ^{54}Fe, and ^{209}Bi. The "direct mechanism" cross sections listed in Table 7.3.1 were obtained by subtraction of the isotropic cross sections from the total cross sections. The ratio of protons to deuterons is ~10 to 20 : 1 and to tritons is ~100 to 300 : 1. Although the total cross section for alpha-particle production is large, the alpha particles are mostly of low energy whereas most of the deuteron and triton total cross section is for particles with energies above ~20 MeV.

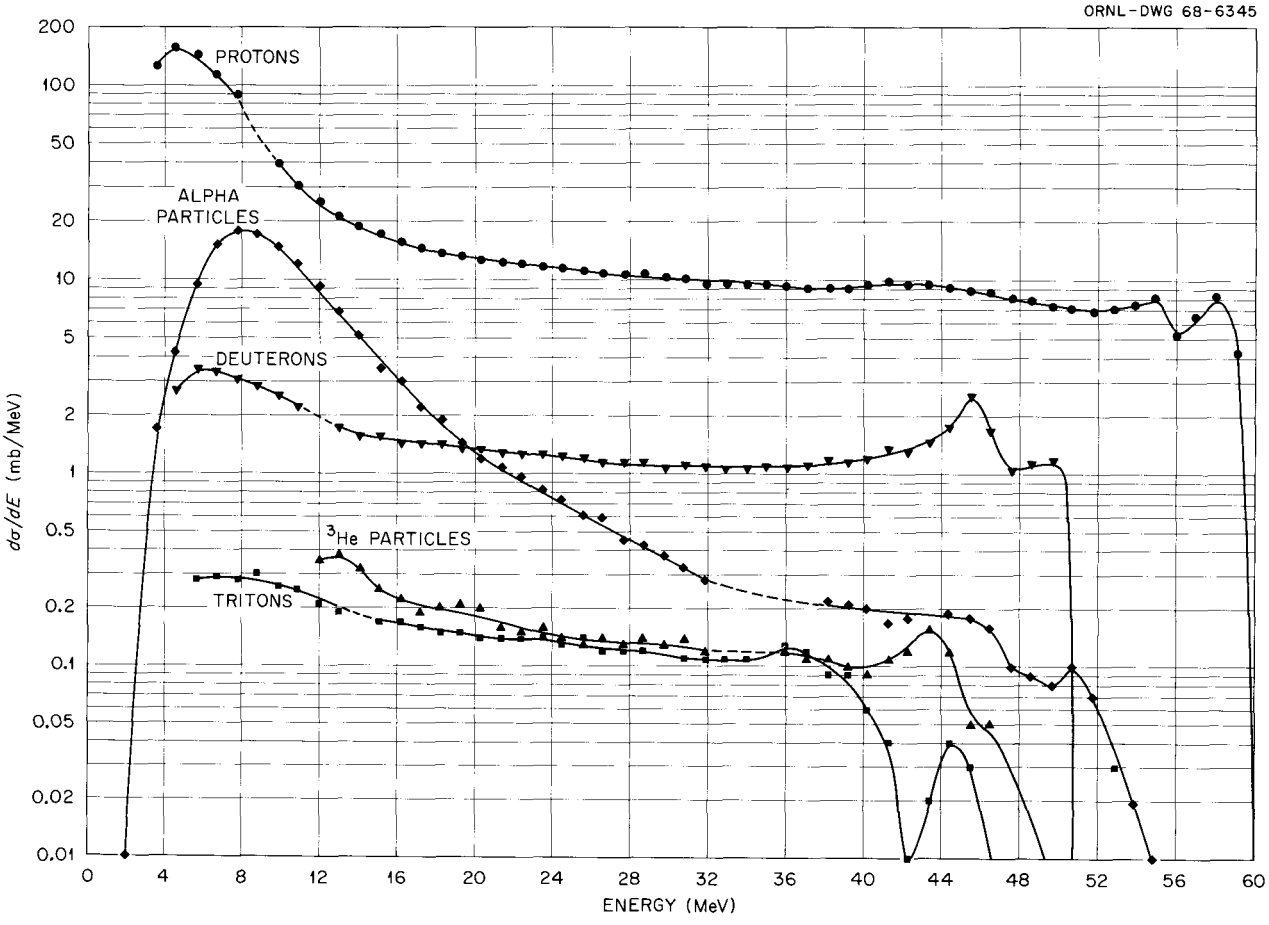

Fig. 7.3.3. Angle-Integrated Proton, Deuteron, Triton, ^{3}He, and Alpha Spectra from ^{54}Fe Bombarded by 62-MeV Protons.

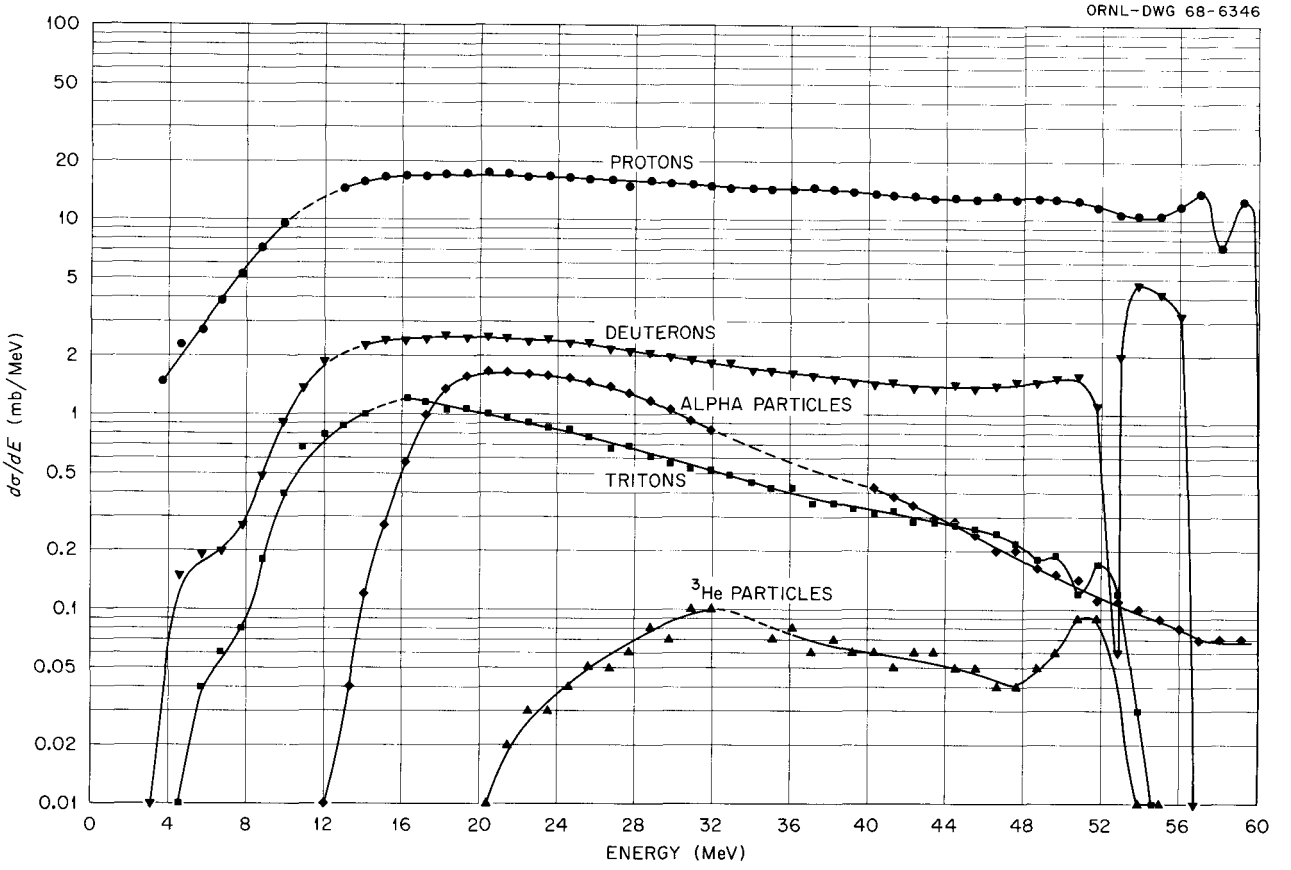

Fig. 7.3.4. Angle-Integrated Proton, Deuteron, Triton, ^{3}He, and Alpha Spectra from ^{209}Bi Bombarded by 62-MeV Protons.

Table 7.3.1. Integrated Cross Sections

Target	Proton	Deuteron	Triton	^{3}He	Alpha
			Total Cross Sections[a] (mb)		
^{12}C[b]	349	65	7.0	14.6	173
^{54}Fe[c]	1271	70	5.6	5.5	136
^{209}Bi[d]	699	91	25.0	2.0	29
			Direct Cross Sections (mb) and Ratio to Proton Cross Section		
^{12}C	217	49 (0.23)	5.5 (0.025)	9.8 (0.045)	119 (0.55)
^{54}Fe	455	48 (0.11)	3.9 (0.009)	3.7 (0.008)	17 (0.037)
^{209}Bi	566	78 (0.14)	20.0 (0.035)	1.7 (0.003)	17 (0.030)
			Isotropic Cross Section (mb)		
^{12}C	132	16	1.5	5.0	54
^{54}Fe	816	22.2	1.7	1.8	119
^{209}Bi	133	13.0	5.0	0.28	12.0

[a]These cross sections include all particles detected between the energy limits given below.
[b]Energy limits: elastic > E_p > 1.2 MeV; E_D > 1.2 MeV; E_T > 5.5 MeV; $E_{^3He}$ > 6 MeV; E_α > 2.5 MeV.
[c]Energy limits: elastic > E_p > 3.5 MeV; E_D > 4.5 MeV; E_T > 5.5 MeV; $E_{^3He}$ > 11 MeV; all alphas.
[d]All particles.

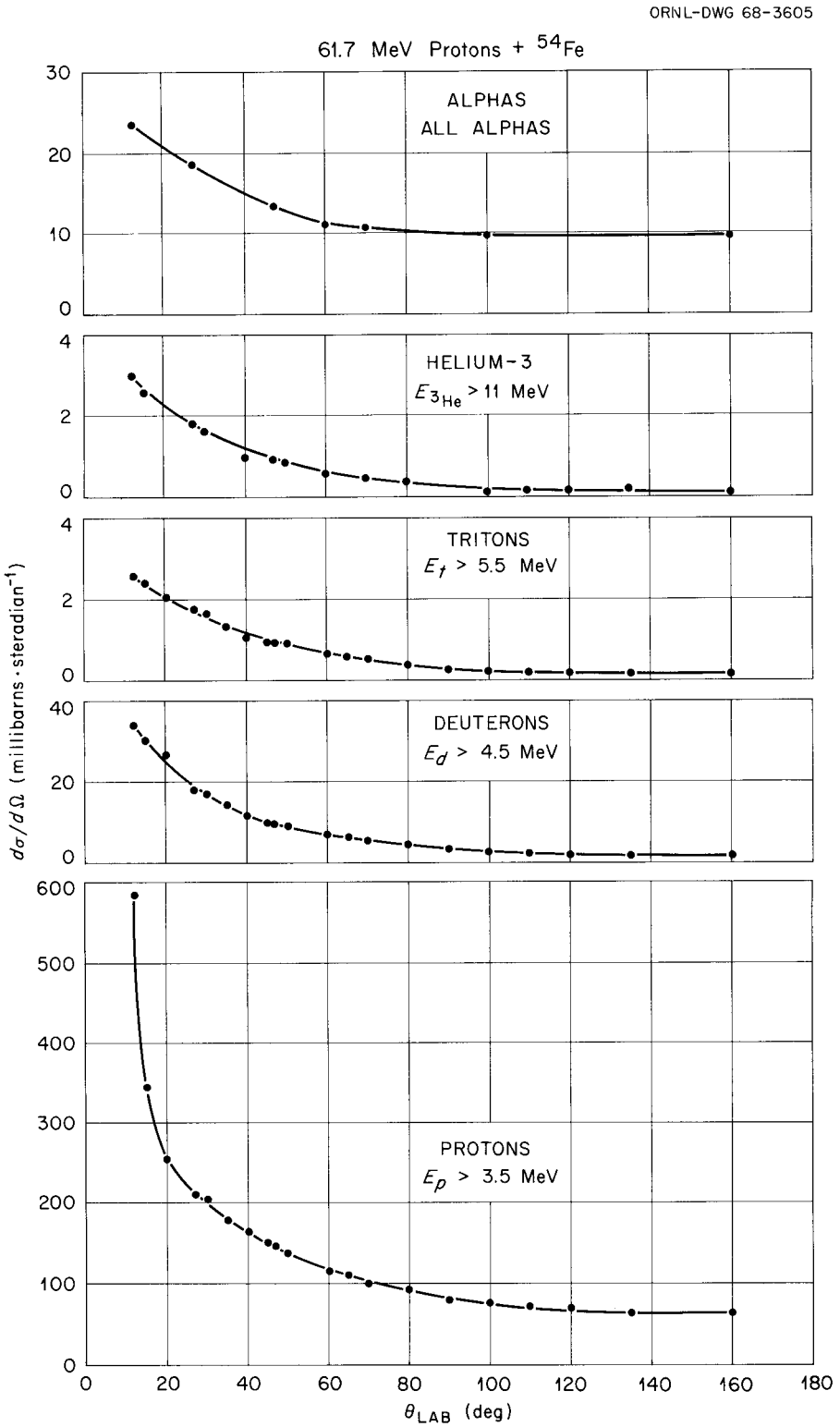

Fig. 7.3.5. Energy-Integrated Differential Cross Sections for Proton, Deuteron, Triton, ^{3}He, and Alpha Particles from ^{54}Fe.

References

[1]Work funded by the National Aeronautics and Space Administration under NASA Orders R-104(1), L-12,186, and H-38280A.

[2]F. E. Bertrand *et al.*, *Differential Cross Sections for Charged Particles Produced by 60-MeV Protons on Carbon, Iron, and Bismuth*, ORNL-4274 (in press).

[3]B. H. Bransden, *Proc. Phys. Soc.* **A65**, 738 (1952).

[4]W. N. Hess and B. S. Moyer, *Phys. Rev.* **101**, 1, 337 (1956).

7.4 A FOUR-PARAMETER E VS dE/dx AND TIME-OF-FLIGHT COMPUTERIZED CHARGED-PARTICLE EXPERIMENT[1]

F. E. Bertrand — T. A. Love
W. R. Burrus[2] — R. W. Peelle
N. W. Hill[3] — B. W. Rust[2]

For detection of charged particles from 1 to 60 MeV, three solid-state detectors are utilized in a dE/dx telescope configuration. Signals are summed digitally and displayed on a two-dimensional flicker box and transmitted off-line to a larger computer for tail corrections, dead-layer corrections, and final analysis. Time of flight is utilized for nonpenetrating particles; p, D, T, ^{3}He, α, etc., can be distinguished from 1 to 60 MeV with $\sim$180-keV system energy resolution.

References

[1]Abstract of paper presented at 14th Annual Nuclear Science Symposium, IEEE, Los Angeles, October 1967 (proceedings to be published); work funded by the National Aeronautics and Space Administration under NASA Orders R-104(1) and L-12,186.

[2]Present address: Tennecomp Inc., P. O. Box J, Oak Ridge, Tennessee.

[3]Instrumentation and Controls Division.

7.5 DIRECT AND COMPOUND-NUCLEUS NEUTRONS FROM 14- TO 18-MeV PROTONS ON ^{9}Be, ^{14}N, ^{27}Al, ^{56}Fe, ^{115}In, ^{181}Ta, AND ^{208}Pb AND FROM 33-MeV BREMSSTRAHLUNG ON ^{27}Al, ^{206}Pb, ^{208}Pb, AND ^{209}Bi[1]

V. V. Verbinski[2] — W. R. Burrus[3]

The angle-integrated (p,xn) spectra, fitted with precompound and evaporation spectra from Griffin's statistical model of intermediate structure, produced g, the number of independent particle states per MeV, and f_c, the compound fraction. For ^{27}Al, ^{56}Fe, ^{115}In, and ^{181}Ta, g increased linearly with A, from 2 to 13, but decreased to 9 for ^{208}Pb at 18-MeV proton energy E_p. At $E_p = 14$ MeV, $g = 7$ for ^{208}Pb, which may signify vanishing shell effects at large E_p. Monte Carlo intranuclear-cascade-plus-evaporation calculations yielded spectra and cross sections in agreement with the measurements, allowing for several calculational defects that were made obvious by the comparisons. The Monte Carlo calculations yielded f_c values close to those derived from Griffin's calculations for targets heavier than ^{27}Al. Nuclear temperatures, obtained from LeCouteur's evaporation analysis for multiple-nucleon emissions, agree for (p,xn) and giant-resonance (γ,xn) reactions via the intermediate nucleus ^{209}Bi, but differed considerably for the target ^{27}Al, where direct and evaporation neutrons are not well separated in mean energy. The three types of analyses utilized here are therefore much more applicable for heavy nuclei than for light nuclei. Energy and angle dependence of (γ,xn) reactions indicate negligible direct effects, in sharp contrast to (p,xn) reactions, which display a strong forward anisotropy at the high-energy end of the spectra.

References

[1]Abstract of paper to be submitted to *Physical Review;* work funded by the National Aeronautics and Space Administration under NASA Orders R-104(1) and L-12,186.

[2]Present address: Gulf General Atomic, P. O. Box 608, San Diego, California.

[3]Present address: Tennecomp, Inc., P. O. Box J, Oak Ridge, Tennessee.

7.6 A FLIGHT-TIME SPECTROSCOPY SYSTEM FOR NEUTRONS FROM 25- TO 60-MeV PROTONS ON NUCLEI[1]

J. W. Wachter T. A. Love
R. T. Santoro J. K. Millard[2]

A flight-time spectroscopy system is being designed to enable measurements of secondary neutron energy spectra from various targets bombarded by 20- to 60-MeV protons. The proposed experiments are part of a larger effort to evaluate spacecraft radiation shielding requirements by experimental and theoretical investigations of secondary radiations from protons incident on various materials. The incident proton energy range used will be of particular interest for defining spacecraft shielding effectiveness and the measurements will complement existing secondary charged-particle and gamma-ray measurements (Sects. 7.1 and 7.8, this report, and Ref. 3). The experimental difficulties of neutron measurements make it prohibitively costly to secure data with resolution comparable to that of the charged-particle data; however, cross sections to ±10% and energy resolutions of approximately ±5% would be desirable.

To achieve these design criteria, it appears feasible to use a time-of-flight method, because the protons from the Oak Ridge Isochronous Cyclotron (ORIC) are naturally bunched, with one bunch per rf cycle, so that the time interval within which the secondary neutron is formed is established to within the short time interval required for protons of the burst to irradiate the target. A measurement is then made of the time required for a pulse to occur in the scintillator as the result of a neutron reaction in the detector which leads to an energetic charged particle. Since confusion may arise between a fast neutron arising from the proton burst and a slow neutron from the preceding one, only a small range of energies may be measured without foldover. To expand this range, an electrostatic sweeper must be used to deflect all but a fraction of the proton bursts away from the entrance slit of the experimental equipment, thus increasing the effective time between bursts.

Preliminary experiments have been performed on the ORIC machine to establish its suitability for the required measurements. The measurement of burst characteristics, described in a separate paper (Sect. 5.10, this report), is important in defining the error in the "start" time of the flight, i.e., the interval during which the proton-induced reactions take place. This time indeterminancy, together with the instrumental timing errors, defines the ultimate energy resolution attainable at each path length. Under the conditions of the experiment the apparent burst width for ~63-MeV protons was ~475 psec. The uncertainty in measuring the start time during a neutron experiment includes errors in establishing a reliable signal from the machine rf pickoff. This overall timing uncertainty is ~0.5 nsec at ~60 MeV. It therefore appears feasible to construct a reasonably efficient detector system capable of the desired ±5% energy resolution.

The beam sweeper was found to be capable of selecting one proton burst for every seven entering the sweeper at a proton energy of ~60 MeV. The resultant time between proton bursts striking the target can therefore be increased from 44 to 308 nsec, permitting an expanded range of energies to be measured at a single flight path.

The burst characteristics of ORIC appear suitable for our purpose; however, at the long flight paths, problems from neutrons scattered by the air and by the walls and floor of the experimental room will arise. Suitable baffles will be installed, and the detector positions will be carefully selected (and perhaps elevated) to avoid sources of extraneous neutrons.

Figure 7.6.1 is a block diagram of the proposed apparatus. The beam sweeper is operated at a fixed fraction of the rf frequency, i.e., proton burst repetition rate. The time fiducial pulse, bearing fixed relation to the time at which protons strike the target, is developed so as to be accurately timed by the rf but controlled by the beam sweeper frequency.

The proposed neutron detector is an NE-213 liquid scintillator in which charged particles scattered by the incident neutrons are detected. An anticoincidence counter in front of the detector serves to reject unwanted counts from incident charged particles. The efficiency for the neutron detection process is low and must be estimated from cross-section data using the 05S Monte Carlo calculation.[4] At the higher neutron energies for which cross sections are not well known, uncertainties in the efficiency introduce a large portion of the experimental error.

The scintillator is viewed by a photomultiplier tube selected for its timing resolution and light collection capabilities. To improve timing resolu-

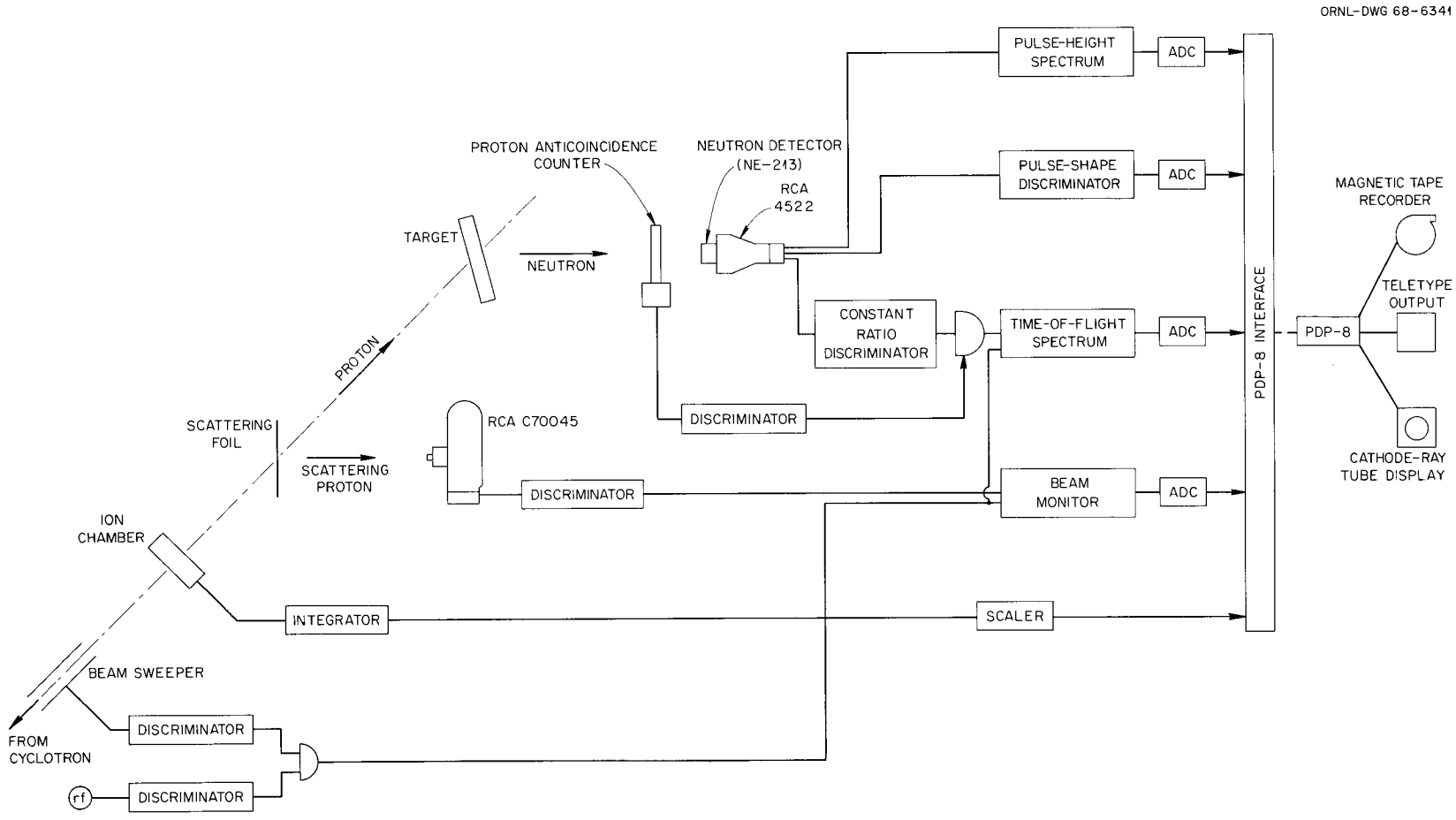

Fig. 7.6.1. Block Diagram of Proposed Neutron Flight-Time Spectroscopy System.

tion, a discriminator will be built which fires at a constant fraction of the pulse height.

Both neutrons and gamma rays are detected in the NE-213, and the slow light emission characteristics of the neutron reactions in the scintillator are used to distinguish between neutron and gamma pulses. A novel pulse-shape discrimination circuit has been developed (described in detail in Sect. 5.5, this report) and has been found to operate satisfactorily for neutrons up to 14 MeV; it will be evaluated at the higher neutron energies contemplated for these experiments.

In order to minimize the errors implicit in the timing system and in the neutron detector and to facilitate data handling, the outputs of the ADC circuits will be fed to a PDP-8 on-line computer. Data will be recorded on magnetic tape and also processed internally for continuous monitoring purposes. Retention of the data will enable a two-dimensional presentation of the neutron counts as a function of light output from the scintillator and time of flight. Suitable lower limits for the light output data (the effective threshold setting) can then be chosen for each time of flight so as to use only the scintillator response characteristics for which the efficiency is best established. Similarly, timing errors depending on pulse heights can be evaluated and compensated. Additionally, the pulse-shape discriminator and the bombarding proton pulse-width monitor outputs can be recorded and viewed during operation.

References

[1]Work funded by the National Aeronautics and Space Administration under NASA Orders R-104(1) and L-12,186.

[2]Instrumentation and Controls Division.

[3]W. Zobel *et al.*, *Gamma Rays from Bombardment of ^{7}Li, Be, ^{11}B, C, O, Mg, Al, Co, Fe, and Bi by 16-160 MeV Protons and 59 MeV α Particles*, ORNL-4183 (November 1967).

[4]R. E. Textor and V. V. Verbinski, *05S: A Monte Carlo Code for Calculating Pulse-Height Distributions Due to Monoenergetic Neutrons Incident on Organic Scintillators*, ORNL-4160 (February 1968).

7.7 NEUTRON AND PROTON SPECTRA FROM TARGETS BOMBARDED BY 450-MeV PROTONS[1]

J. W. Wachter W. A. Gibson[2]
W. R. Burrus[2]

The energy spectra of secondary neutrons in the energy region between 100 and 450 MeV emitted by targets bombarded by 450-MeV protons were measured using a proton recoil spectrometer. Secondary proton measurements were also made with this spectrometer. The measurements were made on Be, C, Al, Cu, Co, Pb, and Bi targets at several angles between 0 and 60°. Two types of targets were employed: thin targets in which the primary beam lost little energy and in which further interaction of the secondary particle was small, and thick targets in which the primary beam lost all or a significant fraction of the initial energy and in which the probability of the secondary particles undergoing further interaction was large. The thin-target results are expressed as cross sections and the thick-target results represent a nucleon transport and are expressed as a yield.

References

[1]Abstract of paper to be submitted to *Physical Review* and of ORNL-TM-2253 (in press); work partly funded by National Aeronautics and Space Administration under NASA Orders R-104(1) and L-12,186.

[2]Present address: Tennecomp, Inc., P. O. Box J, Oak Ridge, Tennessee.

7.8 A SPECTROMETER SYSTEM FOR STUDYING 2- TO 40-MeV NEUTRONS IN THE UPPER ATMOSPHERE

W. Zobel T. A. Love
J. T. DeLorenzo[1]

Cosmic-ray particles interacting with the atmosphere produce, among others, fast neutrons which may be reflected out of the atmosphere. It is

thought that a fraction of these neutrons, upon decay into protons, are trapped in the earth's magnetic field and thus constitute a source for the radiation in the Van Allen belts. This source, however, appears to be too small by a factor of 50 to account for the high-energy ($E_p \geqq 20$ MeV) protons.[2] In order to shed further light on this phenomenon, a program has been initiated to measure the neutron spectrum at altitudes between 70,000 and 130,000 ft in the atmosphere, with a proposed extension of this work at a later date to measurements on board a satellite outside the atmosphere. Special emphasis will be placed on the energy range above $\sim$15 MeV, since data at these energies are particularly sparse. As a first step in these measurements we plan to measure the neutron spectrum at $\sim$100,000 ft in the energy range from $\sim$1.5 to $\sim$40 MeV, using a balloon to carry the spectrometer to this altitude.

The detector assembly of the spectrometer is shown in Fig. 7.8.1. The neutron detector is a right circular cylinder of NE-213,[3] a liquid organic scintillator in which the charged particles produced by nuclear interactions (e.g., protons from incident neutrons, electrons from incident gamma rays) cause the light output. In this particular scintillator the light produced by different particles has different ratios of a fast- to a slow-decay component, thus making it possible to use pulse-shape discrimination to distinguish between particles.

Detectors using NE-213 have been in use in this laboratory for some time. Extensive calibrations covering the energy range from 0.2 to 22 MeV have been performed on a 4.60- by 4.65-cm-diam detector.[4] In order to make use of this work we chose our detector to have approximately the same dimensions: 4.57 cm in diameter by 4.32 cm high. The NE-213 is encapsulated in a thin-walled ($\frac{1}{32}$-in.) aluminum cylinder coated on the inside with a special reflector paint. The cell is then mounted on a RCA Type 8575 photomultiplier tube, which is a 12-stage tube with a high cathode efficiency, somewhat shorter than the RCA Type 6810A previously used.

In order to eliminate pulses in the NE-213 due to charged particles incident upon it, the whole assembly is enclosed in a "mantle" of NE-110,[3] a plastic scintillator. The $\frac{1}{4}$-in. thickness was chosen so that an incident charged particle will deposit at least 1 MeV in this mantle. The output from the mantle, which is mounted on its own 8575 photomultiplier tube, is placed in anticoincidence with the output from the NE-213 to eliminate the response to incident charged particles. It is expected that the interaction of a neutron in the mantle which would significantly alter the neutron energy will result in a recoil pulse, which would also be detected and thus eliminated.

Gamma rays interacting in the NE-213 will produce electrons. Since the light output from the scintillator will have a different ratio of fast to slow light for electrons and heavy charged particles, e.g., protons, with the latter showing a larger slow component, discrimination against gamma rays can be accomplished by pulse-shape discrimination. Several methods exist to accomplish this. We have chosen to use the time difference of the zero-crossing point of the doubly differentiated linear signal from the dynode of the photomultiplier. A block diagram of the electronics is shown in Fig. 7.8.2.

The anode signals from the photomultipliers pass through discriminators and are then placed in anticoincidence. The discriminator for the signal from the mantle has been modified to place a negative level on the input of the coincidence circuit in the absence of an input pulse and to raise the voltage level at the coincidence circuit input to zero if a pulse is present. Since the coincidence circuit requires negative inputs, this effectively changes the coincidence circuit to an anticoincidence circuit. The output of this circuit is then placed in coincidence with the output of a zero-crossing discriminator. The pulse from the latter is sufficiently wide and the delays are adjusted so that the output of the second half of coincidence module C102B/N is governed, in duration and timing, by the output of the first half.

The pulse-shape discrimination is performed by the combination of the time-to-amplitude converter and the following single-channel analyzer. The time-to-amplitude converter (TAC) obtains a "start" signal from the output of the second half of module C102B/N which, as pointed out above, is in proper time relation to the fast signal from the anode, effectively the front edge of the photomultiplier pulse. The zero-crossing discriminator output is suitably delayed and supplied to the "stop" input to the TAC. Since we are interested in only the difference in the zero-crossing time produced by pulses from different particles, the exact amount of delay is immaterial and is chosen to produce a convenient pulse height at the TAC output. The single-channel analyzer accepts the

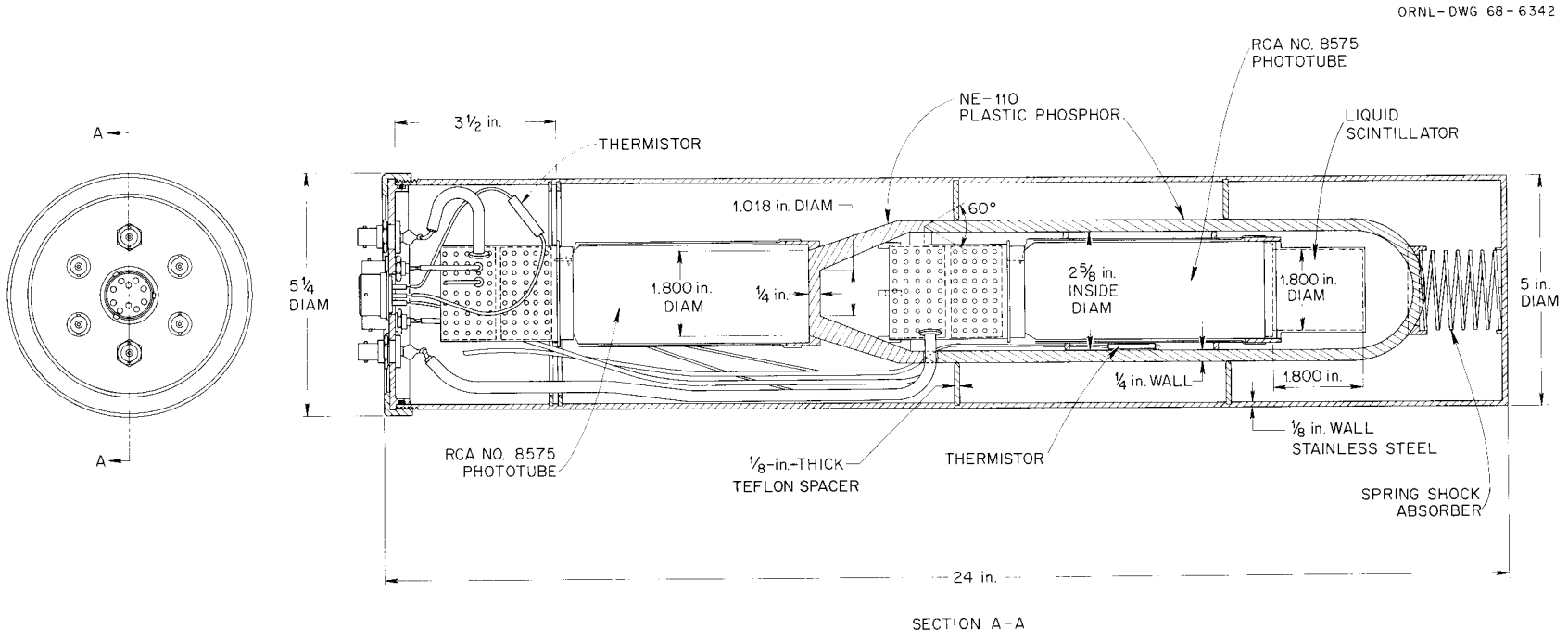

Fig. 7.8.1. Neutron Spectrometer Detector Assembly.

ORNL-DWG 68-6343

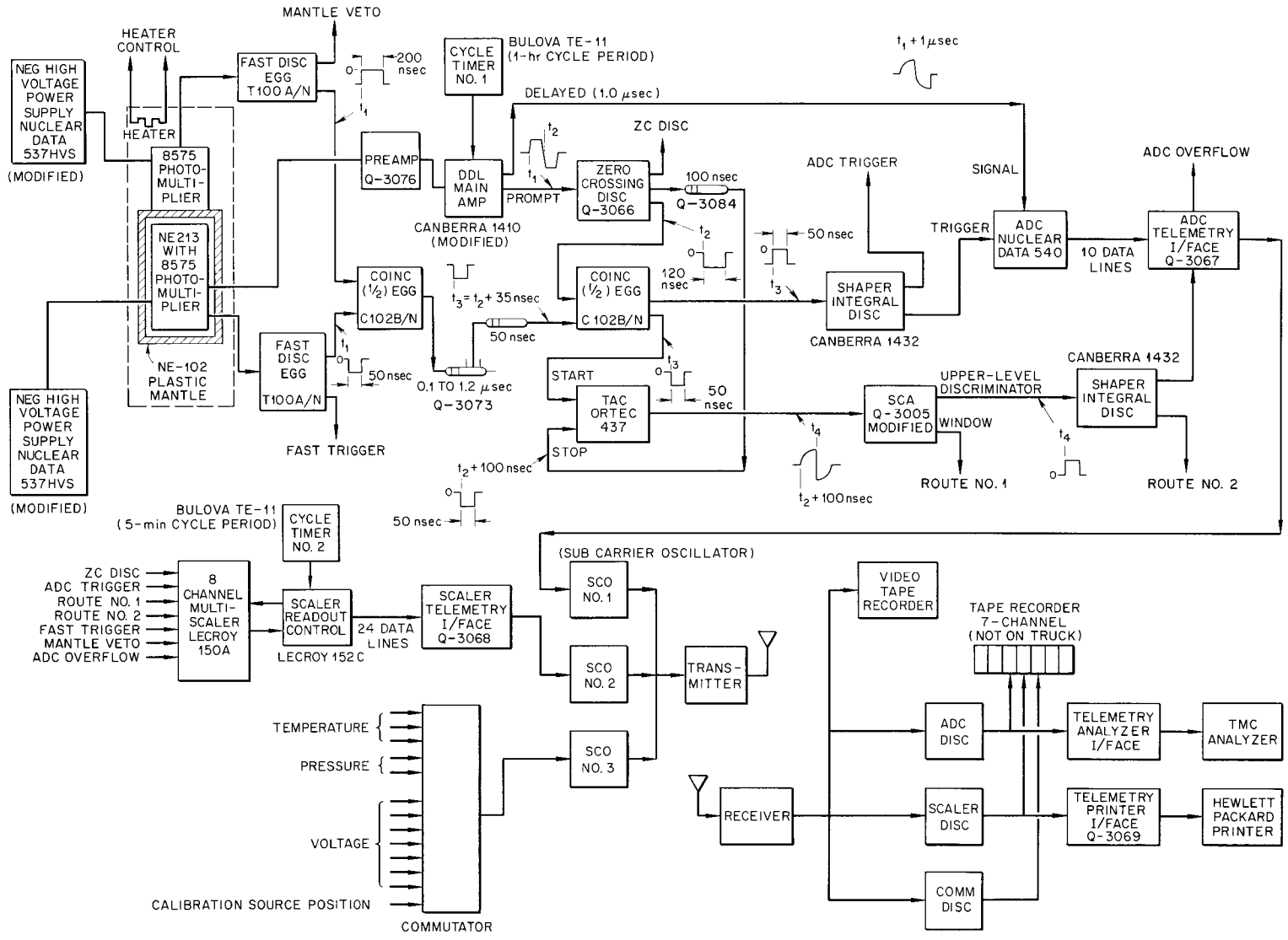

Fig. 7.8.2. Block Diagram for Neutron Spectrometer.

TAC output and produces an output signal if the pulse height lies in a range (window) chosen to encompass only those pulses which crossed the base line early (electrons) or if the pulse height exceeds the upper level (protons). The latter output produces a flag at the telemetry interface to denote this fact. Pulses corresponding to electrons do not carry this bit.

The remainder of the system is rather conventional. Provision has been made to read out the scalers at 5-min intervals. A calibration source is positioned close to the detector once every hour. Since the gain of the system is adjusted to accept pulses corresponding to ~40-MeV protons, the amplifier gain must be changed during this calibration period to accommodate the (much smaller) pulses from this calibration source.

As of May 1968 the system has been tested in all components except those depending on the anticoincidence mantle, and the telemetry. The telemetry is in use on another experiment, but is expected to be available upon its conclusion. The detector assembly embodying the anticoincidence shield will be delivered in the very near future. A short feasibility experiment has been performed using a detector of the same dimensions and ~60-MeV incident protons to confirm that pulse-shape discrimination can be performed even for particles with that much energy; the results confirm feasibility.

A balloon flight has been requested for June 1968, and it is expected that the spectrometer will be used on that flight.

References

[1]Instrumentation and Controls Division.

[2]D. S. Intriligator, *Phys. Rev. Letters* **20**, 1048–1049 (1968).

[3]Nuclear Enterprises, Ltd., Winnipeg, Canada.

[4]V. V. Verbinski *et al.*, *Calibration of an Organic Scintillator for Neutron Spectrometry* (submitted to *Nuclear Instruments and Methods;* also to be published as ORNL-TM-2183).

Publications and Papers Presented at Scientific Meetings

PUBLICATIONS

ALSMILLER, R. G., Jr.
"The Nucleon-Meson Cascade and Shielding," *Science* **157**, 1399 (1967).

ALSMILLER, R. G., Jr., and J. BARISH*
"Analytic Representation of Nucleon- and Pion-Emission Spectra from Nucleon-Nucleus Collisions in the Energy Range 750–2000 MeV," ORNL-TM-2277 (July 1, 1968).

"NCDATA – Nuclear Collision Data for Nucleon-Nucleus Collisions in the Energy Range 25 to 200 MeV," ORNL-4220 (February 1968).

ALSMILLER, R. G., Jr., J. BARISH,* R. T. BOUGHNER,* and W. W. ENGLE*
"Shielding Calculations for a 400-MeV Linear Electron Accelerator," ORNL-4211 (January 1968).

ALSMILLER, R. G., Jr., and R. T. BOUGHNER*
"Solar Neutron Transport in the Earth's Atmosphere," ORNL-TM-2194 (April 1968).

ALSMILLER, R. G., Jr., D. C. IRVING, and H. S. MORAN
"The Validity of the Straightahead Approximation in Space Vehicle Shielding Studies – Part II," *Nucl. Sci. Eng.* **32**, 56 (1968); ORNL-TM-1848 (June 23, 1967).

ALSMILLER, R. G., Jr., and H. S. MORAN
"Dose Rate from High-Energy Electrons and Photons," *Nucl. Instr. Methods* **58**, 343 (1968); ORNL-TM-2026 (Oct. 20, 1967).

"The Electron-Photon Cascade Induced in Lead by Photons in the Energy Range 15 to 100 MeV," ORNL-4192 (January 1968).

ARMSTRONG, T. W.
"Monte Carlo Calculations of Residual Nuclei Production in Thick Iron Targets Bombarded by 1- and 3-GeV Protons and Comparison with Experiment," ORNL-TM-2287 (July 1, 1968).

ARMSTRONG, T. W., and R. G. ALSMILLER, Jr.
"An Estimate of the Prompt Photon Spectrum Arising from Cosmic-Ray Bombardment of the Moon," ORNL-TM-2100 (Jan. 4, 1968).

"Monte Carlo Calculations of the Nucleon-Meson Cascade in Iron Initiated by 1- and 3-GeV Protons and Comparison with Experiment," ORNL-TM-2177 (Mar. 1, 1968).

BERTINI, H. W.
"Comparison of Calculated Radiochemical Cross Sections with Experimental Results for Incident Protons and π-Mesons in the 50- to 400-MeV Region: Effect of Varying a Few Nuclear Parameters in the Calculations," ORNL-4105 (April 1968).

---

*Non-division personnel.

"Pion-Nucleon Differential Cross Sections in the 0- to 700-MeV Energy Region in Terms of the Coulomb Scattering Amplitude, Coulomb Phase Shifts, and Nuclear Phase Shifts up to $l = 4$," ORNL-4197 (January 1968).

"Preliminary Data from Intranuclear-Cascade Calculations of 0.75-, 1-, and 2-GeV Protons on Oxygen, Aluminum, and Lead and 1-GeV Neutrons on the Same Elements," ORNL-TM-1996 (December 1967).

"Secondary Particle Spectra from the Interaction of 30- and 340-MeV Protons on Complex Nuclei: Experimental Data and Comparison with Theory," *Phys. Rev.* **162**, 976 (1967).

BERTINI, H. W., M. P. GUTHRIE, and E. H. PICKELL
"Graphs of Scattered Particle Energies vs Scattering Angles and Graphs of Center-of-Mass Scattering Angles vs Laboratory Scattering Angles for Nucleon-Nucleon Reactions from 25 to 3500 MeV and for Pion-Nucleon Reactions from 25 to 2500 MeV," ORNL-TM-1945 (Aug. 18, 1967).

BERTRAND, F. E., R. W. PEELLE, T. A. LOVE, N. W. HILL,* and W. R. BURRUS
"Differential Cross Sections for the Charged Particles Produced by 60-MeV Protons on Carbon, Iron and Bismuth," ORNL-4274 (1968); also submitted to Louisiana State University by F. E. Bertrand as a doctoral thesis.

BERTRAND, F. E., J. K. DICKENS, and T. A. LOVE
"Distorted-Wave Analysis of Inelastic Scattering of 61.7-MeV Protons from ^{60}Ni," *Phys. Letters* **24B**, 653 (1967).

BERTRAND, F. E., T. A. LOVE, N. BARON,* F. G. PEREY, and J. K. DICKENS
"Elastic and Inelastic Scattering of Protons from ^{120}Sn for $E_p = 20.6$, 25.2, 30.6, and 36.2 MeV; Tabulated Differential Cross Sections," ORNL-4252 (May 1968).

BOGERT, D.,* and W. R. BURRUS
"Comparison of Least-Squares Algorithms," ORNL-TM-2248 (June 11, 1968).

BLOSSER, T. V., and G. E. THOMAS, Jr.*
"Neutron Flux and Neutron and Gamma-Ray Spectra Measurements at the HFIR," ORNL-TM-2221 (June 24, 1968).

BURRUS, W. R., E. MADDEN,* C. O. McNEW,* and R. W. PEELLE
"A PDP-8 Interface for a Charged-Particle Nuclear Physics Experiment," ORNL-TM-2013 (Oct. 4, 1967).

BURRUS, W. R., and V. V. VERBINSKI
"Fast-Neutron Spectroscopy with Thick Organic Scintillators," ORNL-TM-2225 (June 25, 1968).

BURRUS, W. R., and M. H. YOUNG*
"SEGO: A Computer Code for Unfolding Experimental Pulse-Height Distributions," ORNL-TM-2172 (July 3, 1968).

CALLIHAN, A. D.
"Excursion at the Oak Ridge Critical Experiments Facility January 30, 1968," ORNL-TM-2207 (June 1968).

CHAPMAN, G. T.
"Gamma-Ray Attenuation Coefficients for Germanium," *Nucl. Instr. Methods* **52**, 101 (1967).

CHAPMAN, G. T., and W. R. BURRUS
"Spectrum of Gamma Rays Emitted by a Stainless-Steel-Clad Pool-Type Reactor (BSR-II)," ORNL-TM-1284 (May 17, 1968).

CHERN, B.*
"Reaction Products Resulting from the Absorption of Slow Negative Pions by the Light Nuclei C, N, and O," ORNL-TM-2152 (Nov. 17, 1967).

*Non-Division personnel.

CLARK, F. H. S.,* and D. K. TRUBEY
"Energy and Dose Buildup Factors for Various Concretes," *Nucl. Appl.* **4**(1), 37 (1968).

CLIFFORD, C. E., F. J. MUCKENTHALER, R. E. MAERKER, E. A. STRAKER, and F. R. MYNATT*
"Neutron Transport Studies in Ducts and Simple Shields: Comparison of Monte Carlo and Discrete Ordinates Calculations with Experimental Results from the Tower Shielding Facility," ORNL-TM-1965 (Oct. 6, 1967).

CARROLL, R. M.,* O. SISMAN,* and R. B. PEREZ
"The Effect of Fission Density on Fission-Gas Release," *Nucl. Sci. Eng.* **32**, 430 (1968).

COLEMAN, W. A.
"Mathematical Verification of a Certain Monte Carlo Sampling Technique and Applications of the Technique to Radiation Transport Problems," *Nucl. Sci. Eng.* **32**, 76 (1968); ORNL-TM-1944 (Sept. 29, 1967).

"Thermal-Neutron Flux Generation by High-Energy Protons," ORNL-TM-2206 (July 1968); also submitted to the University of Tennessee as a doctoral thesis.

DeSAUSSURE, G., R. GWIN, L. W. WESTON, R. W. INGLE,* R. R. FULLWOOD,* and R. W. HOCKENBURY*
"Simultaneous Measurements of the Neutron Fission and Capture Cross Sections for ^{235}U for Incident Neutron Energies from 0.4 eV to 3 keV," ORNL-TM-1804 (Nov. 20, 1967).

DICKENS, J. K., and E. EICHLER*
"The ^{91}Zr$(d,p)^{92}$Zr Reaction at $E_d = 6.25$ MeV," *Nucl. Phys.* **A101**, 408 (1967).

DICKENS, J. K., E. EICHLER,* F. G. PEREY, and P. H. STELSON*
"The ^{14}N$(n,n'\gamma)$ Reaction for $5.8 \leqq E_n \leqq 8.6$ MeV," ORNL-TM-2267 (June 21, 1968).

DICKENS, J. K., E. EICHLER,* and G. R. SATCHLER*
"^{90,92,94}Zr(p,p') Reactions at 12.7 MeV," *Phys. Rev.* **168**, 1355 (1968).

DICKENS, J. K., F. G. PEREY, and R. J. SILVA*
"Elastic and Inelastic Scattering of 11.0-MeV Protons from ^{48}Ti, ^{51}V, ^{52}Cr, ^{54}Fe, ^{56}Fe, ^{59}Co, ^{60}Ni, ^{62}Ni, ^{64}Ni, ^{63}Cu, ^{65}Cu, ^{64}Zn, ^{66}Zn, and ^{68}Zn: Tabulated Differential Cross Sections," ORNL-4182 (November 1967).

FREESTONE, R. M., Jr.
"DORO 2: An Organic Scintillator Pulse-Height Analysis Code," ORNL-TM-2112 (Feb. 9, 1968).

GUTHRIE, M. P., and R. G. ALSMILLER, Jr.
"Bibliography, Subject Index, and Author Index of the Literature Examined by the Radiation Shielding Information Center (Space and Accelerator Shielding)," ORNL-RSIC-11 (Rev. 1) (September 1967).

HUBNER, R. S.*
"Methods for Calculating Fast-Neutron Leakage from the SNAP-TSF Reactor and Preliminary Results," ORNL-TM-1666 (NAA-SR-MEMO-12184) (October 1967).

IRVING, D. C.
"Evaluation of Neutron Cross Sections for Boron-10," ORNL-TM-1872 (ENDF-109) (Oct. 9, 1967).

KINNEY, W. E.
"Neutron Elastic and Inelastic Scattering from ^{56}Fe from 4.60 to 7.55 MeV," ORNL-TM-2052 (January 1968); also submitted to University of Tennessee as a doctoral thesis.

KINNEY, W. E., and F. G. PEREY
"Calculated ^{56}Fe Neutron Scattering and Gamma-Ray Production Cross Sections from 1.0 to 7.6 MeV," ORNL-4249 (1968).

KISTNER, G.,* and J. T. MIHALCZO
"Critical Experiments for the Repetitively Pulsed Reactor SORA," ORNL-4263 (June 1968).

*Non-Division personnel.

LEIMDORFER, M.*
"The Transport of 500-MeV/c Muons in Iron," ORNL-TM-2048 (Nov. 7, 1967).

LEWIN, J., and L. B. HOLLAND
"TSR-II Heat Transfer," ORNL-TM-1779 (July 26, 1967).

LOVE, T. A., R. T. SANTORO, R. W. PEELLE, and N. W. HILL*
"Absolute Efficiency Measurements of NE-213 Organic Phosphors for Detecting 14.5- and 2.7-MeV Neutrons," *Rev. Sci. Instr.* **39**(4), 541 (1968).

MAERKER, R. E., and F. J. MUCKENTHALER
"Neutron Fluxes in Concrete Ducts Arising from Incident Thermal Neutrons: Calculation and Experiment," *Nucl. Sci. Eng.* **29**, 444 (1967).

"Calculations, Using the Albedo Concept, of Thermal-Neutron Fluxes, Epicadmium-Neutron Fluxes, and Fast-Neutron Dose Rates Along the Center Lines of Square Concrete Ducts; Comparison with Experiment," ORNL-4147 (October 1967).

"Neutron Fluxes in Concrete Ducts Arising from Incident Epicadmium Neutrons: Calculations and Experiments," *Nucl. Sci. Eng.* **30**, 340 (1967).

MAGNUSON, D. W.
"Critical Experiments with Enriched Uranium-Polyethylene, -Plexiglas, and -Teflon Mixtures," ORNL-TM-2082 (February 1968).

MARUSAK, A. L.
"FLOTSAM – A Two-Parameter On-Line Data Acquisition Program for the PDP-7," ORNL-4299 (1968).

MASKEWITZ, B. F., V. A. JACOBS, and J. GURNEY
"Bibliography of the Computer Codes Literature Examined by the Radiation Shielding Information Center," ORNL-RSIC-15 (Rev. 1) (July 1967).

MASKEWITZ, B. F., and D. K. TRUBEY
"The Radiation Shielding Information Center Computer Codes Collection, 1963–1967," ORNL-TM-1956 (Sept. 6, 1967).

MIHALCZO, J. T.
"Prompt Neutron Decay and Reactivity Measurements in Subcritical Uranium Metal Cylinders," *Nucl. Sci. Eng.* **32**, 292 (1968); ORNL-TM-1736 (1968).

PEELLE, R. W., and T. A. LOVE
"Establishing an Energy Scale for Pulse-Height Distributions from Gamma-Ray Spectrometers Based on Inorganic Scintillators," ORNL-4118 (October 1967).

PEELLE, R. W., T. A. LOVE, N. W. HILL,* and R. T. SANTORO
"Differential Cross Sections for the Production of Protons in the Reactions of 160-MeV Protons on Nuclei," *Phys. Rev.* **167**, 981 (1968).

PEREY, C. M., and F. G. PEREY
"On the Real Part of the Proton Optical Model Potential," *Phys. Letters* **26B**(3), 123 (1968).

PEREY, C. M., F. G. PEREY, J. K. DICKENS, and R. J. SILVA*
"11-MeV Proton Optical Model Analysis," ORNL-TM-2291 (July 18, 1968).

RITTS, J. J.,* M. SOLOMITO, and P. N. STEVENS*
"Calculations of Neutron Fluence-to-Kerma Factors for the Human Body," ORNL-TM-2079 (January 1968).

RUST, B. W.,* and W. R. BURRUS
"Flexi-Kludge – A Multiparameter Nuclear Spectrum Summing System for the PDP-8," ORNL-TM-1879 (Aug. 18, 1967).

*Non-Division personnel.

SANTORO, R. T.
"A Fortran IV/63 Program Package for Calculating the Time Channel Response Function in Neutron Time-of-Flight Spectroscopy," ORNL-TM-1836 (Aug. 18, 1967).

SCHMIDT, F. A. R.*
"Revised Neutron Kerma Values at the Boundary of a Semi-Infinite Concrete Medium," ORNL-TM-2284 (July 10, 1968).

SCHNEEBERGER, C. M., and W. R. BURRUS
"Significance Arithmetic Based on a Random Computer," ORNL-TM-2255 (July 18, 1968).

SCOTT, W. W.,* and R. G. ALSMILLER, Jr.
"Comparisons of Results Obtained with Several Proton Penetration Codes – Part II," ORNL-RSIC-22 (June 1968).

SELPH, W. E.*
"Neutron and Gamma-Ray Albedos," ORNL-RSIC-21 (reissue of DASA-1892-2) (February 1968).

SELPH, W. E.,* and H. C. CLAIBORNE
"Methods for Calculating Effects of Ducts, Access Ways, and Holes in Radiation Shields," ORNL-RSIC-20 (reissue of DASA-1892-1) (January 1968).

SILVER, E. G.
"A Pulsed-Neutron Investigation of the Effect of Temperature on the Decay of a Thermal-Neutron Population in H_2O Ice," ORNL-TM-2234 (June 7, 1968).

SILVER, E. G.
"Magnetic Field Compensation with Pairs of Rectangular Coils," ORNL-TM-2129 (Mar. 1, 1968).

SOLOMITO, E., and J. STOCKTON*
"Modification of the Point-Kernel Code QAD-P5A: Conversion to the IBM-360 Computer and Incorporation of Additional Geometry Routines," ORNL-4181 (1968).

STEVENS, P. N.,* and D. K. TRUBEY
"Methods for Calculating Neutron and Gamma-Ray Attenuation," Chapter 3 of *Weapons Radiation Shielding Handbook,* L. S. Abbott, H. C. Claiborne, and C. E. Clifford, editors, Defense Atomic Support Agency, Washington, DASA-1892-3 (March 1968).

STRAKER, E. A.
"Comments on Shielding Standards," in *Proceedings of the Special Panel Discussion of Shielding Standards, Thirteenth Annual Meeting of the American Nuclear Society,* ANS-SD-6 (June 12, 1967).

"Experimental Evaluation of Minima in the Total Neutron Cross Sections of Several Shielding Materials," ORNL-TM-2242 (June 1968).

"Sensitivity of Neutron Transport in Oxygen to Various Cross-Section Sets," ORNL-TM-2252 (June 26, 1968).

STRAKER, E. A., and F. R. MYNATT*
"Calculations of the Effect of the Air-Ground Interface on the Transport of Fission Neutrons Through the Atmosphere," ORNL-TM-1819 (Nov. 1, 1967).

STRAKER, E. A., and D. K. TRUBEY
"Comments on Benchmarks, Milestones, and Testing in the Area of Radiation Transport," ORNL-TM-2148 (Mar. 22, 1968).

TEXTOR, R. E.,* and V. V. VERBINSKI
"05S: A Monte Carlo Code for Calculating Pulse-Height Distributions Due to Monoenergetic Neutrons Incident on Organic Scintillators," ORNL-4160 (February 1968).

*Non-Division personnel.

THOMAS, J. T.
"The Effect of Unit Shape on the Criticality of Arrays," ORNL-CDC-4 (October 1967).

TRUBEY, D. K.
"Use of ICRU-Defined Quantities and Units in Shielding," ORNL-RSIC-16 (1968).

VERBINSKI, V. V., and W. R. BURRUS
"Direct and Compound-Nucleus Neutrons from 14-18 MeV Protons on ^{9}Be, ^{14}N, ^{27}Al, ^{56}Fe, ^{115}In, ^{181}Ta, and ^{208}Pb and from 33 MeV Bremmstrahlung on ^{27}Al, ^{206}Pb, ^{208}Pb, and ^{209}Bi," ORNL-TM-2270 (July 3, 1968).

VERBINSKI, V. V., W. R. BURRUS, T. A. LOVE, W. ZOBEL, and N. W. HILL*
"Calibration of an Organic Scintillator for Neutron Spectrometry," ORNL-TM-2183 (Apr. 8, 1968).

VERBINSKI, V. V., F. G. PEREY, J. K. DICKENS, and W. R. BURRUS
"Neutrons from ^{9}Be(α,n) Reaction for E_{α} Between 6 and 10 MeV," ORNL-TM-1891 (Aug. 24, 1967).

WACHTER, J. W., W. R. BURRUS, and W. A. GIBSON
"Neutron and Proton Spectra from Targets Bombarded by 160-MeV Protons," *Phys. Rev.* **161**, 971 (1967).

WEBSTER, J. W.
"Minimum Thickness of a Water-Reflected Infinite Slab of an Aqueous Solution of $^{235}UO_2F_2$ at Optimum Concentration," *Nucl. Sci. Eng.* **32**, 133 (1968).

WESTON, L. W., R. GWIN, G. DeSAUSSURE, R. R. FULLWOOD,* and R. W. HOCKENBURY*
"Measurement of the Neutron Fission and Capture Cross Sections for ^{233}U in the Energy Region 0.4 to 2000 eV," ORNL-TM-2140 (Apr. 8, 1968).

YOST, K. J.
"A Method for the Calculation of Neutron-Capture Gamma-Ray Spectra," *Nucl. Sci. Eng.* **32**, 62 (1968).

YOST, K. J., and N. M. GREENE*
"CSP-I: A Neutron Cross-Section Averaging Package for Use with the 05R Data Tape," ORNL-4130 (December 1967).

YOST, K. J., and M. SOLOMITO
"Sensitivity of Gamma-Ray Dose Calculations to the Energy Dependence of Gamma-Ray Production Cross Sections," ORNL-TM-2209 (May 24, 1968).

YOUNG, M. H.,* and W. R. BURRUS
"A Digital Filter for Unfolding Pulse-Height Distributions," *Nucl. Instr. Methods* **62**, 82 (1968).

ZOBEL, W., F. C. MAIENSCHEIN, J. H. TODD,* and G. T. CHAPMAN
"Gamma Rays from Bombardment of ^{7}Li, Be, ^{11}B, C, O, Mg, Al, Co, Fe, and Bi by 16- to 160-MeV Protons and 59-MeV Alpha Particles," ORNL-4183 (November 1967).

"Gamma Rays from Bombardment of Light and Intermediate Weight Nuclei by 16- to 160-MeV Protons and 59-MeV Alpha Particles," *Nucl. Sci. Eng.* **32**, 392 (1968).

PAPERS

SIAM National Meeting, Conference on Applied Probability Theory, Washington, D.C., June 12–15, 1967 – proceedings not yet available.

COVEYOU, R. R., "The Mathematics of Random Number Generation: 'Random Number Generation is Too Important to be Left to Chance.'"

---

*Non-Division personnel.

Seminar-Workshop on the Discrete Ordinates (S_n) Method for Radiation Transport Calculations, August 14–16, 1967 – papers published in *A Review of the Discrete Ordinates S_n Method for Radiation Transport Calculations,* ORNL-RSIC-19 (October 1967), D. K. Trubey and Betty F. Maskewitz, editors.

ALSMILLER, R. G., Jr., J. BARISH,* R. T. BOUGHNER,* and W. W. ENGLE,* "The Discrete Ordinates Method Coupled with the Straightahead Approximation for Use in High-Energy Accelerator Shielding Studies" (p. 109).

CAIN, V. R., "The Use of Discrete Ordinates Adjoint Calculations" (p. 85).

MYNATT, F. R.,* "Angle-Dependent Spectra Emergent from Large Lead and Polyethylene Slab Shields" (p. 139).

STRAKER, E. A., N. M. GREENE,* and R. J. RODGERS,* "Calculations of Neutron Transport in the Atmosphere and the Effect of Input Cross Sections" (p. 155).

YOST, K. J., "The Energy Dependence of Gamma-Ray Production Cross Sections and Their Utilization in S_n Codes" (p. 175).

International Conference on the Physics Problems of Reactor Shielding, September 26–29, 1967, Harwell, England, Sponsored by the British Nuclear Energy Society with The Institute of Physics and The Physical Society – proceedings not yet available.

CLIFFORD, C. E., F. J. MUCKENTHALER, R. E. MAERKER, E. A. STRAKER, and F. R. MYNATT,* "Neutron Transport Studies in Ducts and Simple Shields: Comparison of Monte Carlo and Discrete Ordinates Calculations with Experimental Results from the Tower Shielding Facility."

First Regular Meeting of the Division of Nuclear Physics, Madison, Wisconsin, October 23–25, 1967 – papers abstracted in *Bulletin of the American Physical Society,* Series II, Vol. 12, No. 8.

DICELLO, J. R.,* G. J. IGO,* W. T. LELAND,* and F. G. PEREY, "Differential Cross Sections for the Elastic Scattering of Protons from ^{40}Ca Between 9.8 MeV and 21.7 MeV" (p. 1184).

14th Annual Nuclear Science Symposium, IEEE, October 31–November 2, 1967, Los Angeles, California – proceedings not available.

BURRUS, W. R., F. E. BERTRAND, and T. A. LOVE, "A Four-Parameter E vs dE/dx and Time-of-Flight Computerized Charged Particle Experiment."

RUST, B. W.,* and W. R. BURRUS, "Counting Schemes for Nuclear Data Acquisition on Small Computers."

YOUNG, M. H.,* and W. R. BURRUS, "A True Gamma-Radiation Spectrometer."

1967 Fall Meeting of the Southeastern Section of the American Physical Society, Clemson, South Carolina, November 2–4, 1967 – papers abstracted in *Bulletin of the American Physical Society,* Series II, Vol. 13, No. 2.

GUTHRIE, M. P., R. G. ALSMILLER, Jr., and H. W. BERTINI, "π^- Capture in Carbon, Oxygen, and Aluminum" (p. 243).

COLEMAN, W. A., and R. G. ALSMILLER, Jr., "Thermal-Neutron Production from High-Energy Protons in Thick Targets" (p. 242).

1967 Winter Meeting of the American Nuclear Society, Chicago, Illinois, November 5–9, 1967 – papers summarized in *Transactions of the American Nuclear Society,* Vol. 10, No. 2.

DeSAUSSURE, G., and H. DERRIEN,* "A Simultaneous Multilevel Analysis of the ^{235}U Capture and Fission Cross Sections for Neutron Energies Below 60 eV" (paper presented at special session but not published).

FRENCH, R. L.,* "An Extension of the Engineering Method to Improve Fallout Protection Factor Calculations for Basements" (p. 722).

*Non-Division personnel.

GREENE, N. M.,* and F. R. MYNATT,* "Fast-Neutron Response Function Calculations for Polyethylene-Moderated Fission Chambers" (p. 640).

MIHALCZO, J. T., J. J. LYNN, J. E. WATSON,* and R. W. DICKINSON,* "Superprompt Critical Behavior of a Uranium-Molybdenum Assembly" (p. 611).

STRAKER, E. A., and R. J. RODGERS,* "Neutron Transport in the Atmosphere" (p. 730).

THOMAS, J. T., "Criticality of ^{233}U Aqueous Nitrate Solution in Reflected and Unreflected Arrays" (p. 538).

WEBSTER, J. W., "Monte Carlo Criticality Calculations for Low-Enriched Thermal Reactors" (p. 539).

WEBSTER, J. W., "The Nuclear Safety of Aqueous Solutions of ^{233}U and ^{235}U" (p. 539).

YOST, K. J., "Calculation of Neutron-Capture Gamma-Ray Spectra" (p. 522).

Meeting of the American Physical Society, Chicago, Illinois, January 29–February 1, 1968 – papers abstracted in *Bulletin of the American Physical Society,* Series II, Vol. 13, No. 1.

BERTRAND, F. E., R. W. PEELLE, T. A. LOVE, W. R. BURRUS, and N. W. HILL,* "Differential Cross Sections for the Charged Particles Produced by 60-MeV Protons on Carbon, Iron, and Bismuth" (p. 82).

Second Conference on Neutron Cross Sections and Technology, American Physical Society, Washington, D.C., March 4–7, 1968 – proceedings to be published by the National Bureau of Standards (D. T. Goldman, chairman).

DICKENS, J. K., E. EICHLER,* F. G. PEREY, P. H. STELSON,* J. ASHE,* and D. O. NELLIS,* "The ^{14}N($n,n'\gamma$) Reaction for $6.0 \leqq E_n \leqq 8.4$ MeV.

YOST, K. J., and M. SOLOMITO, "Sensitivity of Gamma-Ray Dose Calculations to the Energy Dependence of Gamma-Ray Production Cross Sections."

1968 Spring Meeting of the American Physical Society, Washington, D.C., April 22–25, 1968 – papers abstracted in *Bulletin of American Physical Society,* Series II, Vol. 13, No. 4.

CHAPMAN, G. T., R. L. MACKLIN,* J. H. GIBBONS,* and R. NUTT,* "Observations of Upper Atmospheric Gamma Radiation [$60 < E_\gamma$ (keV) < 2000 eV] Using Ge(Li) Detectors" (p. 695).

MARUSAK, A. L.,* F. G. PEREY, and P. H. STELSON,* "Measurements of (d,n) Reactions on ^{58}Ni, ^{60}Ni, ^{62}Ni, and ^{64}Ni" (p. 725).

VERBINSKI, V. V., "Measurements and Calculations of (p,xn) Spectra and 33-MeV-Bremsstrahlung (γxn) Spectra" (p. 718).

Fourteenth Annual Meeting of the American Nuclear Society, Toronto, Ontario, Canada, June 9–13, 1968 – papers summarized in *Transactions of the American Nuclear Society,* Vol. 11, No. 1.

ALSMILLER, R. G., Jr., M. LEIMDORFER,* and J. BARISH,* "High-Energy Muon Transport and the Muon Backstop for a 200-GeV Accelerator" (p. 404).

ALSMILLER, R. G., Jr., F. R. MYNATT,* J. BARISH,* and W. ENGLE,* "The Use of the Discrete Ordinates Method to Transport High-Energy (<400 MeV) Neutrons" (paper presented at special session but not published).

ARMSTRONG, T. W., "Monte Carlo Calculation of the Nucleon-Meson Cascade Induced in Iron by 1- and 3-GeV Protons," (p. 405).

ARMSTRONG, T. W., "Monte Carlo Calculations of Residual Nuclei Production on a Thick Iron Target Bombarded by 1- and 3-GeV Protons and Comparison with Experiment" (paper presented at special session but not published).

---

*Non-Division personnel.

ARMSTRONG, T. W., and R. G. ALSMILLER, Jr., "An Estimate of the Prompt Photon Spectrum Arising from Cosmic-Ray Bombardment of the Moon" (p. 20).

COLEMAN, W. A., and R. G. ALSMILLER, Jr., "Calculation of Several Characteristics Associated with Particle Behavior of an ING Concept Using a Revised Version of NTC" (p. 402).

DeSAUSSURE, G., "Multilevel Analysis of the ^{233}U Capture and Fission Cross Sections up to 60 eV" (paper presented at special session but not published).

ELLIS, J. F., "An Instrument for Measuring Mechanical Vibrations in Fast Pulse Reactor Cores" (p. 342).

GWIN, R., L. W. WESTON, G. DeSAUSSURE, R. W. INGLE,* J. H. TODD,* F. E. GILLESPIE,* R. W. HOCKENBURY,* and R. C. BLOCK,* "Measurement of the Neutron Fission and Absorption Cross Sections of ^{239}Pu Over the Energy Region 0.01 eV to 30 keV" (paper presented at special session but not published).

JOHNSON, E. B., and C. E. NEWLON,* "The Effect of Steel-Water Reflectors on the Criticality of Low-Enriched Uranyl Fluoride Solution" (p. 383).

MAGNUSON, D. W., "Critical Experiments at H:^{235}U Ratios from 0 to 5" (p. 383).

MIHALCZO, J. T., "Monte Carlo Calculations of Thick-Graphite-Reflected Uranium-Metal Critical Assemblies" (p. 385).

MYNATT, F. R., F. J. MUCKENTHALER, and P. N. STEVENS,* "Angle-Dependent Spectra Emergent from Slab Shields – Comparison of Two-Dimensional Discrete Ordinates Calculations with Experiment" (p. 195).

MOONEY, L. G.,* and M. B. WELLS,* "Calculations of Fission-Product Gamma-Ray Doses in Single-Compartment Above-Ground Concrete Structures" (p. 423).

PEREZ, R. B., "The Experimental Aspects of Neutron Wave and Pulse Propagation" (p. 41).

PEREZ, R. B., G. M. WATSON,* P. NELSON,* R. M. CARROLL,* and O. SISMAN,* "A Dynamic Method to Study In-Pile Fission-Gas Release" (p. 271).

RITTS, J. J.,* E. SOLOMITO, and P. N. STEVENS,* "Calculations of Neutron Fluence-to-Kerma Factors for the Human Body" (p. 403).

SELPH, W. E.,* J. M. NEWELL,* and C. E. BAYER,* "Albedo Monte Carlo Analysis of Fast-Neutron Transport in a Missile Launch Tube" (p. 412).

STRAKER, E. A., "Application of Adjoint Flux Calculations to Monte Carlo Biasing," invited paper, listed by title only (p. 414).

STRAKER, E. A., "Time-Dependent Neutron and Secondary Gamma-Ray Transport in an Air-Over-Ground Geometry" (p. 410).

THOMAS, J. T., "Monte Carlo Calculated Criticality of Subcritical ^{233}U-Metal Spheres in Cubic Geometry" (p. 386).

YOST, K. J., "A Method for Approximating the Effect of the Energy Dependence of Neutron-Capture Gamma-Ray Spectra on Capture Gamma-Ray Dose Calculations" (p. 417).

Fifth Air Force Cambridge Research Laboratory Scientific Balloon Symposium, Wentworth by the Sea, Portsmouth, New Hampshire, June 17–19, 1968 – papers abstracted in *Preliminary Program.*

CHAPMAN, G. T., J. H. GIBBONS,* R. L. MACKLIN,* R. P. CUMBY,* and H. W. PARKER,* "The Use of Large Lithium-Drifted Germanium Diodes in Gamma-Ray Spectral Measurements at High Altitudes" (p. 16).

---

*Non-Division personnel.

ORNL-4280
UC-34 – Physics

INTERNAL DISTRIBUTION

1. L. S. Abbott
2. F. S. Alsmiller
3. R. G. Alsmiller, Jr.
4. T. W. Armstrong
5. J. Ashe
6. J. Barish (K-25)
7. H. W. Bertini
8. N. A. Betz
9. A. L. Boch
10. T. V. Blosser
11. R. S. Booth
12. R. T. Boughner
13. C. E. Burgart
14. V. R. Cain
15. A. D. Callihan (Y-12)
16. G. T. Chapman
17. H. C. Claiborne
18. F. H. S. Clark
19. C. E. Clifford
20. R. R. Coveyou
21. S. N. Cramer
22. J. T. DeLorenzo
23. G. de Saussure
24. J. K. Dickens
25. L. Dresner
26. E. Eichler
27. J. F. Ellis (Y-12)
28. M. B. Emmett
29. W. W. Engle, Jr. (K-25)
30. J. L. Fowler
31. R. M. Freestone, Jr.
32. C. Y. Fu
33. T. Gabriel
34. F. E. Gillespie
35. L. W. Gilley
36. J. H. Gillette
37. N. M. Greene (K-25)
38. M. L. Gritzner (K-25)
39. Jane Gurney
40. M. P. Guthrie
41. R. Gwin
42. J. A. Harvey
43. K. M. Henry, Jr.
44. N. W. Hill
45. L. B. Holland
46. J. L. Hull
47. R. W. Ingle
48. D. C. Irving
49. E. B. Johnson (Y-12)
50. W. H. Jordan
51. D. T. King
52. W. E. Kinney
53. S. Kremer
54. R. Kuebbing
55. C. E. Larson
56. C. LeRigoleur
57. J. Lewin
58. E. C. Long (K-25)
59. T. A. Lewis
60. T. A. Love
61. H. G. MacPherson
62. E. Madden
63. R. E. Maerker
64. D. W. Magnuson (Y-12)

65–114. F. C. Maienschein

115. J. J. Manning
116. A. L. Marusak
117. B. F. Maskewitz
118. J. W. McConnell
119. C. O. McNew
120. J. T. Mihalczo (Y-12)
121. J. K. Millard
122. H. C. Moran
123. F. J. Muckenthaler
124. F. R. Mynatt (K-25)
125. D. O. Nellis
126. C. E. Newlon (K-25)

127–128. R. B. Parker

129. R. W. Peelle
130. S. K. Penny
131. C. M. Perey
132. F. G. Perey
133. R. Perez
134. P. H. Pitkanen
135. S. J. Raffety
136. J. W. Reynolds
137. J. J. Ritts
138. R. J. Rodgers (K-25)
139. E. R. Rohrer (Y-12)
140. B. W. Rust (K-25)
141. R. T. Santoro
142. G. R. Satchler

143. F. A. R. Schmidt
144. Y. Shima
145. E. G. Silver
146. M. J. Skinner
147. E. Solomito
148. P. H. Stelson
149. P. N. Stevens
150. J. R. Stockton
151. E. A. Straker
152. R. Textor (K-25)
153. J. T. Thomas (Y-12)
154. C. L. Thompson
155. H. A. Todd
156. J. H. Todd
157. D. K. Trubey
158. W. C. Tunnell (Y-12)
159. J. W. Wachter
160. D. H. Wallace (K-25)
161. D. R. Ward
162. J. W. Webster
163. A. M. Weinberg
164. L. W. Weston
165. G. C. Williams
166. L. R. Williams (K-25)
167. D. R. Winkler
168. G. Young
169. K. J. Yost
170. W. Zobel
171. E. R. Cohen (consultant)
172. B. C. Diven (consultant)
173. W. N. Hess (consultant)
174. M. H. Kalos (consultant)
175. L. V. Spencer (consultant)
176. Radiation Shielding Information Center
177. Biology Library
178–180. Central Research Library
181–182. ORNL Y-12 Technical Library, Document Reference Section
183–231. Laboratory Records Department
232. Laboratory Records ORNL R.C.

EXTERNAL DISTRIBUTION

233–682. Given external distribution
683. P. B. Hemmig, Division of Reactor Development, U.S. Atomic Energy Commission, Washington, D.C.
684. I. F. Zartman, Division of Reactor Development, U.S. Atomic Energy Commission, Washington, D.C.
685. J. A. Swartout, Union Carbide Corporation, New York
686. W. W. Grigorieff, Assistant to the Executive Director, Oak Ridge Associated Universities, Oak Ridge, Tennessee
687. Laboratory and University Division, AEC, ORO
688–958. Given distribution as shown in TID-4500 under Physics category (25 copies – CFSTI)